

Aus der Radiologischen Universitätsklinik der Universität Heidelberg
Abteilung für Radioonkologie und Strahlentherapie
Ärztlicher Direktor: Prof. Dr. med. Dr. rer. nat. Jürgen Debus

Probabilistic Treatment Planning for Carbon Ion Therapy

Inauguraldissertation zur Erlangung des
Doctor scientiarum humanarum (Dr. sc. hum.) an der Medizinischen
Fakultät Heidelberg der Ruprecht-Karls-Universität

vorgelegt von
Hans-Peter Wieser
aus
Bad Reichenhall, Deutschland

May 2, 2019

Dekan: Herr Prof. Dr. Andreas Draguhn
Doktorvater: Herr Prof. Dr. Christian Karger

Preface

"The only certainty in science is uncertainty!"

anonymous scientist

Every prediction, measurement or estimation is inevitably subject to uncertainty. No matter how precisely predictions or estimation models will be designed or how accurately measurement devices will be built, under the assumption of real-world conditions, there is always going to be a residual uncertainty. This is why the best path forward is to accept and mitigate uncertainties. The same paradigm also holds true for radiotherapy where ionizing radiation is targeted to malignant cells. This manuscript presents an uncertainty quantification and mitigation method for carbon ion therapy which is known to be prone to uncertainties. In a subsequent optimization step the influence of uncertainties is minimized to obtain a treatment plan that potentially results in safer patient treatments.

This work was funded by the German Research Foundation Grant No. BA 2279/3-1 and was carried out at the German Cancer Research Center (DKFZ) in Heidelberg in close collaboration with the Max Planck Institute for Intelligent Systems in Tübingen between February 2015 and September 2018.

Disclosure: This manuscript builds upon the work of (Bangert et al., 2013) for protons and photons. To implement and evaluate the new methodology, first, an open-source treatment planning module for carbon ions was realized and validated against a clinical system. Results in that regard were published in print (Wieser et al., 2017a, 2018). The first findings of the new methodology are presented in Chapter III and were first presented 2016 at the ICCR meeting in London and later published in print (Wieser et al., 2017b). Further, I contributed to two other publications from my colleague Niklas Wahl investigating two specific aspects of the new approach (Wahl et al., 2017, 2018a). The latest findings, presented in the second half of Chapter III, have not yet been published but were orally presented at the ESTRO Physics Workshop 2017 and the ESTRO 37 annual meeting. Full disclosure of scientific contributions can be found at the end of the manuscript. Lastly, the new algorithm and the core result of this Ph.D. thesis are made available in a Matlab-based code repository APMtoolbox* and are publicly accessible from the file hosting service GitHub.

Animations: The digital version of this manuscript contains PDF-animations that can be viewed on screen. The animations are generated employing the animate[†] L^AT_EX package and are displayed correctly if the PDF is viewed in Adobe[‡] Acrobat Reader > 3 (non-mobile), PDF-XChange[§] or Foxit Reader[¶]. However, all relevant information is still available if other PDF viewers or the printed version is used for reading as the animations are mainly of illustrative value.

*<https://github.com/e0404/APMtoolbox>

†<https://ctan.org/pkg/animate> [accessed May 2, 2019]

‡<https://get.adobe.com/reader/> [accessed May 2, 2019]

§<https://www.pdf-xchange.de> [accessed May 2, 2019]

¶<https://www.foxitsoftware.com/pdf-reader/> [accessed May 2, 2019]

Contents

| | |
|---|------------|
| List of Figures | vii |
| List of Tables | x |
| I. Introduction | 1 |
| II. Background | 6 |
| II.1. Particle Therapy Physics | 6 |
| II.1.1. Particle Interaction Mechanisms | 6 |
| II.1.2. Linear Energy Transfer | 10 |
| II.2. Radiobiology | 11 |
| II.2.1. Relative Biological Effectiveness - RBE | 12 |
| II.2.2. Cell Survival and the Linear Quadratic Model | 12 |
| II.2.3. Local Effect Model LEM | 14 |
| II.3. Radiation Treatment Planning | 17 |
| II.3.1. Treatment Planning and Intensity Modulated Particle Therapy | 18 |
| II.3.2. Pencil Beam Scanning | 20 |
| II.4. Treatment Planning and Robust Optimization | 21 |
| II.4.1. Physical Beam Model | 21 |
| II.4.2. Biological Treatment Planning Pipeline | 22 |
| II.4.3. Biological Beam Model | 25 |
| II.4.4. Inverse Planning | 26 |
| II.4.4.1 The Optimization Problem | 26 |
| II.4.4.2 Clinical Objectives and Constraints | 28 |
| II.4.4.3 Single Field and Multi Field Optimization | 29 |
| II.5. Uncertainties in Carbon Ion Therapy | 29 |
| II.5.1. Physical Uncertainties | 30 |
| II.5.2. Biological Uncertainties | 32 |
| II.5.3. Uncertainty Quantification and Mitigation | 34 |
| II.5.3.1 Uncertainty Quantification | 35 |
| II.5.3.2 Uncertainty Mitigation | 36 |
| II.5.4. Uncertainty Considerations for Carbon Ion Therapy | 39 |
| III. Material and Methods | 41 |
| III.1. Functional Approximation of Base Data | 42 |
| III.1.1. Physical Dose of Protons & Carbon Ions | 42 |
| III.1.2. Biological Effect | 44 |
| III.2. Physical Uncertainties | 46 |

CONTENTS

| | |
|---|------------|
| III.2.1. Uncertainty Model | 46 |
| III.2.2. Expectation Value - First Raw Moment | 48 |
| III.2.3. Mixed Terms and Covariance | 51 |
| III.2.4. Fractionation Effects | 55 |
| III.3. Biological Uncertainties | 60 |
| III.3.1. Gaussian Process | 61 |
| III.3.2. Integration into APM | 61 |
| III.3.3. Biological Uncertainty Model | 63 |
| III.3.4. Moment Calculation | 65 |
| III.4. Probabilistic Optimization of the Biological Effect | 70 |
| III.5. From Effect to RBE weighted Dose | 71 |
| III.6. Validation and Evaluation | 73 |
| III.6.1. Basic Dose Calculation and Optimization Functionalities | 73 |
| III.6.2. Analytical Probabilistic Modeling | 74 |
| III.6.3. γ -analysis | 77 |
| III.6.4. Smooth Animations | 79 |
| IV. Results | 80 |
| IV.1. Results of Validating a Treatment Planning System | 80 |
| IV.1.1. Particle Dose Calculation Module | 80 |
| IV.1.1.1 Elemental Proton Pencil Beams | 81 |
| IV.1.1.2 Elemental Carbon Ion Pencil Beams | 82 |
| IV.1.1.3 Cranial Patient | 83 |
| IV.1.2. Optimization Validation | 86 |
| IV.1.3. Performance Analysis | 87 |
| IV.2. Results of Analytical Probabilistic Modeling | 88 |
| IV.2.1. One dimensional Artificial Phantom | 88 |
| IV.2.1.1 Uncertainty Quantification | 88 |
| IV.2.1.2 Conventional vs. Probabilistic Optimization | 94 |
| IV.2.1.3 Robustness Analysis for different PDFs | 99 |
| IV.2.1.4 Probabilistic Optimization of different LEM Versions | 102 |
| IV.2.1.5 Fractionation | 104 |
| IV.2.2. Implementation of APM | 105 |
| IV.2.2.1 Proof of concept - physical uncertainties | 105 |
| IV.2.2.2 Proof of concept - biological and physical uncertainties | 108 |
| IV.2.2.3 Comparison of robust optimization techniques | 119 |
| IV.2.2.4 Smooth Animations | 121 |
| V. Discussion | 122 |
| V.1. Numerical Approximations | 123 |
| V.2. Accuracy of Pencil Beam Algorithm | 125 |
| V.3. Probabilistic Optimization | 127 |

CONTENTS

| | | |
|--------------------|---|------------|
| V.4. | Sampling | 128 |
| V.5. | Impact of Biological Uncertainties | 129 |
| V.6. | Gaussian Error Assumption | 132 |
| V.7. | Performance | 133 |
| V.8. | Applicability to other Ion Types | 135 |
| VI. | Conclusion | 137 |
| VII. | Summary | 141 |
| VIII. | Zusammenfassung | 143 |
| Appendix A. | Appendix A | 145 |
| I.1. | Properties of Multivariate Normal distributions: | 145 |
| I.2. | Recurring Symbols and Notation: | 146 |
| Appendix B. | Appendix B | 147 |
| II.1. | Analytical Moment Calculations | 147 |
| II.1.1. | First moment of the Biological Effect | 147 |
| II.1.2. | Second raw moment of the Biological Effect | 147 |
| II.1.3. | First Raw Moment of the Lateral Dose | 149 |
| II.1.4. | Second Raw Moment of the Lateral Dose | 149 |
| II.1.5. | Third Raw Moment of the Lateral Dose | 150 |
| II.1.6. | First Raw Moment of Depth Dose | 151 |
| II.1.7. | Second Raw Moment of Depth Dose | 151 |
| II.1.8. | Third Raw Moment of Depth Dose | 153 |
| II.1.9. | Fractionation | 154 |
| II.1.10. | First Raw Moment of Depth Dose of Biological Uncertainties | 155 |
| II.1.11. | Second Raw Moment of Depth Dose of Biological Uncertainties | 156 |
| | Bibliography | 157 |
| | Disclosure | 163 |
| | Curriculum Vitae | 167 |
| | Acknowledgments | 169 |
| | Affidavit | 170 |

List of abbreviations

| | |
|--------------|---|
| APM | Analytical Probabilistic Modeling |
| CT | Computed Tomography |
| CTV | Clinical Target Volume |
| DNA | Deoxyribonucleic Acid |
| DTA | Distance to Agreement |
| DVH | Dose Volume Histogram |
| EDVH | Expected RBE weighted Dose Volume Histogram |
| EUD | Equivalent Uniform Dose |
| GP | Gaussian Process |
| HU | Hounsfield Units |
| IMPT | Intensity Modulated Particle Therapy |
| ITV | Internal Target Volume |
| LEM | Local Effect Model |
| LET | Linear Energy Transfer |
| LQM | Linear Quadric Model |
| MFO | Multi Field Optimization |
| MKM | Micro Dosimetric Kinect |
| PDF | Probability Density Function |
| PTV | Planning Target Volume |
| RBE | Relative Biological Effectiveness |
| RMF | Repair Misrepair Fixation |
| rSP | Stopping Power relative to Water |
| SDDVH | Standard Deviation RBE weighted Dose Volume Histogram |
| SFUD | Single Field Uniform Dose |
| SOBP | Spread out Bragg peak |
| TPS | Treatment Planning System |
| WEPL | Water Equivalent Path Length |
| VOIs | Volumes of Interest |

List of Figures

| | | |
|---------------|--|----|
| Figure I.1 | Dose deposition characteristics of photons, protons and carbon ions | 2 |
| Figure II.1 | Stopping power and energy range relationship of protons and carbon ions | 7 |
| Figure II.2 | Relative fluence of a pseudo mono-energetic carbon ion beam | 10 |
| Figure II.3 | Relative unrestricted LET of a pseudo mono-energetic carbon ion beam . | 11 |
| Figure II.4 | Linear Quadratic Model describing the cell survival | 13 |
| Figure II.5 | Schematic illustration of the Local Effect Model | 15 |
| Figure II.6 | Schematic illustration of the ray-pencil beam concept used for treatment planning | 18 |
| Figure II.7 | 1D spread out Bragg peak of a proton beam | 19 |
| Figure II.8 | Local Effect Model I and IV predictions | 23 |
| Figure II.9 | Single particle approximation of LEM I | 24 |
| Figure II.10 | Range under- and overshoot of protons and carbon ions | 30 |
| Figure III.1 | Gaussian parameterization of proton and carbon ion depth dose profile . | 43 |
| Figure III.2 | Biological base data for carbon ion treatment planning | 44 |
| Figure III.3 | Gaussian parameterization of physical and biological carbon ion base data | 45 |
| Figure III.4 | Covariance matrixes to model the uncertainty structure | 47 |
| Figure III.5 | Expected lateral dose and expected depth-dependent linear part of the biological effect | 50 |
| Figure III.6 | Standard deviation of lateral dose and standard deviation of depth-dependent linear part of the biological effect | 55 |
| Figure III.7 | Fractionation effects of a 1D carbon ion SOBP | 59 |
| Figure III.8 | Modeling of biological uncertainties for elemental carbon ion pencil beams | 62 |
| Figure III.9 | Covariance matrix modeling biological uncertainties | 64 |
| Figure III.10 | Artificial example to mimic biological uncertainties for 1D toy problem . | 68 |
| Figure III.11 | Probabilistic quantities of the depth-dependent linear component of the biological effect | 69 |
| Figure III.12 | Nominal 1D SOBP of carbon ions in water | 76 |
| Figure IV.1 | Validation of pseudo mono-energetic proton pencil beams | 81 |
| Figure IV.2 | Validation of the physical dose of pseudo mono-energetic carbon pencil beams | 82 |
| Figure IV.3 | Validation of the RBE weighted dose of pseudo mono-energetic carbon pencil beams | 82 |
| Figure IV.4 | First part of matRad's validation for the proton patient case | 84 |
| Figure IV.5 | Second part of matRad's validation for the proton patient case | 84 |
| Figure IV.6 | First part of matRad's validation for the carbon ion patient case. | 85 |
| Figure IV.7 | Second part of matRad's validation for the carbon ion patient case. | 85 |
| Figure IV.8 | Validation of optimization functionalities within matRad | 86 |
| Figure IV.9 | Biological effect of a 1D carbon ion SOBP considering physical uncertainties | 89 |
| Figure IV.10 | Linear and quadratic components of the biological effect of a 1D carbon ion SOBP considering physical uncertainties | 91 |

LIST OF FIGURES

| | |
|--|-----|
| Figure IV.11 RBE weighted dose of a 1D carbon ion SOBP considering physical uncertainties | 91 |
| Figure IV.12 RBE weighted dose of a 1D carbon ion SOBP considering biological uncertainties | 93 |
| Figure IV.13 RBE weighted dose of a 1D carbon ion SOBP considering biological and physical uncertainties | 94 |
| Figure IV.14 Probabilistic optimization for physical uncertainties | 95 |
| Figure IV.15 Biological effect from probabilistic optimization for physical uncertainties | 96 |
| Figure IV.16 Probabilistic optimization for biological uncertainties | 97 |
| Figure IV.17 Probabilistic optimization for physical and biological uncertainties | 98 |
| Figure IV.18 Comparison of probabilistic optimization accounting for different sources of uncertainties | 99 |
| Figure IV.19 Histogram of 5000 random samples modeling a range error for a single pencil beam | 99 |
| Figure IV.20 Probability density functions used for uncertainty analysis | 100 |
| Figure IV.21 Comparisons of probabilistic quantities assuming different PDFs | 101 |
| Figure IV.22 Impact of probabilistic optimization on different LEM versions | 103 |
| Figure IV.23 Analysis of fractionation effects of a 1D carbon ion SOBP | 104 |
| Figure IV.24 Probabilistic quantities of RBE weighted dose of 3D carbon ion treatment plans | 106 |
| Figure IV.25 Standard deviation RBE weighted dose volume histogram of conventional and probabilistic optimization. | 108 |
| Figure IV.26 Probabilistic quantities of RBE weighted dose of a liver treatment plan . . | 109 |
| Figure IV.27 Probabilistic quantities of RBE weighted dose of a liver treatment plan based on probabilistic optimization | 110 |
| Figure IV.28 Expected and standard deviation RBE weighted dose volume histogram of conventional and probabilistic optimization for the liver patient | 111 |
| Figure IV.29 Fractionation effects of a liver treatment plan based on probabilistic optimization | 112 |
| Figure IV.30 Probabilistic quantities of RBE weighted dose of a intra-cranial treatment plan | 113 |
| Figure IV.31 Probabilistic quantities of RBE weighted dose of a intra-cranial treatment plan based on probabilistic optimization | 114 |
| Figure IV.32 Expected and standard deviation RBE weighted dose volume histogram of conventional and probabilistic optimization for the intra-cranial patient | 114 |
| Figure IV.33 Fractionation effects of an intra-cranial treatment plan based on conventional optimization | 115 |
| Figure IV.34 Probabilistic quantities of RBE weighted dose of a lung treatment plan based on conventional and probabilistic optimization | 116 |
| Figure IV.35 Expected and standard deviation RBE weighted dose volume histogram of conventional and probabilistic optimization for the lung patient | 116 |
| Figure IV.36 Probabilistic quantities of RBE weighted dose of a cranial treatment plan based on conventional and probabilistic optimization | 117 |
| Figure IV.37 Expected and standard deviation RBE weighted dose volume histogram of conventional and probabilistic optimization for the cranial patient . . . | 118 |
| Figure IV.38 Beam dose of RBE weighted dose of a cranial treatment plan based on conventional and probabilistic optimization | 118 |

LIST OF FIGURES

| | | |
|--------------|--|-----|
| Figure IV.39 | Expected RBE for the cranial treatment plan based on conventional and probabilistic optimization | 118 |
| Figure IV.40 | Comparison of worst case and probabilistic optimization | 119 |
| Figure IV.41 | Animation of the intra-cranial patient case modeling physical uncertainties | 121 |
| Figure V.1 | Impact of biological uncertainties for optimizing the expected squared deviation objective | 132 |
| Figure V.2 | Biological effect and its quadratic components for protons considering a variable RBE | 136 |

List of Tables

| | | |
|-------------|---|-----|
| Table II.1 | Objectives and constraints function for inverse treatment plan optimization | 28 |
| Table III.1 | Overview of statistical moments | 41 |
| Table III.2 | Patient dimensions and treatment plan parameter | 77 |
| Table IV.1 | Performance table of matRad | 87 |
| Table IV.2 | Analysis of using different PDFs for uncertainty quantification | 100 |
| Table IV.3 | LEM parameter for two different configurations | 103 |
| Table IV.4 | γ -pass rates for the validation of Analytical Probabilistic Modeling (APM) implemented in matRad | 107 |
| Table A.1 | Notation and symbols used to describe analytical probabilistic modeling for biological treatment planning | 146 |

"Growth for the sake of growth is the ideology of the cancer cell."

Edward Abbey, 1988



Introduction

Cancer is the unregulated growth of human cells anywhere in the human body with the ability to spread to other locations or organs. Causes for cancer are contributed to genetic mutations which are either inherited or triggered by environmental factors. Epidemiology studies revealed that cancer is ranked as the leading cause of death in economically developed countries. Notably, the situation for developing countries is slightly different, as cancer represents the second highest leading cause of death (Stewart and Wild, 2014). From a global perspective, the absolute number of cancer cases amounts to 14.1 million as reported in 2011 and this number is expected to rise to 24.6 million in 2030 mainly due to demographic aging and the increasing world population (Atun et al., 2015). In about ten years, nearly every sixth death will be evoked by cancer* (WHO, 2018). Despite various approaches to treat cancer such as surgery, chemotherapy, immunotherapy or new treatments, nearly two-thirds of all cancer patients are either treated with radiation therapy as primary treatment or in combination with approaches mentioned above (Atun et al., 2015). Therefore, radiotherapy represents an effective and fundamental component of cancer treatment.

The principal aim of radiotherapy is to prevent the division of cancerous cells by applying hazardous ionizing radiation. Although other parts of the cell might get damaged too, the primary goal is to break up the Deoxyribonucleic Acid (DNA) of cancerous cells. Specifically, the most employed type of radiation therapy is external beam radiation therapy which is characterized by directing high-energetic ionizing radiation (either wave- or corpuscular-radiation) from the outside into the cancerous tissue to release bound electrons from the atomic nucleus and to subsequently break the DNA. Ionizing radiation induces mutual reactions in different domains and time scales. Firstly physical-, then chemical- and ultimately biological processes are triggered. Depending on the tumor's micro-environment and other biological interdependencies (e.g. cell composition, cell cycle, oxygenation level) a relevant clinical outcome, such as tumor control, is ideally reached.

*<http://www.who.int> [accessed June 2018]

Most of external beam radiation therapy patients are treated with radiation in the form of megavolt (MV) photons generated with linear accelerators (LINACs). Another technique is provided by particle (hadron) therapy which utilizes corpuscular-radiation by means of accelerated mono-energetic charged particles created by synchrotrons or cyclotrons. Particle therapy is currently applied to only $\sim 1\%$ of radiotherapy patients because of the significantly higher costs to operate such facilities. Nevertheless, this small subfield of radiotherapy has been receiving increased attention over the past two decades due to their very different physical interactions with matter (Combs and Debus, 2013; Kamada et al., 2015). More precisely, the characteristic inverse depth dose profile of high-energetic charged particles is of interest revealing a maximum dose deposition in a certain depth. Moreover, the spatial location of the maximum dose deposition depends on the kinetic energy of the incident primary particle, which can be controlled precisely by particle accelerators (synchrotrons or cyclotrons).

Unlike photons, charged particles exhibit an increasing energy deposition in depth, which results in a pronounced maximum towards the end of the particle range. This maximum is usually referred to as Bragg peak in honor of William Bragg, who discovered this phenomenon in 1903 (Charlie Ma and Lomax, 2012). Then, 43 years later Robert R. Wilson suggested in 1946 the therapeutic use of charged particles for cancer treatment (Wilson, 1946). The characteristic depth dose profile of charged particles mainly drove the exponentially increasing number of particle acceleration installations for radiotherapy worldwide. As of now, there are 81 facilities in operation and 50 under construction[†] and close to 200.000 patients[†] have been treated with particle therapy (PTCOG, 2018). Markedly only a tenth of the patients were treated with carbon ions due to the additional technical effort.

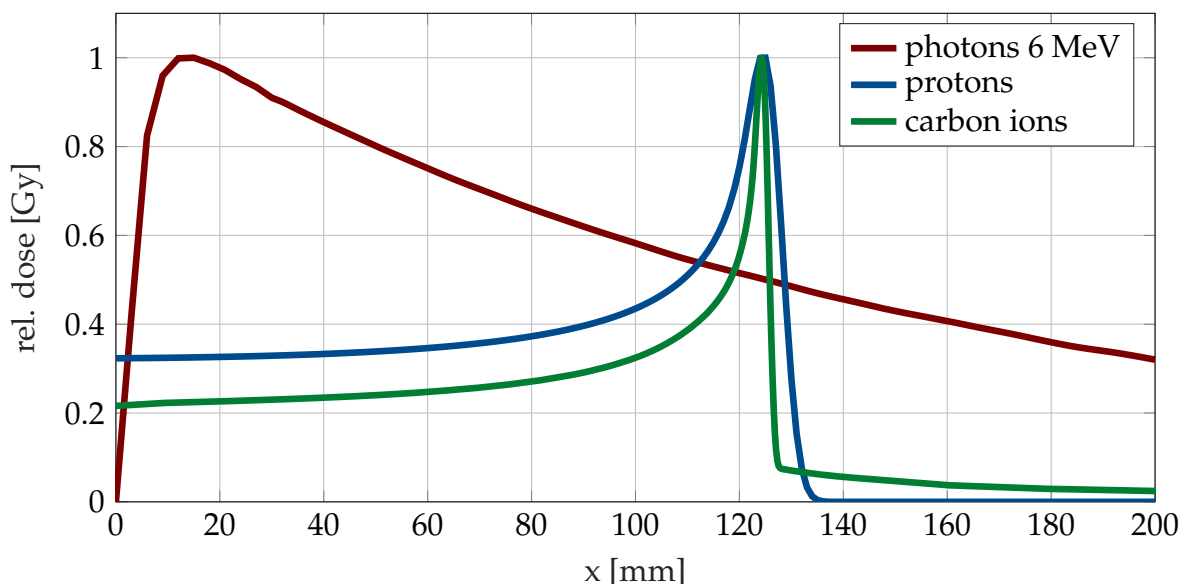


Figure I.1: Normalized depth dose profiles in water of 6 MeV photons (—), 133 MeV u^{-1} protons (—) and 250 MeV u^{-1} carbon ions (—) considering fragmentation. Protons and carbon ions reveal their characteristic Bragg peak around 124 mm, whereas the photon dose profile (—) is decaying after the initial build up effect from 0 mm to 15 mm. Note that (—) and (—) denote laterally integrated depth dose (IDD) profiles.

[†]<https://www.ptcog.ch> [accessed Nov. 2018]

Exemplary, Figure I.1 shows the decreasing depth dose profiles of photons (—) together with the Bragg peak of protons (—) and carbon ions (—). The greater selectivity of dose deposition of accelerated charged particles make it possible to create superior dose distribution compared to photons mainly due to their increased energy deposition density in depth and the abrupt dose fall-off. As a result, the integral dose to healthy tissue is reduced by a factor of 2 to 3 (Lomax et al., 1999). Protons are the most familiar charged particle employed for radiotherapy treatments followed by carbon ions. Also helium ions are available in some institutions but are as of now only used for research. A major advantage of particle therapy is the localized energy deposition pattern triggering denser ionization events than photons. Whereby the ionization density itself increases with the mass of the primary projectile. These high ionization densities induce clustered lesions to the DNA double helix structure, which is considered as damage of greater complexity since it is harder for the cell to repair. Therefore, charged particles are, at the same physical dose, more effective regarding cell killing compared to photon radiation, which is on the contrary treated as sparsely ionizing. More details about the induced biological effects and the increased effectiveness of charged particles are given later in Chapter II.2.

A state of the art component of external beam radiation therapy is treatment planning, a heavily computer-aided process, performed before the actual patient irradiation. The purpose of treatment planning is to simulate and optimize a dose distribution/deposition for the individual patient. Ideally, the tumor receives 100% of the dose needed to control the tumor, whereas the normal tissue or organs at risk (OAR) should not receive any dose in order to avoid complications in healthy tissue. However, in practice this condition can never be met due to the deposited dose in the entrance channel of each beam. For that reason, the treatment planner needs to define clinical objectives and constraints that represent a trade-off between tumor irradiation and sparing of adjacent healthy tissue. An introduction to the process of treatment planning is provided in Chapter II.3.

Analogous to any physical experiment or measurement, also the application of ionizing radiation to the patient's body is inevitably prone to uncertainties for which reason an adequate uncertainty analysis is desirable to increase the informative value of the results. In the context of radiotherapy, a simulated treatment plan is unavoidably associated with physical uncertainties, for example, due to the imperfect knowledge of the patient geometry. Especially accelerated charged particles are sensitive to such changes and are consequently susceptible to uncertainties simply because of the advantageous highly peaked depth-dose profile (see (—) and (—) in Figure I.1). This phenomenon implies that the dose distribution, simulated during treatment planning, will most probably not be the one that is applied and effective on the patient's body during irradiation as it only represents one unique "best guess" and neglects a number of uncertainty sources along the workflow (Bortfeld, 2006). Although clinicians and the medical physics community refer to treatment planning, a more suitable term in the context of uncertainties is treatment simulation or estimation as the simulated in-silico irradiation might differ substantially from the actual real world irradiation.

This work focuses on carbon ion treatment planning which requires an accurate modeling of the physical energy deposition and the biological response to radiation. In comparison to lighter ions such as protons, carbon ions produce (i) a sharper Bragg peak (dose maximum), (ii) a steeper lateral dose fall off and (iii) secondary fragments. The latter causes a non-negligible dose behind the Bragg peak (Suit et al., 2010). Focusing on biological properties, carbon ions elicit reduced cellular repair capabilities and exhibit a reduced sensitivity to radioresistant tumors, which makes them a promising radiation modality. It is known in the medical physics community that the biological properties of carbon ions play a superior role due to the lower cell survival rate they induce. It is necessary to integrate these pronounced radiobiological effects into the treatment planning process (Karger and Peschke, 2017; O. Jäkel, M. Krämer, C. P. Karger, 2001) which is why adequate bio-physical models have been developed in the past decades to predict the tissue response of heavier charged particles. The most prominent models nowadays are the Local Effect Model (LEM) (Scholz et al., 1997), the mixed-beam model (Kanai et al., 1997), and the Micro Dosimetric Kinect (MKM) (Inaniwa et al., 2015). Among other, the Heidelberg Ion Therapy (HIT) facility utilizes the LEM to account for radiobiological effects of heavier charged particles. As clinical experience in middle Europe is based on the LEM, it is also considered in this work. Admitting that these biological models are subjected to pronounced uncertainty (Friedrich et al., 2013a,b), their variability has hardly been incorporated into robust treatment planning. Moreover, even physical uncertainties are only starting to be considered in simplified form. As of now existing robust carbon ion treatment planning approaches cannot include physical and biological uncertainties alongside fractionation effects due to conceptual limitations and the involved high computational effort.

To boil down the essence, physical and biological uncertainties compromise the dose distribution and might yield to a sub-optimal patient treatment. Therefore, a full exploitation of the advantages of intensity-modulated carbon ion therapy for clinical application is hindered. To create a one-to-one correspondence between simulated and applied dose, it is key for radiotherapy to quantify and mitigate uncertainties. The aim of this thesis is to overcome problems arising from physical and biological uncertainties in carbon ion therapy by introducing a new method for robust carbon ion treatment planning. The specific goals of this thesis are first to investigate uncertainty quantification of carbon ion treatment plan uncertainties. Secondly, this information is used for uncertainty mitigation to create robust treatment plans that are less sensitive to the aforementioned uncertainties. This is achieved by developing a closed-form uncertainty quantification method that allows to simultaneously incorporate physical uncertainties, biological uncertainties as well as fractionation effects. On this basis, probabilistic optimization is carried out to create robust carbon ion treatment plans. The advantages of probabilistic optimization are investigated and quantified for several clinical scenarios. These clinical cases demonstrate how the developed methodology can be applied to clinical patient cases. The novel methodology not only increases treatment confidence but might also lower the variability of future patient treatment outcomes.

The thesis in hand is divided into the following chapters: The background is provided in Chapter II. Physical and radiobiological fundamentals are presented first in Sections II.1 and II.2. Next, the physical and biological beam model of an implemented treatment planning system serving as a basic framework for algorithm development are described in Sections II.3 and II.4. Further, Section II.5 presents existing approaches to quantify and mitigate uncertainties in carbon ion therapy. The materials and methods Chapter III outlines a newly developed methodology for uncertainty quantification and mitigation for carbon ion therapy. The first IV.1 out of two result Sections contains the validation of the developed treatment planning system whereas the second Section IV.2 focuses on the outcome of uncertainty quantification and mitigation of carbon ion treatment plans. Last, Chapters V and VI discuss and conclude the thesis.

"Nothing in life is to be feared, it is only to be understood. Now is the time to understand more, so that we may fear less."

Marie Curie, 1867- 1934

II

Background

II.1 Particle Therapy Physics

Since 1946, when charged particles were proposed for cancer treatment, the understanding of the involved physical processes have advanced substantially. This chapter provides a brief overview of fundamental characteristics of charged particles and their interaction with matter but an in-depth description can be found elsewhere (Bichsel, 2013; Durante and Paganetti, 2016; Lomax, 2009; Newhauser and Zhang, 2015; Schardt et al., 2010).

The most important physical quantity in radiotherapy is the absorbed dose d in the patient's tissue caused by ionizing radiation, which is given in Gray [$\text{Gy} = \text{J kg}^{-1}$] and defined as follows:

$$d = \frac{1}{\rho} \frac{dE}{dx} \Phi = \frac{S \Phi}{\rho} \quad (\text{II.1})$$

where $\frac{dE}{dx}$ denotes the linear stopping power S in [MeV cm^{-1}], Φ the particle fluence/flux in [cm^{-2}], which is the quotient of the number of particles N per unit and area A . Lastly ρ expresses the material density given in [g cm^{-3}]. For dose calculation, the initial particle fluence at the patient surface is determined by the particle accelerator, the density of the patient tissue is assessed via medical imaging and lastly, the stopping power S , which depends on (i) the type of charged particle (ii) its energy (iii) and the target materials, is derived from physical interaction models that are described next.

II.1.1 Particle Interaction Mechanisms

There are several interaction pathways, which according to the ICRU report 85 (Seltzer et al., 2011) can be broken down into nuclear-, radiative- and electromagnetic- (electronic) interactions. Every interaction causes the charged particle to experience a stopping power. In

detail, the mean energy loss E per unit path length x is called mass stopping power $\frac{S}{\rho}$ and depends on the type of charged particle and its energy. The mass stopping power $\frac{S}{\rho}$ given in Equation II.2 is the sum of three independent mass stopping powers caused by (i) nuclear interactions $\frac{S_{nuc}}{\rho}$, (ii) the emission of bremsstrahlung $\frac{S_{rad}}{\rho}$ and (iii) electronic interactions $\frac{S_{el}}{\rho}$:

$$\frac{S}{\rho} = \frac{1}{\rho} \left(\frac{dE}{dx} \right)_{nuc} + \frac{1}{\rho} \left(\frac{dE}{dx} \right)_{rad} + \frac{1}{\rho} \left(\frac{dE}{dx} \right)_{el} = \frac{S_{nuc}}{\rho} + \frac{S_{rad}}{\rho} + \frac{S_{el}}{\rho} \quad (\text{II.2})$$

Practically, the nuclear stopping power S_{nuc} contributes only marginally in the low-energy domain to the total mass stopping power $\frac{S}{\rho}$ as illustrated by (— · — · —) and (— · · · —) in Figure II.1(a) and can therefore, in first approximation, be neglected. In addition, the radiative stopping power S_{rad} can also be omitted for therapeutic particle energies due to their negligible contribution. On the contrary, the electronic stopping power S_{el} represents the main contributor to $\frac{S}{\rho}$. A physical theory behind the electronic stopping power S_{el} was developed by Bethe (Bethe, 1930) and Bloch (Bloch, 1933) and is given by:

$$\frac{S_{el}}{\rho} = -\frac{1}{\rho} \frac{dE}{dx} = 4\pi N_A r_e^2 m_e c^2 \frac{Z}{A} z^2 \frac{1}{\beta^2} \left[\ln \frac{2m_e c^2 \gamma^2 \beta^2}{I} - \beta^2 - \frac{\delta}{2} - \frac{C}{Z} \right] \quad (\text{II.3})$$

where N_A denotes the Avogadro's number, r_e and m_e the electron radius and mass, c the speed of light, Z the atomic number of the target material, A the atomic weight of the target material, z the charge of the projectile, $\beta = \frac{v}{c}$ with v the velocity of the projectile, γ equals $(1 - \beta^2)^{-\frac{1}{2}}$, I the mean excitation potential of the target material and finally two correction terms δ and C according to (Fano, 1963).

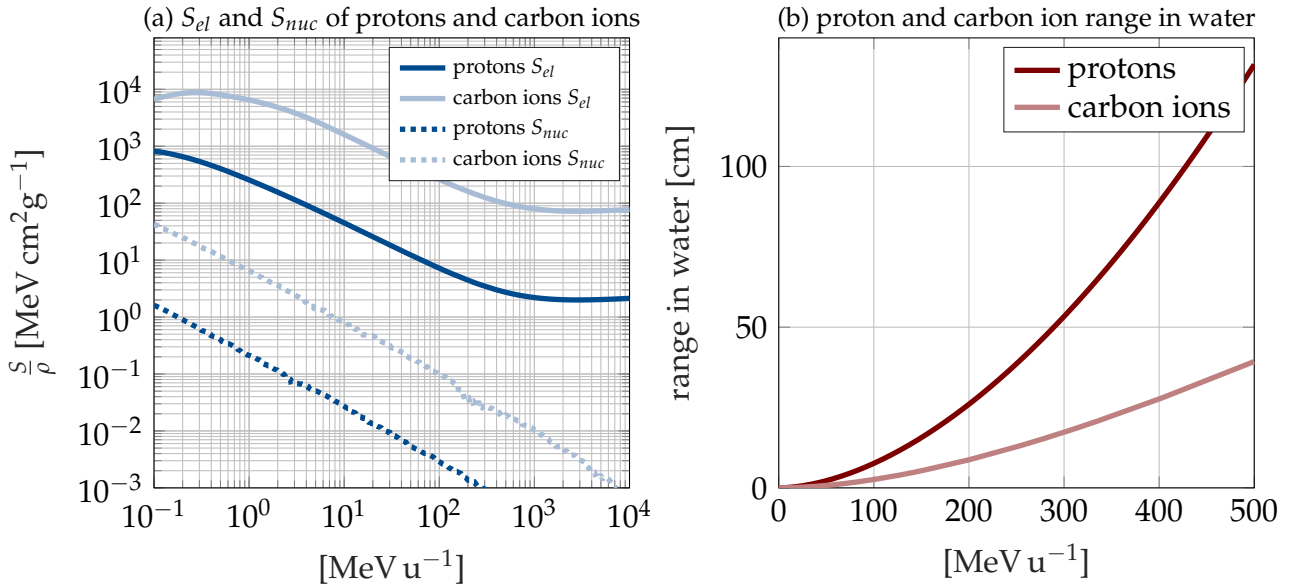


Figure II.1: Plot (a) depicts the electronic stopping powers of protons (—) and carbon ions (—) as well as the respective nuclear stopping powers (— · — · —, — · · · —) in water based on ICRU report 90. Plot (b) denotes the range-energy relation of protons (—) and carbon ions (—) in water. The range is defined as the position where the deposited energy reaches 80 % of its maximum value behind the peak which coincides with the position, where half of the incident projectiles stop. A power law fit was used to obtain the range r in [cm] by $r = \alpha E^p$, where E is given in $[\text{MeV u}^{-1}]$ and $\alpha = 0.22$. The p parameter was set to $p = 1.74$ ($p = 1.65$) for protons (carbon ions) (Bortfeld, 1997; Sanchez-Parcerisa, 2009; Sigmund et al., 2005).

Equation II.3 was taken from (Newhauser and Zhang, 2015) and defines the electronic stopping power of a set of particles and not a single particle which would be affected by statistical fluctuations. The most essential characteristics of Equation II.3 are (i) the dependence on the chemical composition $\frac{Z}{A}$ of the target material and (ii) the inversely proportional relation of energy loss and the square of the particle's velocity $\frac{dE}{dx} \propto \frac{1}{v^2}$. Directly speaking, low-energetic (low velocity) particles possess a higher stopping power than high-energetic (high velocity) particles because interaction times with bound electrons become larger. This behavior is illustrated in the left plot of Figure II.1 depicting the electronic stopping power S_{el} of protons (—) and carbon ions (—) in water. Moreover, the plot shows that heavier particles with a greater charge entail for the same energy a higher stopping power than lighter particles.

The process behind the electronic stopping power S_{el} can be explained via inelastic Coloumb interactions (inelastic collisions) and occurs when the incident particle interacts with the electromagnetic field of the target atom. The orbiting negatively charged electrons (hull electrons) of the target atom can be released by the incident positively charged particle, thereby ionizing the target atom. The freed electron can then in turn trigger a cascade of ionizations of neighboring atoms. As protons are ~ 1800 and carbon ions ~ 22000 times heavier than electrons, they stay on an almost straight trajectory and undergo depending on the target material, many thousands of such processes and continuously slow down due to loss of kinetic energy when penetrating matter.

Recapped, a fundamental rationale for charged particles is that, the higher the initial energy, the higher the velocity and the deeper particles can penetrate a medium. Particles with high kinetic energy deposit less energy and vice versa. While slowing down progressively more and more energy is deposited. Focusing on the entrance channel ($x=0$ mm) of the Bragg peak shown in the introduction in Figure I.1, where projectiles have the highest energy (highest velocity), the dose deposition is low. In contrast, when a projectile almost stops it exhibits the maximum dose deposition (Bragg peak). Referring back to the right plot of Figure II.1, which highlights the energy-range relationship of protons and carbons, it is clear that a higher energy per nucleon is required for carbon ions (250 MeV u^{-1}) to match the range of protons (133 MeV u^{-1}) by reasons of the increased weight and charge.

Although the literature often refers to mono-energetic particles, i.e., an ensemble of particles that possess the exact same kinetic energy, the situation in practice is different. Accelerators produce particles with an energy spectrum of $\sigma \sim 1\%$. As a result, different particles possess slightly different ranges and cause a longitudinal modulation or widening of the Bragg peak. This is why the expression *pseudo mono-energetic* is used in this manuscript to highlight an initial energy spread. But even if the incident primary particles would theoretically possess the exact same initial energy, a widening would still occur as the energy deposition is a stochastic process. Each particle undergoes different interactions with the target atoms and loses along the way varying amount of energy. Some undergo more and some undergo fewer interactions. This effect is called range straggling. In consequence, the effect of range

straggling will even spread or blur the Bragg peak for perfect mono-energetic particles. As a rule of thumb, heavier charged particles suffer, due to their heavier weight, much less from range straggling, which can be observed by the sharper lateral dose profile and sharper carbon ion Bragg peak.

The second dominant interaction mechanism of charged particles is represented by nuclear interactions which can, in turn, be broken down into two processes, namely elastic Coulomb interactions with the atomic nucleus and inelastic nuclear interactions. Both are described next. The first process is given by Coulomb interaction with the atomic nucleus, also termed elastic scattering, where the target nucleus stays intact. These processes occur when the particle is deflected from its trajectory by a repulsive force with the nucleus. The repulsive force is evoked by a positive charge of the incident particle and the target nucleus, which simply repel each other. In contrast, to the interaction with hull electrons, where the projectile trajectory is almost unchanged, for elastic scattering both, the incident particle and the target nucleus are in a similar mass domain and cause therefore a deflection of the projectile. Elastic scattering is the leading process for the lateral shape of dose deposition and increases with depth resulting in a divergence of incident projectiles. It is worth mentioning that carbon ions are less affected by elastic scattering because of their weight and consequently produce a sharper lateral dose gradient.

The second process of nuclear interactions, responsible for the nuclear stopping power S_{nuc} , is given by inelastic (nonelastic) interactions. Here, the projectile breaks through the Coulomb barrier of the target nucleus and enables direct interactions with hadrons of the nuclei. These processes are less common but have a profound impact. Depending on the particle type, the projectiles may fragment into their constituents and the projectiles may knock out nucleons from the target material (abrasion-ablation model) (Serber, 1947). Regardless of how, this process involves a change of the projectile trajectory, creation of fragments and yield to a reduction of primaries. Heavier charged particles, such as carbon ions, can release in the nuclear fragmentation process lighter ions which can penetrate to far deeper depths than the initial range of the projectile. Well illustrated is this phenomenon by the dose deposition behind the carbon ion Bragg peak shown in the introduction in Figure I.1 (—). Generally, only fragments possessing a lower atomic number Z than the initial projectile deposit dose behind the Bragg peak (dose tail). Logically protons do not exhibit a dose tail.

Figure II.2 illustrates the relative fluences of a pseudo mono-energetic carbon ion beam with 350 MeV u^{-1} in water and its fragments. It can be seen that carbon ions (—) stop at a range of $\sim 22.4 \text{ cm}$ and only lighter fragments, in particular, deuterium (-.-.-), helium (-.-.-), and lithium (-.-.-) contribute to the dose tail. The effect of a reduction of projectiles due to nuclear interaction can also be observed in Figure II.2 in (—). Only $\sim 40\%$ of the carbon ions reach the Bragg peak $\sim 22.4 \text{ cm}$. This effect is even more pronounced for carbon ions with higher initial energies, i.e., 400 MeV u^{-1} where only $\sim 30\%$ reach the peak. This implies that 60% , respectively 70% of the carbon ions already stopped before the Bragg peak due to nuclear interactions. As carbon ions produce multiple lighter ions when traversing matter, a

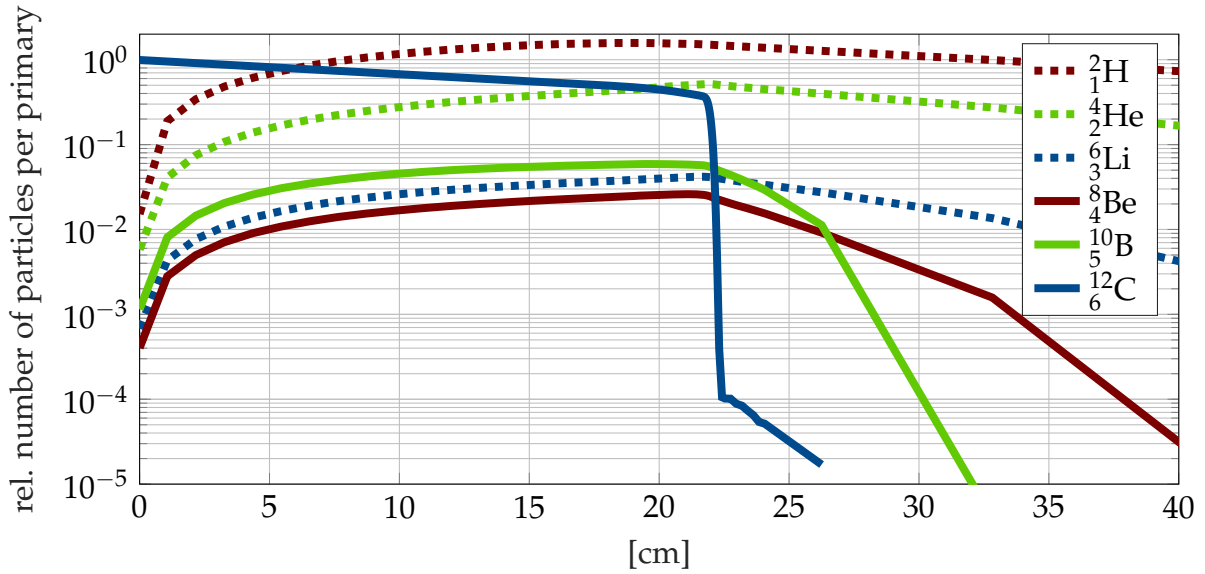


Figure II.2: Relative fluence of a pseudo mono-energetic carbon ion beam with 350 MeV u^{-1} in water including fragments. All carbon ions (—) stop around 22.4 cm and lighter ions $A \leq 6$ contribute to the dose tail. Fluences are obtained from Monte Carlo Fluka simulations modelling the Heidelberg Ion Therapy beam line.

mixed-radiation field composed of fragments with varying biological impact is created. It is described later in Section II.3 how these mixed-field effects are considered in the treatment planning process.

II.1.2 Linear Energy Transfer

The Linear Energy Transfer (LET), often referred to as restricted linear electronic stopping power, is closely related to the stopping power S and denotes for a given projectile and material according to the ICRU report 85 (Seltzer et al., 2011), the ratio of mean energy loss dE_{Δ} of charged particles due to electronic interactions by penetrating a distance dx .

$$LET_{\Delta} = \frac{dE_{\Delta}}{dx} = S_{el} - \frac{dE_{ke,\Delta}}{dx} \quad (\text{II.4})$$

where dE_{Δ} is the mean energy loss only considering secondary electrons with kinetic energy smaller than Δ . For $\Delta \rightarrow \infty$ the LET becomes the unrestricted LET (LET_{∞}) which equals directly the electronic stopping power S_{el} (Seltzer et al., 2011). Thus $E_{ke,\Delta}$ indicates the energy carried away from the primary track by high energetic secondary electrons with kinetic energy greater than Δ (Seltzer et al., 2011). Since projectiles and possible fragments are for a given initial kinetic energy in a certain depth in water not mono- but poly-energetic and consequently possess different stopping powers, it is practical to define an average LET. The two most common definitions are track-averaged and dose-averaged LET. The latter is given next:

$$LET_d(x, E_0) = \frac{\sum_Z \int_0^{\infty} \phi(x, Z, E, E_0) S_{el}^2(Z, E) dE}{\sum_Z \int_0^{\infty} \phi(x, Z, E, E_0) S_{el}(Z, E) dE} \quad (\text{II.5})$$

where x denotes the depth [mm], E_0 the initial energy of the incident primaries [MeV u^{-1}] and E the energy spectrum [MeV] of ion type Z . Figure II.3 details the unrestricted LET_∞ of a pseudo mono-energetic carbon ion beam in water with an initial energy of 350 MeV u^{-1} including corresponding fragments. The dose-averaged LET_d according to Equation II.5 is represented by (—). As all carbon ions stop $\sim 22.4 \text{ cm}$, only lighter fragments with smaller stopping powers are present in the tail, which is the main reason for the drop in LET_d (—) behind the Bragg peak.

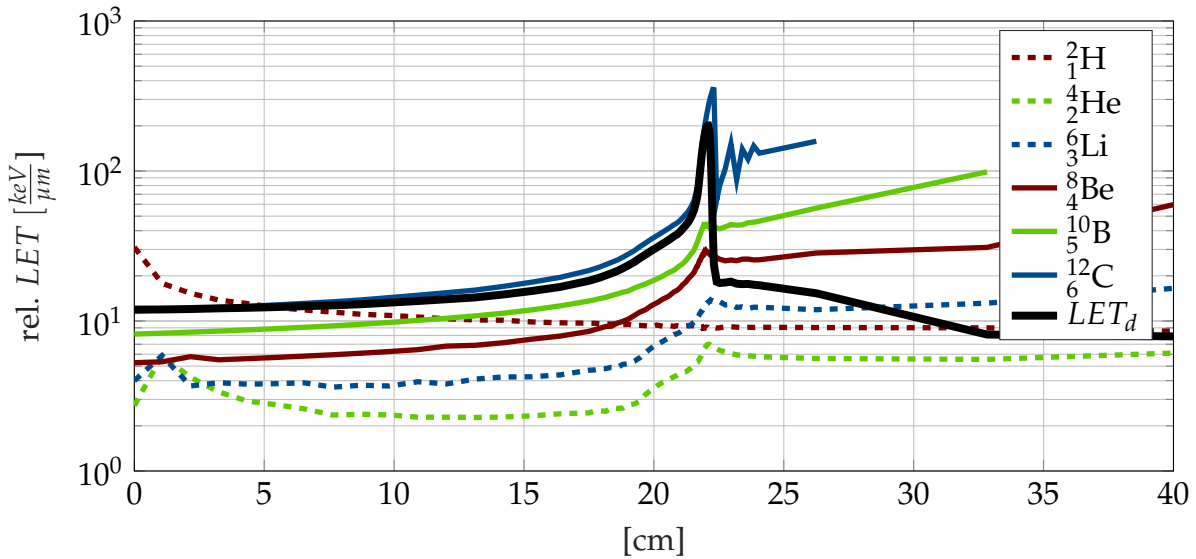


Figure II.3: Relative unrestricted LET (LET_∞) from deuterium (---) to carbon ions (—) of a pseudo mono-energetic carbon ion beam with 350 MeV u^{-1} in water. The dose-averaged LET_d considering all fragments according to Equation II.5 is shown by (—). The wiggles in (—) from 22 to 25 cm are due to statistical noise induced by the underlying Monte Carlo Fluka simulation of the HIT beam line (Krämer and Scholz, 2000).

Generally, charged particles such as carbon ions are considered as high LET radiation causing dense ionization events. The LET_d of carbon ions is roughly (Z^2) 36 times higher compared to protons. In contrast, photons are treated as low LET radiation as they induce sparse ionization events. In practice, the LET is often considered as a synonym for the radiation quality (ionization density) and its variation along the particle track directly motivates a non-linear biological response to the physical particle dose. The next chapter introduces radiobiological aspects of charged particles and then focuses on carbon ions.

II.2 Radiobiology

Radiobiology investigates radiation effects on the living organism. The affected physical, radiochemical and biological processes range in space from the atomic sub-nm level to tissue dimensions in mm and in time from fs to years. It is commonly known, that different radiation modalities induce depending on the dose, dose rate and tissue under consideration, a distinct effect on the biological system. To enable a comparison between effects of different radiation modalities, the concept of a conversion factor, labeled Relative Biological Effectiveness (RBE) was defined by the ICRU (2008).

II.2.1 Relative Biological Effectiveness - RBE

For the same physical dose (see Equation II.1), it was found empirically, that carbon ions are biologically more effective than photons (Kraft, 2000; Schardt et al., 2010). The ratio of photon dose d_x and dose deposited by ions d_I , under the premise both induce an identical effect (iso-effective), is called RBE and depicted in Equation II.6:

$$RBE = \frac{d_x}{d_I} \Big|_{iso-effective} \quad (II.6)$$

For real treatments, the RBE shows a complex three-dimensional variability and depends, among other, on the dose level, LET, tissue type and the selected endpoint. In a clinical setting, the RBE of protons relative to photons is ~ 1.1 and ranges for carbon ions from 2 to 5 within the tumor. In charged particle therapy, the RBE is weighted with the physical ion dose d_I ($RBE \times d$) and used for clinical decision making. However, to calculate the RBE it is necessary to determine iso-effectiveness by selecting a relevant endpoint for the actual clinical problem under investigation. There are numerous endpoints to identify iso-effectiveness ranging from DNA lesion induction over Normal Tissue Control Probability (NTCP) and Tumor Control Probability (TCP) to late radiation effects on the living thing. Notably, the most common endpoint for radiotherapy is cell survival, which will be described next.

II.2.2 Cell Survival and the Linear Quadratic Model

Cell survival curves are dose-response models and depict the surviving fraction of cells, i.e. cells that maintain proliferation as a function of absorbed dose. Although there are different forms of cell death, such as necrosis, apoptosis, autophagy or senescence which can be reached by various pathways, typically, if not explicitly stated otherwise, clonogenic cell survival is considered as endpoint. The expression "clonogenic" implies that a colony of cells (cell culture) is grown in-vitro from a single cell. The underlying technique is called clonogenic cell survival assay and was invented by (Puck and Marcus, 1956) in the 1950s and essentially determines the number of proliferating cells after irradiation. To obtain cell survival curves, clonogenic cell survival assays have to be repeated multiple times for several dose points to obtain confident values. An example of cell survival curves is illustrated in Figure II.4. The left plot shows a comparison of generic in-vitro cell survival curves of low LET (—) and high LET (—) radiation. The vertical lines (· · · ·) indicate the photon dose d_x and the carbon ion dose d_c , respectively, for a cell survival level of 1.16%. The corresponding RBE on this cell kill level equals $8 \text{ Gy} / 4 \text{ Gy} \approx 2$.

A cell survival curve can be parameterized sufficiently by a second order curve with two parameters α and β that can be fitted to the experimentally measured data points (Kellerer and Rossi, 1978; Sinclair, 1966). α and β are considered as radio-sensitivity parameters of the underlying Linear Quadratic Model (LQM). Although the involved processes from ionization to cell death are complex, the shape of the cell survival curve as a function of absorbed dose

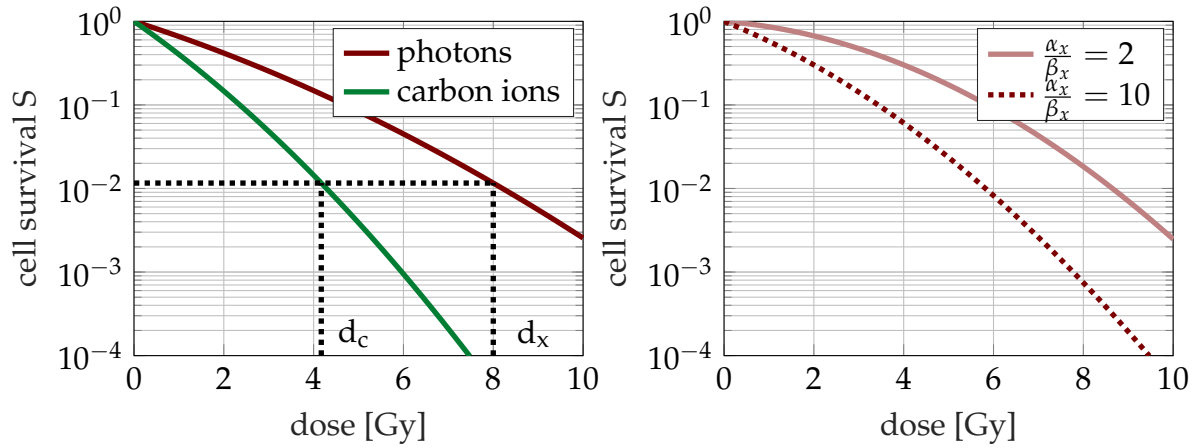


Figure II.4: Left: Generic in-vitro cell survival curves of sparsely ionizing photons (—) and densely ionizing carbon ions (—). Right: Cell survival curves irradiated with photons of two distinct generic tissues characterized by $\frac{\alpha_x}{\beta_x} = 2$ Gy (—) and 10 Gy (· · · ·).

is rather simple. The fraction of cell survival S is then given by:

$$S = e^{-\varepsilon} = e^{-(\alpha d + \beta d^2)} \quad \text{with: } \varepsilon = \alpha d + \beta d^2 \quad (\text{II.7})$$

where ε represents the biological effect, α characterizes the initial slope and β the curvature of the cell survival curve. Albeit in-vitro cell survival curves represent simplistic cell inactivation as endpoint, they are not directly applicable to more complex in-vivo endpoints as they represent an integral response influenced, among others, by the organ structure (serial or parallel), the tissue micro-environment, metabolic factors, interaction of healthy and cancerous cells. (Tommasino and Durante, 2015).

The radiation damage does not only depend on physical properties, but also on tissue characteristics of the target. The underlying principle is that different tissues (cells) react differently to ionizing radiation. This phenomenon is illustrated in the right plot of Figure II.4 showing photon survival curves for two different tissues characterized by $\frac{\alpha_x}{\beta_x} = 2$ Gy (—) and $\frac{\alpha_x}{\beta_x} = 10$ Gy (· · · ·). Further, the bending of the cell survival curve entails relevant tissue characteristics. Focusing on the solid red curve (—), a shoulder can be observed implying damages can be repaired sufficiently in the low dose region. On the contrary, the repair capabilities increasingly fail for higher doses (more complex damage caused by clustered DNA lesions). The $\frac{\alpha}{\beta}$ -ratio essentially quantifies cell repair capabilities and marks the dose level from which on the quadratic component in Equation II.7 is the dominant contributor.

Steeper cell survival curves, such as the carbon ion curve (—) in Figure II.4, do not show a shoulder and indicate that already at smaller doses the induced cell damage cannot be repaired. In general, tissues associated with low $\frac{\alpha}{\beta}$ -ratios [1 to 4 Gy] indicate functioning repair capabilities making such tissues radio-resistant. On the contrary, tissues described with a high $\frac{\alpha}{\beta}$ -ratio [4 to 10 Gy] are considered to be radio-sensitive.

Treatment planning for carbon ions requires the knowledge of the radio-sensitivity parameters α_I and β_I . Unlike for photons, where α_x and β_x are constant, α_I and β_I show for

particles various dependencies, e.g., on the particle type, stopping power, the target cell, and irradiation conditions. The number of combinations to cover all dependencies with clonogenic cell survival assays is practically infeasible as assays are not only time intense to grow but also beam time is a limited resource. For this reason, biophysical models have been intensively developed in the past. The biophysical model used throughout this work is the Local Effect Model (LEM) and described next.

II.2.3 Local Effect Model LEM

The goal of the LEM is to predict the radio-sensitivity parameters α_I and β_I of the LQM for heavier charged particles from the photon radios-sensitivity parameters α_x and β_x . The LEM is grounded on the *amorphous track structure* approach where the radial dose distribution of a single particle is continuous representing an average quantity over many tracks. The most obvious difference between photons and charged particles which helps to describe the RBE, is the microscopic dose deposition pattern (Scholz et al., 1997; Scholz and Kraft, 1996). As the expected energy deposition of photons in small sub-volumes is constant over the cell nucleus volume, the local cell survival of photon irradiation coincides with the global cell survival. On the contrary, the expectation value of the energy deposition of charged particles is sharply peaked around the ion's trajectory. For that reason, the local effect does not equal the global effect. To obtain the global effect on the basis of the LEM, it is necessary to firstly average the local effect over the cell nucleus and then secondly over multiple cells to account for traversal statistics.

The core assumption of the LEM is that equal local doses yield equal local effects. This theory implies that the macroscopic damage to the cell's DNA is independent of the radiation modalities and only differs in magnitude. For both, photons and ions, DNA strand breaks are primarily the result of ionizations via secondary electrons, which firstly deposit the most substantial fraction of energy and are secondly independent of the primary projectile. Assuming cell damage is identical for all radiation modalities requires consequently only to consider the ionization density – which varies considerably (Kraft and Krämer, 1993). To ultimately predict the radio-sensitivity of charged particles α_I and β_I with the LEM, three parameters are required: **(i)** the photon dose-response curve, **(ii)** the cell nucleus and **(iii)** the radial dose distribution of the incident projectile. All three inputs are described next and additionally shown in Figure II.5.

(i) Photon dose-response curve: It is assumed that the photon dose-response curve (photon radio-sensitivity) is represented by an adaption of the LQM:

$$N_{lethal} = -\ln(S_x) = \begin{cases} \alpha_x D + \beta_x D^2 & \text{for } D \leq D_t \\ \alpha_x D_t + \beta_x D_t^2 + s_{max}(D - D_t) & \text{if } D > D_t \end{cases} \quad (\text{II.8})$$

with: $s_{max} = \alpha_x + 2\beta_x D_t$

where D_t describes a transition from a shouldered to a pure exponential trend after 10% survival. As LEM requires interpolation at very high local doses of up to several thousand Gy, this adaption was chosen to be in line with limited experimental data (Saager et al., 2015, 2016, 2014). Nevertheless, the elemental problem is the cell survival curve can practically, due to the meager cell survival at high doses, hardly be determined. Further, it is important to mention that α_x, β_x and D_t are considered as input parameters of the LEM, which could in principle depict any other relevant endpoint than clonogenic cell survival.

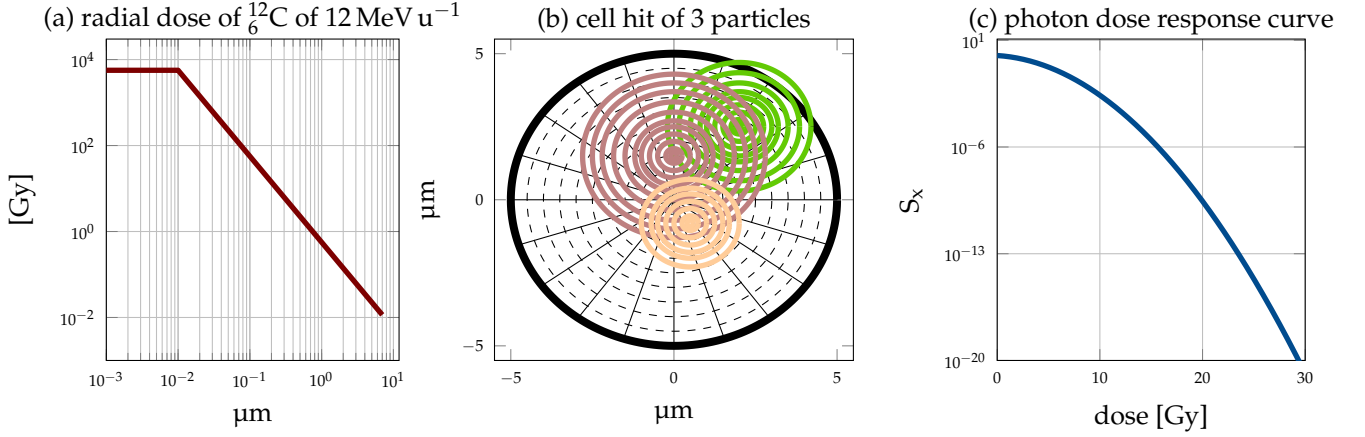


Figure II.5: Schematic illustration of the LEM. Plot (a) presents the radial dose distribution (—) of a carbon ion particle with 12 MeV u⁻¹ which translates to a electronic stopping power of 1401 MeV cm g⁻². Plot (b) shows the cell nucleus (—) hit by three projectiles with different energies. Concentric circles represent iso-dose lines of three dose distributions each induced by a charged particle. The local total physical dose is then used to assess the local cell survival by means of the adapted cell survival curve (—) of photons depicted in the right plot (c).

(ii) Cell nucleus / geometrical structure: It is assumed the cell nucleus represents the sensitive component for radiation and is, in first approximation, of cylindrical shape. Further, an uniformly distributed radio-sensitivity throughout the whole cell nucleus is considered. Damages to other parts of the cell are neglected and are not modeled. The size (radius) of the cell nucleus is typically in the range of 5 μm to 10 μm (depending on the cell type). Assuming the ion tracks traverse parallel to the central axis of the cell cylinder reduces the calculation to a two-dimensional problem. Although the radio-sensitivity depends in theory on the cell cycle, type, -stage, -age etc., these aspects are neglected at this point for simplicity.

(iii) Radial dose distribution: The dose distribution around an ion track can be approximated by a piece-wise function up to a certain threshold, labeled as track radius r_{max} . The most energetic electrons referred to as δ -electrons produced by the primary projectile determine the track radius r_{max} . The radial dose distribution in the first LEM version is defined as a piece-wise function:

$$D(r) = \begin{cases} \frac{\lambda LET}{r_{min}^2} & \text{if } r < r_{min} \\ \frac{\lambda LET}{r^2} & \text{if } r_{min} < r < r_{max} \\ 0 & \text{if } r > r_{max} \end{cases} \quad \text{with:} \quad \lambda = \frac{1}{\rho\pi(1+\ln(\frac{r_{max}^2}{r_{min}^2}))} \quad (\text{II.9})$$

The dose D is set to be constant within the region of r_{min} . Typical values of r_{min} and r_{max} are

10 nm and 1-10 μm , respectively. λ represents a normalization constant to ensure the integral over the whole track yields the LET. r_{max} can be assessed by using a fit of $r_{max} = \gamma E^\delta$ with r_{max} in [μm], E in [MeV u^{-1}] and $\gamma = 0.05$, $\delta = 1.7$ (Scholz and Kraft, 1996).

It is assumed that the inactivation of a cell is a point-like event (lethal event) induced by the deposited dose. The average number of such lethal events $N_x(D)$ after photon irradiation correlates with the dose D since higher doses yield more lethal events. The inventors of LEM (Scholz and Kraft, 1996) assumed the lethal event distribution obeys a Poisson distribution and derived the fraction of surviving cells via:

$$S_x(D) = e^{-N_x(D)} \Leftrightarrow N_x(D) = -\ln(S_x(D)) = \alpha_x D + \beta_x D^2 \quad (\text{II.10})$$

As the distribution of sensitive sites is homogenous throughout the cell nucleus, lethal events $N_x(D)$ are randomly distributed over the cell nucleus volume V and a dose-dependent photon event density ν_x can be derived:

$$\nu_x(D) = \frac{N_x(D)}{V} = \frac{-\ln S_x(D)}{V} \quad (\text{II.11})$$

where ν_x is assumed to be constant for cells and all neighboring cells. On the contrary, charged particles induce an inhomogeneous dose distribution $d(x, y, z)$ which is sharply peaked around the ions track resulting consequently in an inhomogeneous lethal event density ν_{ion} . Therefore, it is necessary to integrate the local event density over the cell nucleus volume to obtain the average number of lethal events N_{ion} :

$$N_{ion} = \int_V \nu_{ion}[d(x, y, z)] dV \quad (\text{II.12})$$

Following the underlying assumption of LEM, i.e., equal local doses yield equal local effects, independent of the radiation modality, allows to equate ν_x and ν_{ion} to derive:

$$N_{ion} = -\ln(S_{ion}) = -\int_V \frac{\ln(S_x(d(x, y, z)))}{V} dV \quad (\text{II.13})$$

Thus, the effect of particle radiation in a macroscopic subvolume can be calculated from the effect of photon irradiation, if the corresponding physical particle dose is known. The biological effect in a cell can then be calculated by averaging the local effect over the cell nucleus volume.

Equation II.13 highlights the link between the biological effect of photons $\ln(S_x)$ to that of ions $\ln(S_{ion})$. The integration in Equation II.13 is not straightforward as the spatial distribution of $d(x, y, z)$ is strongly peaked and therefore highly irregular on the submicroscopic level.

Ions produce a very localized but high biological effect in a small subvolume due to high local doses ($>1000\text{Gy}$). Nevertheless, a high localized biological effect over a bigger subvolume results in a decreased overall biological effect.

To account for different spatial distributions (ion hit positions) and fluences, $\ln(S_{ion})$ is

considered to be the average number of multiple repetitions to account for the stochastic spatial behavior. However, considering small fraction doses with low hit statistics allows to obtain the initial slope α_I employing an approximation. Here the ion cell survival curve of a single particle can be obtained according to (Scholz et al., 1997) via:

$$\alpha_I(Z, E) = \frac{1 - S_{ion}}{N_{ion}} \quad (\text{II.14})$$

where $\alpha_I(Z, E)$ denotes the predicted radio-sensitivity parameter of the LQM of particle type Z and energy E on the basis of the LEM.

Summarized, the cell survival S_{ion} induced by ions can be obtained via $S_{ion} = e^{-N_{ion}}$ according to their response to photons (Scholz et al., 1997; Scholz and Kraft, 1996). The LEM was further improved in its second version to more accurately predict the radio-sensitivity of lighter ions such as protons and helium ions (Elsässer and Scholz, 2007). In particular, an enhancement factor to model the increased damage of DNA lesions in close vicinity and a smoothed radial dose profile were introduced. The third LEM version considered an energy-dependent track core radius r_{min} , instead of a constant core radius of ~ 10 nm (Elsässer et al., 2008). In the latest LEM version IV, an intermediate step was introduced. From the physical dose distribution of charged particles, an initial spatial DNA damage distribution is inferred. The underlying assumption is that the relevant quantity to derive the local effect is supposed to be the microscopic damage distribution of DNA lesions and not the physical dose (Elsässer et al., 2010). Thus the narrative switches to equal local damage distributions lead to equal local effects.

Shifting the focus back to this manuscript, then treatment planning for carbon ions is based on the LEM I and IV. The version number is indicated by Roman numbers. I refers to the first version and IV to the fourth model version. Up to here, all relevant physical and biological properties of accelerated charged particles have been introduced which allows now to describe the treatment planning process of carbon ions in the next section.

II.3 Radiation Treatment Planning

Radiation Treatment planning is one essential chain link in the radiotherapy workflow. Usually, the patient is first immobilized to ensure a consistent patient position for the subsequent imaging procedure as well as for multiple patient irradiations. Afterward, a Computed Tomography (CT) scan and potentially other anatomical or functional imaging scans (MRT, PET) are acquired and eventually fused. The tumor volume and multiple Volumes of Interest (VOIs) are outlined/segmented in a further step to start *in silico* radiation treatment planning.

II.3.1 Treatment Planning and Intensity Modulated Particle Therapy

The treatment planner defines firstly beam angles to determine the directions from which ionizing radiation will be guided into the patient's body by the irradiation device. Next, the irradiation geometry along with the pencil beam positions are determined by the Treatment Planning System (TPS) before dose calculation for unit intensities is carried out. Figure II.6 recaps the calculation of the irradiation geometry (steering information).

The yellow point indicates the virtual source of irradiation, the green line the patient surface and the red contour the target volume. This example depicts a single beam, whereby the black dotted line (---) presents bixel/beamlet edges required for photon treatment planning and black dots (●) on (—) show the spot placement for treatment planning with charged particles. For the latter, it is essential to know the exact location of the pencil beam spots (black dots ●) in the patient.

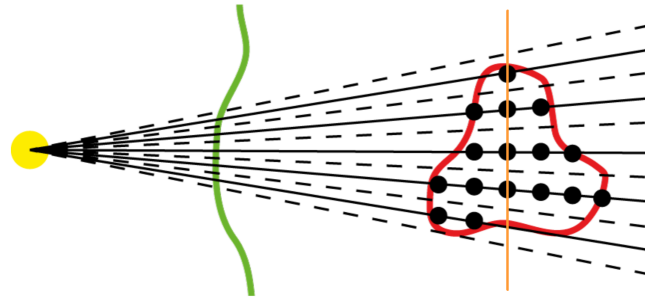


Figure II.6: Schematic illustration of the ray-pencil beam concept. Taken from <https://github.com/e0404/matRad/wiki/Dose-influence-matrix-calculation>

Therefore, the discretized patient's geometry is initially obtained via a CT scan measuring the photon attenuation in Hounsfield Units (HU). Then HU values are converted to Stopping Power relative to Water (rSP) using a machine-specific calibrated look-up table (Newhauser and Zhang, 2015). Next, ray tracing is performed to obtain the integral rSP for each ray (Siddon, 1985). The integral rSP is also often referred to as Water Equivalent Path Length (WEPL). Only if the ray hits the target, multiple pencil beams are positioned longitudinally along the ray as indicated by (●) in Figure II.6. An important parameter in this regard is the lateral pencil beam spacing which is determined based on a plane through the iso-center (—) that is perpendicular to the central ray of the irradiation angle. It specifies the lateral spacing of rays and consequently the lateral density of pencil beam spots. Once the beam geometry, including pencil beam positions, are calculated for each beam direction, dose calculation can then be carried out. Unlike Monte Carlo dose calculation algorithms, which simulate dose in material, analytical dose calculation algorithms calculate dose in water.

As dose calculation is done on a regular three-dimensional grid, a linear voxel index i $\{i \in \mathbb{N} | 1 \leq i \leq I\}$ is introduced to replace subscripts x, y, z . Dose calculation is performed for each pencil beam spot successively for unit intensity. As it is necessary to re-evaluate the dose distribution for different pencil beam intensities during optimization, the dose information for unit intensities needs to be saved throughout the treatment planning process. In this case, a matrix, referred to as dose influence matrix D , is created to store column-wise the dose contribution to all voxels i for each pencil beam j , $\{j \in \mathbb{N} | 1 \leq j \leq J\}$. Let I be the

total number of voxels and J be the total number of spots then the dose influence concept is represented by:

$$d_i = \sum_{j=1}^J D_{ij} w_j \quad \text{or} \quad \mathbf{d} = D \mathbf{w} \quad (\text{II.15})$$

where \mathbf{d} denotes the physical dose $\in \mathbb{R}^{I \times 1}$, \mathbf{w} the pencil beam weights $\in \mathbb{R}^{J \times 1}$ and D the dose influence matrix in $\in \mathbb{R}^{I \times J}$. Equation II.15 shows the linear dose mapping to calculate the deposited dose d_i in voxel i . The dose contribution of each pencil beam is weighted by its intensity w_j and summed up. The implemented analytical dose calculation to derive individual dose influence elements D_{ij} is described later in Chapter II.4. After dose calculation, inverse optimization is the next link in the chain.

Here, the treatment planner needs to translate clinical goals into mathematical objectives and constraints to sculpt the dose distribution to the patient's needs. This process is iteratively repeated until the optimized dose distribution is satisfying. For quality assurance reasons the treatment plan is then reviewed by a clinician. Moreover, the application of the treatment plan is tested before the patient is ordered into the hospital for the actual treatment. To cover the complete tumor volume with the prescribed dose, it is required to place multiple particle pencil beams with distinct range and lateral position inside the tumor volume as shown in Figure II.6. As an example, a one-dimensional proton treatment plan is presented in

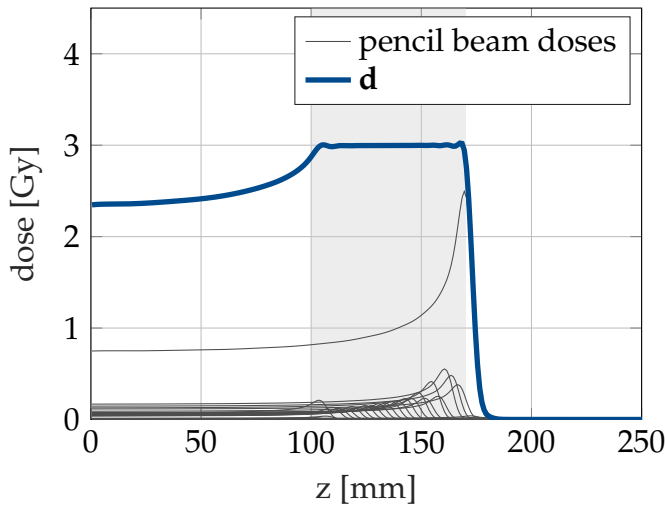


Figure II.7: One-dimensional Spread out Bragg peak (SOBP) in water comprised of 30 scanned proton pencil beams (—) optimized for 3 Gy. The weighted superposition \mathbf{d} of all individual pencil beams is shown by (—).

Figure II.7 in which proton pencil beams with increasing beam energies are positioned in the target area (□) from 100 mm to 170 mm. During optimization an optimal set of pencil beam intensities \mathbf{w} producing according to given objectives and constraints a minimal objective function value. In this case, a homogenous dose of 3 Gy was specified for the target while keeping the dose to the healthy tissue at the same time low. The weighted superposition of all individual pencil beams $D \mathbf{w}$ results in the total dose \mathbf{d} (—) commonly known as SOBP. The technique to modulate the in-

tensity of each pencil beam individually is called Intensity Modulated Particle Therapy (IMPT) and is conceptually closely related to intensity modulated photon therapy (IMRT). Analyzing Figure II.7, then special attention needs to be paid to the highly modulated pencil beam at the distal edge of the SOBP as a miss-estimation of the pencil beam range might result in under- or over-dosage of the tumor. This work focuses apart from uncertainty quantification also on optimization strategies to create robust treatment plans that are less sensitive to such

miss-estimations. The possibility to steer not only the depth position of the Bragg peak but also the lateral position of each of the up to fifty thousand pencil beams for a single patient is enabled by active pencil beam scanning, which is described next.

II.3.2 Pencil Beam Scanning

Currently, there are two distinct beam delivery techniques in clinical use. The common denominator of both methods is the ability to control the intensity of the initial beam by adapting the number of particles, but the range and lateral coverage are achieved differently.

The first beam application technique is given by passive beam shaping. Here the particle beam is modulated by generic and patient-specific passive beam line elements (Krämer et al., 2000). The main components of this method are (i) a range shifter wheel (ii) a scatterer for broadening the beam to cover the whole tumor volume laterally, (iii) a collimator to block unnecessary dose to healthy tissue and (iv) a patient-specific compensator to conform the dose deposition to the target in depth. Besides the need to manufacture compensators for each patient and beam individually, such systems induce due to the passive beam line elements secondary radiation (neutrons), which increases the integral dose to the patient. Further, the dose to nontumor tissue is increased in the proximal region of the SOBP since dose conformity can only be achieved in the distal edge of the SOBP.

An evolving beam application system that allows for IMPT, is represented by active pencil beam scanning (Haberer et al., 1993; Krämer et al., 2000). Here, each unscattered pseudo mono-energetic pencil beam is deflected at the beam nozzle by so-called scanning magnets. The magnetic field of these magnets alters the direction vector of the charged particle beam to laterally cover (paint) the tumor as illustrated in Figure II.6 by different ray directions (—). To cover the tumor longitudinally, distinct initial pencil beam energies are applied, which is schematically shown in Figure II.6 by black dots (●) positioned on the same ray. Moreover, at the HIT facility in Heidelberg, the pencil beam scanning technique allows to vary the initial pencil beam width with respect to the tumor volume and initial beam energy. This mainly affects protons, since lateral scattering is roughly ~ 3 times higher compared to carbon ions. Active pencil beam scanning does usually not require any additional beam modifying devices (collimators, compensators). However, there is one exception to the latter statement. As the carbon ion depth dose profile is extremely peaked, a ripple filter is added into the beam line, to artificially increase range straggling (blurring the Bragg peak longitudinally) to ensure a broader width of the Bragg peak. Otherwise, a homogenous dose distribution in the target could not be reached by superimposing such extremely peaked pencil beam dose profiles.

II.4 Treatment Planning and Robust Optimization

To implement uncertainty quantification and mitigation methods for carbon ion treatment planning, firstly basic principles explained in the previous chapter needed to be translated to computational algorithms to perform *in silico* radiation treatment planning. In a joint effort, our group* developed a Matlab-based open-source treatment planning system called matRad† (Cisternas et al., 2015; Wieser et al., 2017a). This chapter highlights the underlying concepts of matRad’s dose calculation (physical- and biological-beam model) and inverse optimization functionalities. Throughout this chapter, a particular focus is set on biological treatment planning for carbon ions since this was one of my main contributions and more importantly builds the groundwork for probabilistic carbon ion treatment planning explained in the following chapters.

II.4.1 Physical Beam Model

In the physical beam model, it is assumed the physical dose d factorizes into two lateral components L_x, L_y and one depth component Z . According to (Hong et al., 1996) and an adaption of (Schaffner et al., 1999), the dose d of pencil beam j with initial beam energy E_0 at the spatial position x, y, z is defined as follows:

$$d(x, y, z, E_0) = L_x(x, z, l, E_0) L_y(y, z, l, E_0) Z(z, E_0) \quad (\text{II.16})$$

Equation II.4.1 can be further refined for the single Gaussian lateral beam model to:

$$d(x, y, z, E_0) = \frac{1}{\sqrt{2\pi\sigma_x^2}} e^{-\frac{x^2}{2\sigma_x^2}} \frac{1}{\sqrt{2\pi\sigma_y^2}} e^{-\frac{y^2}{2\sigma_y^2}} Z(z, E_0) \quad (\text{II.17})$$

$$\text{with : } \sigma_x = \sigma_y = \sqrt{\sigma_{ini}^2(E_0) + \sigma_{air}^2(l, E_0) + \sigma_{scat}^2(z, E_0)}$$

where x and y represent geometrical distances from the current point of interest to the central pencil beam axis, z the integral stopping power relative to water (= WEPL), σ_{ini} the initial beam width at the beam nozzle, σ_{air} the divergence of primaries in air by travelling a distance l from the beam nozzle to the patient surface and σ_{scat} the beam widening inside the patient due to elastic scattering. Further, $Z(z, E_0)$ denotes the laterally integrated physical depth-dose profile of the corresponding radiation modality. The total integral energy deposition is guaranteed by the normalized two-dimensional lateral dose model in Equation II.4.1. $Z(z, E_0)$ profiles are stored for each initial beam energy and were obtained from Monte Carlo Fluka

*<https://www.dkfz.de/radopt>

†www.matrad.org

simulations (Parodi et al., 2012) which were in line with experimental measurements. The lateral dose distribution is characterized in the simplest modeling approach via a single radially symmetric two-dimensional Normal distribution. However, this approach does not accurately capture the low-dose halo created by strongly scattered particles. Instead, a superposition of two weighted normal distribution was proposed by (Parodi et al., 2012, 2013; Schwaab et al., 2011) and is also currently in clinical use and implemented in matRad (Wieser et al., 2017a). An advisable overview of other parameterizations of the lateral dose is provided by (Bellinzona et al., 2015).

All depth and energy dependent parameters in Equation II.4.1 are stored in a base data file that is loaded into the matRad TPS upon dose calculation. A detailed description of the base data parameters and their units can be found in (Wieser et al., 2017a). For a description of the base data format and structure the reader is referred to (Wieser et al., 2018).

As previously mentioned, the dose of each pencil beam j is stored in the dose influence matrix D , which is for a typical scenario a matrix of size $D \in \mathbb{R}^{I \times J}$ with $I = 500 \times 500 \times 100$ and $J = 15000$. To reduce storage requirements a sparse matrix format is facilitated. Following the clinical standard, a constant scaling factor (RBE=1.1) is considered for proton treatment planning. On the contrary, carbon ion treatment planning requires another level of complexity because of the varying RBE throughout the treatment field, which will be described in the next section.

II.4.2 Biological Treatment Planning Pipeline

Utilizing the LEM, the radio-sensitivity parameter α_I can be obtained for different ion types as a function of energy E from their response to photon radiation. Here, α_I denotes an intrinsic microscopic parameter which does not depend on the dose or particle fluence (Krämer and Scholz, 2000). However, for treatment planning, it is required to obtain radio-sensitivity parameter α_c, β_c in a mixed radiation field, where multiple fragments from different pencil beams with varying energy and flux are present. Exemplary, Figure II.8(a) shows the output of the LEM I for chordoma cells. In addition, the right plot in Figure II.8(b) illustrates the output of LEM IV for the spinal cord. These values represent the essential biological information to perform carbon ion treatment planning based on the LEM. To obtain the dependence on higher doses (β_I) the following derivation was proposed by (Scholz et al., 1997):

$$\beta_I(Z, E) = \frac{S_{max} - \alpha_I(Z, E)}{2D_t} \quad (\text{II.18})$$

Herewith, the α_I, β_I parameters are entirely decoupled from the actual treatment situation and only need to be produced once to be used for routine treatment planning.

In principle, there exist two approaches to derive α_c and β_c for a mixed radiation field. The first approach is known as *full simulation* and is comprised of a two-step sampling process. Firstly, the number of cell hits (ion traversals) are sampled from a Poisson distribution for each voxel i considering the actual particle fluence. Next, the biological effect is determined

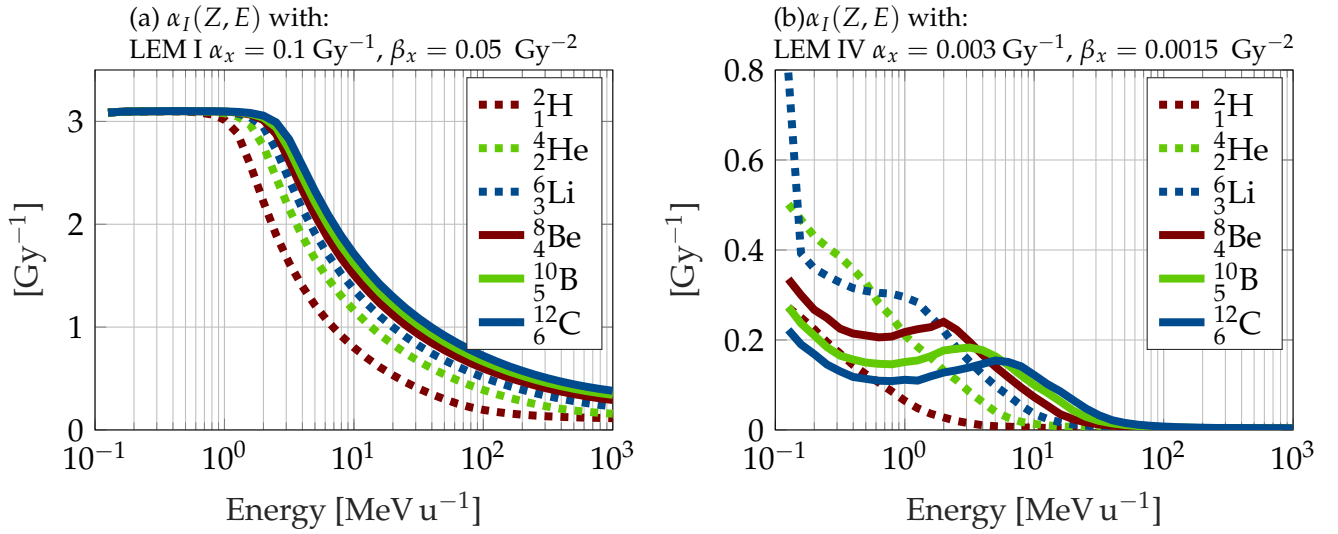


Figure II.8: Raw LEM I and IV outputs for different particle types and tissues. Both figures show the initial slope $\alpha_I(Z, E)$ of the ion cell survival curve of a single central particle hit.

for each particle type from its local particle spectrum. The individual biological effects are then accumulated to obtain the total effect. This procedure is repeated 500 to 1000 times to finally assess a mean value which accounts for various particle combinations (Krämer and Scholz, 2000). This approach is capable of predicting the RBE even for high doses, but the two-step sampling process needs to be repeated every time pencil beam intensities change, which is problematic for optimization.

The second approach to determine the radio-sensitivity parameters α_c, β_c is given by an analytical approximation followed by the application of a beam mixing model. Admittedly this approach is only valid in the low dose domain $< 10\text{Gy(RBE)}$. The underlying assumption of the approximation is the cell hit probability to reduce to a single hit probability in the low dose domain - either hit or no hit. Furthermore, it is assumed the macroscopic cell survival can also be described with the LQM. For that regard an approximation was found to account for all possible ion traversal positions in a single cell (Krämer and Scholz, 2006):

$$\alpha_I^{\text{single}}(Z, E) = \frac{1 - S_1(Z, E)}{d_1(Z, E)} \quad \text{with: } S_1(Z, E) = e^{-\alpha_I(Z, E) d_1(Z, E)}, d_1(Z, E) = C \frac{LET(Z, E)}{A} \quad (\text{II.19})$$

where the subscript 1 highlights a single particle traversal, A indicates the cell nucleus area and C the elementary charge. This approach is known as *single particle approximation* (SPA). To obtain the high dose dependency β_I^{single} the following scaling was proposed (Krämer and Scholz, 2006):

$$\beta_I^{\text{single}}(Z, E) = \left(\frac{\alpha_I^{\text{single}}(Z, E)}{\alpha_I(Z, E)} \right)^2 \beta_I(Z, E) \quad (\text{II.20})$$

As an example, Figure II.9(a) presents the single particle approximation $\alpha_I^{\text{single}}(Z, E)$ based

on Equation II.19 using LEM I with $\alpha_x = 0.1 \text{ Gy}^{-1}$ and $\beta_x = 0.05 \text{ Gy}^{-2}$. The respective underlying data (α_I) is already shown in Figure II.9(a).

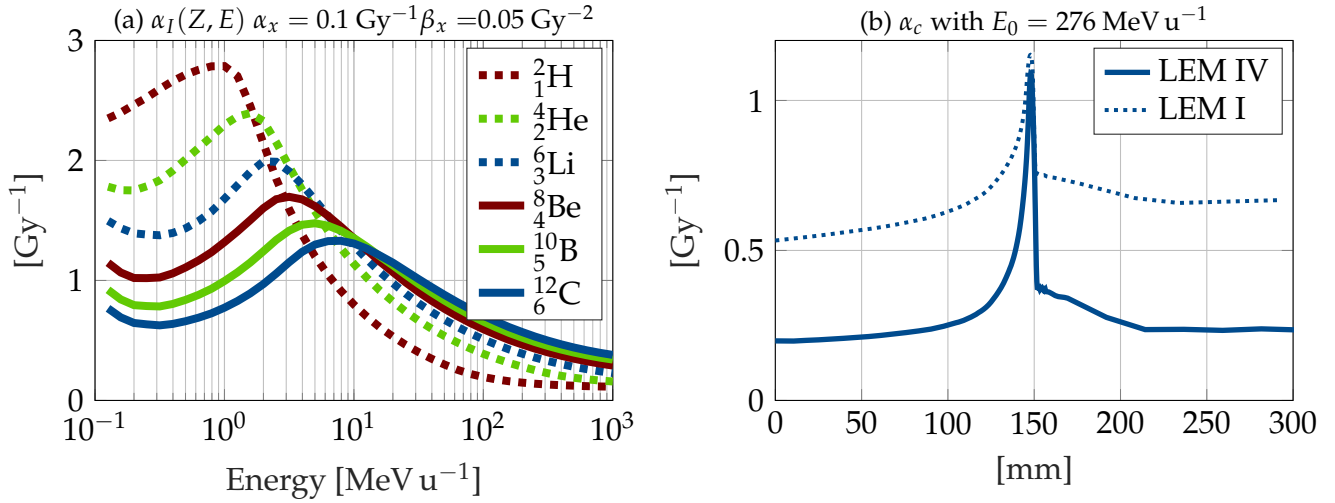


Figure II.9: Plot (a) shows the result of the single particle approximation (SPA) for LEM I based on the data shown in Figure II.8(a). Plot (b) presents the resulting α_c profiles of a carbon ion pencil beam with 275 MeV u⁻¹ for LEM I and IV on the basis of dose-averaged slope parameters (α_I) considering fragmentation.

As a pseudo mono-energetic carbon ion pencil beam already creates a mixed radiation field due to fragmentation, synergistic mixed field effects occur which need to be taken into account (Zaider and Rossi, 1980). Depth-dependent dose-averaged radio-sensitivity LQM parameters for a carbon ion pencil beams with initial energy E_0 can be calculated via:

$$\alpha_c(x, E_0) = \frac{\sum_Z \int_0^\infty \alpha_I^{\text{single}}(Z, E) \phi(x, Z, E, E_0) S_{el}(Z, E) dE}{\sum_Z \int_0^\infty \phi(x, Z, E, E_0) S_{el}(Z, E) dE} \quad (\text{II.21})$$

$$\sqrt{\beta_c}(x, E_0) = \frac{\sum_Z \int_0^\infty \sqrt{\beta_I^{\text{single}}}(Z, E) \phi(x, Z, E, E_0) S_{el}(Z, E) dE}{\sum_Z \int_0^\infty \phi(x, Z, E, E_0) S_{el}(Z, E) dE} \quad (\text{II.22})$$

The resulting profiles, given in Equation II.21 and II.22, are calculated once for each tissue type and are stored in the matRad base data so that they can be used for daily carbon ion treatment planning. Figure II.9(b) illustrates the depth-dependent dose-averaged α_c profile of a carbon ion pencil beam with an initial beam energy of 276 MeV u⁻¹. This plot shows not only the α_c profile based on LEM I predictions for $\alpha_x = 0.1 \text{ Gy}^{-1}$, $\beta_x = 0.05 \text{ Gy}^{-2}$ (—), but also the prediction of LEM IV (· · · · ·).

Although (—) and (· · · · ·) are calculated with different particle spectra, their main characteristics can still be compared. Both LEM I and LEM IV predict a similar radio-sensitivity around the Bragg peak, however, bigger differences can be observed in the entrance channel and tail for which LEM I predicts a higher radio-sensitivity than LEM IV. This observation implies that LEM I is currently overestimating the RBE weighted dose in the normal tissue compared to LEM IV. This behavior is considered conservative and safe for the patient.

β_c profiles are not explicitly shown here, but represent supplementary to the α_c - and the dose-profiles the underlying base data to perform carbon ion treatment planning.

All previous steps describe basically the creation of biological base data that can be used for routine analytical carbon ion treatment planning. The last missing link to compute the RBE weighted dose, i.e., is its computation according to the LQM, which will be explained in the next section.

II.4.3 Biological Beam Model

Clinically, the most relevant quantity for carbon ion treatment planning is the RBE weighted dose ($RBE \times d$). Let γ be $\frac{\alpha_x}{2\beta_x}$ and ε be the biological effect then the RBE weighted dose can be calculated on the basis of the LQM via:

$$RBE \times d = \sqrt{\frac{\varepsilon}{\beta_x} + \gamma^2} - \gamma = \sqrt{\frac{\alpha_c d + \beta_c d^2}{\beta_x} + \left(\frac{\alpha_x}{2\beta_x}\right)^2} - \frac{\alpha_x}{2\beta_x} \quad (\text{II.23})$$

Focusing on Equation II.23, it can be seen that the biological effect ε is part of the calculation of the $RBE \times d$. It was shown by (Wilkins and Oelfke, 2006), that the biological effect ε can be used as an intermediate quantity for carbon ion treatment planning. To calculate the biological effect in voxel i in a discretized patient geometry, dose contributions from all pencil beams need to be considered (Wilkins and Oelfke, 2006):

$$\varepsilon_i = \alpha_i(\mathbf{w})d_i(\mathbf{w}) + \beta_i(\mathbf{w})d_i^2(\mathbf{w}) \quad (\text{II.24})$$

Equation II.24 demonstrates that different to α_x and β_x the radio-sensitivity parameters α_i and β_i of charged particles depend on the pencil beam intensities and consequently on the particle fluence. Very similar to the dose-averaging already performed to account for fragmentation of individual carbon ion pencil beams (see Equation II.21 and II.22), now dose-averaging is carried out to consider the synergistic effects of multiple pencil beam contributions impinging within a short period of time into the patient tissue (Wilkins and Oelfke, 2006; Zaider and Rossi, 1980):

$$\alpha_i(\mathbf{w}) = d_i^{-1} \sum_{j=1}^J w_j D_{ij} \alpha_{ij}; \quad \sqrt{\beta_i(\mathbf{w})} = d_i^{-1} \sum_{j=1}^J w_j D_{ij} \sqrt{\beta_{ij}}; \quad d_i = \sum_{j=1}^J w_j D_{ij} \quad (\text{II.25})$$

where α_{ij} and $\sqrt{\beta_{ij}}$ depict the radio-sensitivity of pencil beam j to voxel i for the current tissue under consideration. Substituting Equation II.25 into Equation II.24 then yields:

$$\varepsilon_i = \frac{\sum_{j=1}^J w_j D_{ij} \alpha_{ij}}{\sum_{j=1}^J w_j D_{ij}} \sum_{j=1}^J w_j D_{ij} + \left(\frac{\sum_{j=1}^J w_j D_{ij} \sqrt{\beta_{ij}}}{\sum_{j=1}^J w_j D_{ij}} \sum_{j=1}^J w_j D_{ij} \right)^2 \quad (\text{II.26})$$

$$\Rightarrow \varepsilon_i = \sum_{j=1}^J w_j D_{ij} \alpha_{ij} + \left(\sum_{j=1}^J w_j D_{ij} \sqrt{\beta_{ij}} \right)^2 = \sum_{j=1}^J w_j A_{ij} + \left(\sum_{j=1}^J w_j B_{ij} \right)^2 \quad (\text{II.27})$$

where $D_{ij}\alpha_{ij}$ and $D_{ij}\sqrt{\beta_{ij}}$ can directly be multiplied and stored in two separate sparse

matrices A_{ij} and B_{ij} during dose calculation in the TPS. Unlike the linear dose mapping for photons and protons (RBE= 1.1), a linear-quadratic dose mapping is required to calculate the biological effect for carbon ions. It is noteworthy that the radio-sensitivity parameters are assumed to be laterally constant and thereby only influence the depth dose component.

During dose calculation α_{ij} and β_{ij} are interpolated from the base data file based on the integral rSP of voxel i . Similar to the physical beam model, each component can again be broken into two lateral (L^x, L^y) and two depth components (Z^α, Z^β), respectively:

$$\varepsilon_i = \sum_{j=1}^J w_j A_{ij} + \left(\sum_{j=1}^J w_j B_{ij} \right)^2 = \sum_{j=1}^J w_j L_{ij}^x L_{ij}^y Z_{ij}^\alpha + \left(\sum_{j=1}^J w_j L_{ij}^x L_{ij}^y Z_{ij}^\beta \right)^2 \quad (\text{II.28})$$

Equation II.28 represents the core equation of probabilistic carbon ion treatment planning based on the biological effect ε . The exact calculation of each component of Equation II.28 will be introduced later in Chapter III. Having the linear and quadratic influence matrices (A_{ij}, B_{ij}) of the biological effect calculated allows then for optimization.

II.4.4 Inverse Planning

Inverse planning can be understood as the reversion of forward planning. The goal of inverse planning is to recover a set of parameters that produce the desired solution. In the context of radiotherapy, inverse planning aims to reverse engineer a 'good' treatment plan from experience. Instead of re-evaluating different pencil beam intensities over and over again, they are optimized according to prescribed treatment plan quality measures which produce an optimum intensity distribution. The uppermost goal of the radiation oncologist is to design a treatment plan that maximizes the biologically motivated Tumor Control Probability (TCP) with a tolerable Normal Tissue Complication Probability (NTCP). However, in clinical routine, although both TCP and NTCP can be calculated from radiation treatment plan metrics, they are not directly used for treatment plan optimization. Instead, dose and dose-volume criteria are facilitated as clinical input for inverse planning. This section describes firstly the underlying optimization problem followed by clinical objectives/constraints and lastly various robust optimization techniques.

II.4.4.1 The Optimization Problem

Given a prescribed dose vector \mathbf{d}^* , optimal pencil beam intensities \mathbf{w}^* could in principle be obtained by inverting the dose influence matrix $D \in \mathbb{R}^{I \times J}$ via $\mathbf{w}^* = D^{-1} \mathbf{d}^*$. However, assuming an ideal prescribed dose \mathbf{d}^* with zero dose to healthy tissues and full dose to the Planning Target Volume (PTV), does not allow to carry out matrix inversion because of singularity. Using instead a realistic prescribed dose \mathbf{d}^* vector permitting dose to healthy tissue to be greater than zero in the entrance channels of each beam, might result in a matrix inversion with negative fluences. Negative fluences can not only be applied but also the

matrix inversion might be computationally more expensive than inversely solving the system. Because of the previously mentioned limitations, inverse planning is performed to derive optimal pencil beam intensities by minimizing an objective function.

Given multiple objective functions f_n , which denote individual clinical goals, inverse optimization ideally finds a set of pencil beam weights \mathbf{w} , such that the resulting dose distribution produces overall a minimum objective function \mathcal{F} according to defined objectives:

$$\begin{aligned} \mathbf{w}^* = \underset{\mathbf{w}}{\operatorname{argmin}} \quad & \mathcal{F}(\mathbf{d}(\mathbf{w})) = \sum_n p_n f_n(\mathbf{d}(\mathbf{w})) \\ \text{subject to} \quad & \mathbf{w} \geq 0 \\ & c_k^l \leq c_k(\mathbf{w}) \leq c_k^u \end{aligned} \quad (\text{II.29})$$

where p_n is the penalty of objective function f_n . Equation II.29 depicts the elemental inverse optimization problem in radiotherapy. The overall objective function \mathcal{F} is usually given as a weighted sum of potentially non-linear objectives f_n . The problem is solved subject to (i) a positivity constraint on \mathbf{w} that guarantees that no negative radiation fluences are used for the solution and (ii) optional constraints on the dose c_k , where c_k^l and c_k^u represent the lower and upper bound of the k -th constraint.

The work presented here is based on an interior-point method, implemented in an open source software package called IPOPT[‡] that is provided by the COIN-OR initiative[§]. IPOPT stands for interior-point optimizer and can be used to solve large-scale non-linear problems considering constraints (Nocedal et al., 2009; Wächter and Biegler, 2006). The IPOPT project is implemented in C++ and provides among others, an interface to Matlab in the form of MEX-files. These wrapper files have been integrated into the optimization engine of matRad to invoke the core C++ functionalities from the Matlab environment.

To calculate the first derivatives of the optimization parameters \mathbf{w} , the chain rule needs to be applied as the overall objective function \mathcal{F} , is a function of dose, which in turn depends on the pencil beam weights \mathbf{w} .

$$\nabla_{\mathbf{w}} \mathcal{F} = \frac{\partial \mathcal{F}}{\partial \mathbf{w}} = \frac{\partial \mathcal{F}}{\partial \mathbf{d}} \frac{\partial \mathbf{d}}{\partial \mathbf{w}} \quad (\text{II.30})$$

Similar expressions can be derived for constraints, which requires the calculation of partial derivatives (Jacobian). The second derivatives, i.e., the Hessian of the optimization parameters \mathbf{w} are approximated within IPOPT by means of the Quasi-Newton method using first derivatives. Objective functions, constraints and corresponding gradient calculations are implemented in matRad and are passed on via function-handles to the IPOPT interface. The next subsection presents relevant clinical objectives f_n and constraints c_k .

[‡]<https://projects.coin-or.org/Ipopt>

[§]<http://www.coin-or.org>

II.4.4.2 Clinical Objectives and Constraints

An excerpt of clinical objectives and constraints for inverse planning is presented in Table II.1 (Wu and Mohan, 2000). Before explaining them in detail, it is worth mentioning that objectives are usually defined for individual VOIs S and are secondly normalized by the total number of voxels N_S of the corresponding VOI. By this means, equal importance between volumetrically small and big structures is ensured.

One of the most common objectives is the squared deviation objective ($f_{sq\ dev}$) which aims to minimize the squared dose deviation between the actual dose d_i and a prescribed reference dose d_i^* (Oelfke and Bortfeld, 2001). This objective is mostly used for target structures to create a homogenous dose distribution on a specific dose level, whereas both, under and overdosage are equally important. The next two objectives are the piecewise squared under and overdosage objective ($f_{sq\ underdosage}$, $f_{sq\ overdosage}$). Both rely on the Heaviside function Θ to trigger the particular objective. If the dose d_i falls below the reference dose d_i^* , then the square underdosage objective becomes effective and vice versa, if the dose d_i exceeds the reference dose d_i^* , the square overdosage objective comes into force.

Table II.1: Objective and constraint functions with dose d_i in voxel i , prescribed reference dose d_i^* , dose \tilde{d} at prescribed volume, structure S , number of voxels in structure N_S , equivalent uniform dose (EUD) exponent a , Heaviside function $\Theta(x)$, and log-sum-exp function parameter $\kappa = 10^{-3}$ (Wieser et al., 2017a).

| objectives | | constraints | |
|-----------------------|--|-----------------|--|
| $f_{sq\ dev}$ | $= \frac{1}{N_S} \sum_{i \in S} (d_i - d_i^*)^2$ | | |
| $f_{sq\ underdosage}$ | $= \frac{1}{N_S} \sum_{i \in S} \Theta(d_i^* - d_i) (d_i - d_i^*)^2$ | $c_{min\ dose}$ | $= d_{min} - \kappa \log \left(\sum_{i \in S} e^{\frac{d_{min} - d_i}{\kappa}} \right)$ |
| $f_{sq\ overdosage}$ | $= \frac{1}{N_S} \sum_{i \in S} \Theta(d_i - d_i^*) (d_i - d_i^*)^2$ | $c_{max\ dose}$ | $= d_{max} + \kappa \log \left(\sum_{i \in S} e^{\frac{d_i - d_{max}}{\kappa}} \right)$ |
| f_{mean} | $= \frac{1}{N_S} \sum_{i \in S} d_i$ | c_{mean} | $= \frac{1}{N_S} \sum_{i \in S} d_i$ |
| f_{EUD} | $= \left(\frac{1}{N_S} \sum_{i \in S} d_i^a \right)^{\frac{1}{a}}$ | c_{EUD} | $= \left(\frac{1}{N_S} \sum_{i \in S} d_i^a \right)^{\frac{1}{a}}$ |
| $f_{min\ DVH}$ | $= \frac{1}{N_S} \sum_{i \in S} \Theta(d_i^* - d_i) \Theta(d_i - \tilde{d}) (d_i - d_i^*)^2$ | $c_{min\ DVH}$ | $= \frac{1}{N_S} \sum_{i \in S} \Theta(d_i^* - d_i)$ |
| $f_{max\ DVH}$ | $= \frac{1}{N_S} \sum_{i \in S} \Theta(d_i - d_i^*) \Theta(\tilde{d} - d_i) (d_i - d_i^*)^2$ | $c_{max\ DVH}$ | $= \frac{1}{N_S} \sum_{i \in S} \Theta(d_i - d_i^*)$ |

Further, the mean dose objective (f_{mean}) and the equivalent uniform dose (EUD) objective (f_{EUD}) are common measures to minimize dose to normal tissue. In particular, the latter is biologically motivated as the EUD represents the homogenous dose given to a structure S yielding an identical biological response as the actual non-uniform dose. Notably, this concept has already been applied to carbon ion treatment planning considering the equivalent uniform effect (EUE) instead of the EUD (Brüningk et al., 2015). The last two objectives are minimum ($f_{min\ DVH}$) and maximum dose-volume ($f_{max\ DVH}$) objectives penalizing doses that fall below or exceed a respective dose-volume prescription. Every objective can also be defined as a hard constraint as shown in the right half of Table II.1 but is not explicitly explained here.

It is important to mention that all objectives and constraints shown in Table II.1 are equally applicable to the RBE-weighted dose and the biological effect ε , although for the latter the trade-off between the target and normal tissue of the prescribed biological effect is

slightly different due to the non-linear mapping from RBE-weighted dose to biological effect. Following (Wilkens and Oelfke, 2006), the biological effect ε is employed throughout this work for optimization.

II.4.4.3 Single Field and Multi Field Optimization

There are two main optimization approaches currently facilitated in IMPT, namely Single Field Uniform Dose (SFUD) and Multi Field Optimization (MFO). SFUD is characterized by optimizing all pencil beam intensities of the same beam direction simultaneously (Lomax, 2008a). Thus, a SOBPs is optimized for each beam direction separately and the superposition of each homogenous beam dose yields the total prescribed dose. On the contrary, MFO optimizes pencil beam intensities of all beams simultaneously, thereby allowing for greater flexibility to achieve the desired clinical goals (Lomax, 1999). In MFO the individual beam doses might be highly modulated and certain tumor areas might only be covered from a single beam.

Focusing on treatment plan robustness, MFO is generally more sensitive to changes in the integral rSP due to highly modulated beam doses. Only if all beam dose contributions match perfectly, they yield the desired and planned homogenous target dose.

Besides choosing robust beam angles and the margin concept, SFUD optimization is often used as a first measure to create treatment plan robustness. Usually, the dose contributions of each beam direction are equally split up so that a change in the integral rSP affects the total dose distribution to a lesser extent. Although SFUD creates robust treatment plans, the full potential of IMPT remains unused (Fredriksson et al., 2011).

Before further explaining robust treatment planning approaches in detail, it is necessary to provide in the next section background information on potential uncertainty sources of uncertainties in carbon ion therapy.

II.5 Uncertainties in Carbon Ion Therapy

The dose delivered to the patient's body might not be the one simulated and displayed in the TPS. The increased selectivity of dose deposition due to the inverse depth dose profile of carbon ions along with its elevated RBE are inherently more sensitive to uncertainties and impose new challenges to treatment planning. Moreover, carbon ions show a sharper lateral dose gradient and a more distinct Bragg peak for which reasons the consideration of uncertainties may particularly be important for carbon ions (Suit et al., 2010). There are various factors of physical and biological nature that cause a discrepancy of planned and delivered dose. For that reason, this section is split up to cover physical in II.5.1 and biological uncertainties in II.5.2 separately. Section II.5.3 presents existing uncertainty quantification and mitigation approaches of intensity-modulated particle therapy in general and then focuses in the last Section II.5.4 on carbon ion therapy.

II.5.1 Physical Uncertainties

There are various sources of physical uncertainties which might be broken into range, setup, and motion. Additionally, fractionation induces the problem of handling the interplay of random and systematic uncertainties which affects all sources of errors. Each source of uncertainty is addressed individually next:

Range: Charged particles exhibit a strong dependence on the integral rSP experienced by traversing matter. A change of material density causes a change of stopping powers and consequently impacts the entire dose deposition (Lomax, 2008b). As of now, a patient-specific range uncertainty analysis is not the clinical standard, because it is hard and partly impossible to quantify the exact magnitude of each contributing factor. Instead, each particle therapy center estimates a site- and machine-specific overall range uncertainty. Paganetti analysed and quantified in this regard the contributing factors, which are mainly caused by an imperfect knowledge of the actual stopping powers of the patient. Paganetti estimated the total range uncertainty to lie between 2.7% and 4.6% plus an absolute error of 1.2 mm[¶] assuming an analytical dose calculation (Paganetti, 2012). Two artificial examples to showcase the impact of range errors are presented in Figure II.10. Here, an over- (—) and under-estimation (—) of the rSP are shown for both, protons and carbon ions.

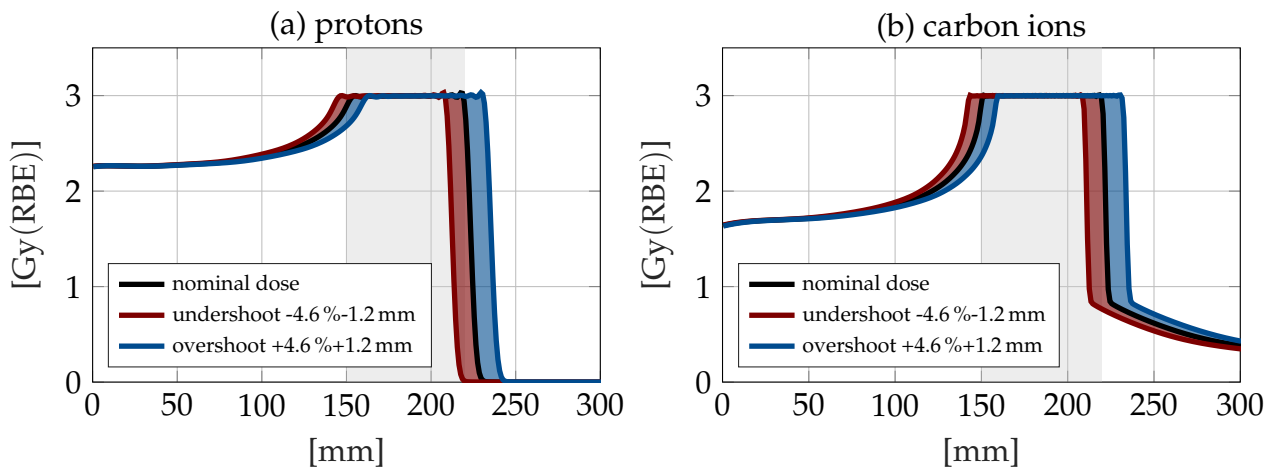


Figure II.10: Two range error scenarios for a proton SOBP and carbon ion SOBP in a one-dimensional water phantom. (—) represents for each modality the optimized nominal dose distribution. The y-axis represents the optimized RBE weighted dose and (—) indicates for both radiation modalities a range undershoot and (—) denotes a range overshoot. A constant RBE of 1.1 was assumed for protons and calculations for carbon ions are based on LEM IV utilizing $\alpha_x = 0.1 \text{ Gy}^{-1}$ and $\beta_x = 0.05 \text{ Gy}^{-2}$. Lastly, the gray area (▭) denotes the PTV.

The elemental problem is that the patient's stopping power can in clinical practice not be measured directly. Therefore, HU values of the CT scanner are converted to rSP or tissue densities employing a piece-wise linear transformation to carry out an analytical- or Monte Carlo-based dose calculation. To establish the linear mapping, a stoichiometric calibration method with known material compositions is performed during commissioning (Schaffner and Pedroni, 1998; Yang et al., 2012).

Further, submillimeter density variations result in different stopping powers that cannot be

[¶](i) excluding biological range extension and (ii) given 1.5 standard deviations

captured as they point to an identical HU value. Also the mean excitation potential I , as part of the Bethe-Bloch Equation shown in Equation II.3, is subject to uncertainty and introduces errors in the stopping power. Such errors have an accumulating effect and are therefore given relatively. Besides CT related uncertainties, e.g., CT noise, grid, and calibration, there are also range errors introduced by the analytical dose calculation algorithm. The first one is given by range degradation caused by multiple high material density gradients in the beam path like bone-soft tissue interfaces or alveoli in the lung (Taylor et al., 2017). As a result, the Bragg peak spreads out longitudinally because of increased range straggling. This effect results in an under-dosage of the tumor plus an additional dose to the healthy dose tissue. Moreover, lateral heterogeneities induce, dependent on the patient case, a disequilibrium of elastically scattered particles, which can cause substantial errors in dose distribution of up to 2.5 % ¹¹ (Paganetti, 2012). These two degradation effects are not captured by analytical pencil beam dose calculation algorithms motivating the use of MC algorithms in particle therapy.

Setup: Patients cannot be positioned consistently throughout all fractions with respect to the planning CT. Thus, the positioning variability introduces a lateral setup uncertainty. Setup errors cause different densities to move into the beam path which then results in particles to penetrate suddenly different tissues than on the planned CT scenario (Lomax, 2008b). It is known that particles are sensitive to setup errors and cause not only a lateral dose deposition uncertainty but also a range uncertainty, which is more pronounced in heterogeneous than in homogenous sites (Liebl et al., 2014).

Anatomical changes: Anatomical changes occur in different time scales and result, similar to setup errors, in altered densities along the beam path. It is important to distinguish here between inter- and intra-fractional anatomical changes. The former is caused by a systematic organ or target displacement, induced by tumor shrinkage or an organ drift over the course of treatment. In contrast, intra-fractional motion represents anatomical changes occurring in a single fraction such as inter-field motions (Lomax, 2008b) or movements of the target itself (lung cancer). In particular, for moving targets, an additional effect, referred to as the interplay effect was observed for pencil beam scanning beam delivery (Seco et al., 2009). This effect is caused by the interplay of two time-dependent processes. A temporal sequence of consecutive pencil beams is applied to the patient's body while the target is moving. This effect distorts the homogenous dose distribution as individual pencil beams are administered to a different target location.

Fractionation: A radiotherapy treatment is applied in several timely separated treatments to make use of the greater cell repair capabilities of normal tissue. Usually 8 to 30 particle fractions are applied to a single patient (Jensen et al., 2012) for which reason uncertainties must be broken down into a random and systematic component. The nature of random and systematic errors can be modeled with distinct correlation models. As systematic errors are the same for all fractions, they can be considered perfectly correlated. Random errors, however, which manifest differently in each realization (fraction) and must therefore be

¹¹ more pronounced for small tumor volumes

considered completely uncorrelated.

Errors in the stopping power estimation of the patient are usually based on a single CT acquired before treatment planning. Thus, the rSP of a patient is systematically wrong in each fraction. Further the inaccurate modelling of range degradation, as it is the case for analytical dose calculation algorithms, also introduces systematic errors. On the other hand, positioning errors have primarily a random error component because systematic positioning errors are inferior due to the technical developments of positioning systems.

Fractionation effects are, in most robust planning approaches, not considered since (i) random errors partly compensate over the course of treatment and (ii) the additional complexity to model fractionation effects. Nevertheless, it is still important to consider the interplay of systematic and random errors for treatment planning due to their varying impact on different fractionation schemes, especially for boost treatments which are employed at the HIT facility.

Others: There are also physical uncertainties which are not directly addressed in this manuscript, for instance, errors in the segmentation of VOIs, CT artifacts, tumor shrinkage, beam properties and beam reproducibility (Lomax, 2008b).

Regarding this thesis, lateral positioning errors and range errors are both modeled via random and systematic error components to consider fractionation effects. A detailed explanation of the utilized physical uncertainty model can be found in Chapter III.2.1.

II.5.2 Biological Uncertainties

A major problem in radiotherapy is the inability to measure the in-vivo radio-sensitivity of a patient directly. Instead, clonogenic cell survival assays or preclinical in-vitro and in-vivo studies are used as reference (Karger and Peschke, 2017). Treatment planning with carbon ions based on the LEM, however, requires the knowledge of the radio-sensitivity parameters of the LQM (α_x, β_x) along with intrinsic LEM parameters (e.g. D_t in Equation II.8) to infer the radio-sensitivity parameters of carbon ions (α_c, β_c) in a mixed radiation field. Along this workflow various biological uncertainties directly influence the resulting RBE and can potentially yield to under- and over-dosage of the tumor and normal tissue, thereby causing a suboptimal or even a failed treatment. For that reason, it is essential to quantify and predict the RBE as accurately as possible. Different to photon therapy, where a dosimetric accuracy of 5% is recommended in the clinic, this threshold can most certainly not be met in carbon ion therapy.

All measurement experiments are prone to uncertainties. This also holds true for the determination of photon cell survival curves and the intrinsic LEM parameters. Not only variabilities between different institutions arise due to differences in the actual experiment or measurement but also inter and intra cell population variabilities are present. The transition from in-vitro results to in-vivo conditions further complicate the situation. Usually, the radio-sensitivity parameters of the LQM (α_x, β_x) represent mean values of multiple experiment

repetitions. It is of great importance to report such values with corresponding probability distributions to fully understand derived quantities like the $\frac{\alpha}{\beta}$ -ratio (Friedrich et al., 2010). Especially, the β_x parameter can only be measured to a certain extent as high doses result in low survival which is hard to quantify in an experimental setup.

Sensitivity studies on this subject obtained from (Böhlen et al., 2012; Friedrich et al., 2013a) show that a single-variation from 25 % to 50 % of LEM input parameters (e.g. $\alpha_x, \beta_x, D_t, r_{nuc}$) result mainly in a proportionally lower impact on the RBE with very few exceptions. Notably, the greatest impact was observed for (α_x, β_x) . It was also found that (i) a miss-estimation of the input parameter mainly resulted in an absolute RBE-error and (ii) RBE uncertainties decreased in a SOBP compared to a single pseudo-mono energetic carbon ion pencil beam, due to compensating mixed field effects. In addition, both studies suggest that a more homogeneous radiation quality (LET) in the target might lower the impact of biological uncertainties on the treatment outcome. With the development of the LEM from I to IV, the accuracy of RBE predictions increased, in particular for lighter ions and high LET regions. With the advancement of the LEM, it was also shown by (Elsässer et al., 2008) that the shape of the track structure model, characterized by the microscopic radial dose profile (see Figure II.5), proved to be a determining factor of the predicted RBE.

Uncertainties in the input parameters of the LEM directly propagate to uncertainties of the model's output. However, any model, including the LEM, needs to make assumptions and can only predict data with a certain accuracy. Intrinsic model limitations can only be detected by systematic deviations between the predicted and reference radio-sensitivity, which reciprocate in clinical studies. However, it is generally difficult to assess errors introduced by the model when the benchmark data itself is associated with uncertainties (Friedrich et al., 2013b).

Not only radio-sensitivity parameters of photons (α_x, β_x) are subject to uncertainty, but also the one of charged particles (α_c, β_c). A well-sorted in-vitro collection, called PIDE** of dose-response data after particle irradiation including carbon ions (α_c, β_c) was published for various irradiation conditions by (Friedrich et al., 2013b). From the database, it can be observed, that the cell's radio-sensitivity variation is lower after ion irradiation compared to photons. Carbon ions possess a higher LET, which causes more complex damage to the DNA. This is why LET and RBE are correlated for therapeutic beam energies. Interestingly, this observation is also in line with a lower sensitivity to radioresistant tumors. It can be inferred that the uncertainties in RBE after particle irradiation trace back to uncertainties in the photon parameters as indicated by the sensitivity analysis presented in (Böhlen et al., 2012; Friedrich et al., 2013a). However, again the in-vivo situation is influenced by many biological interdependencies which elevate the level of uncertainty. Only scarce data is available to validate predictions of the LEM (Karger et al., 2006; Saager et al., 2015, 2016, 2014).

Kamp et al. performed a variance-based sensitivity analysis for a one-dimensional carbon ion treatment plan on the basis of LEM I. Different to (Böhlen et al., 2012; Friedrich et al.,

**Particle Irradiation Data Ensemble: <https://www.gsi.de/bio-pide>

2013a), who varied LEM input parameter individually and did not account for potential interplay, Kamp et al. varied multiple input parameters of an optimized carbon ion treatment plan (dose, α_c and β_c) simultaneously without considering correlation (Kamp et al., 2014). They came to the conclusion, that α_c was the most sensitive parameter with the most significant impact on the resulting RBE-weighted dose. In contrast, β_c only played an inferior role for the fractionated plan under investigation.

Biological uncertainties also arise from the assumption of a single biological system, which is distinctly different to the one that is actually treated (Böhlen et al., 2012). It is common clinical practice to assume a homogenous radio-sensitivity not only throughout the tumor but also for the normal tissue, thereby ignoring potential differences in radiosensitivity. This is still the case due to the lack of knowledge of normal tissue radio-sensitivities. Further inter-patient variabilities are currently not being considered in the clinic.

According to the PIDE database, a lower variation in α_c and β_c , is expected due to the increased LET, but the determination of representative in-vivo mean values itself is associated with large uncertainties. Ideally, radiobiological models should consider input uncertainties in the form of probability distributions and transport this information to output uncertainties in order to create a greater informative value.

To the best of my knowledge, very few publications, which will be discussed in the next two subsections, can be found in the literature that include biological uncertainties for carbon ion therapy. For this reason, the manuscript also addresses uncertainties in the biological response to ion radiation by modeling uncertainties in the α_c and β_c parameters.

II.5.3 Uncertainty Quantification and Mitigation

Uncertainties in particle therapy, introduced in the previous chapter, can be addressed in the TPS and complemented by hardware-related approaches. Before focusing on the former, hardware-related mitigation approaches are briefly introduced below, although some of them are at the moment admittedly far away from clinical application.

Errors originating from CT artifacts might be tackled by better reconstruction algorithms or by new imaging devices, e.g., dual energy CT, whereas uncertainties caused by anatomical changes and patient positioning might be minimized in the future with online adaptive replanning and image guidance (Veiga et al., 2016). Moreover, range uncertainties can be addressed by dual-energy CTs as they increase the accuracy of rSP predictions (Wohlfahrt et al., 2018). Additionally, there are also experimental approaches currently under investigation, such as prompt gamma imaging for in-vivo range verification (Hueso-González et al., 2018; Xie et al., 2017), proton CT imaging (Civinini et al., 2017) and ionoacoustic wave measurements (Kellnberger et al., 2016; Lehrack et al., 2017).

The remaining chapter is about software-related approaches as part of the TPS to quantify and/or mitigate uncertainties.

II.5.3.1 Uncertainty Quantification

Adequate uncertainty analyses in radiotherapy are not part of daily clinical routine. The size of the dose influence matrix D is the main limitation which is in the order of giga bytes. This makes dose calculations for different error scenarios not only computationally challenging but also time consuming. For that reason, sampling strategies and uncertainty quantification methods were developed in the past decade.

Focusing briefly on photon therapy, (Baum et al., 2004; van Herk et al., 2002) applied dose blurring techniques using uncertainty kernels to reveal the treatment plan's variability induced by geometrical uncertainties. Further, Sobotta et al. modeled the distribution of treatment plan quality indicators (e.g. EUD) with a Gaussian Process (GP) in closed-form, thereby only relying on a few discrete error scenarios (Sobotta et al., 2012). However, these approaches considered photon irradiation and are only applicable in a limited way to particle treatment plans.

Shifting the focus back to particle therapy, Albertini et al. proposed an importance sampling strategy for proton therapy in which discrete samples are taken from the surface of a spherical error-space to derive error bar dose distributions (Albertini et al., 2011). Each voxel in the error bar dose distribution denotes the dose range on the 85 % confidence limit across all samples. It was further shown that SFUD generally results in more robust treatment plans than IMPT when comparing error bar volume histograms.

An extension was presented by Lowe et al., who additionally considered systematic and random errors individually for protons herewith neglecting potential interdependencies (Lowe et al., 2016). Here, two error bar distributions were obtained separately and then weighted according to current fractionation scheme under investigation by a linear fractionation model. Specifically, the first error bar distribution denotes a single fraction treatment and the second one a F fractionated treatment. For the reported head case considering range and setup errors the error bar distribution resulted in a maximum value of 24 % with respect to the prescribed dose. This means, that single voxels possessed a dose range (within the 85 % confidence limit) of almost a quarter of the total dose. Furthermore, Lowe et al. pointed out that neglecting fractionation effects yields to a considerable overestimation of dose uncertainties. Casiraghi et al. (2013) compared the sampling approach of Albertini et al. against random sampling and concluded that for a volumetric analysis the lower and upper Dose Volume Histogram (DVH) error estimates are accurately predicted. This is due to the fact as four-dimensional information (x,y,z,d) is collapsed onto the two-dimensional DVH plane thereby averaging out potential differences. On a voxel by voxel comparison, the dose error obtained from the sphere-surface sampling underestimates the uncertainty, especially in high dose-gradient regions due to the small number of sampled scenarios.

Considering random sampling, then Authors mentioned in (Maleike et al., 2006; Sobotta et al., 2012; Wieser et al., 2017b) and in particular (Wahl et al., 2017) showed that a high

number of random samples ($\sim 5000 - 10000$)^{††} are required to obtain an accurate uncertainty estimate. Five thousand samples ensured the standard deviation of standard deviation $\sigma[\sigma_d]$ to be less than 1 %. Further, Wahl et al. came to the conclusion that grid and importance sampling strategies tend to underestimate the uncertainty in dose which is in line with findings of (Casiraghi et al., 2013).

In a recent paper by Perkó et al., polynomial chaos expansion was introduced to derive the probability distribution of proton treatment plan quality indicators. The idea is to approximate an exact solution with a set of polynomials under the presence of errors on the basis of a discrete set of error scenarios. Once the meta-model is trained, various dose statistics can be derived (Perkó et al., 2016). For head and neck cancer patients irradiated with protons and a prescribed target dose of 66 Gy, a standard deviation in dose in the Clinical Target Volume (CTV) of up to ~ 13 Gy was observed when considering ± 3 mm setup and $\pm 3\% + 1$ mm range uncertainties. This method allows reducing the computational complexity compared to random sampling without significantly affecting the model's accuracy. However, such meta-model approaches (Perkó et al., 2016; Sobotta et al., 2012) do not generalize to optimization for which a re-evaluation of the dose distribution for different pencil beam weights is needed.

Sakama et al. studied carbon ion treatment plan uncertainties taking fractionation into account (Sakama et al., 2016). Up to 34 individual setup and range errors were modeled to derive discrete dose error scenarios using a fast dose wrapping technique. The authors reported a standard deviation of 30 % for setup errors of ± 3 mm. Moreover, the consideration of $\pm 3\%$ range errors resulted in a standard deviation of nearly 50 % of the prescribed dose for the reported prostate case. The mean value of relative standard deviation in the rectum resulted in 12 %. For the reported head and neck case, the mean value of the relative standard deviation reached for the optic nerve almost 18 %. These numbers directly motivate further research not only for uncertainty quantification but also for uncertainty mitigation in carbon ion therapy.

II.5.3.2 Uncertainty Mitigation

Nowadays, it is clinical standard to compensate geometrical uncertainties for unproblematic cases during treatment planning with a generalized isotropic expansion of the CTV. The resulting VOI is commonly known as PTV (Van Herk, 2004). For problematic cases besides choosing robust beam angles, site- and beam-specific margins are facilitated considering range uncertainties (Paganetti, 2012; Park et al., 2012). This safety margin concept is based on the static dose cloud approximation originating from photon irradiation assuming the delivered dose stays unaltered by density changes in the beam path (Bortfeld et al., 2004). Admittedly, this assumption is not transferable to particle therapy as the geometrical position

^{††}This number might be lower for less complex cases.

of the Bragg peak strongly depends on the integral rSP (Albertini et al., 2011; Lomax, 2008b; Unkelbach and Paganetti, 2018). Therefore, the safety margin concept does in general not suffice to account for geometrical uncertainties in particle therapy.

The PTV margin concept and SFUD optimization are applied to patients that show manageable risk. However, to manage high-risk patients, other robust treatment planning approaches have been developed in the past employing MFO. These approaches receive increased attention as not only high risk but also patient cases associated with moderate setup and range uncertainties might benefit. A general overview of robust optimization techniques in intensity-modulated proton therapy is given in (Unkelbach et al., 2018).

For the mitigation of patient motion during a particle therapy treatment, the interested reader is referred to (Graeff, 2014) who discusses different motion mitigation approaches for scanned ion beam therapy with an emphasis on 4D optimization.

Worst Case Optimization Several papers appeared reporting on worst case optimization where multiple discrete worst case error scenarios with equal occurrence probability built the common basis. Instead of using a single dose influence matrix D , which corresponds to the nominal patient geometry, multiple dose influence matrices D^e for the respective error scenarios e , are calculated during dose calculation. Let e be the superscript enumerating over a discrete set of E error scenarios. Typically, several fully correlated under and overshoot range error scenarios are combined with multiple setup error scenarios. On the one hand range error scenarios are realized by scaling the rSP (WEPL) and on the other hand, setup error scenarios are realized by spatially shifting the iso-center. There are different flavors of worst case optimization which mainly vary in the definition of the worst-case dose distribution or the worst case objective function value \mathcal{F}^{WC} (Chen et al., 2012; Fredriksson and Bokrantz, 2016; Fredriksson et al., 2011; Liu et al., 2013; Lowe et al., 2016; Pflugfelder et al., 2008). The most prominent worst case optimization approaches are explained next.

Voxel Wise Worst Case: In this approach, a physically inconsistent worst case dose distribution is created on the basis of E error scenarios according to Equation II.31:

$$d_i^{WC} = \begin{cases} \min(d_i^e) & \text{if: } i \in \text{Target} \\ \max(d_i^e) & \text{if: } i \in \text{OAR} \end{cases} \quad (\text{II.31})$$

where the minimum/maximum dose across all scenarios in voxel i is considered if i belongs to the target/OAR structure. The worst case objective function \mathcal{F}^{WC} is calculated on the basis of \mathbf{d}^{WC} , penalized with p^{WC} and then added to the existing objective function value (Pflugfelder et al., 2008). An extension of this approach was presented by Liu et al., who considered, in addition to the minimum worst case dose in the target, a maximum worst case dose. By this means, the lower and upper worst case doses in the target are constrained separately (Liu et al., 2013). This allows assigning a higher penalty on the under dose objective to avoid under-dosage of the tumor which is considered to be of greater importance.

Objective Wise Worst Case: Objective wise worst case optimization requires the evaluation

of each individual objective function f_n^e on all error scenarios E . The overall objective function value f is then calculated by taking the maximum of each individual objective function. Hence, $\max(f_1^e) + \max(f_2^e) + \dots$ are added up and again a physically inconsistent total objective function value \mathcal{F}^{WC} is obtained (Chen et al., 2012).

Composite Worst Case: Here, the total objective function value \mathcal{F}^{WC^e} is calculated for each scenario e in each step of the optimization. Next, the scenario with the maximum objective function value (= current worst case) is chosen to be minimized in the next optimization iteration. By this means the current worst case scenario is minimized which translates mathematically to: $\min\left(\max\left(\mathcal{F}^{WC^e}(\mathbf{d})\right)\right)$. This approach is known as min max or composite worst case optimization (Fredriksson et al., 2011) and different to the strategies mentioned above, a physically consistent scenario is optimized.

Robust optimization approaches based on discrete error scenarios are computationally demanding as (i) multiple dose influence matrices need to be held in storage and (ii) the respective worst case objective function needs to be evaluated every time pencil beam intensities change. As a consequence, the consideration of more error scenarios increases the computation time linearly in each iteration of the optimization. Further, robust optimization suffers from the number of combinations when interdependencies between different sources of uncertainties, correlation models and fractionation effects are considered (the curse of dimensionality).

Moreover, also from a theoretical point of view, a worst case scenario in the input space does not per se correspond to the worst case dose distribution in the output space. This means that there might be an intermediate error scenario, that actually represents the worst case that is not covered by the E error scenarios. Nevertheless, all methodologies presented so far can be used for robust optimization but can only be applied in a limited way for uncertainty quantification. Although they yield robust treatment plans, these approaches strongly dependent on the considered discrete error scenarios (point estimates), which act as a lower bound for the treatment plan quality. The consideration of improbable scenarios for worst case optimization might then result in a treatment plan that is too conservative (Fredriksson and Bokrantz, 2014).

To facilitate a comparison between worst case optimization and probabilistic optimization, which is described next, the calculation of dose influence error scenarios D^e was implemented in matRad. Using a multi-dimensional cell array of sparse matrices allowed to store and access respective error scenarios efficiently. However, the dose calculation time scaled linearly with the number of E error scenarios. The comparison between robust and probabilistic optimization is shown in the result Chapter IV.2.2.3.

Stochastic Programming - Probabilistic Optimization A key aspect of stochastic programming approaches is the consideration of a weighting factor p^e that allows steering the importance of each dose scenario. A special flavor is given by probabilistic optimization which

treats p^e as a probability. This allows associating more probable scenarios with a higher and less probable scenarios with a lower probability (Sobotta et al., 2010; Unkelbach, 2006; Unkelbach et al., 2018, 2009, 2007).

$$\begin{aligned}
\mathbf{w}^* &= \underset{\mathbf{w}}{\operatorname{argmin}} \sum_{e=1}^E p^e \mathcal{F}(\mathbf{d}(\mathbf{w})) \\
&\approx \underset{\mathbf{w}}{\operatorname{argmin}} \mathbb{E}[\mathcal{F}(\mathbf{d}(\mathbf{w}))] \\
&\text{subject to } \mathbf{w} \geq 0
\end{aligned} \tag{II.32}$$

Here the overall goal is to estimate the expected value of the objective function value $\mathbb{E}[\mathcal{F}]$ from discrete error scenarios and then optimize $\mathbb{E}[\mathcal{F}]$ as illustrated in Equation II.32. Unkelbach et al. estimated the expected objective function value $\mathbb{E}[\mathcal{F}]$ from discrete error scenarios, whereby each individual objective function value is weighted with its occurrence probability. In each step of the applied stochastic gradient descent optimization, a subset of error scenarios is sampled to firstly reduce storage requirements and secondly still account for different combinations. Sampling and calculating dose in each step of the optimization resulted in run-times of several hours as reported by (Unkelbach et al., 2009). A simplification of this approach is to consistently use a predefined set of discrete errors scenarios (D^e) throughout optimization without sampling different scenarios in each optimization iteration. One potential drawback of probabilistic optimization is essentially the optimization of the expectation value of the objective function value which might result in too less conservative treatment plans that are not robust against actual worst case scenarios.

To avoid sampling, authors mention in (Bangert et al., 2013) proposed to optimize the expectation value of a squared deviation objective $\mathbb{E}[f_{sq dev}]$ in closed-form on the basis of (Imhof, 1961; Liu et al., 2009). On the one hand, optimizing $\mathbb{E}[f_{sq dev}]$ in closed-form requires the knowledge of the expectation value and (co-variance) of the dose distribution before optimization but induces on the hand only minimal computational overhead to probabilistic optimization. This approach represents the underlying probabilistic optimization strategy used throughout this work. More details are presented later in Chapter III.4.

One group of probabilistic optimization strategies not covered here is given by coverage-based methods which aim to optimize the coverage probability over a discrete set of error scenarios. Herewith, the width of the resulting probability density is minimized. For detailed information the reader is referred to (Baum et al., 2006; Gordon et al., 2010; Hysing et al., 2011; Mescher et al., 2017).

II.5.4 Uncertainty Considerations for Carbon Ion Therapy

Most of the recent approaches were applied to proton therapy and so far only view publications can be found about carbon ions. Besides the work of Sakama et al., who quantified the standard deviation in the RBE weighted dose to range from 30 to 50 % for individual

voxels, Steitz et al. focused on carbon ion treatment plans too. Steitz et al. investigated dosimetric implications of inter-fractional motion on pancreatic cancer patients on the basis of conventional, SFUD and voxel wise worst case optimization. They concluded that robust optimization can be applied to carbon ion therapy and that it is a beneficial tool to increase target coverage (Steitz et al., 2016).

Both papers (Sakama et al., 2016; Steitz et al., 2016) motivate further investigations into uncertainty quantification to subsequently mitigate their impact on the resulting carbon ion treatment plan. Hence, the scope of this work is to quantify setup, range and biological uncertainties within treatment planning and to mitigate their impact by re-modulating pencil beam intensities in a robust manner.

The foundation of this work is called Analytical Probabilistic Modeling (APM) and was first published by (Bangert et al., 2013) for protons and photons. The main difference between previously discussed approaches and APM is that APM does not require the calculation of discrete error scenarios to derive treatment plan uncertainties in the form of expectation value and standard deviation. This concept was further developed for protons by (Wahl et al., 2017, 2018a). In contrast, this work focuses on the application of APM on carbon ion treatment planning thereby taking the non-linear biological effects of carbon ions into account. The central principle of APM is the closed-form calculation of statistical moments of treatment plan quality indicators which is explained in detail in the next Chapter III.

"How to quantify uncertainty?"

III

Material and Methods

The idea of Analytical Probabilistic Modeling APM is to calculate the expectation value and higher order statistical moments of a function $I(\mathbf{X})$ under the premise the probability distribution $p_{\mathbf{X}}(x)$ of ζ random variables $\mathbf{X} \in \mathbb{R}^{\zeta}$ is known. The underlying concept is often referred to as *method of moments* or *law of the unconscious statistician* (LOTUS) and is shown in Equation III.1. In the context of radiotherapy, APM allows quantifying statistical moments of radiation treatment plan quality indicators I in closed-form under the influence of uncertainties:

$$\mathbb{E}[I(\mathbf{X})^n] = \int_{\mathbb{R}^{\zeta}} p_{\mathbf{X}}(x) I(x)^n dx \quad (\text{III.1})$$

Following Table III.1 and setting in Equation III.1 $n = 1$ allows to derive the expectation value which is represented by the first raw moment (μ'_1), whereas the variance is given by the second central moment (μ_2). Also, higher order moments $n > 2$, shown in Table III.1, can in principle be calculated to obtain for instance the skewness (μ_3) or kurtosis (μ_4) permitting a more accurate description of the unknown probability distribution of $p(I)$.

In this work, an analytical probabilistic model is built upon the biological effect ε (see Equation II.7) and not the RBE weighted dose because it is mathematically convenient to

Table III.1: Overview of the first four raw and central statistical moments of a treatment plan quality indicator I . The expectation value is given by the first raw moment μ'_1 and the variance by the second central moment μ_2 .

| Type definition | raw moment - about origin $\mu'_k = \mathbb{E}[I^k]$ | central moment - about mean $\mu_k = \mathbb{E}[(I - \mu)^k]$ |
|-----------------|---|--|
| M0 | $\mu'_0 = \mathbb{E}[I^0]$ | $\mu_0 = \mathbb{E}[(I - \mu)^0]$ |
| M1 | $\mu'_1 = \mathbb{E}[I^1]$ | $\mu_1 = \mathbb{E}[(I - \mu)^1]$ |
| M2 | $\mu'_2 = \mathbb{E}[I^2]$ | $\mu_2 = \mathbb{E}[(I - \mu)^2]$ |
| M3 | $\mu'_3 = \mathbb{E}[I^3]$ | $\mu_3 = \mathbb{E}[(I - \mu)^3]$ |
| M4 | $\mu'_4 = \mathbb{E}[I^4]$ | $\mu_4 = \mathbb{E}[(I - \mu)^4]$ |

avoid the square root dependence of the RBE weighted dose (see Equation II.23). Thus a focus is set on quantifying the expectation value and standard deviation of the distribution of the biological effect $p(\varepsilon)$ in a three-dimensional carbon ion treatment plan. In a subsequent step, covered in Subsection III.5, moments of the biological effect ε are propagated to moments of the RBE weighed dose.

Assuming the biological effect ε is a function of uncertain input parameters \mathbf{X} , that follow a specific probability distribution $p_{\mathbf{X}}(x)$, the n -th raw moment can then be obtained via:

$$\mathbb{E}[\varepsilon(\mathbf{X})^n] = \int_{\mathbb{R}^c} p_{\mathbf{X}}(x)\varepsilon(x)^n dx \approx \int_{\mathbb{R}^c} \mathcal{N}(x, \bar{\mathbf{X}}, \Sigma^{\mathbf{X}}) \hat{\varepsilon}(x)^n dx \quad (\text{III.2})$$

In this formulation, the biological effect becomes a function of treatment plan uncertainties, where \mathbf{X} denotes uncertain input parameters such as the patient position, range, and radio-sensitivity of charged particles. The uncertainty of the input parameters can as first approximation be described with a multivariate Normal distribution $\mathcal{N}(x, \bar{\mathbf{X}}, \Sigma^{\mathbf{X}})$, which is explained in Section III.3. However, to solve Equation III.2 in closed-form, also the biological effect ε needs to be integrable against Normal probability densities. Although a non-trivial analytical formulation of the proton depth dose curve exists (Bortfeld, 1997), there is no adequate analytical formulation of carbon ion depth dose profiles and dose-averaged α_c and β_c profiles. This is why an analytical approximation is established for $\hat{\varepsilon}$ in Section III.1 that allows solving the integral in Equation III.2 in closed-form. From a mathematical point of view, the solution of Equation III.2 is exact, if limitations of the pencil beam algorithm are neglected and Gaussian error assumptions are correct. More details about the limitations of APM are provided in the discussion Chapter in V.2.

The upcoming sections explain step by step how to propagate input uncertainties in closed-form to output uncertainties without the need to sample discrete error scenarios.

III.1 Functional Approximation of Base Data

This section presents the functional approximations of physical depth-dose profiles, of α_c and β_c profiles required to (i) calculate the biological effect $\hat{\varepsilon}$ of carbon ions and (ii) to solve the integral of Equation III.2 in closed-form. Thus, the primary challenge is to find approximations that are at the same time accurate and computationally efficient.

III.1.1 Physical Dose of Protons & Carbon Ions

Bangert et al. decided to fit a weighted superposition of ten Gaussian components to the proton depth dose profile (Bangert et al., 2013). The choice for using non-normalized Gaussian components is motivated by their convenient mathematical properties (conditioning, marginalization) as highlighted in Appendix A. Further, Bangert et al. showed that the average deviation between the functional approximation and the original proton depth dose

curves is less than 0.3%. In a previous publication, Schölkopf showed that every Lipschitz-continuous function such as particle depth dose profiles, can be approximated with increasing quality by simply adding more and more Gaussian components to the fit (Schölkopf, 2002). Increasing the number of Gaussian components results on the one hand in more accurate approximations but causes on the other hand longer computation times.

Here, thirteen Gaussian components were used to describe the physical depth dose profile of carbon ions. The choice for increasing the number of components to thirteen was motivated due to the sharper Bragg peak and the additional dose tail that needs to be modeled for carbon ions.

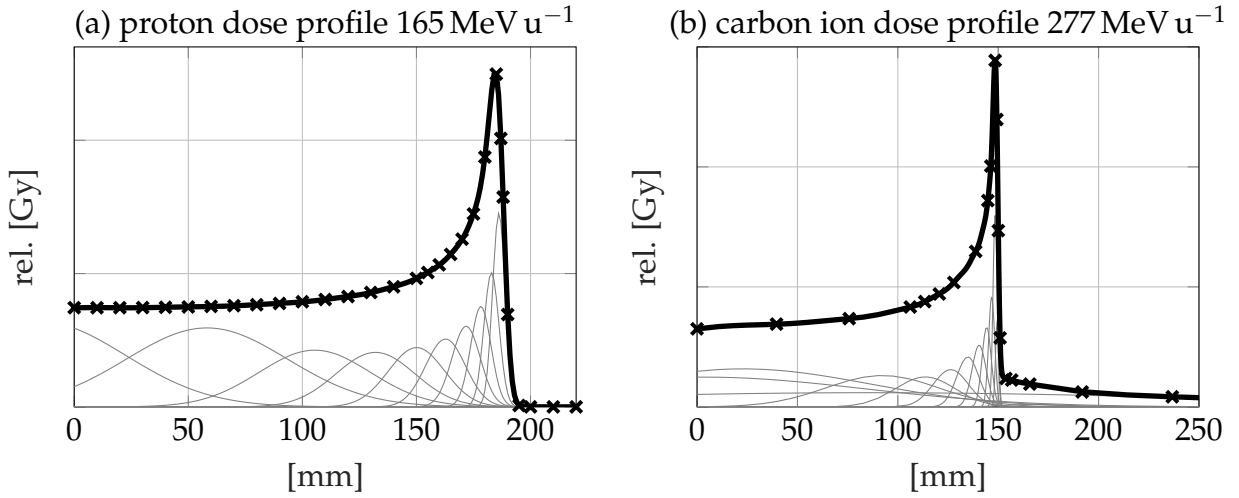


Figure III.1: Plot (a) presents the functional approximation of the laterally integrated proton depth dose profile (165 MeV u^{-1}) using ten Gaussian components (Bangert et al., 2013). Plot (b) shows the functional approximation of the laterally integrated carbon ion depth dose profile (277 MeV u^{-1}) using thirteen Gaussian components. Crosses indicate an excerpt of the original proton and carbon ion depth dose profiles.

Figure III.1(a) illustrates the fitting result of a laterally integrated physical proton depth dose profile whereas Figure III.1(b) presents a laterally integrated carbon ion depth dose profile. Crosses (\times) represent an excerpt of the corresponding original depth dose profile. Least square fits were performed, similar to that of protons, to obtain for each initial beam energy and each Gaussian component (—) the mean μ , standard deviation σ and weight ω . Thus, each tabulated depth dose profile is replaced by a functional approximation parameterized with a set of 39 parameters (3×13).

Let k be the index of the k -th Gaussian component and z_{ij} be the WEPL of pencil j in voxel i , then the physical depth dose can be calculated according to:

$$Z_{ij} = \sum_{k=1}^K \frac{\omega_{jk}}{\sqrt{2\pi\sigma_{jk}^2}} e^{-\frac{(z_{ij}-\mu_{jk})^2}{2\sigma_{jk}^2}} \quad (\text{III.3})$$

The fitting procedure is done in an offline pre-computation that only needs to be carried out once, to be used for routine treatment planning. The proton base data, exemplarily shown in Figure III.1(a) for 165 MeV u^{-1} builds the basis for APM developments on the proton side assuming a constant RBE of 1.1 (Wahl et al., 2017, 2018a). The proton base data is made

available publicly in a one-dimensional treatment planning toolkit on Github*.

Focusing on carbon ion treatment planning additionally requires knowledge of the non-linear biological response to irradiation of the current tissue under consideration. Thus, physical depth dose profiles alone are not sufficient for clinical carbon ion treatment planning for which reason the next subsection explains the functional approximation of the biological effect $\hat{\epsilon}$.

III.1.2 Biological Effect

Depth-dependent physical and biological properties of a pseudo mono-energetic carbon ion pencil beam for a certain tissue, can be described with a set of three profiles, namely a laterally integrated physical dose-, a α_c - and a β_c -profile. The left plot of Figure III.2 depicts these three profiles for a 277 MeV u^{-1} carbon ion beam. Following the formulation of the biological effect ϵ from Equations II.7 and II.24 allows combining the α_c and β_c profile with the d profile, respectively, employing a point-wise multiplication. The corresponding result is shown in the right plot of Figure III.2. Herewith, the number of profiles that need to be stored for a single tissue type is reduced from three to two.

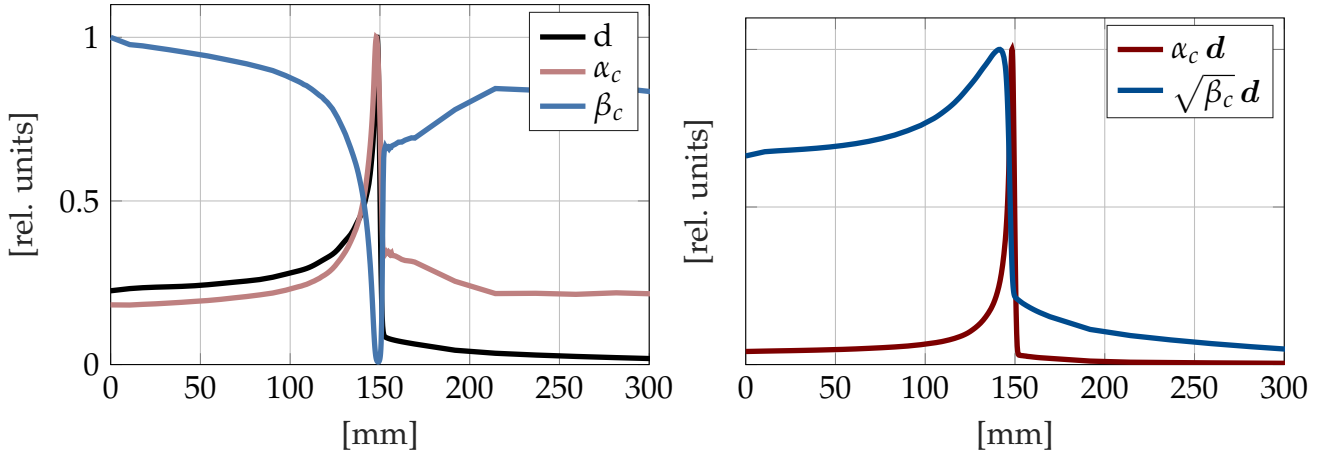


Figure III.2: The left plot shows the normalized integrated carbon ion depth dose profile of a 277 MeV u^{-1} beam (—) in water along with corresponding dose-averaged α_c (—) and β_c (—) profiles of the LQM predicted by LEM IV using $\alpha_x = 0.1 \text{ Gy}^{-1}$ and 0.05 Gy^{-2} . The right plot shows the point-wise multiplication of α_c and d in (—) and $\sqrt{\beta_c}$ times d in line (—).

Each profile, shown in Figure III.2(b), was used to fit thirteen Gaussian components. The resulting parameters for each initial beam energy can afterwards be used to calculate the depth-dependent components Z_{ij}^α and Z_{ij}^β of the biological effect of each pencil beam j in the patient according to Equation III.4: ω_{jk}^α , ω_{jk}^β , μ_{jk}^α , μ_{jk}^β and δ_{jk}^α , δ_{jk}^β :

$$Z_{ij}^\alpha = \sum_{k=1}^K \frac{\omega_{jk}^\alpha}{\sqrt{2\pi\delta_{jk}^{\alpha 2}}} e^{-\frac{(z_{ij}-\mu_{jk}^\alpha)^2}{2\delta_{jk}^{\alpha 2}}}; \quad Z_{ij}^\beta = \sum_{k=1}^K \frac{\omega_{jk}^\beta}{\sqrt{2\pi\delta_{jk}^{\beta 2}}} e^{-\frac{(z_{ij}-\mu_{jk}^\beta)^2}{2\delta_{jk}^{\beta 2}}} \quad (\text{III.4})$$

*<https://github.com/e0404/APMtoolbox>

The fitting results of the $\alpha_c d$ and $\sqrt{\beta_c d}$ profiles are shown in Figure III.3 for one exemplary energy. Comparing the fitting data against the ground truth yields a mean relative difference of 0.25 % for $\alpha_c d$ and 0.06 % for $\sqrt{\beta_c d}$ profiles. Because of the extremely peaked $\alpha_c d$ profile, it can be observed that the mean relative difference of $\alpha_c d$ profiles is higher than the one of $\sqrt{\beta_c d}$ profiles. Crosses (\times , \times) in Figure III.3 indicate an excerpt of the corresponding ground truth data.

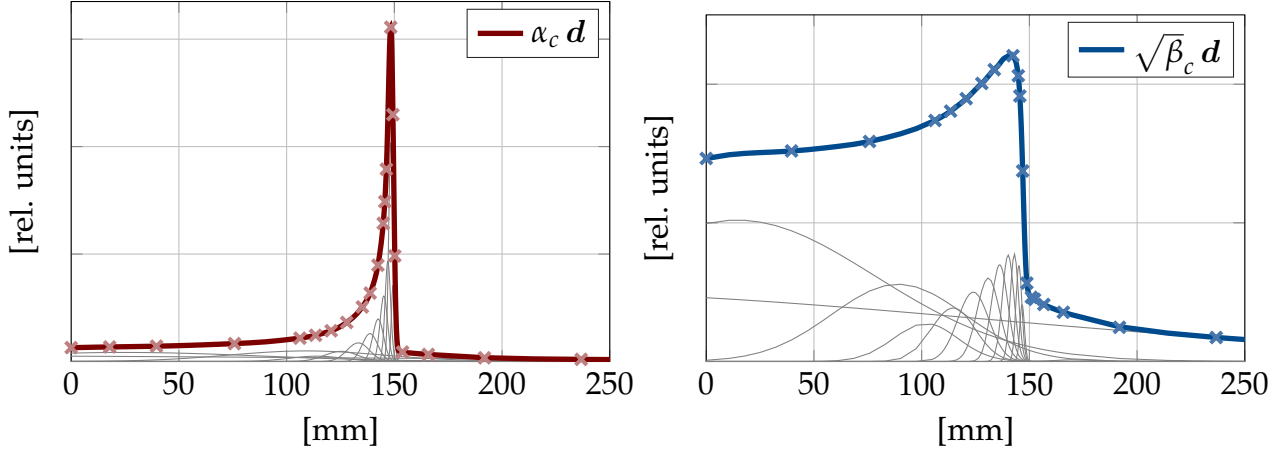


Figure III.3: The left plot shows the fitting result of the $\alpha_c d$ profile of a 277 MeV u^{-1} carbon ion beam (—), whereas the right plot presents the corresponding $\sqrt{\beta_c d}$ profile (—). Crosses represent an excerpt of the corresponding ground truth data. (\times , \times) represent an excerpt of the original data.

For simplicity, it is assumed the lateral dose profile can be described in first approximation with a single Gaussian profile. Let λ_{ij} be the width of pencil beam j in voxel i taking into account the WEPL z_{ij} and let $\mathcal{N}(x|\mu, \lambda)$ define a Normal distribution with mean μ and standard deviation λ . Additionally, let x_{ij} and y_{ij} be the geometrical distances from the central ray of pencil beam j to voxel i , then the biological effect computation of ε_i in Equation II.27 can be reformulated to:

$$\varepsilon_i \approx \hat{\varepsilon}_i = \sum_{j=1}^B w_j \mathcal{N}(x_{ij}|\mu_j^x, \lambda_{ij}) \mathcal{N}(y_{ij}|\mu_j^y, \lambda_{ij}) \sum_{k=1}^{13} \omega_{jk}^\alpha \mathcal{N}(z_{ij}|\mu_{jk}^\alpha, \delta_{jk}^\alpha) + \left[\sum_{j=1}^B w_j \mathcal{N}(x_{ij}|\mu_j^x, \lambda_{ij}) \mathcal{N}(y_{ij}|\mu_j^y, \lambda_{ij}) \sum_{k=1}^{13} \omega_{jk}^\beta \mathcal{N}(z_{ij}|\mu_{jk}^\beta, \delta_{jk}^\beta) \right]^2 \quad (\text{III.5})$$

It can be seen from Equation III.5, that the computation of ε_i solely relies on Gaussian components, laterally as well as in depth. As the consideration of a superposition of Gaussian components instead of tabulated data introduces only minor differences compared to the uncertainties, discussed in the previous chapter, the *hat*-symbol in $\hat{\varepsilon}$ will be dropped for further considerations.

The fitted carbon ion beam parameters depicting a generic machine, were published on Github[†] for two different tissue types on the basis of the LEM IV. The functional approxi-

[†]<https://github.com/e0404/APMtoolbox>

mation in Equation III.5 allows now to integrate the biological effect against a multivariate Normal distribution analytically.

III.2 Physical Uncertainties

This section details the mathematical methodology of channeling setup and range uncertainties through the analytical calculation of the biological effect to derive the first and second statistical moments of the biological effect. Firstly, Subsection III.2.1 covers the underlying uncertainty model for setup and range uncertainties and secondly Subsections III.2.2 and III.2.3 detail the respective moment calculation.

III.2.1 Uncertainty Model

Unlike most of the uncertainty quantification methods outlined in II.5 which consider uncertainty sources in the voxel domain $i \{i \in \mathbb{N} | 1 \leq i \leq I\}$, APM models setup and range uncertainties in the pencil beam space $j \{j \in \mathbb{N} | 1 \leq j \leq J\}$. By this means physical uncertainties are not modeled in the patient geometry (CT scan) but instead they are modelled in the lower dimensional pencil beam space ($J \ll I$) by being uncertain in their exact position. For that reason setup and range errors affect each pencil beam by an offset $(\Delta^x, \Delta^y, \Delta^z \in \mathbb{R}^{J \times 1})$ in the Gaussian components required for the biological effect calculation:

$$\varepsilon_i = \sum_{j=1}^J w_j \mathcal{N}(x_{ij} + \Delta_j^x | \mu_j^x, \lambda_{ij}) \mathcal{N}(y_{ij} + \Delta_j^y | \mu_j^y, \lambda_{ij}) \sum_{k=1}^{13} \omega_{jk}^\alpha \mathcal{N}(z_{ij} + \Delta_j^z | \mu_{jk}^\alpha, \delta_{jk}^\alpha) + \left[\sum_{j=1}^J w_j \mathcal{N}(x_{ij} + \Delta_j^x | \mu_j^x, \lambda_{ij}) \mathcal{N}(y_{ij} + \Delta_j^y | \mu_j^y, \lambda_{ij}) \sum_{k=1}^{13} \omega_{jk}^\beta \mathcal{N}(z_{ij} + \Delta_j^z | \mu_{jk}^\beta, \delta_{jk}^\beta) \right]^2 \quad (\text{III.6})$$

In first approximation, it is assumed that Δ^x , Δ^y and Δ^z are jointly distributed $p(\Delta^x, \Delta^y, \Delta^z)$ and obey a multi-variate Normal distribution $\mathcal{N}^{tot}(\Delta^x, \Delta^y, \Delta^z)$. In second approximation, Δ^x , Δ^y and Δ^z are assumed to be independent from each other which implies uncorrelated error sources although setup errors are in reality correlated with range errors. In principle, APM permits to model such correlations between spatial dimensions to more accurately reflect complex spatial interdependencies. However, the dimensionality of Gaussian evaluations increases accordingly and with that the computational complexity. The simplification of independent error sources made here are empirically evaluated in the result Section IV.2.2.1 and allow for the following factorization:

$$\mathcal{N}^{tot}(\Delta^x, \Delta^y, \Delta^z | 0, \Sigma^{tot}) = \mathcal{N}(\Delta^x | 0, \Sigma^x) \mathcal{N}(\Delta^y | 0, \Sigma^y) \mathcal{N}(\Delta^z | 0, \Sigma^z) \quad (\text{III.7})$$

where each distribution is characterised with zero mean and a covariance matrix $\Sigma^{x/y/z} \in \mathbb{R}^{J \times J}$. Specifically, the latter allows to model arbitrary correlation assumptions in the pencil

beam space while keeping the calculation and optimization complexity for different correlation patterns constant. Not only the magnitude of the uncertainty of a pencil beam can be modeled but also the correlation between different pencil beam combinations.

Examples for different correlation assumptions in the covariance matrix Σ assuming in total thirteen pencil beams are shown in Figure III.4. Here, j and m denote pencil beam indices and ρ depicts the correlation coefficient. The covariance matrices presented in Figure III.4 corresponds to a schematic treatment plan comprised of two beams, whereas each beam consists of three rays and each ray is, except the second ray of the first beam is composed of two pencil beams. Each element of the covariance matrix is defined via $\Sigma(j, m) = \rho \sigma_j \sigma_m$ and $\rho = 1$ (yellow) indicates a perfect correlation between offsets for pencil beam j and m . In contrast $\rho = 0$ (blue) implies uncorrelated offsets between pencil beam j and m . Figure III.4 depicts three different correlation patterns whereby all exhibit a block structure.

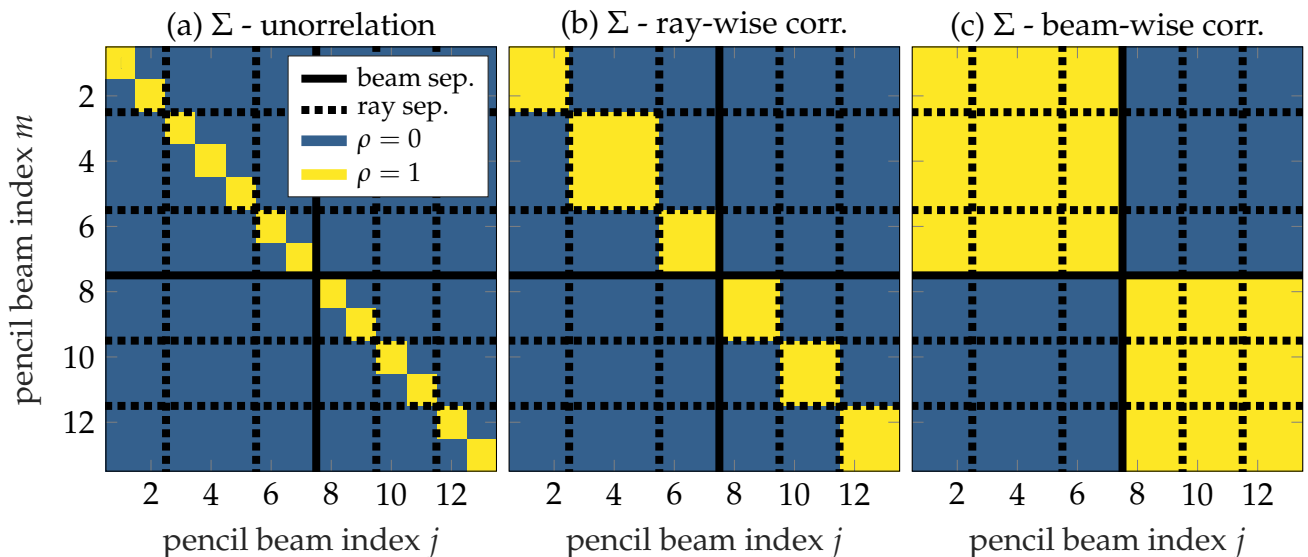


Figure III.4: Three distinct correlations patterns for pencil beam interdependencies. The covariance matrices exhibit block structure and schematically denote a treatment plan comprised of thirteen pencil beams delivered by two beam directions. (—) indicates the beam-separator and (- - -) denotes the ray separator.

Firstly, Figure III.4(a) shows uncorrelated pencil beam combinations. All off-diagonal elements are zero and only diagonal elements which define the variance of pencil beam j , are greater than zero. The second Figure III.4(b) employs a ray-wise correlation model. As highlighted by the ray-separation lines (- - -) all pencil beam combinations belonging to the same ray are perfectly correlated. On the contrary, pencil beam combinations from different rays are uncorrelated. Lastly, Figure III.4(c) shows a beam-wise correlation model through separator lines (—). Here, all pencil beam combinations from the same beam direction are correlated and uncorrelated otherwise.

A fully correlated covariance, as used for worst case optimization strategies modeling range errors, might also be employed but is not explicitly shown here. For such cases, perfect correlation means that we only consider scenarios where either all errors correspond to a simultaneous over- or underestimation of the computed range.

Following the work of (Unkelbach et al., 2009) and (Bangert et al., 2013), a beam-wise

correlation (see Figure III.4(c)) is assumed for the lateral positioning error in x and y dimension. The background to this is the assumption that positioning errors realize for each beam direction independently. For the range error, a ray-wise correlation structure (see Figure III.4(b)) is assumed, since all pencil beams belonging to the same ray penetrate the same tissue and are therefore perfectly correlated.

The probability density $p(\Delta^x, \Delta^y, \Delta^z)$ induces an uncertainty over the biological effect ε that can be described with a probability distribution $p(\varepsilon)$. Generally, the unknown distribution $p(\varepsilon)$ is of non-Gaussian shape and can be described with statistical moments which will be described next.

III.2.2 Expectation Value - First Raw Moment

On the basis of the derivations for the biological effect computation in Equation II.28, the first raw moment, also known as expectation value of the biological effect ε_i can be derived via:

$$\begin{aligned}
 \mathbb{E}[\varepsilon_i] &= \int d\Delta^x d\Delta^y d\Delta^z p(\Delta^x) p(\Delta^y) p(\Delta^z) \varepsilon_i(\Delta^x, \Delta^y, \Delta^z) \\
 &= \int d\Delta^x d\Delta^y d\Delta^z p(\Delta^x) p(\Delta^y) p(\Delta^z) \sum_{j=1}^J w_j L_{ij}^x L_{ij}^y Z_{ij}^\alpha + \left(\sum_{j=1}^J w_j L_{ij}^x L_{ij}^y Z_{ij}^\beta \right)^2 \\
 &= \sum_j w_j \mathcal{L}_{ij}^x \mathcal{L}_{ij}^y \mathcal{Z}_{ij}^\alpha + \sum_{jm} w_j w_m Y_{ijm}^x Y_{ijm}^y \Xi_{ijm}^\beta
 \end{aligned} \tag{III.8}$$

where $\mathcal{L}_{ij}^{x/y}$, $\mathcal{Z}_{ij}^{\alpha/\beta}$ in $\mathbb{R}^{I \times J}$ depict elements of the first raw moment influence matrices of $L_{ij}^{x/y}$ and $Z_{ij}^{\alpha/\beta}$, respectively. Additionally, $Y_{ijm}^{x/y}$, Ξ_{ijm}^β in $\mathbb{R}^{I \times J^2}$ denote elements of the corresponding influence tensor of second raw moments and model the influence of pencil beam combinations jm on the quadratic component of the expected biological effect $\mathbb{E}[\varepsilon_i]$. Notably, $\mathbb{E}[\varepsilon_i]$ requires, due to the quadratic form of the second additive term of the biological effect, the calculation of the second raw moment influence matrices ($Y_{ijm}^{x/y}$ and Ξ_{ijm}^β). This is different from the expectation value of the physical dose of protons which only requires first raw moment influence matrices because of the purely linear dose mapping. The detailed derivation of Equation III.8 is shown in Appendix B.1.

Usually, in treatment planning and also throughout this work, the dose per fraction is optimized and then applied in F fractions. For a fraction dose in a carbon ion treatment, the linear term of the biological effect is the main contributing factor, because of $A_{ij}\mathbf{w} \gg (B_{ij}\mathbf{w})^2$ which was also observed by (Kamp et al., 2014).

To reduce the computational complexity, it is a reasonable approximation to neglect covariance elements (e.g. $j \neq m$) in the computation of terms $Y_{ijm}^{x/y}$ and Ξ_{ijm}^β . By this means the interdependencies of $\mathcal{L}_{ij}^{x/y}$ and \mathcal{Z}_{ij}^β in the computation of the quadratic component of $\mathbb{E}[\varepsilon_i]$ are neglected. As a result only diagonal elements ($j = m$) of terms $Y_{ijm}^{x/y}$, Ξ_{ijm}^β need to

be considered. This can be done conveniently by simply squaring the first raw moments $\mathcal{L}_i^{x/y}$, \mathcal{Z}_i^β or by taking the outer product $\Xi^\beta \approx \mathcal{Z}^\beta \mathcal{Z}^{\beta T}$. The full analytical calculation of $\mathbb{E}[\varepsilon_i]$ can then be approximated by $\hat{\mathbb{E}}[\varepsilon_i]$:

$$\hat{\mathbb{E}}[\varepsilon_i] = \sum_j w_j \mathcal{L}_{ij}^x \mathcal{L}_{ij}^y \mathcal{Z}_{ij}^\alpha + \left(\sum_j w_j \mathcal{L}_{ij}^x \mathcal{L}_{ij}^y \mathcal{Z}_{ij}^\beta \right)^2 = \sum_j w_j \mathcal{A}_{ij} + \left(\sum_j w_j \mathcal{J}_{ij} \right)^2 \quad (\text{III.9})$$

where \mathcal{A}_{ij} and \mathcal{B}_{ij} represent the expected probabilistic analog of A_{ij} and B_{ij} of Equation II.28. This approximation reduces the computation of the expected biological effect to the computation of $\mathcal{L}_{ij}^{x/y}$ and $\mathcal{Z}_{ij}^{\alpha/\beta}$ thereby minimizing the computational complexity from $\mathcal{O}(I \times J^2)$ to $\mathcal{O}(I \times J)$. Consequently, the calculation of the expectation value of the biological effect $\mathbb{E}[\varepsilon_i]$ is as expensive as the nominal biological effect ε_i . An analysis and evaluation of the proposed approximation is provided in the result Chapter IV.2. In the remaining manuscript, the expected biological effect is calculated according to Equation III.9 and the hat-symbol in $\hat{\mathbb{E}}[\varepsilon_i]$ will be dropped.

As an example, the calculation of the expectation value of the lateral dose component \mathcal{L}_{ij}^x in x direction, assuming a Gaussian positioning error $\mathcal{N}(\Delta^x|0, \Sigma^x)$ is given below in Equation III.11:

$$\begin{aligned} \mathcal{L}_{ij}^x &= \mathbb{E}[L_{ij}^x(\Delta^x)] = \int_{-\infty}^{\infty} d\Delta^x p(\Delta^x) L_{ij}^x(\Delta^x) \\ &= \int_{-\infty}^{\infty} d\Delta^x \mathcal{N}(\Delta^x|0, \Sigma^x) L_{ij}^x(\Delta^x) = \int_{-\infty}^{\infty} d\Delta_j^x \mathcal{N}(\Delta_j^x|0, \Sigma_{jj}^x) L_{ij}^x(\Delta_j^x) \quad (\text{III.10}) \\ &= \int_{-\infty}^{\infty} d\Delta_j^x \frac{1}{\sqrt{2\pi\Sigma_{jj}^x}} e^{-\frac{(\Delta_j^x)^2}{2\Sigma_{jj}^x}} \frac{1}{\sqrt{2\pi\lambda_{ij}^2}} e^{-\frac{(x_{ij}-\mu_j^x+\Delta_j^x)^2}{2\lambda_{ij}^2}} \\ &= \frac{1}{\sqrt{2\pi(\Sigma_{jj}^x + \lambda_{ij}^2)}} e^{-\frac{(x_{ij}-\mu_j^x)^2}{2(\Sigma_{jj}^x + \lambda_{ij}^2)}} \underbrace{\int_{-\infty}^{\infty} d\Delta_j^x \frac{1}{\sqrt{2\pi\tilde{\sigma}^2}} e^{-\frac{(\tilde{\mu}-\Delta_j^x)^2}{2\tilde{\sigma}^2}}}_{=1} \quad (\text{III.11}) \end{aligned}$$

where Equation III.10 can be derived from the marginalization properties of multivariate Normal distributions (see Appendix A.3). Further, the integration of a Gaussian density against another Gaussian density yields a new Gaussian distribution with an adapted mean $\tilde{\mu}$ and width $\tilde{\sigma}$ (see Appendix A.4). As a result the expectation value of the lateral dose \mathcal{L}_{ij}^x is given by a single Gaussian evaluation[†] with a modified width $(\Sigma_{jj}^x + \lambda_{ij}^2)$.

Similar expressions can be derived for the depth-dependent components $\mathcal{Z}_{ij}^{\alpha/\beta}$ by taking additionally the sum over K Gaussian components into account:

[†]assuming a single gaussian lateral beam profile

Figure III.5: The left plot (a) shows the normalized nominal lateral dose profile (—) and the corresponding expected lateral dose (· · · ·) assuming a setup uncertainty of 6 mm. The right plot (b) presents the normalized nominal Z^α profile (—) profile. Moreover, the line (· · · ·) denotes the expected depth dependent profile $\mathbb{E}[Z^\alpha]$, which is comprised of thirteen Gaussian components (—) assuming a relative range uncertainty of 6%. **The digital version of this manuscript shows an animation with varying setup and range uncertainties from 0 mm to 6 mm and from 0% to 6%.**

$$\begin{aligned}
 Z_{ij}^{\alpha/\beta} &= \mathbb{E}[Z_{ij}^{\alpha/\beta}(\Delta^z)] = \int_{-\infty}^{\infty} d\Delta^z p(\Delta^z) Z_{ij}^{\alpha/\beta}(\Delta^z) \\
 &= \sum_{k=1}^K \frac{\omega_{jk}^{\alpha/\beta}}{\sqrt{2\pi \left(\delta_{jk}^{\alpha/\beta^2} + \Sigma_{jj}^z \right)}} e^{-\frac{(z_{ij} - \mu_{jk}^{\alpha/\beta})^2}{2 \left(\delta_{jk}^{\alpha/\beta^2} + \Sigma_{jj}^z \right)}}
 \end{aligned} \tag{III.12}$$

The calculation shown in Equation III.12 is identical for the physical depth dose profile of protons as well as for αd - and $\sqrt{\beta}d$ -profiles for carbon ions. They only differ in the total number of Gaussian components and in the corresponding Gaussian parameters itself. A detailed derivation of Equation III.12 is given in the Appendix B.12.

Figure III.5(a) presents the nominal lateral dose component in (—) and the corresponding expectation value (first raw moment) $\mathbb{E}[L^x] = \mathcal{L}^x$ in (· · · ·). It can be observed, the higher the input uncertainty, the more the expected lateral dose profile becomes washed out. In addition, Figure III.5(b) depicts a nominal (—) and expected (· · · ·) depth-dependent Z^α profile assuming a relative range uncertainty of 6%. With increasing range uncertainty, the expected profile $\mathbb{E}[Z^\alpha]$ (· · · ·) gets increasingly blurred.

To compute the variance/standard deviation in closed-form second raw moments, also referred to as mixed terms, need to be calculated which are described next.

III.2.3 Mixed Terms and Covariance

The calculation of the covariance (second central moment) of the biological effect $\Sigma^\varepsilon[\varepsilon_i, \varepsilon_l]$ requires the multiplication of first central moments $\mathbb{E}[\varepsilon_i]\mathbb{E}[\varepsilon_l]$ and the second raw moment characterized by mixed terms $\mathbb{E}[\varepsilon_i\varepsilon_l]$:

$$\Sigma_{il}^\varepsilon[\varepsilon_i, \varepsilon_l] = \mathbb{E}[\varepsilon_i\varepsilon_l] - \mathbb{E}[\varepsilon_i]\mathbb{E}[\varepsilon_l] \quad (\text{III.13})$$

$$\Sigma_{ii}^\varepsilon[\varepsilon_i, \varepsilon_i] = \mathbb{E}[\varepsilon_i^2] - \mathbb{E}[\varepsilon_i]^2 \quad (\text{III.14})$$

Setting $i = l$ allows deriving the variance of the biological effect $\Sigma_{ii}^\varepsilon[\varepsilon_i, \varepsilon_i]$ as shown in Equation III.14. Let i, l be voxel- and j, m, o, q be pencil beam-indices, then the full analytical computation of the second raw moment of the biological effect $\mathbb{E}[\varepsilon_i\varepsilon_l]$ is given by:

$$\begin{aligned} \mathbb{E}[\varepsilon_i\varepsilon_l] &= \int d\Delta^x d\Delta^y d\Delta^z p(\Delta^x)p(\Delta^y)p(\Delta^z)\varepsilon_i(\Delta^x, \Delta^y, \Delta^z)\varepsilon_l(\Delta^x, \Delta^y, \Delta^z) \\ &= \sum_{jm}^J w_j w_m Y_{ijlm}^x Y_{ijlm}^y \Xi_{ijlm}^\alpha + 2 \sum_{jmo}^J w_j w_m w_o Y_{ijlmio}^x Y_{ijlmio}^y \Xi_{ijlmio}^{\alpha 2\beta} + \\ &\quad \sum_{jmoq}^J w_j w_m w_o w_q Y_{ijlmioq}^x Y_{ijlmioq}^y \Xi_{ijlmioq}^\beta \end{aligned} \quad (\text{III.15})$$

where $Y_{ijlm}^{x/y}$, $Y_{ijlmio}^{x/y}$ and $Y_{ijlmioq}^{x/y}$ denote four-, six- and eight-dimensional tensors and represent higher order raw moment influence tensors of the lateral dose $L^{x/y}$. The full derivation of Equation III.15 is provided in the Appendix B.2-B.5. To obtain now the variance of the biological effect, which is stored in the diagonal ($i = l$) of the covariance matrix Σ_{ii}^ε as shown in Equation III.14, the second voxel index l can be dropped to obtain:

$$\begin{aligned} \mathbb{E}[\varepsilon_i\varepsilon_i] &= \sum_{jm}^J w_j w_m Y_{ijm}^x Y_{ijm}^y \Xi_{ijm}^\alpha + 2 \sum_{jmo}^J w_j w_m w_o Y_{ijmo}^x Y_{ijmo}^y \Xi_{ijmo}^{\alpha 2\beta} + \\ &\quad \sum_{jmoq}^J w_j w_m w_o w_q Y_{ijmoq}^x Y_{ijmoq}^y \Xi_{ijmoq}^\beta \end{aligned} \quad (\text{III.16})$$

where $Y_{ijmo}^{x/y} \in \mathbb{R}^{I \times J^3}$ and $Y_{ijmoq}^{x/y} \in \mathbb{R}^{I \times J^4}$ denote sum-elements of the third and fourth raw moment influence tensors of the lateral dose component $L_i^{x/y}$. Furthermore, $\Xi_{ijm}^\alpha \in \mathbb{R}^{I \times J^2}$ represent sum-elements of the second raw moment influence tensor required to calculate the second raw moment of Z_i^α . Analog indicates $\Xi_{ijmo}^{\alpha 2\beta} \in \mathbb{R}^{I \times J^3}$ an element to derive the mixed third raw moment of $Z_i^{\alpha/\beta}$ and lastly, $\Xi_{ijmoq}^\beta \in \mathbb{R}^{N \times J^4}$ an element of the fourth raw moment

influence tensor to assess the fourth raw moment of Z_i^β . Individual entries of the three (e.g. Y_{ijm}), four (e.g. Y_{ijmo}) and five (e.g. Y_{ijmoq}) dimensional tensors correspond to bi-, tri and quadivariate Normal distributions obtained from the integration over multivariate Normal distributions.

It is not feasible to store these four or five-dimensional tensors in memory for a clinical scenario with 10^6 voxels and 2×10^4 pencil beams during routine therapy treatment planning despite accounting for sparsity and symmetry.

Grounded on the approximations already made for the expectation value of the biological effect $\mathbb{E}[\varepsilon_i]$, higher order moments $n > 1$ based on the $\sqrt{\beta d}$ term in $\mathbb{E}[\varepsilon_i \varepsilon_i]$ are again represented by outer products of lower order moments. This approximation is motivated by the fact that dose fractions are mainly determined by the linear component (αd) of the biological effect for which reason it can be expected the variance of the biological effect is mainly driven by the second raw moment of αd , derived from the second raw moment influence tensor Ξ_{ijm}^α . On the contrary, higher order influence tensors of the $\sqrt{\beta d}$ term show a decreasing contribution to the overall computation and correspond therefore only to a minor correction. Thus, interdependencies between pencil beam combination jm , jmo and $jmoq$ in the $\sqrt{\beta d}$ term, stored in the off-diagonals, are neglected which allows deriving an approximated second raw moment of the biological effect $\hat{\mathbb{E}}[\varepsilon_i \varepsilon_i]$ as follows:

$$\begin{aligned} \hat{\mathbb{E}}[\varepsilon_i \varepsilon_i] &= \sum_{jm} w_j w_m Y_{ijm}^x Y_{ijm}^y \Xi_{ijm}^\alpha + 2 \sum_{jmo} w_j w_m w_o Y_{ijm}^x \mathcal{L}_{io}^x Y_{ijm}^y \mathcal{L}_{io}^y Z_{ij}^\alpha Z_{im}^\beta Z_{io}^\beta + \\ &\quad \sum_{jm} w_j w_m (Y_{ijm}^x)^2 (Y_{ijm}^y)^2 (Z_{ij}^\beta Z_{im}^\beta)^2 = \sum_{jm} w_j w_m \hat{\mathcal{D}}_{ijm}^\varepsilon \end{aligned} \quad (\text{III.17})$$

Neglecting covariances between double, triple and quadruple spot combinations in $\sqrt{\beta d}$ terms allows to define $Y_{ijmo}^{x/y} \approx Y_{ijm}^{x/y} \mathcal{L}_{io}^{x/y}$ and $\Xi_{ijmo}^{\alpha 2\beta} \approx Z_{ij}^\alpha Z_{im}^\beta Z_{io}^\beta$, which actually represent the integration of a trivariate Gaussian distribution but now factorizes for $Y_{ijmo}^{x/y}$ into the integration over a univariate and a bivariate Gaussian distribution. Further, $\Xi_{ijmo}^{\alpha 2\beta}$ can even be factorized into three univariate Gaussian distributions. Lastly, the integration over a quadivariate Gaussian distributions (e.g. Y_{ijmoq}^x) is approximated by the product over two bivariate distributions (e.g. $(Y_{ijm}^x)^2$).

To obtain the second raw moment $\hat{\mathcal{D}}_{ijm}^\varepsilon$ in Equation III.17, the sum for w_o in the second additive term has been collapsed to reduce the complexity for further consideration. The approximations postulated for the second raw moment of the biological effect reduce the computational complexity from $\mathcal{O}(I \times J^4)$ to $\mathcal{O}(I \times J^2)$. However, second raw moment influence tensors ($Y_{ijm}^{x/y}$, Ξ_{ijm}^α) of the lateral dose $L^{x/y}$ and Z^α the depth component still need to be fully calculated to derive $\hat{\mathbb{E}}[\varepsilon_i \varepsilon_i]$.

Let i, l be voxel indices and j, m be pencil beam indices and $\mathcal{N}(\mathbf{x}_{ijlm} | \boldsymbol{\mu}_{ijm}^x, \Lambda_{ijlm})$ be a Normal

bivariate distribution with the following parameters:

$$\mathbf{x}_{ijlm} = \begin{pmatrix} x_{ij} \\ x_{lm} \end{pmatrix}, \boldsymbol{\mu}_{jm}^x = \begin{pmatrix} \mu_j^x \\ \mu_m^x \end{pmatrix}, \boldsymbol{\Delta}_{jm}^x = \begin{pmatrix} \Delta_j^x \\ \Delta_m^x \end{pmatrix}, \Lambda_{ijlm} = \begin{pmatrix} \lambda_{ij}^2 & 0 \\ 0 & \lambda_{lm}^2 \end{pmatrix}, \Sigma^{jm} = \begin{pmatrix} \Sigma_{jj}^x & \Sigma_{jm}^x \\ \Sigma_{mj}^x & \Sigma_{mm}^x \end{pmatrix}$$

where Σ^{jm} denotes the covariance matrix for the setup error between pencil beams j and m . Consequently, the second raw moment of the lateral dose $\mathbb{E}[L_{ij}^x L_{lm}^x]$ in x direction is given by:

$$\begin{aligned} Y_{ijlm}^x &= \mathbb{E}[L_{ij}^x L_{lm}^x] = \int d\boldsymbol{\Delta}^x p(\boldsymbol{\Delta}^x) L_{ij}^x L_{lm}^x \\ &= \int_{-\infty}^{\infty} d\boldsymbol{\Delta}^x \frac{1}{2\pi\sqrt{|\Sigma^x|}} e^{-\frac{1}{2}\boldsymbol{\Delta}^{xT}(\Sigma^x)^{-1}\boldsymbol{\Delta}^x} \frac{1}{\sqrt{2\pi\lambda_{ij}^2}} e^{-\frac{(x_{ij}-\mu_j^x+\Delta_j^x)^2}{2\lambda_{ij}^2}} \frac{1}{\sqrt{2\pi\lambda_{lm}^2}} e^{-\frac{(x_{lm}-\mu_m^x+\Delta_m^x)^2}{2\lambda_{lm}^2}} \\ &= \frac{1}{2\pi\sqrt{|\Lambda_{ijlm} + \Sigma^{jm}|}} e^{-\frac{1}{2}(\mathbf{x}_{ijlm}-\boldsymbol{\mu}_{jm}^x)^T(\Lambda_{ijlm}+\Sigma^{jm})^{-1}(\mathbf{x}_{ijlm}-\boldsymbol{\mu}_{jm}^x)} \end{aligned} \quad (\text{III.18})$$

The second raw moment influence tensor of the lateral dose Y_{ijlm}^x is represented by an integration over a bivariate Normal distribution. Detailed derivations are again presented in the Appendix B.8. The full analytical expressions for elements of the third raw moment influence tensor of the lateral dose ($Y_{ijmo}^{x/y}$) and the depth dose ($\Xi_{ijmo}^{\alpha\beta}$) can also be found in the Appendix (Equation B.11 and Equation B.16) although they are not employed throughout this work.

To calculate the second moment of depth dose components, additionally a sum of Gaussians needs to be considered. Let k and p be indices of individual Gaussian components, K, P be the total number of Gaussian components and $\mathcal{N}(z_{ijlm} | \boldsymbol{\mu}_{jkmq}^{\alpha/\beta}, \boldsymbol{\theta}_{jkmp}^{\alpha/\beta})$ be a bivariate Normal distribution with the following parameters:

$$\mathbf{z}_{ijlm} = \begin{pmatrix} z_{ij} \\ z_{lm} \end{pmatrix}, \boldsymbol{\mu}_{jkmq}^{\alpha/\beta} = \begin{pmatrix} \mu_{jk}^{\alpha/\beta} \\ \mu_{mq}^{\alpha/\beta} \end{pmatrix}, \boldsymbol{\Delta}_{jm}^z = \begin{pmatrix} \Delta_j^z \\ \Delta_m^z \end{pmatrix}, \boldsymbol{\theta}_{jkmp}^{\alpha/\beta} = \begin{pmatrix} \delta_{jk}^{\alpha/\beta^2} & 0 \\ 0 & \delta_{mp}^{\alpha/\beta^2} \end{pmatrix}, \Sigma^{jm} = \begin{pmatrix} \Sigma_{jj}^z & \Sigma_{jm}^z \\ \Sigma_{mj}^z & \Sigma_{mm}^z \end{pmatrix}$$

employing a range error covariance matrix Σ_{jm}^z allows deriving elements of the second raw moment influence tensor of Z_{ij}^α and Z_{ij}^β as follows:

$$\begin{aligned}
 \Xi_{ijlm}^{\alpha/\beta} &= \mathbb{E}[Z_{ij}^{\alpha/\beta} Z_{lm}^{\alpha/\beta}] = \int d\Delta^z Z_{ij}^{\alpha/\beta} Z_{lm}^{\alpha/\beta} = \int_{-\infty}^{\infty} d\Delta^z \frac{1}{2\pi\sqrt{|\Sigma^{jm}|}} e^{-\frac{1}{2}\Delta^z T (\Sigma^{jm})^{-1} \Delta^z} \\
 &\quad \sum_{k=1}^K \frac{\omega_{jk}^{\alpha/\beta}}{\sqrt{2\pi\delta_{jk}^{\alpha/\beta^2}}} e^{-\frac{(z_{ij}-\mu_{jk}^{\alpha/\beta}+\Delta_j^z)^2}{2\delta_{jk}^{\alpha/\beta^2}}} \sum_{p=1}^P \frac{\omega_{mp}^{\alpha/\beta}}{\sqrt{2\pi\delta_{mp}^{\alpha/\beta^2}}} e^{-\frac{(z_{lm}-\mu_{mp}^{\alpha/\beta}+\Delta_m^z)^2}{2\delta_{mp}^{\alpha/\beta^2}}} \\
 &= \sum_{kp}^{KP} \frac{\omega_{jk}^{\alpha/\beta} \omega_{mp}^{\alpha/\beta}}{2\pi\sqrt{|\theta_{jkm}^{\alpha/\beta} + \Sigma^{jm}|}} e^{-\frac{1}{2}(z_{ijlm}-\mu_{jkm}^{\alpha/\beta})^T (\theta_{jkm}^{\alpha/\beta} + \Sigma^{jm})^{-1} (z_{ijlm}-\mu_{jkm}^{\alpha/\beta})} \quad (\text{III.19})
 \end{aligned}$$

where, $\Xi_{ijlm}^{\alpha/\beta}$ can be interpreted as the sum over Normal bivariate distributions originating from a two-dimensional integration. The reader is referred to the Appendix B.14 for detailed derivation. Throughout this work only Ξ_{ijlm}^{α} is fully calculated, whereas other depth-dependent second or higher order moments are approximated.

On the basis of Equation III.13 and the second raw moment of the biological effect in Equation III.17, the variance of the biological effect $\hat{\sigma}^2[\varepsilon_i]$ can then be calculated via:

$$\begin{aligned}
 \hat{\sigma}^2[\varepsilon_i] &= \Sigma_{ii}^{\varepsilon}[\varepsilon_i, \varepsilon_i] = \mathbb{E}[\varepsilon_i^2] - \mathbb{E}[\varepsilon_i]^2 \quad (\text{III.20}) \\
 &= \sum_{jm}^J w_j w_m \underbrace{\hat{\mathcal{D}}_{ijm}^{\varepsilon} - [\mathcal{A}_{ij} w_j + (\mathcal{B}_{ij} w_j)^2] [\mathcal{A}_{im} w_m + (\mathcal{B}_{im} w_m)^2]}_{= \mathfrak{V}_{ijm} = \mathfrak{C}_{ijm}} = \sum_{jm}^{JM} w_j w_m \mathfrak{V}_{ijm}
 \end{aligned}$$

where \mathfrak{V}_{ijm} represents the variance influence tensor in $\in \mathbb{R}^{I \times J \times J}$ which maps \mathfrak{V}_{ijm} for given pencil beam weights \mathbf{w} to the variance. For the sake of completeness, calculating Equation III.20 for $i \neq l$ allows deriving the covariance influence tensor \mathfrak{C}_{ijlm} in $\in \mathbb{R}^{I \times J \times I \times J}$. Setting $i = l$ demonstrates that the variance influence tensor $\mathfrak{V}_{ijm} = \mathfrak{C}_{ijm}$ is a sub-structure of the covariance influence tensor. Ultimately, the covariance matrix for the biological effect can be obtained via $\Sigma_{il}^{\varepsilon}[\varepsilon_i, \varepsilon_l] = \sum_{jm} w_j w_m \mathfrak{C}_{ijlm}$.

Figure III.6(a) presents the normalized nominal lateral dose component in (—), the corresponding expectation value (first raw moment) $\mathbb{E}[L^x] = \mathcal{L}^x$ in (⋯⋯) and the standard deviation (second central moment) $\sigma[L^x]$ in (—) considering a setup uncertainty of 6 mm. Figure III.6(a) reveals that with increasing setup uncertainty the more pronounced the standard deviation bumps at the lateral dose fall-off region become. Additionally, Figure III.5(b) shows the normalized nominal (—) and expectation value (⋯⋯) of the depth-dependent Z^{α} profile assuming a relative range uncertainty of 6%. Similar to the lateral dose profile, the standard deviation, denoted by (—) is of non-Gaussian shape and rises with increasing range uncertainty.

Considering the two to threefold increased numerical computations required for carbon

Figure III.6: The left plot shows the normalized nominal lateral dose profile (—), the corresponding expected lateral dose (---) and the standard deviation (—) assuming a setup uncertainty of 6 mm. The right plot presents the normalized nominal Z^α profile (—), which is comprised of thirteen Gaussian components (—). Furthermore, the lines (---) and (—) indicate the corresponding expected depth dependent profile $\mathbb{E}[Z^\alpha]$ and standard deviation modelling a relative range uncertainty of 6%. The digital version of this manuscript shows an animation with varying setup and range uncertainties from 0 mm to 6 mm and from 0% to 6%, respectively.

ion treatment planning in relation to proton treatment planning, the order of computational complexity $\mathcal{O}(I \times J^2)$ for the variance is identical due to the omission of interdependencies of triple and quadruple spot combinations.

Despite the approximations, it is still challenging to keep the full second raw moment $\hat{\mathcal{D}}^\varepsilon$ for different voxel combinations il in memory. Therefore, $\hat{\mathcal{D}}^\varepsilon$ is calculated for each voxel on the fly and only the integral variance $\Omega_{jm} \in \mathbb{R}^{J \times J}$ over all voxels is kept in storage. The integral variance Ω_{jm} can then be used in a further step to optimize the expectation value of the squared deviation objective which will be explained later in Section III.4.

The hat symbol in Equation III.20 emphasizes the variance of the biological effect is approximated and derived from the full analytical expression shown in Equation III.16. The quality of these approximations are investigated in Chapter IV.2.1.1 and are used throughout this work if not explicitly stated otherwise.

So far, no distinction was made between random and systematic errors. Therefore, the next chapter explains how the interplay between random and systematic errors and their dependence on the number of fractions is modeled for carbon ions as part of the APM formalism.

III.2.4 Fractionation Effects

A radiation treatment plan is typically delivered in multiple fractions $f \{f \in \mathbb{N} | 1 \leq f \leq F\}$ for which reason errors must be broken down into random (execution) and systematic (preparation) errors. In this regard caution has to be taken since the total biological effect ε^F directly derived from the total physical dose delivered in F fractions does not equal the

additive effect from the individual fraction doses:

$$\varepsilon \left(\sum_{f=1}^F d_f \right) \neq \sum_{f=1}^F \varepsilon_f \quad (\text{III.21})$$

The APM framework permits to incorporate the interplay of random and systematic errors by exploiting an additional correlation model between the two error types and was first published for the physical dose by (Bangert et al., 2013). That is, systematic errors, as for instance a miscalculated WEPL, realize identical throughout the whole course of treatment and are therefore assumed to be perfectly correlated. On the contrary, random errors (e.g. a miss-positioned patient) are uncorrelated between fractions as they mainly realize differently in each treatment fraction f . Given a carbon ion treatment plan delivered in F fractions, the total biological effect ε_i^F is represented by:

$$\varepsilon_i^F(\Delta^{sys}, \Delta^{rnd}) = \sum_{f=1}^F \left[\sum_{j=1}^J w_j A_{ij}^f(\Delta^{sys}, \Delta_f^{rnd}) + \left(\sum_{j=1}^J w_j B_{ij}^f(\Delta^{sys}, \Delta_f^{rnd}) \right)^2 \right] \quad (\text{III.22})$$

where Δ_f^{rnd} is different for each fraction f , A_{ij}^f represents the linear part of the biological effect in voxel i from pencil beam j in fraction f . Similarly, denotes B_{ij}^f the squared component of the biological effect. Assuming an identical Normal distribution for Δ_f^{rnd} for each fraction f allows in a further step to model systematic and random errors with respective covariance matrices from multivariate Normal distributions $p(\Delta_f^{rnd}) \sim \mathcal{N}(\Delta_f^{rnd} | 0, \Sigma^{rnd})$ and $p(\Delta^{sys}) \sim \mathcal{N}(\Delta^{sys} | 0, \Sigma^{sys})$. Knowing from Equation II.28 that A_{ij} and B_{ij} factorize into $L_{ij}^x L_{ij}^y Z_{ij}^\alpha$ and $L_{ij}^x L_{ij}^y Z_{ij}^\beta$, the expected lateral dose component $\mathcal{L}^{x/y}$ from Equation III.11 results for a fractionated treatment in:

$$\mathcal{L}_{ij}^{x/y} = \mathcal{N}(x_{ij}/y_{ij}, 0, \lambda_{ij}^2 + \Sigma_{jj}^{x/y,sys} + \Sigma_{jj}^{x/y,rnd}) \quad (\text{III.23})$$

The expectation value of the lateral dose $\mathcal{L}^{x/y} = \mathbb{E}[\mathcal{L}^{x/y}]$ as part of the biological effect shown in Equation III.23 is under fractionation identical to the computation of the physical dose of protons. The identical complexity arises as biological beam properties are incorporated through dose-averaged depth-dependent α - and $\sqrt{\beta}$ -profiles and logically affect only the depth-dose and not the lateral component. Hence biological properties are assumed to be laterally constant. Moreover, the expected depth dose components considering F fractions are then given by:

$$\begin{aligned} {}^F Z_{ij}^\alpha &= F \sum_{k=1}^{13} w_{jk} \mathcal{N}(z_{ij}, \mu_{jk}^\alpha, \delta_{jk}^{\alpha 2} + \Sigma_{jj}^{z,sys} + \Sigma_{jj}^{z,rnd}) \\ {}^F Z_{ij}^\beta &= \sqrt{F} \sum_{k=1}^{13} w_{jk} \mathcal{N}(z_{ij}, \mu_{jk}^\beta, \delta_{jk}^{\beta 2} + \Sigma_{jj}^{z,sys} + \Sigma_{jj}^{z,rnd}) \end{aligned} \quad (\text{III.24})$$

where ${}^F Z_{ij}^\beta$ is weighted with \sqrt{F} due to the quadratic form of the biological effect. Using Equation III.23 and III.24, the expectation value of the biological effect considering fractionation results therefore in:

$$\mathbb{E}[\varepsilon_i^F] = \left[\sum_{j=1}^J w_j \mathcal{L}_{ij}^x \mathcal{L}_{ij}^y {}^F Z_{ij}^\alpha \right] + \left[\sum_{j=1}^J w_j \mathcal{L}_{ij}^x \mathcal{L}_{ij}^y {}^F Z_{ij}^\beta \right]^2 \quad (\text{III.25})$$

$$= \sum_{f=1}^F \mathbb{E}[\varepsilon_i^f] = F \mathbb{E}[\varepsilon_i^f] \quad (\text{III.26})$$

Equation III.25 shows that the linear term is applied F times and the quadratic term is applied F times (considering the square in the latter). Now let f and g enumerate over the total fraction number F , then the second central moment of the biological effect $\mathbb{E}[\varepsilon_i^F \varepsilon_l^F]$ in a fractionated treatment can be derived by:

$$\begin{aligned} \mathbb{E}[\varepsilon_i^F \varepsilon_l^F] &= \int_{-\infty}^{\infty} d\Delta^{sys} \mathcal{N}(\Delta^{sys} | 0, \Sigma^{sys}) d\Delta_f^{rnd} \mathcal{N}(\Delta_f^{rnd} | 0, \Sigma^{rnd}) \\ &\quad \left\{ \sum_{f=1}^F \left[\sum_{j=1}^J w_j A_{ij}^f(\Delta^{sys}, \Delta_f^{rnd}) + \left(\sum_{j=1}^J w_j B_{ij}^f(\Delta^{sys}, \Delta_f^{rnd}) \right)^2 \right] \right\}^2 \\ &= \int_{-\infty}^{\infty} d\Delta^{sys} \mathcal{N}(\Delta^{sys} | 0, \Sigma^{sys}) d\Delta_f^{rnd} \mathcal{N}(\Delta_f^{rnd} | 0, \Sigma^{rnd}) \\ &\quad \left\{ \underbrace{\sum_{fg=1}^F \left[\left(\sum_j w_j A_{ij}^f \right) \left(\sum_m w_m A_{lm}^g \right) \right]}_{\Rightarrow \sum_{j m}^J Y_{ijlm}^x Y_{ijlm}^y \Xi_{ijlm}^\alpha} + 2 \sum_{fg=1}^F \left[\left(\sum_j w_j A_{ij}^f \right) \left(\sum_m w_m B_{lm}^g \right)^2 \right]}_{\Rightarrow \sum_{j m o}^J Y_{ijlmo}^x Y_{ijlmo}^y \Xi_{ijlmo}^{\alpha 2\beta}} + \right. \\ &\quad \left. + \sum_{fg=1}^F \left[\left(\sum_j w_j B_{ij}^f \right)^2 \left(\sum_m w_m B_{lm}^g \right)^2 \right] \right\} \quad (\text{III.27}) \\ &\quad \Rightarrow \text{see Equation III.15} \end{aligned}$$

An intermediate step to derive Equation III.27 is not shown here but is presented in Appendix B in Equation B.17. Each block marked by square brackets $[\]$ in Equation III.27 can be integrated separately. The full computation of III.27 is not shown here but, the computation of the second central moment of the lateral dose component $Y_{ijlm}^x = \mathbb{E}[L_{ij}^x L_{lm}^x]$ considering fractionation is exemplarily fully exercised next. Analog is the computation for the remaining terms (e.g. Ξ_{ijlm}^α). Let the systematic setup error $\Delta_{jm}^{x,sys}$ as well as the random setup error

$\Delta_{jfm}^{x,rand}$ of pencil beam spot j and m be a multivariate Normal distribution with zero mean vectors and corresponding covariance matrices $\Sigma_{jm}^{x,sys}$ and $\Sigma_{jfm}^{x,rand}$. Further, let Λ_{ijlm}^x define the variance of the lateral dose profile, then Y_{ijlm}^x can be derived as follows:

$$Y_{ijlm}^x = \sum_{f=1}^F \sum_{g=1}^F \int_{-\infty}^{\infty} d\Delta^{x,sys} \mathcal{N}(\Delta^{x,sys}, 0, \Sigma_{jm}^{x,sys}) \int_{-\infty}^{\infty} d\Delta^{x,rand} \mathcal{N}(\Delta^{x,rand}, 0, \Sigma_{jfm}^{x,rand}) \frac{1}{2\pi \sqrt{|\Lambda_{ijlm}^x|}} e^{-\frac{1}{2}(\mathbf{x}_{ijlm} - \boldsymbol{\mu}_{jm} + \Delta_{jm}^{x,sys} + \Delta_{jfm}^{x,rand})^T (\Lambda_{ijlm}^x)^{-1} (\mathbf{x}_{ijlm} - \boldsymbol{\mu}_{jm} + \Delta_{jm}^{x,sys} + \Delta_{jfm}^{x,rand})} \quad (\text{III.28})$$

Solving the integrals in Equation III.28 then yields:

$$Y_{ijlm}^x = \sum_{f=1}^F \sum_{g=1}^F \frac{1}{2\pi \sqrt{|\Lambda_{ijlm}^x + \Sigma_{jm}^{x,sys} + \Sigma_{ifmg}^{x,rand}|}} e^{-\frac{1}{2}(\mathbf{x}_{ijlm} - \boldsymbol{\mu}_{jm})^T (\Lambda_{ijlm}^x + \Sigma_{jm}^{x,sys} + \Sigma_{ifmg}^{x,rand})^{-1} (\mathbf{x}_{ijlm} - \boldsymbol{\mu}_{jm})} \quad (\text{III.29})$$

To exercise Equation III.29, two different scenarios have to be considered. Spatial correlations, such as the ray-wise or beam-wise correlation assumptions for random errors, are valid within an individual fraction ($f = g$) and are therefore further denoted as correlated errors Σ_{corr}^{rand} . Across different fractions ($f \neq g$) random errors do not correlate, which is modeled with an uncorrelated random error covariance matrix $\Sigma_{uncorr}^{rand} = \text{diag}(\Sigma_{corr}^{rand})$. Thus, we can define:

$$\Sigma_{jm,sys} = \begin{pmatrix} \Sigma_{jj}^{x,sys} & \Sigma_{jm}^{x,sys} \\ \Sigma_{mj}^{x,sys} & \Sigma_{mm}^{x,sys} \end{pmatrix}; \Sigma_{corr}^{rand} = \begin{pmatrix} \Sigma_{jj}^{x,rand} & \Sigma_{jm}^{x,rand} \\ \Sigma_{mj}^{x,rand} & \Sigma_{mm}^{x,rand} \end{pmatrix}; \Sigma_{uncorr}^{rand} = \begin{pmatrix} \Sigma_{jj}^{x,rand} & 0 \\ 0 & \Sigma_{mm}^{x,rand} \end{pmatrix}$$

This definition allows in a further step to resolve the double sum over fractions f and g :

$$Y_{ijlm}^x \overset{F}{=} \frac{F}{2\pi \sqrt{|\Lambda_{ijlm}^x + \Sigma_{jm,sys} + \Sigma_{corr}^{rand}|}} e^{-\frac{1}{2}(\mathbf{x}_{ijlm} - \boldsymbol{\mu}_{jm})^T (\Lambda_{ijlm}^x + \Sigma_{jm,sys} + \Sigma_{corr}^{rand})^{-1} (\mathbf{x}_{ijlm} - \boldsymbol{\mu}_{jm})} + \frac{F(F-1)}{2\pi \sqrt{|\Lambda_{ijlm}^x + \Sigma_{jm,sys} + \Sigma_{uncorr}^{rand}|}} e^{-\frac{1}{2}(\mathbf{x}_{ijlm} - \boldsymbol{\mu}_{jm})^T (\Lambda_{ijlm}^x + \Sigma_{jm,sys} + \Sigma_{uncorr}^{rand})^{-1} (\mathbf{x}_{ijlm} - \boldsymbol{\mu}_{jm})} = F Y_{ijlm}^{x,corr} + F(F-1) Y_{ijlm}^{x,uncorr} \quad (\text{III.30})$$

where $Y_{ijlm}^{x,corr}$ and $Y_{ijlm}^{x,uncorr}$ present elements of the correlated and uncorrelated second central moment influence tensor of the lateral dose taking into account fractionation. Considering any number of fractions F effectively doubles the number of computation as it stays constant for $F > 1$. Similar expressions in the form $F Y^{corr} + F(F-1) Y^{uncorr}$ were derived for protons

by (Bangert et al., 2013) in Equation 32.

As the fractionated dose is usually considered for carbon ion treatment planning and $Y_{ijlm}^{x,F}$ cannot be directly converted to RBE weighted dose because of the fractionation effect (see Equation III.21), it is desirable to convert elements of the of second central moment influence tensor of the lateral dose $Y_{ijlm}^{x,F}$ to the equivalent single fraction dose level $Y_{ijlm}^{x,f}$. Thus $Y_{ijlm}^{x,F}$ can be divided by F^2 to obtain the average $Y_{ijlm}^{x,f}$ of a single fraction f :

$$Y_{ijlm}^{x,f} = \frac{Y_{ijlm}^{x,F}}{F^2} = \frac{Y_{ijlm}^{x,corr}}{F} + \frac{(F-1)Y_{ijlm}^{x,uncorr}}{F} \quad (\text{III.31})$$

To explain Equation III.31, an example of a one-dimensional fractionated carbon ion SOBP is shown in Figure III.7. The prescribed biological effect is 0.75 which corresponds to a target dose of 3 Gy(RBE) for a tissue characterized by $\alpha_x = 0.1$ [Gy⁻¹] and $\beta_x = 0.05$ [Gy⁻²]. Further, (□) indicates the CTV and (▣) the margin expansion to derive the PTV. The systematic range error is defined to be $\Sigma_{jm}^{z,sys} = 0.035 r_j \times 0.035 r_m$ and the random range error to be $\Sigma_{jm}^{z,rand} = 4^2 \text{ mm}^2$, where r_j and r_m depict the range of pencil beam j and m , respectively.

Figure III.7 illustrates the standard deviation of the fractionated biological effect $\sigma[\varepsilon]^f$ for $F = 1$ (.....) and $F = \infty$ (-.-.-) on the basis of Equation III.31. Within the digital version of this manuscript, an animation for different fractionation assumptions is shown. It can be observed that for an increasing number of fractions, the standard deviation shifts towards $\sigma[\varepsilon]_{F=\infty}$.

Figure III.7: Fractionation effects of a 1D carbon ion SOBP with $\alpha_x = 0.1 \text{ Gy}^{-1}$ and $\beta_x = 0.05 \text{ Gy}^{-2}$. The plan was optimized for a reference nominal dose of 3 Gy(RBE), which translates to a prescribed biological effect of 0.75. (—) denotes the optimized nominal biological effect ε . Considering systematic and random range uncertainties, the expected biological effect $\mathbb{E}[\varepsilon]$ results in (—). The standard deviation of the biological effect $\sigma[\varepsilon]^f$ of the actual fractionation scheme for 5 fractions is given by (—) and is enclosed by $\sigma[\varepsilon]_{F=1}^f$ (.....) and $\sigma[\varepsilon]_{F=\infty}^f$ (-.-.-). The digital version of this manuscript shows varying fractionation assumptions resulting in different standard deviations.

Assuming the biological effect (—) is applied once in a single fraction ($F = 1$) then (.....) represents the corresponding standard deviation $\sigma[\varepsilon]_F^f = \sigma[\varepsilon]_1^f$ according to Equation III.31 for which the second additive term containing $Y_{ijlm}^{x,uncorr}$ becomes 0. Considering $F = \infty$ in

Equation III.31 yields to full compensation of random uncertainties and $\lim_{F \rightarrow \infty} Y_{ijlm}^{x,corr f} / F = 0$ whereas $\lim_{F \rightarrow \infty} [(F - 1)Y_{ijlm}^{x,corr f}] / F$ results in $Y_{ijlm}^{x,corr f}$. Section III.5 shows later how to convert $\sigma[\varepsilon]^f$ from Figure III.7 to $\sigma[RBE \times d]^f$, which allows consequently to obtain the total uncertainty of the RBE weighted dose via:

$$\sigma[RBE \times d]^F = \sigma[RBE \times d]^f * F \quad (\text{III.32})$$

A proof of concept for Equation III.32 is shown in the result Section IV.2.1.5 demonstrating that the full fractionation spectrum of quantified carbon ion treatment plan uncertainties can be explored.

Throughout this thesis, setup uncertainties in the spatial dimensions are modeled by a random component of $\sigma_{x/y}^{rnd} = 2$ mm and a systematic component of $\sigma_{x/y}^{sys} = 1$ mm. Complementary, range uncertainties are assumed to possess an absolute random component of $\sigma_z^{rnd} = 1$ mm and a relative systematic component of $\sigma_z^{sys} = 3.5\%$ with respect to the pencil beam's range.

III.3 Biological Uncertainties

Up to now, it was uncertain where the actual biological effect is occurring inside the patient because of physical uncertainties (setup- and range-error). The location uncertainty was modeled by being uncertain in the mean position of individual Gaussian components constituting the lateral and depth-dependent pencil beam components. Calculating statistical moments assuming errors obey a multivariate Normal distribution resulted in turn in multivariate Normal distributions, however, with a modified (co)-variance. In addition, to modeling physical uncertainties the fundamental question arises, how effective the radiation will be on the patient. In general, this is modeled for carbon ions by the RBE, which quantifies the relative effectiveness of carbon ions to photon irradiation. To this end, the RBE modeling approach introduces inevitably biological uncertainties as it is uncertain how effective an individual carbon ion pencil beam will be.

Considering the one-dimensional examples given in previous chapters, range and setup uncertainties were modeled along the first dimension – the x-axis. In contrast, biological uncertainties are now expressed on the y-axis to model a uncertainty in the effectiveness. This is why biological uncertainties result in a varying magnitude and introduce a new uncertainty structure, which will be introduced step by step in this section.

III.3.1 Gaussian Process

Analogously to the extension of a one- to a multi-dimensional (multivariate) Normal distribution, a Gaussian Process (GP) represents the extension to functions. Compared to a multivariate Normal distribution, which specifies the distribution of individual variables \mathbf{x} by a mean vector $\boldsymbol{\mu}_{\mathbf{x}}$ and a covariance matrix $\Sigma^{\mathbf{x}}$, a GP denotes the distribution of a function $h(\mathbf{x})$ and is entirely given by a mean function $m_h(\mathbf{x})$ and a covariance function $k_h(\mathbf{x}, \mathbf{x})$.

Specifically, the mean function $m_h(\cdot)$ of a GP denotes the shape of the expected/average function and the standard deviation, obtained from the covariance function $k(\mathbf{x}, \mathbf{x})$, denotes the variability of function $h(\mathbf{x})$ for different inputs. Equation III.33 shows the general form a GP aiming to parameterize $p(h(\mathbf{x}))$:

$$p(h(\mathbf{x})) = \mathcal{N}(h(\mathbf{x}), m_h(\mathbf{x}), k_h(\mathbf{x}, \mathbf{x})) \quad (\text{III.33})$$

$k(\mathbf{x}, \mathbf{x})$ is also known as the kernel matrix because arbitrary kernels can be defined which allow to model/specify the covariance between any two functions values. GPs are of interest because they are mathematically convenient and allow for Bayesian inference. GPs are well suited for iterative learning processes (e.g. reinforcement learning) in which (i) priors are defined (ii) data is observed and (iii) the posterior likelihood is inferred. However, throughout this manuscript the idea is, to model $\alpha_c \mathbf{d}$ and $\sqrt{\beta_c} \mathbf{d}$ profiles, which are represented by a superposition of Gaussians, as a GP. Instead of considering only the nominal profile, biological uncertainties now introduce a distribution over $\alpha_c \mathbf{d}$ - and $\sqrt{\beta_c} \mathbf{d}$ -profiles yielding due to the GP parametrization to a mean- and a standard deviation-profile.

III.3.2 Integration into APM

Biological uncertainties cause an uncertainty in magnitude. This circumstance can be modeled within the APM framework by introducing variability in the weights $\omega_k^{\alpha/\beta}$ in the k -th Gaussian components defining the $\alpha_c \mathbf{d}$ - and $\sqrt{\beta_c} \mathbf{d}$ -profiles. So far the APM problem that is solved for the biological effect accounting for setup and range uncertainties is given by:

$$\mathbb{E}[\varepsilon(\mathbf{X})^n] = \int_{\mathbb{R}^\zeta} p_{\mathbf{X}}(x) \varepsilon(x)^n dx \approx \int_{\mathbb{R}^\zeta} \mathcal{N}(x, \bar{\mathbf{X}}, \Sigma^{\mathbf{X}}) \hat{\varepsilon}(x)^n dx \quad (\text{III.34})$$

Equation III.34 assumes a multivariate Normal distribution for setup and range uncertainties and derivations made in the previous sections allow to calculate the first raw and second central moment of the biological effect in closed-form.

Now an additional uncertainty parameter \mathbf{Y} is introduced, intended to model the variability in the magnitude of individual Gaussian components. A key feature of APM is that the consideration of an additional uncertainty source does not increase the computational complexity:

$$\begin{aligned}\mathbb{E}[\varepsilon(\mathbf{X}, \mathbf{Y})^n] &= \int_{\mathbb{R}^\zeta} p_{\mathbf{X}, \mathbf{Y}}(x, y) \varepsilon(x, y)^n dx dy = \int_{\mathbb{R}^\zeta} p_{\mathbf{X}}(x) p_{\mathbf{Y}}(y) \varepsilon(x, y)^n dx dy \\ &\approx \int_{\mathbb{R}^\zeta} \mathcal{N}(x, \bar{\mathbf{X}}, \Sigma^{\mathbf{X}}) \mathcal{N}(y, \bar{\mathbf{Y}}, \Sigma^{\mathbf{Y}}) \hat{\varepsilon}(x, y)^n dx dy\end{aligned}\quad (\text{III.35})$$

where, $p_{\mathbf{X}, \mathbf{Y}}$ denotes a new multivariate Normal distribution combining physical and biological uncertainties. But since physical uncertainties are assumed to be uncorrelated to biological uncertainties, $p_{\mathbf{X}, \mathbf{Y}}$ can be factorized into $p_{\mathbf{X}}$ and $p_{\mathbf{Y}}$. As of now, no evidence supports a different correlation assumption because setup and range errors do not show a dependency on biological errors and vice versa.

Notwithstanding, it is important to state, that if a pencil beam is shifted either laterally or longitudinally because of setup or range uncertainties also biological beam properties shift accordingly. This behavior is already modeled by $\alpha_c \mathbf{d}$ and $\sqrt{\beta_c} \mathbf{d}$ profiles as they directly combine physical and biological beam properties in the form of physical depth dose profiles and dose-averaged depth-dependent LQM profiles.

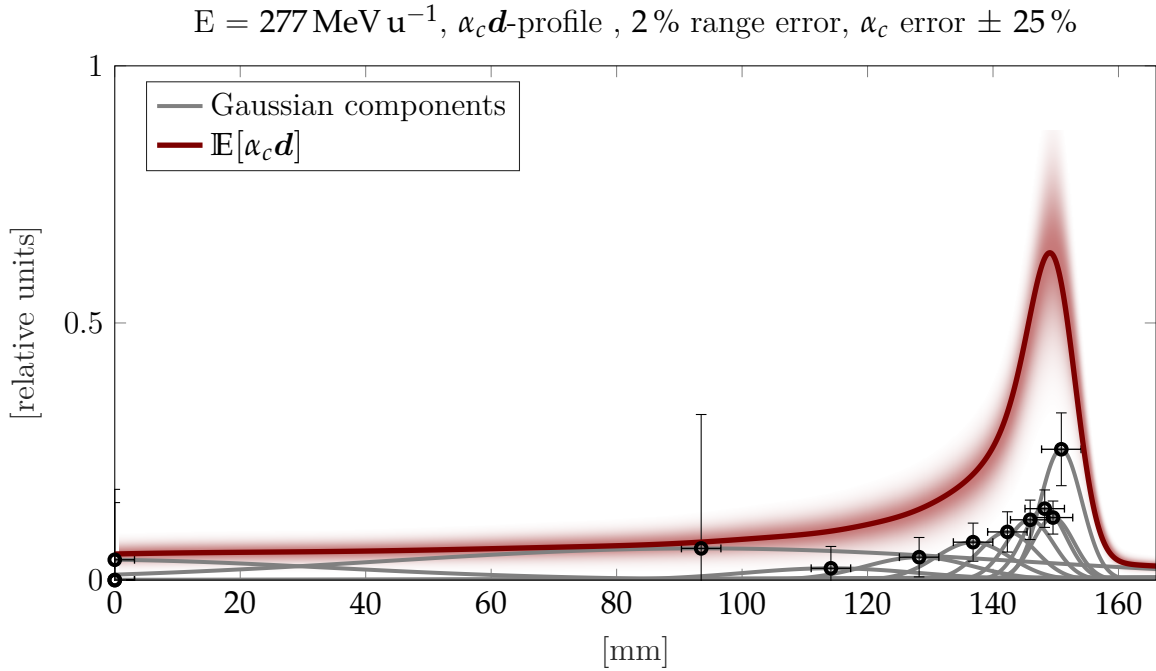


Figure III.8: A pseudo mono-energetic carbon ion pencil beam with 277 MeV u⁻¹ considering a tissue characterized by $\alpha_x = 0.1$ [Gy⁻¹] and $\beta_x = 0.05$ [Gy⁻²]. The (—) line depicts the expectation value considering 2% range uncertainty and a biological uncertainty in the α_c parameter of 25%. The latter directly translates to a of 25% uncertainty in the weight component ω_k^α of each Gaussian, which are illustrated in (—). Their superposition results in (—). Horizontal error bars denote range uncertainties whereas vertical errors bars depict biological uncertainties.

Figure III.8 shows the expectation value of the $\alpha_c \mathbf{d}$ -profile (—) of a pseudo mono-energetic carbon ion pencil beam with 277 MeV u⁻¹ for a tissue characterized with $\alpha_x = 0.1$ [Gy⁻¹] and $\beta_x = 0.05$ [Gy⁻²] and highlights two different aspects. First, physical range uncertainties are expressed by an uncertainty in the mean position along the x-axis of each Gaussian component, highlighted by horizontal error bars. As a result the expectation value (—) is washed out and not as peaked as the nominal profile (not shown). Second, biological

uncertainties are realized by an uncertainty in the weight ω_k^α of each Gaussian component along the y-axis as indicated by vertical error bars. In this work $\sigma[\omega_k^\alpha]$ is assumed to be 25%. Broad gaussian components in Figure III.8, for instance, the component with the mean at 0 mm or around ≈ 95 mm are associated with relatively high weights for which reason a 25% error assumption logically yields a high vertical error bar. The resulting biological uncertainty is shown in Figure III.8 by a light red colorwash and is due to the relative uncertainty assumption biggest around the peak. The same methodology can also be exercised for $\sqrt{\beta_c}d$ -profiles but is not explicitly shown here. The multivariate Normal distribution p_Y , to model biological uncertainties via the weights $\omega^{\alpha/\beta}$ of each Gaussian component, is described next.

III.3.3 Biological Uncertainty Model

Firstly a general uncertainty model is introduced that allows in principle to model biological uncertainties and correlation within and between both, $\alpha_c d$ and $\sqrt{\beta_c} d$ profiles. But because the $\alpha_c d$ profile is the main contributing component in the low fractionated dose domain, a biological uncertainty model is in this work ultimately only used for $\alpha_c d$ profiles and described towards the end of this section. This assumption is in line with the approximations already made for the moment calculations in the quadratic term ($\sqrt{\beta_c} d$) of the biological effect concerning physical uncertainties.

Here, it is assumed that the fitted weights ω obey a multivariate Normal distribution $\sim \mathcal{N}(\omega, \Sigma^\omega)$ with the mean value ω and the covariance matrix Σ^ω in which the fitted $\omega_k^{\alpha/\beta}$ parameters (see Figure III.3) represent directly the mean value. Analog to physical uncertainties, the covariance matrix Σ^ω allows modeling the magnitude and structure of biological uncertainties. In the previous section, range uncertainties were considered for each pencil beam j but now biological uncertainties are modeled for each Gaussian component k of each pencil beam j .

Let J be the total number of pencil beams, K be the number of Gaussian components per pencil beam defined in this manuscript to be $K = 13$ since 13 Gaussian components were fitted to the $\alpha_c d$ - and $\sqrt{\beta_c} d$ -profile. Further, accounting for two different profiles ($\alpha_c d$ and $\sqrt{\beta_c} d$) results then the covariance matrix Σ^ω to be in $\in \mathbb{R}^{O \times O}$ with $O = 2JK$. The factor two comes in because of two components, namely $\alpha_c d$ and $\sqrt{\beta_c} d$.

Figure III.9 illustrates the structure of the covariance matrix Σ^ω for only two pencil beams $J = 2$. As thirteen Gaussian components are used to model the respective $\alpha_c d$ and $\sqrt{\beta_c} d$ profiles, the covariance matrix Σ^ω is in $\in \mathbb{R}^{52 \times 52}$ as $O = 2JK = 2 \times 2 \times 13$.

Let u, v be linear indices from $\{u, v \in \mathbb{N} | 1 \leq u, v \leq O\}$, then the first block (■) in the upper left corner of the first plot in Figure III.9 from $u, v = 1 \dots 26$ models the correlation between all Gaussian components of $\alpha_c d$ profiles of both pencil beams. Focussing on the right plot of Figure III.9, therefore $A11$ denotes a sub-block modelling the correlation of Gaussian components of the $\alpha_c d$ profile of the first pencil beam $j = m = 1$. Whereas $A21$

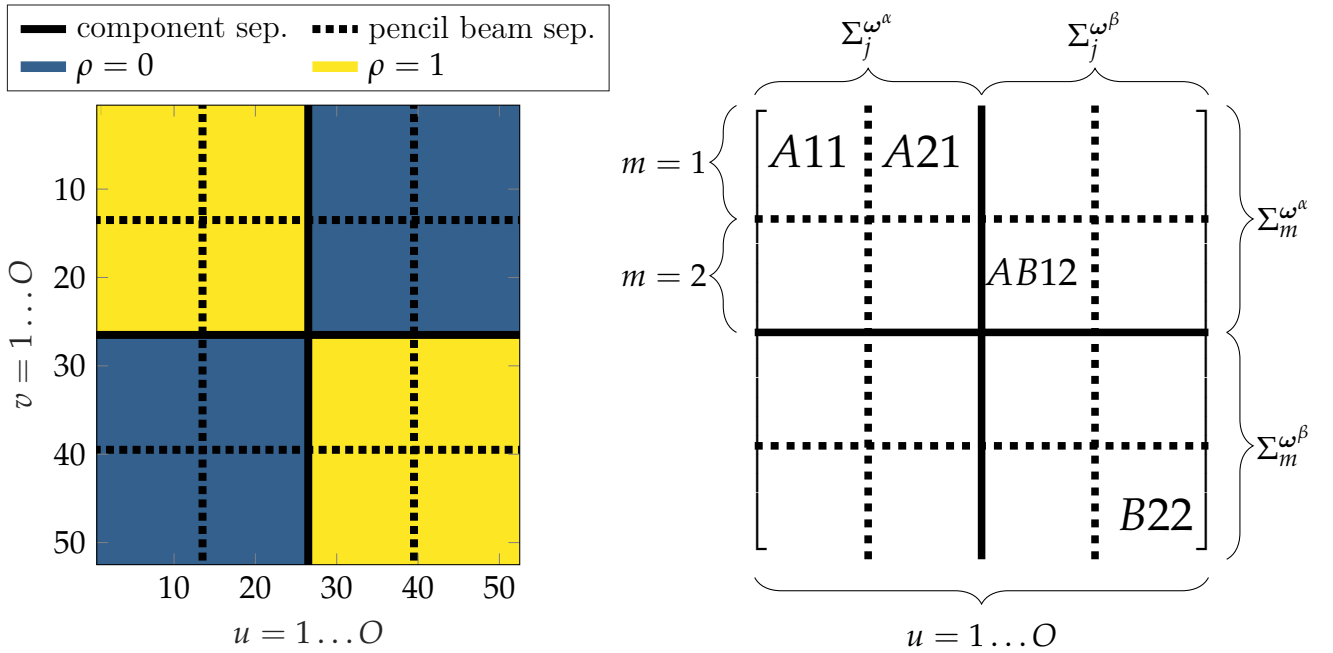


Figure III.9: Illustration of the structure of the covariance matrix Σ^ω to model biological uncertainties. This example corresponds to a dummy treatment plan comprised of two $J = 2$ pencil beams. Assuming $K = 13$ Gaussian components model each $\alpha_c d$ - and each $\sqrt{\beta_c} d$ -profile results in Σ^ω to be in $\mathbb{R}^{52 \times 52}$ thereby exhibiting block structure. (—) indicates the component separator between $\alpha_c d$ and $\sqrt{\beta_c} d$ components and (---) denotes the pencil beam separator.

depicts the correlation of Gaussian components of $\alpha_c d$ profiles between the first ($j = 1$) and second ($j = 2$) pencil beam. Analog represents the second block (■) in the left plot of Figure III.9 from $u, v = 27 \dots 52$, the correlation of all Gaussian components of $\sqrt{\beta_c} d$ profiles. The covariance structure in off-diagonal blocks $u/v = 1 \dots 26, v/u = 27 \dots 52$ (■) permits in principle to model correlation or anti-correlation of biological uncertainties between $\alpha_c d$ and $\sqrt{\beta_c} d$ components.

In this work, biological uncertainties are only modeled for $\alpha_c d$ profiles, whereas uncertainties in $\sqrt{\beta_c} d$ profiles were neglected in first approximation due to their smaller contribution to the biological effect. Further, it is assumed that all Gaussian components of $\alpha_c d$ profiles of all pencil beams are perfectly correlated. This implies biological uncertainties are believed to correlate identical for all pencil beams independent of the beam direction or beam energy. It is assumed that biological uncertainties are of systematic nature and realize equally throughout all fractions. The underlying principle reflected here is that biological models make global predictions which can be consistently (systematically) wrong or right.

The following paragraph describes briefly how the biological uncertainty estimate for $\alpha_c d$ profiles were derived. The LEM I was implemented in a Matlab prototype and validated with ground truth data obtained from a reference implementation. Then, a Monte Carlo sensitivity analysis was performed by varying the LEM input parameter (α_x and β_x) to obtain the variability and further the uncertainty structure of resulting $\alpha_c d$ profiles. The obtained standard deviation profile was then used to design the covariance matrix Σ^ω . In first approximation, a relative uncertainty of 25 % was assumed for depth-dependent dose-averaged LQM α_c parameters, which directly translate to a 25 % uncertainty in $\alpha_c d$ profiles

and further to ω^α . Similar findings were reported by Friedrich et al. (2013a). Hence, the covariance of $\alpha_c \mathbf{d}$ profiles between the j -th and m -th pencil beam $\Sigma^{\omega_{jm}^\alpha}$ is in $\mathbb{R}^{K \times K}$ and can be calculated on the fly, without the need to store a full (co)-variance matrix:

$$\Sigma^{\omega_{jm}^\alpha} = \rho 0.25^2 \left(\omega_j^\alpha \omega_m^{\alpha T} \right) \circ \mathcal{K} \quad (\text{III.36})$$

where ρ is set to 1 as all Gaussian components of the $\alpha_c \mathbf{d}$ profiles of all spot combinations jm are perfectly correlated and the \circ operator denotes the point-wise Hadamard matrix product. Both, $\Sigma_{jm}^{\omega^\alpha}$ and \mathcal{K} are in $\mathbb{R}^{K \times K}$ and $\omega_{j/m}^\alpha$ denotes a vector in $\mathbb{R}^{13 \times 1}$ containing the weights of Gaussian components of pencil beam j and m , respectively.

The \mathcal{K} matrix contains values $\in [0 \dots 1]$ and allows to additionally steer the shape of the uncertainty band. For instance, if only a biological uncertainty should be modeled around the peak then combinations of Gaussian components k and p of pencil beam j and m contributing to peak are associated with a value close to 1, while other component combinations not contributing to the peak are associated with a value of 0. Throughout this work a perfect correlation is assumed, thus the \mathcal{K} matrix is filled with ones. Following Equation III.36, it is not necessary to keep the full covariance matrix Σ^ω in storage, which is in $\mathbb{R}^{O \times O}$. Instead, their block-wise elements $\Sigma^{\omega_{jm}^\alpha}$, also shown by A11, A21... in Figure III.9 can simply be calculated on the fly when needed.

III.3.4 Moment Calculation

As biological uncertainties only affect depth related and not lateral components of the biological effect, a focus is set on the former. The expectation value considering biological and range uncertainties of depth components of the biological effect is given by:

$$\mathcal{Z}_{ij}^{\alpha/\beta} = \mathbb{E}[Z_{ij}^{\alpha/\beta}(\Delta^z, \omega^{\alpha/\beta})] = \int_{-\infty}^{\infty} \int_{-\infty}^{\infty} d\Delta^z d\omega^{\alpha/\beta} p(\Delta^z) p(\omega^{\alpha/\beta}) Z_{ij}^{\alpha/\beta}(\Delta^z, \omega^{\alpha/\beta}) \quad (\text{III.37})$$

We already know from Equation III.12 in Section III.2.1 how to calculate the expectation value of depth components considering range uncertainties. Thus, solving the integral in Equation III.37 for range uncertainties yields:

$$\mathcal{Z}_{ij}^{\alpha/\beta} = \mathbb{E}[Z_{ij}^{\alpha/\beta}(\Delta^z, \omega^{\alpha/\beta})] = \int_{-\infty}^{\infty} d\omega^{\alpha/\beta} p(\omega^{\alpha/\beta}) \sum_{k=1}^K \frac{\omega_{jk}^{\alpha/\beta}}{\sqrt{2\pi(\delta_{jk}^{\alpha/\beta^2} + \Sigma_{jj}^z)}} e^{-\frac{(z_{ij} - \mu_{jk}^{\alpha/\beta})^2}{2(\delta_{jk}^{\alpha/\beta^2} + \Sigma_{jj}^z)}} \quad (\text{III.38})$$

where $p(\omega^{\alpha/\beta})$ obeys a multivariate Normal distribution $\sim \mathcal{N}(\omega^{\alpha/\beta} | \boldsymbol{\mu}^\omega, \Sigma^\omega)$ with mean $\boldsymbol{\mu} = \omega^{\alpha/\beta}$ and covariance matrix Σ^ω . For further consideration, the superscript α/β is dropped because the following derivations are valid for both, $\alpha_c \mathbf{d}$ - and $\sqrt{\beta_c} \mathbf{d}$ -profiles. Due to the

marginalization property, Equation III.38 simplifies to:

$$Z_{ij} = \sum_{k=1}^K \int_{-\infty}^{\infty} \underbrace{d\omega_{jk} \mathcal{N}(\omega_{jk} | \mu_{jk}, \Sigma_{jkk}^{\omega})}_{= \mathbb{E}[\omega_{jk}] = \mu_{jk}^{\omega} = \omega_{jk}} \omega_{jk} \frac{1}{\sqrt{2\pi(\delta_{jk}^2 + \Sigma_{jj}^z)}} e^{-\frac{(z_{ij} - \mu_{jk})^2}{2(\delta_{jk}^2 + \Sigma_{jj}^z)}} \quad (\text{III.39})$$

$$= \sum_{k=1}^K \frac{\omega_{jk}}{\sqrt{2\pi(\delta_{jk}^2 + \Sigma_{jj}^z)}} e^{-\frac{(z_{ij} - \mu_{jk})^2}{2(\delta_{jk}^2 + \Sigma_{jj}^z)}} \quad (\text{III.40})$$

Under the assumption ω_{jk} is normally distributed around the mean ω_{jk} , the integration from $-\infty$ to ∞ yields the mean value, which is ω_{jk} as highlighted by the curly bracket in Equation III.39. Effectively, the expectation value of the biological effect considering biological and range uncertainties, shown in Equation III.40 and Appendix B.20 equals the expectation value of only considering range uncertainties (see Equation III.12).

As the weight of each Gaussian component $\omega_{jk}^{\alpha/\beta}$ directly presents the mean value from a Gaussian error distribution, calculating its expectation results logically in the mean value. This is only the case as the biological error is assumed to follow a Gaussian distribution. Other Probability Density Function (PDF)s, e.g. a skewed distribution would produce a different expectation value.

Focusing on the calculation of the second central moment of $Z_{ij}^{\alpha/\beta}$ considering additionally biological uncertainties yields to:

$$\begin{aligned} \Xi_{ijlm}^{\alpha/\beta} &= \mathbb{E}[Z_{ij}^{\alpha/\beta}(\Delta^z, \omega^{\alpha/\beta}), Z_{lm}^{\alpha/\beta}(\Delta^z, \omega^{\alpha/\beta})] \\ &= \int_{-\infty}^{\infty} \int_{-\infty}^{\infty} d\Delta^z d\omega^{\alpha/\beta} p(\Delta^z) p(\omega^{\alpha/\beta}) Z_{ij}^{\alpha/\beta}(\Delta^z, \omega^{\alpha/\beta}) Z_{lm}^{\alpha/\beta}(\Delta^z, \omega^{\alpha/\beta}) \quad (\text{III.41}) \end{aligned}$$

Next, let $p(\omega^{\alpha/\beta})$ again be a multivariate Normal distribution given by $\mathcal{N}(\omega^{\alpha/\beta} | \mu^{\omega}, \Sigma^{\omega}) = \omega^{\alpha/\beta}, \Sigma^{\omega}$. Similar to the expectation value before, Equation III.41 was already solved for physical uncertainties in Section III.2.2 (see Equation III.19) and resulted in:

$$\begin{aligned} \Xi_{ijlm}^{\alpha/\beta} &= \int_{-\infty}^{\infty} d\omega^{\alpha/\beta} \mathcal{N}(\omega^{\alpha/\beta} | \mu^{\omega}, \Sigma^{\omega}) \\ &\quad \sum_{kp} \frac{\omega_{jk}^{\alpha/\beta} \omega_{mp}^{\alpha/\beta}}{2\pi \sqrt{|\theta_{jkmp}^{\alpha/\beta} + \Sigma^{jm}|}} e^{-\frac{1}{2}(z_{ijlm} - \mu_{jkmp}^{\alpha/\beta})^T (\theta_{jkmp}^{\alpha/\beta} + \Sigma^{jm})^{-1} (z_{ijlm} - \mu_{jkmp}^{\alpha/\beta})} \quad (\text{III.42}) \end{aligned}$$

To explain solving Equation III.42 in a further step, a brief example is given next. Let \mathbf{x} be a multi-dimensional normally distributed variable with mean μ and covariance Σ , then the first raw moment is represented by $\mathbb{E}[\mathbf{x}] = \mu$. This has already been proven in Equation III.39

for calculating the expectation value. Knowing that ω represents the mean, calculating its expectation results in turn in ω . Following the *method of moments*, the second raw moment is then given by $\mathbb{E}[\mathbf{x}\mathbf{x}^T] = \boldsymbol{\mu}\boldsymbol{\mu}^T + \Sigma$ (Bishop, 2006) and Appendix A.5). Since the following derivations are valid for any depth-dependent component we drop again the superscript α/β . Further, moving $\omega_{jk}^{\alpha/\beta} \omega_{mp}^{\alpha/\beta}$ in Equation III.42 out of the double sum result in:

$$\begin{aligned} \mathbb{E}_{ijlm} &= \underbrace{\int_{-\infty}^{\infty} d\omega \mathcal{N}(\omega | \boldsymbol{\mu}^\omega, \Sigma^\omega) \omega_j \omega_m^T}_{\mathbb{E}[\omega_j \omega_m^T] = \boldsymbol{\mu}^\omega \boldsymbol{\mu}^{\omega T} + \Sigma^\omega = \omega_j \omega_m^T + \Sigma^\omega} \\ &\sum_{kp}^{KP} \frac{1}{2\pi \sqrt{|\theta_{jkmp} + \Sigma^{jm}|}} e^{-\frac{1}{2}(\mathbf{z}_{ijlm} - \boldsymbol{\mu}_{jkmp})^T (\theta_{jkmp} + \Sigma^{jm})^{-1} (\mathbf{z}_{ijlm} - \boldsymbol{\mu}_{jkmp})} \end{aligned} \quad (\text{III.43})$$

considering that $\boldsymbol{\mu}^\omega = \omega^{\alpha/\beta}$ the integral in Equation III.42 then results in $\omega_j \omega_m^T + \Sigma^\omega$. Moving these terms back into the double sum yields:

$$\mathbb{E}_{ijlm} = \sum_{kp}^{KP} \frac{\omega_{jk} \omega_{mp} + \Sigma_{kp}^{\omega_{jm}}}{2\pi \sqrt{|\theta_{jkmp} + \Sigma^{jm}|}} e^{-\frac{1}{2}(\mathbf{z}_{ijlm} - \boldsymbol{\mu}_{jkmp})^T (\theta_{jkmp} + \Sigma^{jm})^{-1} (\mathbf{z}_{ijlm} - \boldsymbol{\mu}_{jkmp})} \quad (\text{III.44})$$

where the additive term $\Sigma_{kp}^{\omega_{jm}}$ (see Equation III.36) depicts for biological uncertainties the covariance between different Gaussian components kp from two different pencil beam combinations j and m . The second raw moment of depth-related components, shown in Equation III.44 and in Appendix B.21, allows finally to calculate the standard deviation of the biological effect accounting for biological and physical uncertainties. It can be seen from Equation III.44 that the additional consideration of biological uncertainties results due the analytical formulation only in an additive term which does not increase the computational complexity of $\mathcal{O}(I \times J^2)$ for computing the standard deviation.

A proof of concept for an abstract toy example is shown in Figure III.10. This artificial example mimics the biological effect of a simple treatment plan comprised of two pencil beams f_1 (—) and f_2 (••••).

The first pencil beam f_1 (—) is defined as a linear combination $w_1 \mathbf{a}_1 + w_1 \mathbf{b}_1$ and shown in Figure III.10(a). Analog is the definition for the second pencil beam f_2 (••••) which is presented in Figure III.10(b). Each profile \mathbf{a}_1 , \mathbf{b}_1 , \mathbf{a}_2 and \mathbf{b}_2 , modeling the two pencil beams, is represented by a superposition of three Gaussian components. Range and biological uncertainties are modeled for each Gaussian component as highlighted by vertical and horizontal error bars in III.10(a) and (b). The resulting nominal quantities are shown in Figure III.10(c) and probabilistic quantities considering uncertainties in x and y dimension are shown in Figure III.10(d). The analytical expectation value $\mathbb{E}[f_{tot}]$ (—) is compared to $1e5$ random samples (✖) and results in a maximum relative difference of 0.31 % while the

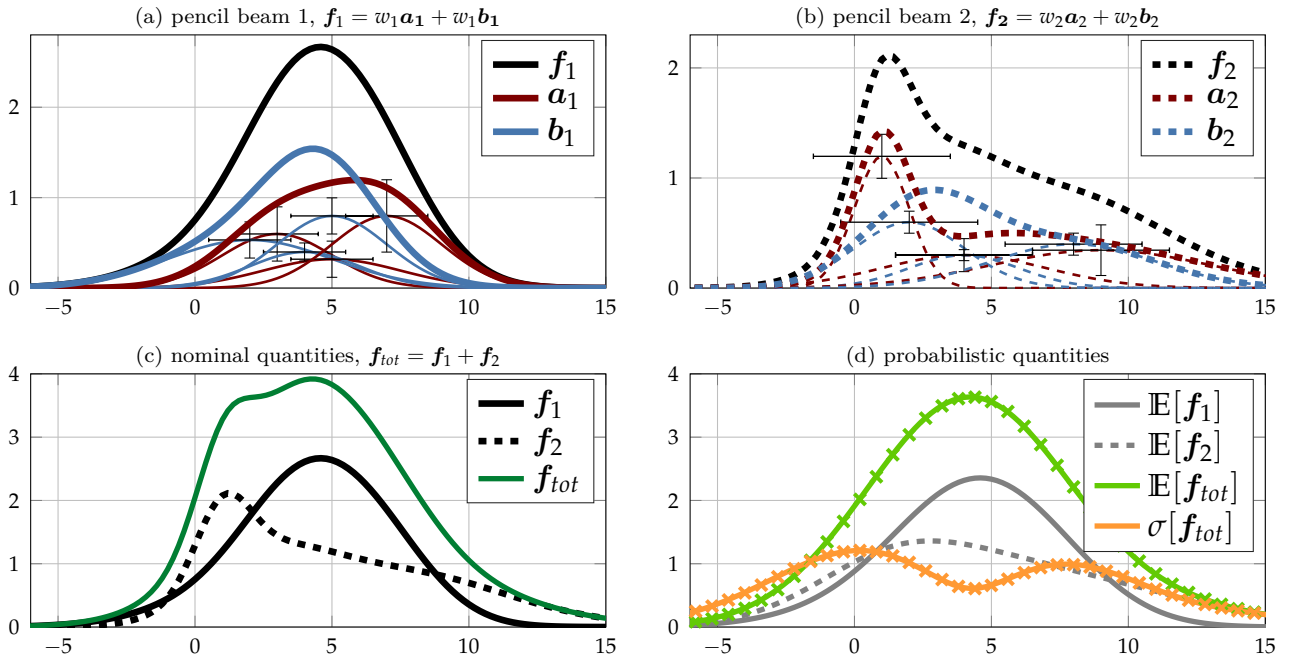


Figure III.10: Artificial example to mimic the situation for APM based carbon ion treatment planning. The first pencil beam shown in plot (a) is comprised of two components a_1 (—) and b_1 (—). Each component is represented by a superposition of three Gaussians and marked with horizontal and vertical error bars to model physical and biological uncertainties. Analog shows plot (b) the second pencil beam with a_2 (---) and b_2 (---). Their superposition $f_{tot} = f_1 + f_2$ is shown in plot (c) in (—) and plot (d) presents the expectation value (—) and standard deviation (—) along with estimations based random sampling results as indicated by crosses.

standard deviation $\sigma[f_{tot}]$ (—) yields compared to (\times) a maximum relative difference of 0.58 %. Figure III.10 (d) proves the correct incorporation of biological uncertainties in form of vertical errors. This permits now the application of the APM formalism to the carbon ion base data, where each depth-dependent profile is parameterized by thirteen Gaussian components.

In that regard, Figure III.11 shows the resulting probabilistic quantities of an $\alpha_c d$ profile assuming 2 % range uncertainty and 25 % uncertainty in the corresponding ω_k^α parameter, which translates due the linear relationship to a biological uncertainty of 25 %. Specifically, (—) shows the nominal $\alpha_c d$ profile and (—) its expectation value $\mathbb{E}[\alpha_c d]$ of a pseudo mono-energetic carbon ion pencil beam with 280 MeV u^{-1} .

Further a tissue, characterized by $\alpha_x = 0.1 [\text{Gy}^{-1}]$ and $\beta_x = 0.05 [\text{Gy}^{-2}]$ is assumed and LEM IV was used to obtain the corresponding LQM parameter of carbon ions. The lines (---) represent the expectation value \pm two standard deviations of simultaneously considering range and biological uncertainties. Moreover, Figure III.11 illustrates two possible realizations (—) of the αd profile during patient treatment. The digital version of this manuscript shows animated realizations (—) on the basis of a technical note presented by (Hennig, 2013) that is introduced later in Section III.6.4.

Throughout this work, biological uncertainties are only modeled in the linear component $\alpha_c d$ of the biological effect. Uncertainties in the quadratic $\sqrt{\beta_c} d$ component are as a first approximation neglected because the main contributing factor is the linear component. It can be

Figure III.11: Probabilistic quantities of a $\alpha_c d$ profile with 280 MeV u^{-1} accounting for $\pm 2\%$ range and $\pm 25\%$ biological uncertainties. The shown profiles refer to a tissue described with $\alpha_x = 0.1 [\text{Gy}^{-1}]$ and $\beta_x = 0.05 [\text{Gy}^{-2}]$. LQM parameter for carbon ions were predicted by the LEM IV. (—) depicts the expectation value of the nominal (—) $\alpha_c d$ profile. The lines (.....) indicate the uncertainty band of two sigma units. Lastly, (—) highlight two possible realizations of the profile during patient treatment. In the digital version of the PDF, continuous samples are drawn for animation to further demonstrate the potential variability of the $\alpha_c d$ profile. Animations are based on (Hennig, 2013).

seen from the calculation of the second raw moment of the biological effect in Equation III.17 that higher order moments ($n > 1$) of the quadratic component are never calculated because of the proposed approximations. To theoretically also consider biological uncertainties in the quadratic $\sqrt{\beta_c} d$ component of the biological effect, third ($\Xi_{ijlmio}^{\alpha 2\beta}$) and fourth raw moments (Ξ_{ijlmio}^{β}) in Equation III.16 need to be calculated which would increase the computational complexity from $\mathcal{O}(I \times J^2)$ to $\mathcal{O}(I \times J^4)$. Therefore, biological uncertainties are neglected for the quadratic $\sqrt{\beta_c} d$ component. On this subject, the result Section IV.2.1.1 analyzes the impact of only modeling biological uncertainties in the linear component $\alpha_c d$ of the biological effect.

In this section, it was shown how to calculate the expectation value and standard deviation of the biological effect in close-form thereby accounting for physical and biological uncertainties. The next section shows how this information can be incorporated for probabilistic optimization.

III.4 Probabilistic Optimization of the Biological Effect

Probabilistic optimization was introduced in Section II.5.3.2 and is used throughout this work in combination with effect-based optimization as shown by (Wilkins and Oelfke, 2006). Here, the prescribed RBE-weighted dose is converted to a reference effect ε^* and the optimization is carried out in the biological effect domain. After the optimization converged the optimized biological effect is converted back to RBE-weighted dose.

So far it was shown how to calculate the first raw moment $\mathbb{E}[\varepsilon_i]$ (see Equation III.8), the second raw moment $\mathbb{E}[\varepsilon_i, \varepsilon_l]$ (see Equation III.15) and how to derive the (co)-variance matrix Σ^ε (see Equation III.13) of the biological effect modeling physical and biological uncertainties as well as fractionation effects. This section is about how this probabilistic information of the biological effect is used for optimization in order to minimize uncertainties in the treatment plan.

Let $P = \text{diag}(p_1, \dots, p_I)$ denote a penalty matrix, then the squared deviation objective function $f_{sq\ dev}$ of the biological effect $\varepsilon \in \mathbb{R}^{I \times 1}$ is given in matrix notation by:

$$f_{sq\ dev} = (\varepsilon - \varepsilon^*)^T P (\varepsilon - \varepsilon^*) \quad (\text{III.45})$$

Assuming the biological effect ε can be described with a multivariate Normal distribution, characterized by the first raw and second central statistical moment (mean $\mathbb{E}[\varepsilon]$ and covariance Σ^ε), the expectation value $\mathbb{E}[\cdot]$ of $f_{sq\ dev}$ can then according to (Imhof, 1961; Liu et al., 2009) be described with a generalized χ^2 -distribution with the analytical expectation value:

$$\mathbb{E}[f_{sq\ dev}(\varepsilon)] = \text{tr}(P \Sigma^\varepsilon) + (\mathbb{E}[\varepsilon] - \varepsilon^*)^T P (\mathbb{E}[\varepsilon] - \varepsilon^*) \quad (\text{III.46})$$

where tr represents the trace operator that only considers diagonal elements of $P \Sigma$ for summation. In this formulation, the expectation value of the squared deviation objective is optimized by considering the full probability masses of ε . To evaluate Equation III.46 for different pencil beam intensities during each step of the optimization, it is necessary to provide firstly expected linear $\mathbb{E}[A] = \mathcal{A}$ and quadratic $\mathbb{E}[B] = \mathcal{B}$ influence matrices of the biological effect (see Equation III.9) such that the expected biological effect $\mathbb{E}[\varepsilon]$ can be derived efficiently in each step of the optimization. Secondly, a variance influence tensor \mathfrak{V}_{ijm} which is $\in \mathbb{R}^{I \times J \times J}$ (see Equation III.20) needs to be available to derive the integral variance for different pencil beam intensities during optimization.

As it is practically infeasible to store the full variance influence tensor \mathfrak{V}_{ijm} for clinical cases, the following re-formulation was introduced by (Bangert et al., 2013) for protons and is now applied to carbon ions. Let p_i be the penalty of voxel i , then we can derive:

$$\text{tr}(P \Sigma^\varepsilon) = \sum_{i=1}^I p_i \Sigma_{ii}^\varepsilon = \sum_{i=1}^I p_i \sum_{jm}^J w_j w_m \mathfrak{V}_{ijm} \quad (\text{III.47})$$

$$= \sum_{jm}^J w_j w_m \sum_{i=1}^I p_i \mathfrak{V}_{ijm} = \mathbf{w}^T \Omega \mathbf{w} \quad (\text{III.48})$$

where $\Omega \in \mathbb{R}^{J \times J}$ represents the penalized integral variance influence matrix of all pencil beam combinations. Equation III.48 reduces the storage requirements drastically and can be evaluated with a minimum amount of overhead. Moreover, Wahl et al. showed that Ω can be computed for each VOI S separately so that re-optimization with different penalties can be done without recomputing the integral variance influence (Wahl et al., 2017). Further, it was shown that the Ω matrix can be approximated by only considering a certain sub set of voxels for the calculation of the integral variance. For more information the interested reader is referred to (Wahl et al., 2017).

To ultimately optimize the expected squared deviation objective on the basis of the biological effect (see Equation III.46), also gradient information is required which can be obtained from:

$$\frac{\partial}{\partial \mathbf{w}} \mathbb{E}[f_{sq\ dev}(\varepsilon)] = \frac{\partial}{\partial \mathbf{w}} \left[(\mathbb{E}[\varepsilon] - \hat{\varepsilon})^T P (\mathbb{E}[\varepsilon] - \hat{\varepsilon}) \right] + 2\Omega \mathbf{w} \quad (\text{III.49})$$

Thus optimizing the expected squared deviation for the biological effect, reduces to computing the following probabilistic quantities: $\mathbb{E}[A]$, $\mathbb{E}[B]$ and Ω . The probabilistic optimization itself imposes negligible overhead compared to a conventional optimization.

Nevertheless, prerequisites for probabilistic optimization for carbon ion therapy are the probability densities of the biological effect distribution $\mathbb{E}[\varepsilon]$ and Σ^ε . On the one hand $\mathbb{E}[A]$, $\mathbb{E}[B]$ and Ω can be estimated by sampling techniques. For instance, $\mathbb{E}[A]$, $\mathbb{E}[B]$ can simply be estimated by taking the (weighted) average and the integral variance Ω can be estimated by exercising the inner product of $A^T A$ and $B^T B$ for multiple samples. On the other hand, $\mathbb{E}[A]$, $\mathbb{E}[B]$ and Ω can be calculated by meta-model approaches such as APM. Different to (Unkelbach et al., 2009), once $\mathbb{E}[A]$, $\mathbb{E}[B]$ and Ω are available no sampling is required during optimization.

Here only the expected squared deviation objective is presented and used throughout this work. For other novel probabilistic objective functions and constraints, the interested reader is referred to the Ph.D. thesis of (Wahl, 2018).

III.5 From Biological Effect to RBE weighted Dose

Based on the APM formalism derived in the previous three sections, probabilistic quantities like the expectation value and standard deviation of the biological effect ε can be derived

analytically and probabilistic optimization can be carried out.

Notably, clinical decision making in carbon ion treatment planning is usually based on the RBE weighted dose, for which reason the expectation value $\mathbb{E}[\varepsilon]$ and variance of the biological effect $\sigma^2[\varepsilon]$ need to be propagated to expectation value $\mathbb{E}[RBE \times d]$ and variance of RBE weighted dose $\sigma^2[RBE \times d]$. Theoretically, the first two moments of the RBE weighted dose could be calculated directly, however, for practical reasons it was decided to calculate the first two moments of the biological effect and then employ a subsequent error propagation to obtain $\mathbb{E}[\varepsilon] \Rightarrow \mathbb{E}[RBE \times d]$ and $\sigma[\varepsilon] \Rightarrow \sigma[RBE \times d]$. Although the actual distribution of ε under the assumption of input uncertainties is unknown, the first two moments can be calculated exactly via APM[§].

With $\gamma = \frac{\alpha_x}{2\beta_x}$, the calculation of the RBE weighted dose from Equation II.23 clearly shows the non-linear dependency on a scaled version of the biological effect ε due to a square root:

$$RBE \times d = \sqrt{\frac{\varepsilon}{\beta_x} + \gamma^2} - \gamma \quad (\text{III.50})$$

For error propagation a fourth order Taylor expansion at $\mathbb{E}[\varepsilon_i]$ evaluating partial derivatives at ε_i was used throughout this work to approximate the non-linear conversion of moments of the biological effect (Anderson and Mattson, 2012):

$$\begin{aligned} \mathbb{E}[RBE \times d_i] \approx & \sqrt{\beta_x^{-1}\mathbb{E}[\varepsilon_i] + \gamma^2} - \gamma - \frac{\beta_x^{-2}}{8(\beta_x^{-1}\mathbb{E}[\varepsilon_i] + \gamma^2)^{\frac{3}{2}}}\sigma[\varepsilon_i]^2 - \\ & \frac{5\beta_x^{-4}}{128(\beta_x^{-1}\mathbb{E}[\varepsilon_i] + \gamma^2)^{\frac{7}{2}}}\sigma[\varepsilon_i]^2 \end{aligned} \quad (\text{III.51})$$

$$\sigma[RBE \times d_i]^2 \approx \frac{\beta_x^{-1}}{2(\beta_x^{-1}\mathbb{E}[\varepsilon_i] + \gamma^2)^{\frac{1}{2}}}\sigma[\varepsilon_i]^2 + \frac{1}{2} \left(\frac{\beta_x^{-2}}{8(\beta_x^{-1}\mathbb{E}[\varepsilon_i] + \gamma^2)^{\frac{3}{2}}} \right)^2 \sigma[\varepsilon_i]^4 \quad (\text{III.52})$$

The Taylor series expansion about ε_i is only locally valid meaning the approximation quality generally shrinks when the variance of the biological effect increases. Another limitation is the assumption of a Normal distribution of the biological effect modeled by two parameters. Any deviation from the Normal distribution (skewed or bimodal distribution) is not captured by the mean and variance and may compromise the accuracy of the proposed error propagation in Equation III.51 and III.52. To increase the description of the unknown probability distribution of the biological effect and the accuracy of error propagation, higher order moments (skewness and kurtosis) of the biological effect need to be calculated.

[§]assuming analytical pencil algorithm and input uncertainty assumptions are correct

III.6 Validation and Evaluation

Since basic treatment planning functionalities are required, this Section explains first in III.6.1 how the particle dose calculation module and the optimization module of the implemented TPS matRad were validated. Based on this work, the APM formalism was implemented on top to calculate statistical moments of the RBE-weighted dose in closed-form. Several artificial and clinical patient cases evaluated with APM are presented in Subsection III.6.2. Statistical moments obtained from APM are compared in a further step to estimated statistical moments based on random sampling. Lastly, Subsection III.6.3 explains the γ -analysis used to quantify the similarity of dose distributions and III.6.4 presents a novel uncertainty visualization technique.

III.6.1 Basic Dose Calculation and Optimization Functionalities

Before implementing the APM formalism, basic dose calculation and optimization functionalities were implemented and validated first. To validate the dose calculation engine of the implemented TPS matRad, reference results were generated from the clinical TPS SyngoRT planning (Siemens, Erlangen, Germany) which is currently used at the Heidelberg Ion Therapy (HIT) facility. In total, eight treatment plans were investigated for protons and carbon ions within SyngoRT.

For both modalities, protons and carbon ions, three dose calculations in water for individual pseudo mono-energetic pencil beams with range 5 cm, 15 cm and 25 cm were performed in SyngoRT. The treatment plan's couch and gantry angle were both 0° . The dimensions of the CT and the dose cube were $512 \times 512 \times 370$ with a voxel resolution of $x, y, z = 1$ mm. In these cases, no optimization within SyngoRT was performed.

Further, a realistic clinical treatment plan for protons and carbon ions for a cranial case with a single beam of gantry angle 270° and couch angle 0° was computed. For protons, a constant RBE of 1.1 was assumed and the plan was optimized for a target dose in the PTV of 2 Gy(RBE). In contrast, for carbon ions a variable RBE was modelled on the basis of the LEM I and the RBE weighted dose was optimized for a dose in the PTV of 3 Gy(RBE). The optimization module of Syngo RT was configured to perform a *full simulation* (see Section II.4.2) in each step of the optimization to assess the RBE. In particular, 1000 Monte Carlo runs were used to obtain the accumulated biological damage produced by different ion types of different energies. The CT and the optimized dose cube were in dimensions of $310 \times 310 \times 339$ representing a voxel dimension of $x, y, z = 1$ mm.

The resulting dose cubes and pencil beam weights \mathbf{w} were then exported together with the CT, structures (VOIs) and the treatment plan information using the DICOM[¶] file format. Next, all DICOM files were imported into matRad. To ensure consistency between matRad and SyngoRT, the same beam data (pencil beam profiles) modeling the HIT beamline and

[¶]format for Digital Imaging and Communications in Medicine

HU look-up tables were used. The imported geometrical beam information such as beam direction and pencil beam positions allowed a forward dose calculation in matRad under the exact same prerequisites. The resulting dose cubes calculated by matRad were then compared in terms of absolute differences and the γ -index (see Subsection III.6.3) to dose cubes calculated by SyngoRT. By this means, the particle dose calculation engine was directly compared and validated against SyngoRT. The main algorithmic difference between matRad and SyngoRT is beside ray tracing that matRad features the *single particle approximation* (SPA) algorithm presented in Equation II.19 to calculate the RBE in a mixed-radiation field, while SyngoRT facilitates the *full simulation*. For more detailed information about the validation of matRad, the reader is referred to (Wieser et al., 2017a). All validation related results of matRad's dose calculation engine are presented in Chapter IV.1 in Section IV.1.1.

To ensure mathematical consistency of the optimization module along with its objective functions (see Table II.1), analytical gradients and partial derivatives were compared to the corresponding numerical gradients. Furthermore, to validate the interface and the communication to the IPOPT optimizer, the open-source TG119 phantom (Craft et al., 2014) is optimized using two carbon ion beam directions from gantry angle 45° and 315° . The corresponding couch angles were 0° . In total, three objectives and two constraints were defined for optimization. The resulting DVH is analyzed in Chapter IV.1.2.

The last part evaluates the performance of the dose calculation and dose optimization in matRad. Therefore, multiple treatment plans for the open-source CORT patient data set (Craft et al., 2014) with varying problem size and a voxel resolution of 0.3 cm were executed three times and the resulting average computation times of dose calculation and optimization are presented in the result chapter in Section IV.1.3. The runtimes were measured on a standalone computer with the following specifications: Intel Core i7 860, 2.6 GHz, 16 GB RAM @ 1333 MHz. For dose calculation within matRad, there are two additional options available which are considered for the performance evaluation. First, either a single or a double Gaussian lateral beam model can be used for dose calculation, which yields for the latter to bigger dose influence matrices in terms of storage and consequently results in longer dose calculation times. This is because the lateral double Gaussian beam model considers the low dose halo more accurately for which reason even dose for voxels far away from the central beam axis of a spot is calculated and stored.

Summarized, the validations done for matRad ensure proper functioning of the dicom import, the beam model, ray-tracing, dose calculation and optimization. APM was then implemented on top of the existing and validated code. The next subsections describe the implementation and validation of the APM related code.

III.6.2 Analytical Probabilistic Modeling

The implemented and validated carbon ion dose calculation was extended to use instead of tabulated base data fitted Gaussian parameter. Instead of performing linear interpolations

on the tabulated base data, a superposition of thirteen Gaussian components is evaluated. Physical setup and range uncertainties are modeled separately for random and systematic errors by covariance matrices stored in the Matlab sparse matrix format. For biological uncertainties the covariance matrix is calculated on the fly and then additionally passed on with the physical covariance matrices to the dose calculation function to determine expected influence matrices. The complexity to calculate the nominal and expected influence matrices is herewith equal.

Further, a function was added to the matRad code base to calculate the standard deviation and the integral variance influence matrix Ω which is required for probabilistic optimization. The core of this function is given by three nested-for loops. As the co-variance- \mathfrak{C}_{ijlm} and variance- \mathfrak{V}_{ijm} influence tensor are too large to be stored on disk, the standard deviation is calculated on the fly with the outer loop running through all voxels i . The two inner loops evaluate all possible pencil beam combinations jm with the two-dimensional Gaussian kernel from Equations III.18 and III.44.

Two applied approaches to optimize the performance of the implemented code were first to replace the outer loop with a `parfor`^{||} loop to compute the standard deviation of different voxel's in parallel and second to provide the two-dimensional Gaussian kernel evaluations in the form of C++ files with MEX interfaces. In particular, the latter allowed to call the Gaussians kernel evaluations implemented in C++ from Matlab. Different solutions to optimize the computational performance of APM are presented in (Wahl et al., 2017). For instance, one approach is given by evaluating only a subset of jm pencil beam combinations in the calculation of the standard deviation of voxel i . In detail, only the diagonal jj plus a random subset of jm combinations is used to derive the standard deviation.

The implemented APM code on the basis of matRad is publicly available on Github** for download. Moreover, a simplified implementation of APM can be found in the APMtoolbox^{††}.

Before evaluating clinical patient cases, a simpler one-dimensional artificial phantom is presented in the result Section IV.2.1 in order to verify first the proposed theoretical approximated deviations of statistical moments of the RBE weighted dose and secondly to investigate various aspects such as accuracy and fractionation. The 1D treatment plan models a water phantom with two opposing carbon ion beams considering 3.5 % range uncertainty and 25 % biological uncertainties. The optimized carbon ion SOBP is illustrated in Figure III.12. The first beam comprised of 45 pencil beams enters the phantom from the left side whereas the second beam also comprised of 45 pencil beams enters from the right side. The light gray area (▬▬▬) denotes the CTV and the dark gray area (▬▬▬) the margin extension of 10 mm to obtain the PTV which ranges from 90 mm to 160 mm.

An effect-based optimization as proposed by (Wilkins and Oelfke, 2006) was carried out

^{||}<https://de.mathworks.com/help/distcomp/parfor.html> [accessed May 2,2019]

^{**}https://github.com/becker89/matRad/tree/dev_varRBEprobOpt [accessed May 2,2019]

^{††}<https://github.com/e0404/APMtoolbox> [accessed May 2,2019]

using a squared deviation objective with a prescribed RBE weighted dose ($RBE \times d$) of 3 Gy(RBE) in the PTV. The water phantom mimics a tissue characterized by $\alpha_x = 0.1 \text{ Gy}^{-1}$ and $\beta_x = 0.05 \text{ Gy}^{-2}$. The LEM IV was used to obtain the radio-sensitivity parameter of carbon ions. A squared overdosing objective with a lower penalty was defined to suppress dose in the adjacent normal tissue structure. The line (—) shows the optimized biological effect ε . Applying the non-linear conversion from Equation III.50 yielded the RBE weighted dose denoted by (—). The resulting physical doses of each pencil beam (spot) is shown by (—). It can be seen from Figure III.12 that the left side of the tumor is covered with spots from the right beam and vice versa. The superposition of all individual pencil beam doses yields the total physical dose deposition of carbon ions (—).

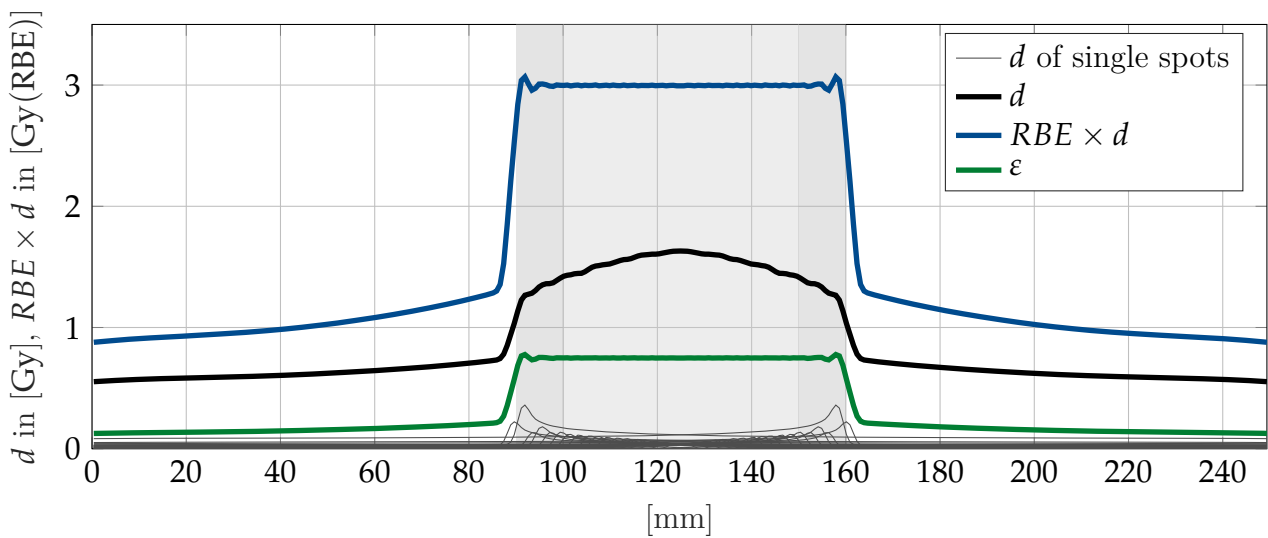


Figure III.12: One-dimensional carbon ion SOBP in water. The treatment plan is comprised of two opposing beams whereby each beam is characterized by 45 pencil beams. A tissue defined by $\alpha_x = 0.1 \text{ Gy}^{-1}$ and $\beta_x = 0.05 \text{ Gy}^{-2}$ and the LEM IV was used to perform an effect-based optimization aiming to deliver a homogenous $RBE \times d$ (—) to the PTV. (—) denotes the biological effect ε and (—) depicts the physical carbon ion d .

In the result section, physical and biological uncertainties are quantified first separately and then combined for conventional optimization. Afterward, also their impact on probabilistic optimization is analyzed. Moreover, the impact of assuming non-Gaussian probability distribution of errors is examined and compared to APM results which are grounded on the Gaussian error assumption (see Result IV.2.1.3). Lastly, the aspect of assuming a different biological model for forward dose calculation is investigated. In particular, a LEM I optimized treatment plan is compared to the forward calculated treatment plan on the basis of LEM IV for both conventional and probabilistic optimization (see Result IV.2.1.4).

In every probabilistic treatment plan optimization that accounts for range uncertainties, the CTV is considered as target structure. Otherwise, the plan was optimized for PTV structure. This holds for the one-dimensional phantom as well as for the patient cases introduced later.

All analytically quantified uncertainties with APM were verified with estimated moments using 5000 random samples drawn from multivariate Normal distribution given in Section III.2.1 and III.3.3. Specifically, 5000 random samples were used because it ensures the standard error of the sampled mean $\sigma[\mathbb{E}[\varepsilon]]$ to fall below 1.4% and the expected relative error of the

standard deviation $\sigma[\sigma[\epsilon]]$ to drop below 1 % (Ahn and Fessler, 2003; Wahl et al., 2017). As the proposed analytical approximations match sampled references, the use of APM is evaluated on clinical cases.

Next, uncertainty quantification and probabilistic optimization for three-dimensional intensity-modulated clinical treatment plans were evaluated. The APM formalism was analyzed for carbon treatment planning studies using conventional and probabilistic optimization considering setup-, range- and biological-errors alongside fractionation effects.

Table III.2: Information about patient cases and their corresponding plan parameters that were used for the APM analysis in Section IV.2. The third row lat. spot distance denotes the lateral spot spacing in the iso-center plane and # voxels σ depicts the number of voxels for which standard deviation was calculated. The number of pencil beams and the number of voxels for σ calculation are the dominant factors for the overall runtime.

| | unit | intra-cranial | para-spinal | prostate | liver | lung | cranial |
|---------------------|-----------|--------------------|-------------------|--------------------|--------------------|-------------------|-------------------|
| gantry angles | [°] | 50°, 135° | 135°, 180°, 225° | 90°, 180° | 310° | 35°, 350° | 90°, 180° |
| couch angles | [°] | 0°, 0° | 0°, 0°, 0° | 0°, 0° | 0° | 0°, 0° | 0°, 0° |
| lat. spot distance | [mm] | 3 | 4 | 5 | 5 | 5 | 5.5 |
| resolution | [mm] | (1.2 × 1.2 × 3) | (3 × 3 × 3) | (2 × 2 × 3) | (3 × 3 × 2.5) | (3 × 3 × 2.5) | (3 × 3 × 2.5) |
| # pencil beam | - | 2022 | 17756 | 15669 | 4312 | 8209 | 7275 |
| # voxels σ | - | 0.95×10^5 | 1.2×10^5 | 0.83×10^5 | 0.72×10^5 | 0.6×10^5 | 0.4×10^5 |
| # fractions f | - | 1 | 5 | 20 | 20 | 20 | 20 |
| pres. fraction dose | [Gy(RBE)] | 3 | 3 | 3 | 3 | 3 | 3 |

The objective function applied for treatment planning features squared deviation objectives with a prescribed fraction dose of 3 Gy(RBE) for the CTV and squared overdosing objectives for the outer contour and critical structures. Both, conventional and probabilistic optimization were performed for each case and the accuracy of APM moment computations was investigated in comparison to random sampling for unfractionated treatment (fraction $f = 1$). Three-dimensional γ -pass rates according to the following Section III.6.3, utilizing a distance to agreement of 2 mm and a dose difference criterion of 2 % were used for the comparison against estimation from sampled references.

The treatment plan parameters of the clinical patient cases are shown in Table III.2 and evaluated in Section IV.2. All results presented in this manuscript assume photon reference radio-sensitivity parameters $\alpha_x = 0.1 \text{ Gy}^{-1}$ and $\beta_x = 0.05 \text{ Gy}^{-2}$. Further, a single biological system characterized by identical photon reference radio-sensitivity parameters for all voxels i , was assumed. A correlation measure between two dose distribution which is used throughout this work is described next.

III.6.3 γ -analysis

The γ -analysis introduced by (Low et al., 1998) is a similarity measure allowing to compare three-dimensional dose distributions quantitatively. Originally, the γ -analysis was introduced to compare measured and calculated dose distributions. Throughout this manuscript, the γ -analysis was used for two different use cases, first, to compare and validate three-dimensional dose distributions calculated by matRad and the reference platform SyngoRT. Secondly, the γ -analysis was used to analyze the similarity of statistical moments (expectation value and standard deviation of dose) of APM and estimations based on random sampling.

The key feature of the γ -analysis is given by a composite evaluation of two different criteria with equal significance, namely a relative dose difference Δd and a Distance to Agreement (DTA) criteria. The γ -analysis is an advancement to absolute or relative dose difference comparisons carried out at identical voxel position. Already small spatial shifts in high dose-gradient regions result in large disagreements, which may be less important than disagreements in low dose-gradient regions. On the contrary, the γ -analysis considers a predefined local neighborhood in the reference cube to search for dose agreement. Only if both criteria, Δd and the DTA are fulfilled the current voxel under investigation passes the γ -analysis.

Let Δd be the relative dose difference criteria (e.g. 2%), which can either chosen to be the local- or the global-relative difference. Further, let DTA be the distance to agreement criteria (e.g. 2 mm) and let \mathbf{r}_m be a single point in the measured reference dose cube. Next, \mathbf{r} denotes the relative spatial location to \mathbf{r}_m of the dose cube to be analyzed. Then $\mathbf{r}_m - \mathbf{r}$ represents the geometrical distance between the measured reference point and the point to be analyzed. Additionally, let $\mathbf{d}_m(\mathbf{r}_m)$ depict the measured reference dose and $\mathbf{d}(\mathbf{r})$ be the dose at spatial location \mathbf{r} that is going to be tested. If $|\mathbf{r}_m - \mathbf{r}| \leq \text{DTA}$ then the DTA is within acceptance whereas $|\mathbf{d}_m(\mathbf{r}_m) - \mathbf{d}(\mathbf{r})| \leq \Delta d$ indicates a passed dose difference criteria. Both criteria are ultimately combined and represent according to

$$1 = \sqrt{\frac{|\mathbf{r}_m - \mathbf{r}|^2}{\text{DTA}} + \frac{|\mathbf{d}_m(\mathbf{r}_m) - \mathbf{d}(\mathbf{r})|^2}{\Delta d}} \quad (\text{III.53})$$

a threshold surface. In the case of a two-dimensional dose distribution, Equation III.53 denotes an ellipsoid whose surface represents the acceptance criteria (Low et al., 1998). The first two principal axes of the ellipsoid are of equal length and are determined by the DTA. The third principal axis is characterized by the dose difference criteria Δd .

Calculating the γ -index for a single point \mathbf{r} requires to loop over all voxels in the measured reference cube:

$$\gamma(\mathbf{r}) = \min \left\{ \sqrt{\frac{|\mathbf{r}_m - \mathbf{r}|^2}{\text{DTA}} + \frac{|\mathbf{d}_m(\mathbf{r}_m) - \mathbf{d}(\mathbf{r})|^2}{\Delta d}}, \forall \mathbf{r} \right\} \quad (\text{III.54})$$

According to Equation III.54 a $\gamma(\mathbf{r}) \leq 1$ represents a point inside or on the surface of the ellipsoid and indicates acceptance. In contrast, $\gamma(\mathbf{r}) > 1$ denotes a failed γ -analysis. The resulting γ -index value quantifies the level of disagreement of the current dose point to the measured reference dose cube.

The γ -analysis is of complexity $\mathcal{O}(I^2)$ because each voxel of the dose distribution needs to be checked against each voxel of the reference cube. To obtain a single quantitative value for each voxel, the minimum value according to Equation III.54 is then used as the resulting γ -analysis value. The implementation of the γ -analysis used throughout this manuscript can

be found on GitHub[‡].

III.6.4 Smooth Animations

The visualization of treatment plan uncertainties is an important aspect in order to make the treatment planner aware of these effects and to provide guidance towards a more robust solution. There are numerous ways to visualize treatment planning uncertainties ranging from error bar distributions, over Standard Deviation RBE weighted Dose Volume Histogram (SDDVH), to a set of DVHs, however, this section presents a new method, initially published by (Hennig, 2013), to visualize treatment plan uncertainties.

First, it is assumed the RBE weighted dose obeys a general multivariate Normal distribution $\mathcal{N}(\boldsymbol{\mu}, \boldsymbol{\Sigma})$, characterized by a mean vector $\boldsymbol{\mu}$ and a covariance matrix $\boldsymbol{\Sigma}$. These two parameters can either be obtained via meta-model approaches such as APM or can be estimated from discrete random samples. Once mean and covariance are determined, individual dose samples \mathbf{d}^s can easily be drawn from \mathcal{N} . The general procedure for this is to firstly draw samples \mathbf{u}^s from the standard multivariate Normal distribution $\mathcal{N}(0, I)$ and secondly to linearly transform (map) this vector via the upper triangular matrix R of the Cholesky-decomposition $RR^T = \boldsymbol{\Sigma}$ back to the general multivariate Normal distribution $\mathcal{N}(0, \boldsymbol{\Sigma})$. In the last step, the mean needs to be added to account for the offset $\mathbf{d}^s = \boldsymbol{\mu} + R\mathbf{u}^s$.

Drawing individual independent samples \mathbf{d}^s limits to express and visualize the structure of $\boldsymbol{\Sigma}$. For that reason (Hennig, 2013), introduced a new sampling strategy by selecting an equipotential set of samples to present covariance information along a third dimension namely time. Displaying the resulting set of samples one after another creates then a smooth animation. Knowing that $\mathcal{N}(0, I)$ denotes a multivariate spherical symmetric distribution, a radius r can be selected that defines a hypersphere with equal probability. Note that each point on the hypersphere represents an individual sample vector. In a further step, multiple samples were then taken from a equipotential circular path around the hypersphere. If Q frames are required for the animation, Q equally spaced points on the circular path are created. In the last step, each point on the circular path \mathbf{u}^s from the multivariate standard distribution was mapped back to the general multivariate Normal distribution via $\mathbf{d}^s = \boldsymbol{\mu} + R\mathbf{u}^s$. For further details, the interested reader is referred to (Hennig, 2013).

Smooth animations of a conventional and a probabilistic carbon ion treatment plan for an intra-cranial case considering physical uncertainties are presented in the results in Section IV.2.2.4.

[‡]https://github.com/e0404/matRad/blob/master/tools/matRad_gammaIndex.m [accessed Sept. 2018]

IV

Results

The results of validating basic dose calculation and optimization functionalities representing the fundamental treatment planning framework used throughout this work are presented in Section IV.1. Next, Section IV.2 presents the results of carbon ion treatment plan uncertainty quantification and mitigation on the basis of Analytical Probabilistic Modeling APM applied to artificial and clinical patient cases.

IV.1 Results of Validating a Treatment Planning System

This Chapter presents the validation results of the Matlab-based open-source TPS matRad* (Cisternas et al., 2015; Wieser et al., 2017a). Firstly, the particle dose calculation module of matRad is validated against the clinical TPS SyngoRT (Siemens, Erlangen, Germany). Secondly, the optimization module is checked for mathematical consistency and seamless communication with the IPOPT optimizer and thirdly, the performance of the implemented dose calculation and optimization code is assessed for various treatment planning scenarios. The results obtained in this Section were initially published in (Wieser et al., 2017a) and represent the groundwork for the APM implementations shown in the subsequent Section IV.2.

IV.1.1 Particle Dose Calculation Module

In the following, the reference dose cube computed with SyngoRT is referred to as Syngo dose cube (ground truth). Analog is the dose cube calculated by matRad referred to as matRad

*www.matrad.org

dose cube. The validation of the particle dose calculation module is split into two parts. First, the validation is done for protons and then for carbon ions. The former is presented next.

IV.1.1.1 Elemental Proton Pencil Beams

Here, the comparison of the SyngoRT and matRad dose cube of three different pseudo mono-energetic proton pencil beams of range 5 cm, 15 cm and 25 cm are grouped together in two separate Figures. The first Figure IV.1(a) denotes the lateral dose profile of each pencil beam at the peak position. Furthermore, the pencil beams are artificially scaled to spread the profiles for visualization. Because of that, the proton pencil beam with 5 cm reaches a dose at the peak of 2 Gy. In contrast, the deepest proton pencil beam with range 25 cm reaches a dose maximum of 0.5 Gy. It is important to mention, that a radial symmetric double Gaussian lateral beam dose profile is considered in the beam model on both platforms, SyngoRT and matRad. Thus the lateral dose is a weighted superposition of a broad Gaussian component modeling the dose halo due to strongly scattered particles and a narrow Gaussian component aiming to model the core dose around the profile's center. It was decided to plot the lateral dose profile at the peak position as this is the most sensitive region. It can be seen in Figure IV.1(a) that the lateral matRad dose is in good agreement not only in the center but also in the low dose region.

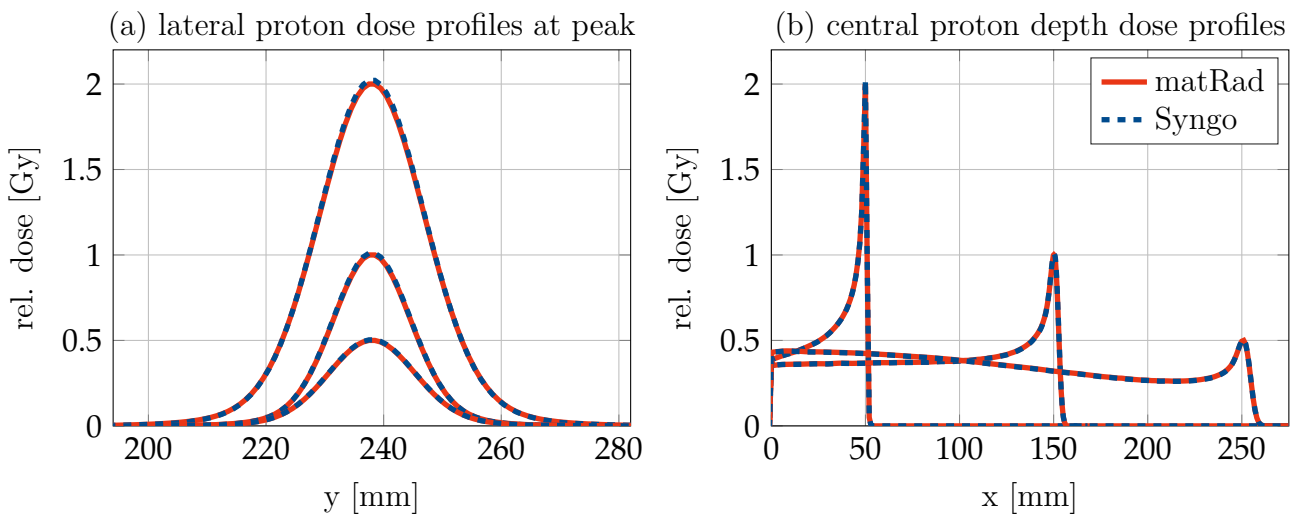


Figure IV.1: Three pseudo mono-energetic proton pencil beams for ranges 5 cm, 15 cm and 25 cm in water based on calculations in matRad (—) and the SyngoRT platform (---). All three profiles were scaled for visualization to 2, 1 and 0.5 Gy. The left plot (a) shows the lateral dose profile at the peak position while the right plot (b) shows the corresponding central depth dose profile.

Figure IV.1(b) presents the corresponding central depth dose profiles of Figure IV.1(b). Specifically, central dose profiles are shown here which reveal potential deviations in magnitude best as presenting laterally integrated depth dose profile might obscure such deviations. A good agreement between matRad and SyngoRT can be observed for the central depth dose profile quantitatively confirmed by a global γ -index of 100 % for all three dose cubes considering a DTA of 2 mm and a relative dose difference Δd of 2 %.

IV.1.1.2 Elemental Carbon Ion Pencil Beams

This section presents the validation of the carbon ion dose calculation for three elemental pseudo mono-energetic pencil beams with range 5 cm, 15 cm and 25 cm in water which is split into two parts. First, the physical dose is analyzed followed by the RBE weighted dose ($RBE \times d$).

The physical dose of the three carbon ion pencil beams, calculated on both platforms, is shown in Figure IV.2. Specifically, Figure IV.2(a) presents the lateral carbon ion dose at the peak position and Figure IV.2(b) highlights the central physical carbon ion depth dose profile. Again (—) denotes results obtained from matRad and (- - -) depicts calculations based on the SyngoRT platform.

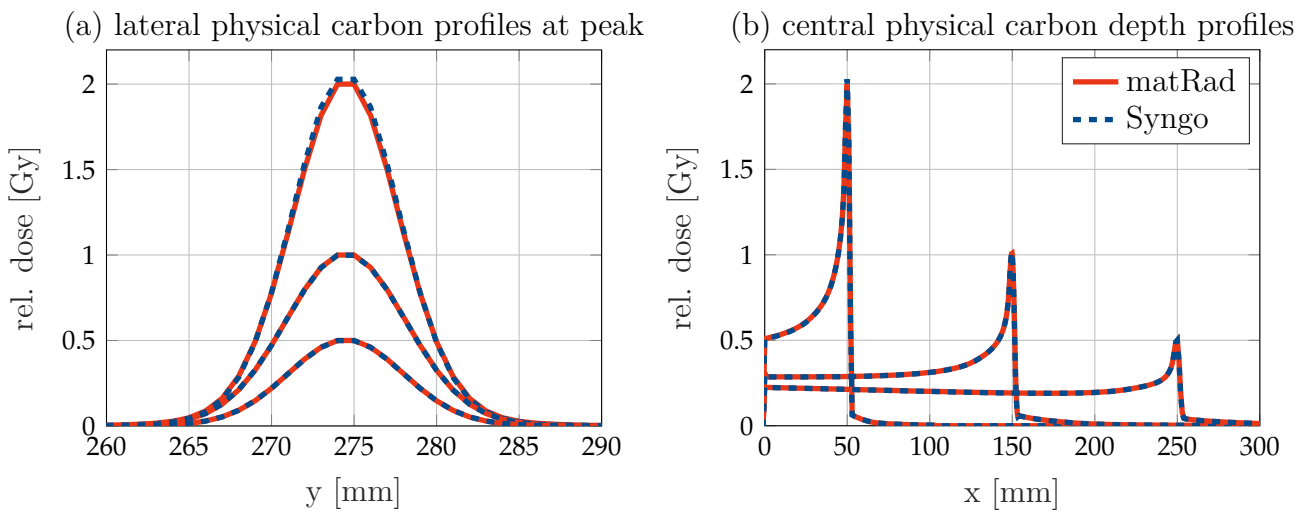


Figure IV.2: Three pseudo mono-energetic carbon ion pencil beams for ranges 5 cm, 15 cm and 25 cm in water based on calculations in matRad (—) and the SyngoRT platform (- - -). All three profiles are scaled for visualization to 2, 1 and 0.5 Gy. The left plot (a) shows the lateral carbon ion profile at the peak position whereas the right plot (b) presents the corresponding central carbon ion depth dose profile of the physical dose.

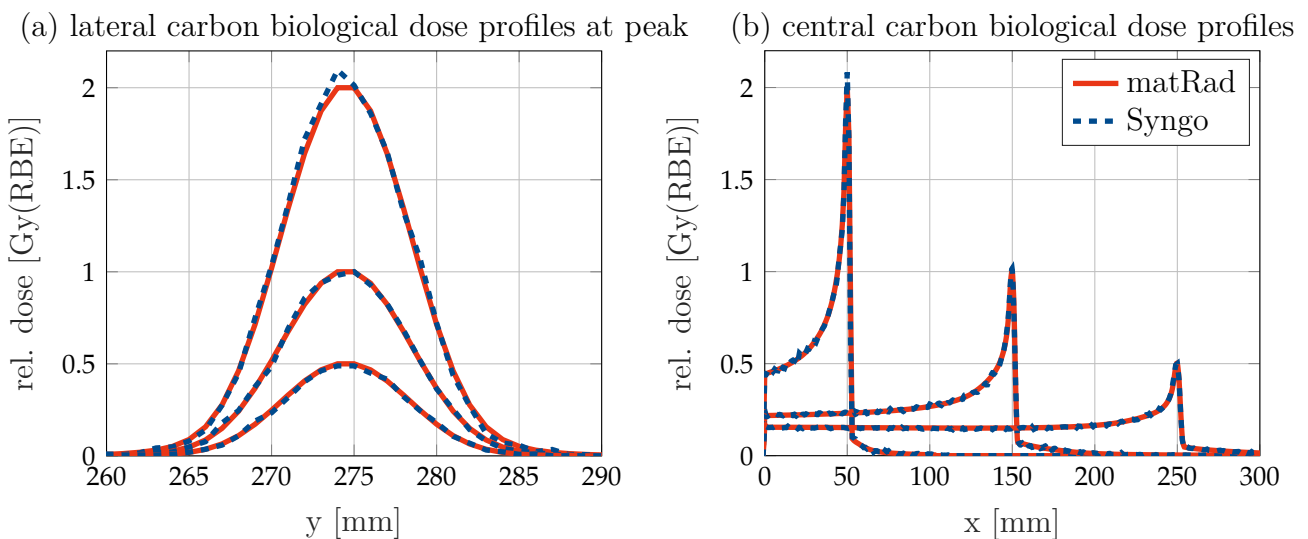


Figure IV.3: Three pseudo mono-energetic carbon ion pencil beams for ranges 5 cm, 15 cm and 25 cm in water based on calculations in matRad (—) and the SyngoRT platform (- - -). All three profiles are scaled for visualization to 2, 1 and 0.5 Gy(RBE). The left plot (a) highlights the lateral $RBE \times d$ profile at the peak position whereas the right plot (b) shows the corresponding central carbon ion depth dose profile of $RBE \times d$.

Similar to the validation of proton pencil beams also the global γ -index for carbon ions resulted in a global pass rate of 100 % for all three pencil beams using γ -criteria of (DTA=2 mm, $\Delta d = 2\%$). In a further step, the same pencil beam energies were validated for the RBE weighted dose ($RBE \times d$). Here, both platforms are based on the same LEM I data but utilize different algorithms to compute the RBE in a mixed radiation field (see Chapter II.2.3). On the one hand SyngoRT features the *full simulation* (Krämer and Scholz, 2000) and on the other hand matRad uses the *single particle approximation* (SPA) (Krämer and Scholz, 2006) which limits the dose calculation to fraction doses ≤ 10 Gy(RBE). It can be observed in Figure IV.3 that (----) encompasses statistical noise originating from the Monte Carlo component as part of the *full simulation*. Although SyngoRT was set to perform 1000 Monte Carlo loops for each calculated voxel, there were still considerable fluctuations present in the resulting dose profiles. However, the Monte Carlo fluctuations are expected to have a lower impact in a clinical setting due to averaging effects where multiple thousand pencil beams are used. Nevertheless, the profiles calculated within matRad (—) are in good agreement and 99 % of the voxels receiving dose deviate less than 0.49 %, 0.21 % and 0.19 % for the pencil beams with range 5 cm, 15 cm and 25 cm. Further, the global γ -index for (DTA=2 mm, $\Delta d = 2\%$) yielded 99.46 %, 99.93 % and 99.95 %, respectively.

IV.1.1.3 Cranial Patient

This section presents the validation result of the dose calculation module of matRad against SyngoRT for a clinical cranial case using a single beam. Detailed information about the patient case can be found in Subsection III.6.1. Figure IV.4 presents the transversal iso-center slices of the CT superimposed by transparent dose colorwash, solid iso dose lines and a black solid contour (—) denoting the PTV. The dose is given in Gy because a constant RBE of 1.1 is used which simply scales up the dose to 2 Gy(RBE). At first, no major visual difference between the matRad dose in Figure IV.4(a) and the SyngoRT dose in Figure IV.4(b) can be observed. Albeit a squared deviation objective was used for the PTV during optimization aiming to homogenize the dose, there are subtle spikes around the 2 % dose level. Interestingly, similar observations are made for the SyngoRT dose cube as well. The root cause for this phenomena traces back to SyngoRT which uses a coarser dose grid for optimization than for the dose recalculation on a finer 1 mm resolution. The finite pencil beam spacing in depth along with the coarser dose grid used for optimization explains the spikes occurring at voxel positions that are not considered during optimization.

Focusing on Figure IV.5(a) presenting the absolute difference of matRad dose slice minus SyngoRT dose slice [IV.4(a) - IV.4(b)] reveals small differences. In detail, a jagged light-blue area can be seen inside the PTV in Figure IV.4(c) indicating that matRad slightly underestimates the dose. Further, the jagged shape of the difference map points out systematic deviations in the dose calculation modules between matRad and SyngoRT. Although both dose cubes possess an identical resolution of ($x, y, z = 1$ mm), ray tracing is implemented differently. SyngoRT performs for each voxel an exact ray-tracing on the original CT reso-

lution ($x = 0.60, y = 0.60, z = 3 \text{ mm}$) while matRad establishes a hit-matrix for each ray to be traced behind the interpolated CT cube with a resolution of ($x, y, z = 1 \text{ mm}$). Both, the different resolution and the different ray-tracing techniques lead to small differences in the WEPL of each voxel and consequently to dose differences.

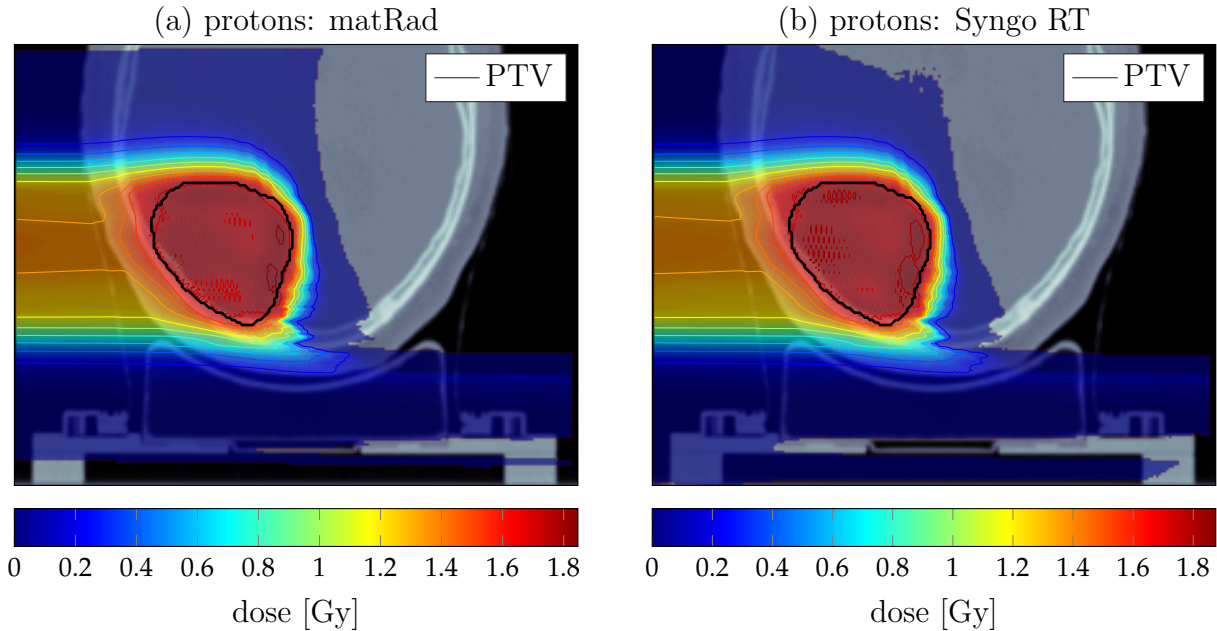


Figure IV.4: Transversal CT slices of the clinical cranial case. The CT is superimposed with transparent dose colorwash, solid iso dose lines and a solid black contour (—) denoting the PTV. The dose is given in [Gy] and originates from an intensity-modulated single beam proton therapy treatment plan with gantry angle 270° and couch angle 0° .

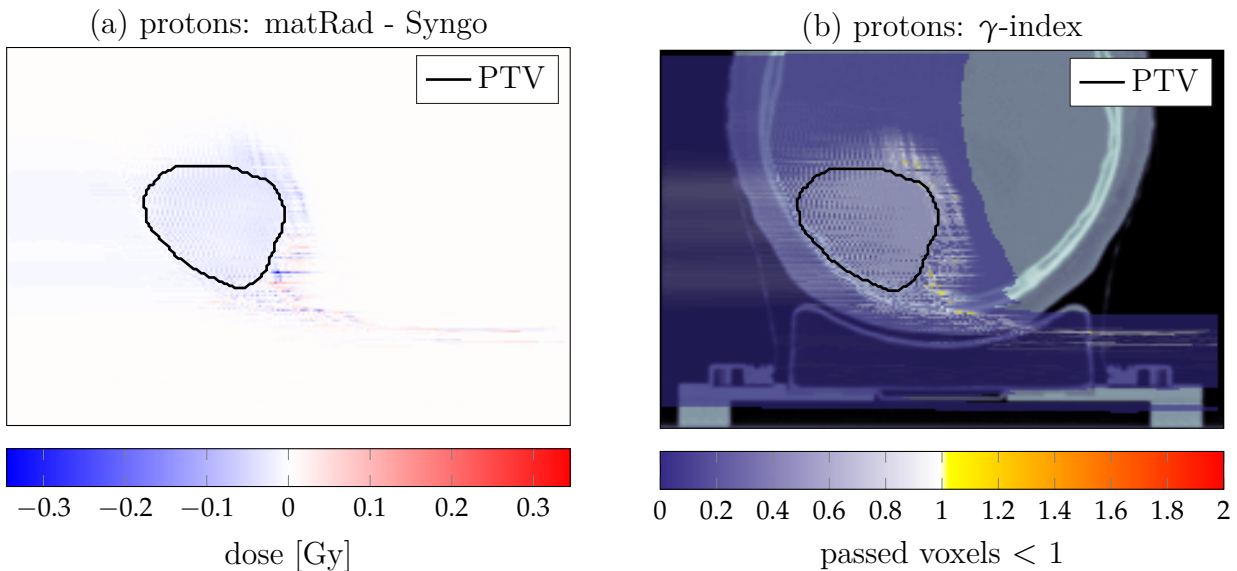


Figure IV.5: A transparent colorwash represents the absolute dose difference of the dose in Figure IV.4(a) minus the dose in Figure IV.4(b). Units are given in [Gy]. Further, (—) denotes the contour of the PTV. Figure (b) represents the global γ -analysis for the same slice using ($DTA=2 \text{ mm}, \Delta d = 2\%$). Values smaller than 1 indicate a passed γ -analysis.

Furthermore, Figure IV.5(b) presents the global γ -index in the form of a transparent colorwash. Values exceeding the value 1 indicate a violation of the tolerance levels ($DTA=2 \text{ mm}, \Delta d = 2\%$) and consequently fail the γ -analysis. It can be observed that mainly voxels in

the dose fall-off at the distal edge of the SOBP do not pass the γ -analysis. Nevertheless, considered globally, the γ -pass rate amounts to 99.84 % indicating good agreement between the dose calculation module of matRad and SyngoRT for the intensity-modulated clinical cranial proton treatment plan under investigation.

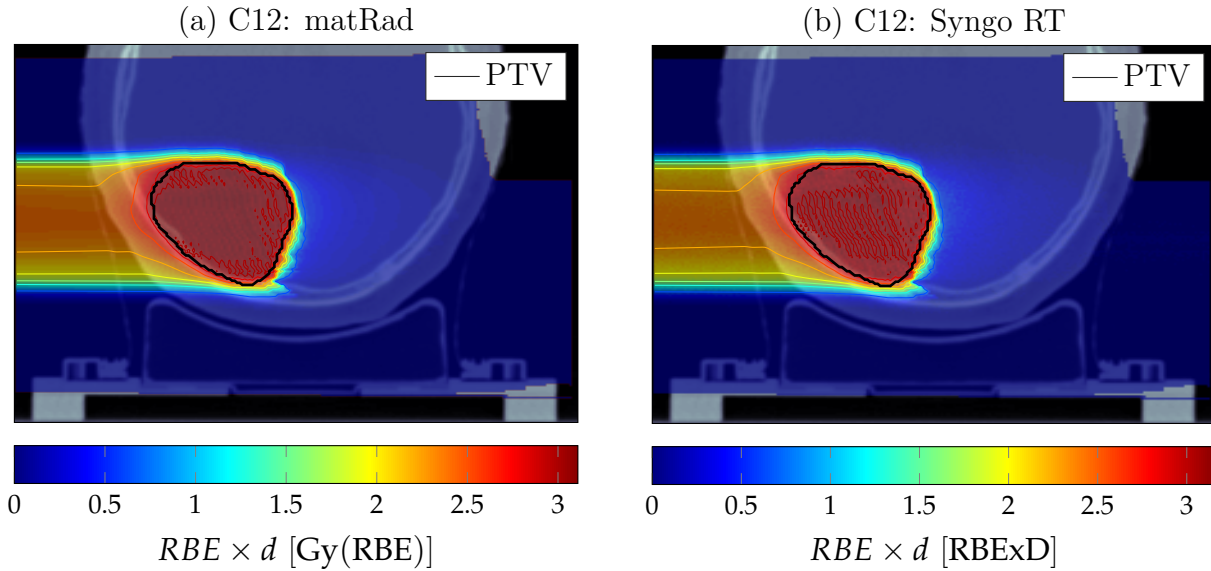


Figure IV.6: Transversal CT slices of the clinical cranial case. The CT is superimposed with transparent dose colorwash, solid iso dose lines and a black contour (—) representing the PTV. The dose is given in [Gy(RBE)] and originates from an intensity-modulated single beam carbon ion therapy treatment plan with gantry angle 270° and couch angle 0° .

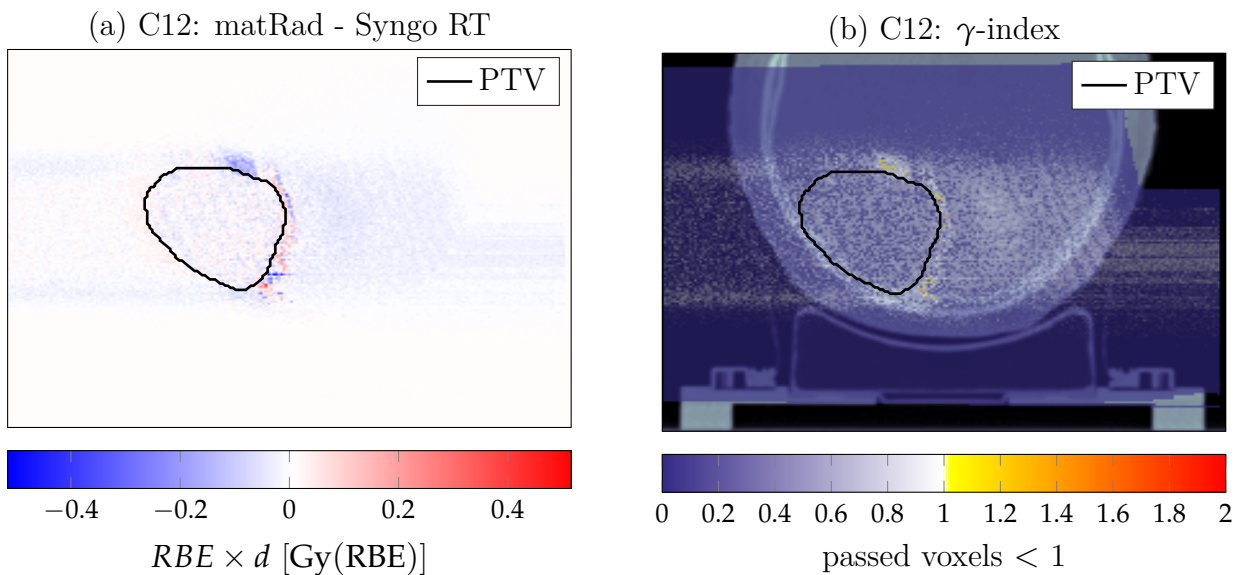


Figure IV.7: Transparent colorwash representing the absolute dose difference of the $RBE \times d$ in Figure IV.6(a) minus the $RBE \times d$ in Figure IV.6(b). Units are given in [Gy(RBE)]. Further, (—) denotes the contour of the PTV. Figure (b) represents the γ -analysis for the same slice using ($DTA=2\text{ mm}$, $\Delta d = 2\%$). Values smaller than 1 indicate a passed γ -analysis.

Figure IV.6 and Figure IV.7 highlight the validation of the carbon ion dose calculation module for the same clinical cranial case analogous to the proton validation, but this time the RBE weighted dose ($RBE \times d$) is presented. The statistical noise in the SyngoRT dose cube originating from the Monte Carlo based RBE calculation is clearly visible in the absolute dif-

ference map of matRad minus SyngoRT in Figure IV.7 (a). The statistical noise superimposes the effects of subtle spikes in the dose previously described for protons due to the coarser optimization grid and a different CT grid used for ray tracing. Similar to the result of protons, differences mainly occurred in the dose fall-off region (high negative dose gradient) but did not increase in the fragmentation tail. 90 % of voxels received dose possess a lower deviation than 1 % to the reference SyngoRT dose cube. Furthermore, the global γ -analysis revealed a pass rate of 99.67 %.

Summarized the global γ -analysis of the pseudo mono-energetic pencil beam profiles and the clinical cranial case resulted in pass rates $\geq 99.67\%$ which is considered to be accurate to implement the APM formalism on top.

IV.1.2 Optimization Validation

Figure IV.8 presents the DVH of the RBE weighted dose ($RBE \times d$) for the C-shaped TG119 phantom provided by the American Association of Physicists in Medicine Task Group 119 for IMRT commissioning. Here two intensity-modulated carbon ion beams with gantry angles 45° and 315° were defined. The treatment plan is optimized for a RBE weighted dose of 2.5 Gy(RBE) in the PTV structure. In particular, a squared deviation objective $f_{sq\ dev}$ associated with the highest priority was used for the PTV. It can be seen from the DVH in Figure IV.8 that (—) obeys this specification. Further, a squared overdosing objective $f_{sq\ over\ dosage}$

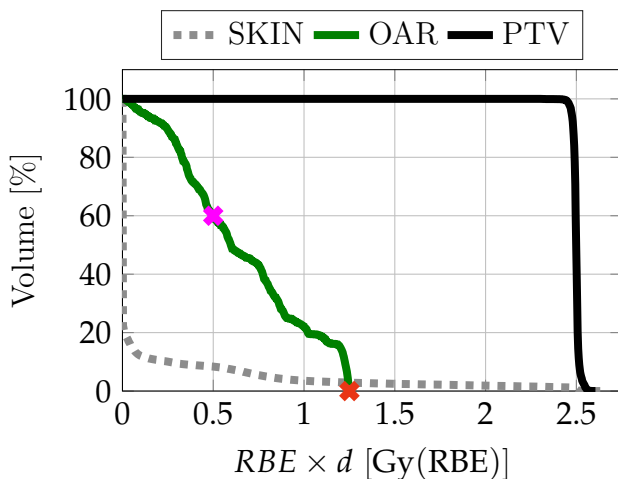


Figure IV.8: Resulting dose volume histogram (DVH) of an inversely optimized intensity-modulated carbon ion treatment plan using two beam directions for the open-source TG119 phantom. Given constraints are shown by the purple and the red cross.

was used for the OAR structure located at the distal edge of the PTV and the skin structure encompassing the whole phantom in order to reduce dose to normal tissue. The RBE weighted dose to the OAR was further limited by a maximum DVH constraint. In detail, 60 % of the OAR voxels are constrained to receive a higher dose than 0.5 Gy(RBE). The constraint is highlighted by the purple cross (\times). Moreover, a dose maximum constraint was used restricting the maximum RBE weighted dose of the OAR to 1.25 Gy(RBE). The latter constraint is indicated by the red cross (\times). The resulting DVH of the TG119 phantom in Figure

IV.8 obeys the given objectives and constraints indicating a proper communication of matRad and the IPOPT optimization interface. Validation results of the optimization module of matRad on the basis of an IMRT photon treatment plan for a head and neck patient can also be found in (Wieser et al., 2017a).

IV.1.3 Performance Analysis

To evaluate the efficiency of the dose calculation and optimization module in matRad, treatment plans for various clinical scenarios with increasing complexity were computed. Default objective functions as part of the open-source patients of matRad's codebase were utilized with standard convergence criteria given by the IPOPT options file. The resulting performance evaluation is summarized in Table IV.1. The settings column in Table IV.1 denotes, depending on the radiation modality different dose calculation settings. For protons and carbon ions the lateral cutoff is assessed during runtime and accounts for X % of the integral lateral dose on the basis of the single Gaussian (SG) or double Gaussian (DG) beam model. The dose values inside the lateral cutoff are then scaled up during dose calculation to retain the integral dose.

Table IV.1: Performance of matRad for selected treatment planning scenarios using a CT and dose grid resolution of 0.3 cm^3 . Columns from left to right show the radiation modality, X % of the integral lateral dose is fully calculated, number of bixels/pencil beams, total number of dose influence elements, storage size of dose influence data, elapsed time for dose calculation, number of optimization iterations, elapsed time for optimization and memory throughput rate per second.

| modality | setting | #beams | #bixel | D_{ij} elem. [1e6] | D_{ij} size [GB] | t_{dose} [s] | #iter. | t_{opt} [s] | throughput [GB s ⁻¹] |
|----------|------------|--------|--------|-------------------------|-----------------------|-------------------|--------|------------------|-------------------------------------|
| p | 99.75 % SG | 1 | 7797 | 19 | 0.29 | 22 | 123 | 41 | 1.78 |
| p | 99.75 % DG | 1 | 5955 | 87 | 1.38 | 46 | 171 | 109 | 4.47 |
| p | 99.75 % SG | 3 | 28097 | 56 | 0.89 | 68 | 67 | 187 | 4.90 |
| p | 99.75 % DG | 3 | 24137 | 269 | 4.30 | 160 | 262 | 330 | 6.85 |
| p | 99.75 % SG | 2 | 45574 | 116 | 1.86 | 97 | 218 | 137 | 6.13 |
| p | 99.75 % DG | 2 | 27683 | 520 | 8.33 | 299 | 197 | 486 | 6.90 |
| C12 | 99.75 % SG | 1 | 11780 | 160 | 2.55 | 67 | 72 | 92 | 3.49 |
| C12 | 99.75 % DG | 1 | 9963 | 537 | 8.61 | 203 | 79 | 225 | 5.14 |
| C12 | 99.75 % SG | 3 | 42810 | 411 | 6.68 | 310 | 117 | 193 | 6.68 |
| C12 | 99.75 % DG | 3 | 31205 | 756 | 12.1 | 560 | 107 | 365 | 6.17 |
| C12 | 99.75 % SG | 2 | 24612 | 336 | 5.88 | 137 | 177 | 273 | 5.88 |
| C12 | 99.50 % DG | 2 | 16889 | 855 | 17.94 | 472 | 134 | 521 | 5.93 |

It can be observed from Table IV.1, that treatment planning for protons and carbon ions can be done in matRad in a couple of minutes. Although the code is highly vectorized and the number of nested for-loops is reduced to a minimum, there is still a gap in performance to other radiotherapy software implemented in higher and more abstract programming languages (Siggel et al., 2012). Total run-times for particles are in the range of 63 s to 993 s thereby requiring a memory consumption of 0.29 GB to 17.94 GB. Considering matRad is entirely written in the interpreted programming language Matlab, matRad is reasonably fast taking into account the beneficial code readability and accessibility of Matlab.

IV.2 Results of Analytical Probabilistic Modeling

This Section presents the results of APM for intensity modulated carbon ion treatment planning to quantify treatment plan uncertainties. First Subsection IV.2.1 shows step by step the proof of concept of the APM formalism introduced in Chapter III on a one-dimensional phantom in water. In particular, various aspects of different uncertainty sources and uncertainty assumptions are presented. Next, Section IV.2.2 highlights results of the APM implementation in the TPS matRad and presents quantified and mitigated treatment plan uncertainties via APM for clinical patient cases alongside a validation.

IV.2.1 One dimensional Artificial Phantom

This section presents the proof of concept to quantify uncertainties in carbon ion treatment plans through APM in a one-dimensional artificial phantom in water introduced in Section III.6.2. Each of the following subsections focuses on different aspects of APM from general uncertainty quantification, over probabilistic optimization to fractionation effects. Focusing on the one-dimensional phantom, the treatment plan previously shown in Figure III.12 is referred to as nominal treatment plan which mimics clinical practice where uncertainties are only considered by the expansion of the CTV (□) to a PTV (□). This treatment plan is the starting point and used for uncertainty quantification in the following subsections.

IV.2.1.1 Uncertainty Quantification

Uncertainty quantification on the basis of APM described in Chapter III, allows deriving statistical moments of the biological effect in closed-form. First only physical, then biological and lastly both, physical and biological uncertainties were considered for uncertainty quantification. Before showing results for the last two aspects, approximations for the expectation value and standard deviation of the biological effect, derived in Sections III.2.1 and III.2.2 were verified, thereby only accounting for physical uncertainties. Parts of this Chapter were published in print in (Wieser et al., 2017b).

Physical Uncertainties Throughout this section a relative range uncertainty of 3.5% was considered. Furthermore, all pencil beams on the same ray were perfectly correlated. This means that in the one-dimensional example all pencil beams from the first beam were perfectly correlated and all pencil beams from the second beam were perfectly correlated (see Figure III.4(b) for ray-wise correlation model) and pencil beam combinations from different beams were uncorrelated. Figure IV.9 shows in (—) again the nominal biological effect ε as a reference which is identical to (—) in Figure III.12.

The consideration of range uncertainties yielded an expected biological effect $\mathbb{E}[\varepsilon]$ as indicated by (—). Because of range uncertainties, $\mathbb{E}[\varepsilon]$ is a blurred version of ε , in particular,

in high-biological-effect gradient regions. Light green crosses (\times) represent the estimated $\mathbb{E}[\varepsilon]$ based on 5000 random samples. The maximum absolute difference between the sampled and the approximated analytical $\mathbb{E}[\varepsilon]$ based on Equation III.9 amounts to 0.89 %. It is important to highlight the approximated analytical calculation of $\mathbb{E}[\varepsilon]$ was used instead of the full analytical calculation to reduce the computational complexity. Herewith, the second raw moment $\mathbb{E}[Z_i^{\beta^2}]$ calculated out of the second raw moment influence tensor $\sum_{jm} w_j w_m \Xi_{ijm}^{\beta}$ is approximated by squaring the first raw moment $(\sum_j w_j Z_{ij}^{\beta})^2$. The maximum difference for $\mathbb{E}[\varepsilon]$ based on sampling and the full analytical calculation results in 0.72 %. Knowing that estimated moments based on random sampling are affected by statistical errors, the approximations made for the expected biological effect $\mathbb{E}[\varepsilon]$ in Equation III.9 were considered to be reasonably accurate to represent the full analytical calculation in Equation III.8.

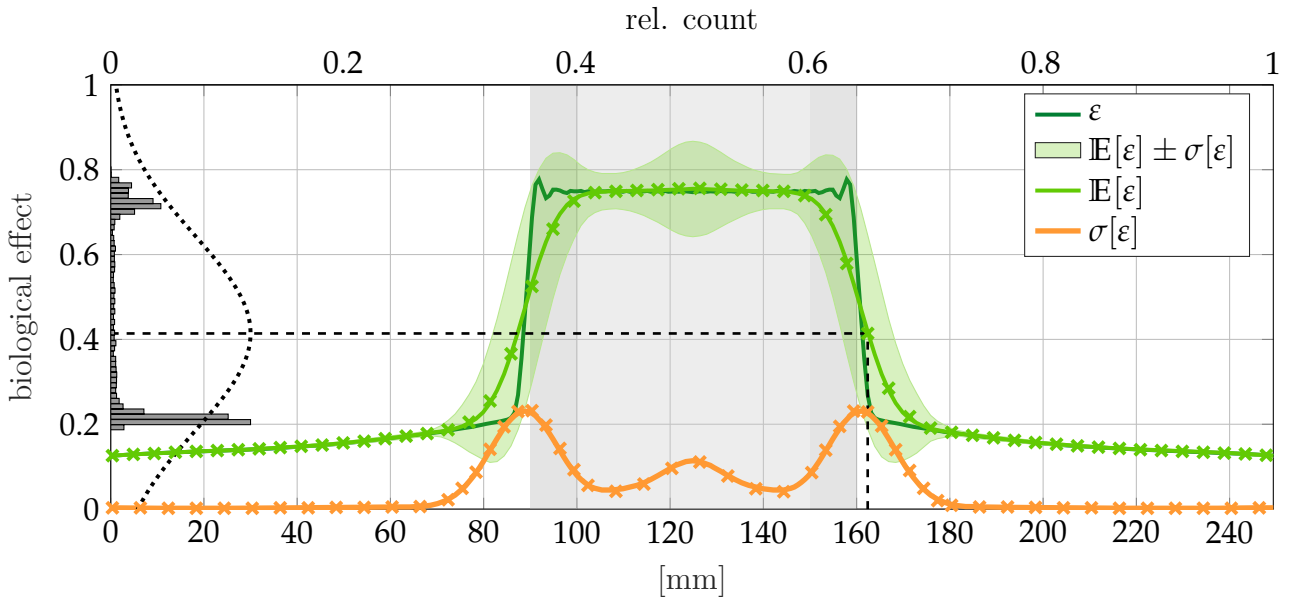


Figure IV.9: Biological effect of a one-dimensional carbon ion SOBP optimized for a $RBE \times d$ level of 3Gy(RBE) , which yields with $\alpha_x = 0.1\text{Gy}^{-1}$ and $\beta_x = 0.05\text{Gy}^{-2}$ a prescribed biological effect of 0.75. (—) denotes the nominal biological effect which is identical to (—) in Figure III.12. (—) depicts the expectation value of the biological effect $\mathbb{E}[\varepsilon]$ considering 3.5% range uncertainty and (—) represents the corresponding standard deviation $\sigma[\varepsilon]$. (—) denotes the 68% confidence level $\mathbb{E}[\varepsilon] \pm \sigma[\varepsilon]$. The histogram on the vertical axis shows the sampling result at voxel position $x = 162\text{mm}$. (.....) depicts the Gaussian approximation, which does not capture the bimodal shape of the histogram, used for error propagation to the RBE weighted dose domain. Crosses (\times, \times) represent the validation result obtained from sampling.

Further, (—) in Figure IV.9 represents the standard deviation of the biological effect $\sigma[\varepsilon]$ as described in Section III.2.2. $\sigma[\varepsilon]$ reaches its highest values at the fall-off regions of the SOBP. This becomes clear when looking at individual pencil beams in Figure III.12 where the left part of the PTV is mainly covered by pencil beams from the right beam and vice versa. Although using opposing beam directions, the plan is not robust against range uncertainties as a range under or overshoot directly results in a high standard deviation in dose fall-off regions.

Again the approximations given in Equation III.17 were used instead of the full analytical calculation shown in Equation III.16 to reduce the computational complexity. Orange crosses

(✖) indicate the $\sigma[\varepsilon]$ based on 5000 random samples and yielded a maximum relative discrepancy of 3.2 % caused by the approximations made in the squared term of the biological effect. Nonetheless, one way to increase the accuracy of the $\sigma[\varepsilon]$ -calculation is, instead of approximating, to fully calculate the third raw moment influence tensors $Y_{ijmo}^{x/y}$ and $\Xi_{ijmo}^{\alpha 2\beta}$ in Equation III.16. Herewith the maximum relative discrepancy can be minimized to 1.7 %. Performing a full analytical calculation including the fourth moment influence tensor Ξ_{ijmoq}^{β} further decreases the maximum relative discrepancy to 1.5 %.

Focusing on the voxel position $x = 162$ mm, then $\mathbb{E}[\varepsilon]$ equals 0.42 as highlighted by (----). The actual sampling distribution of ε at $x = 162$ mm is shown on the vertical axis in form of a histogram revealing a bimodal shape with standard deviation $\sigma[\varepsilon] = 0.23$. The bimodal shape of the histogram can be explained by the voxel position located in the SOBP fall-off region. Because of the high biological effect gradient, small range shifts resulted either in a high biological effect (~ 0.75) or low biological effect (~ 0.2) as indicated by the histogram bumps on the vertical axis. For the subsequent error propagation to the RBE weighted dose domain ($\mathbb{E}[RBE \times d]$, $\sigma[RBE \times d]$), however, we assume a Gaussian approximation, shown by (.....) on the vertical axis in Figure IV.9. This assumption cannot model the full bimodal shape of the underlying distribution.

To better understand the impact of the analytical approximations made for $\mathbb{E}[\varepsilon]$ and $\sigma[\varepsilon]$, the linear and a quadratic component of the biological effect ε were investigated separately next. Since lateral components $L^{x/y}$ of the biological effect were not considered, the linear component of the biological dose based on Equation III.9 is given by Z_i^α and the quadratic component by Z_i^β . Both components are highlighted individually in Figure IV.10 and their calculation is given in the title header. Their sum $\varepsilon_i = Z_i^\alpha + Z_i^\beta$ results in the biological effect (—) from Figure IV.9.

Figure IV.10 shows in addition to the nominal components Z^α (—) and Z^β (—) also the corresponding expectation value in $\mathbb{E}[Z^\alpha]$, $\mathbb{E}[Z^\beta]$ (—, —) along with the standard deviation (—) of the carbon ion treatment plan shown in the previous Figure IV.9 considering 3.5 % range uncertainty. When looking at the different scales of both plots in Figure IV.10 then it can be seen that the biological effect ε is mainly determined by the linear part (—) of the biological effect. The standard deviation of $\sigma[Z^\alpha]$ in Figure IV.10(a) is correctly calculated by APM resulting in a maximum relative deviation of 0.32 % which must be attributed to statistical uncertainties in the sampling to estimate $\sigma[Z^\alpha]$. Although $\sigma[Z^\beta]$ shows a discrepancy of up to 27 % compared to sampled references due to the approximations in the analytical calculation, the impact on $\sigma[\varepsilon]$ plays only an inferior role. Despite neglecting the interdependence of $\sigma[Z^\alpha]$ and $\sigma[Z^\beta]$ in the analytical approximations, the maximum deviation of $\sigma[\varepsilon]$ was 2.9 % proving that the linear component $\sigma[Z^\alpha]$ is the main contributing factor. Similar observations were made for a one-dimensional carbon ion SOBP treatment plan comprised of a single carbon ion beam presented in (Wieser et al., 2017b).

In a subsequent step $\mathbb{E}[\varepsilon]$ and $\sigma[\varepsilon]$ were propagated to the RBE weighted dose domain on the basis of the computation laid out in Section III.5 to obtain $\mathbb{E}[RBE \times d]$ and $\sigma[RBE \times d]$.

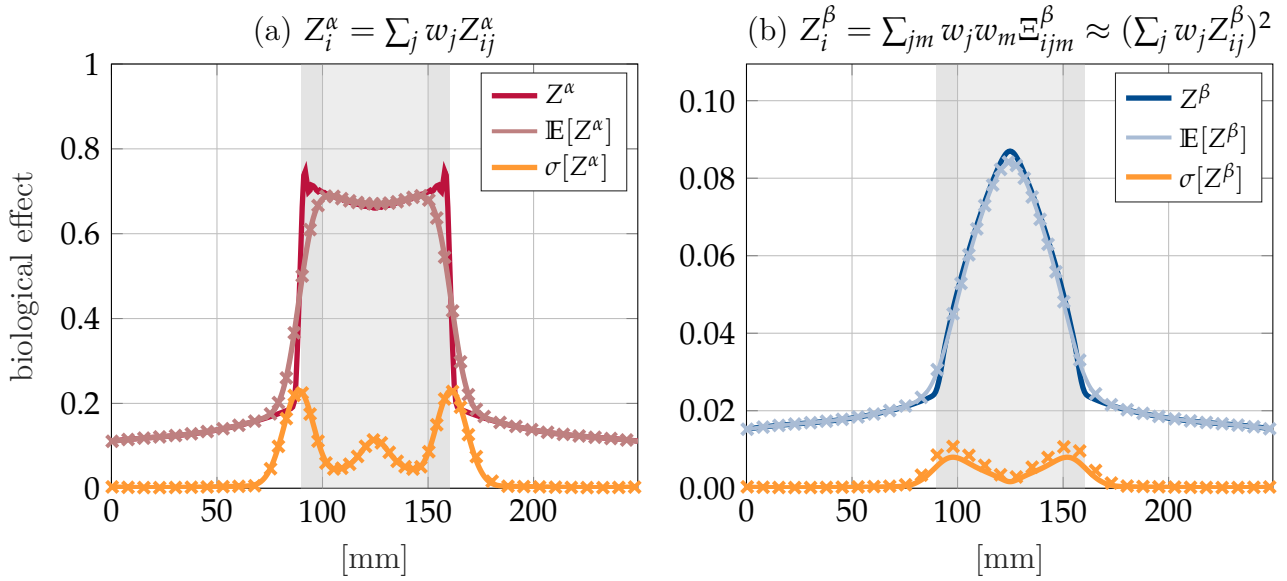


Figure IV.10: The left plot (a) shows the nominal linear component Z^α (—) of the biological effect ε (—) shown in Figures III.12 and IV.9. Correspondingly shows the right plot (b), the quadratic component Z^β . For both components the respective expectation is given in (—) and (—) and the standard deviation in (—). Crosses indicates sampled references on the basis of 5000 random samples. Due to the approximations made for $\sigma[Z^\beta]$ deviations up to 27% can be observed.

The resulting expectation value (—) and standard deviation (—) of the RBE weighted dose are presented in Figure IV.11. The statistical moments $\mathbb{E}[RBE \times d]$ and $\sigma[RBE \times d]$ calculated by means of APM were again compared to estimations based on 5000 random samples (\times, \times). The probability distribution of the RBE weighted dose at $x = 162$ mm is shown in Figure IV.11 in form of a histogram on the vertical axis.

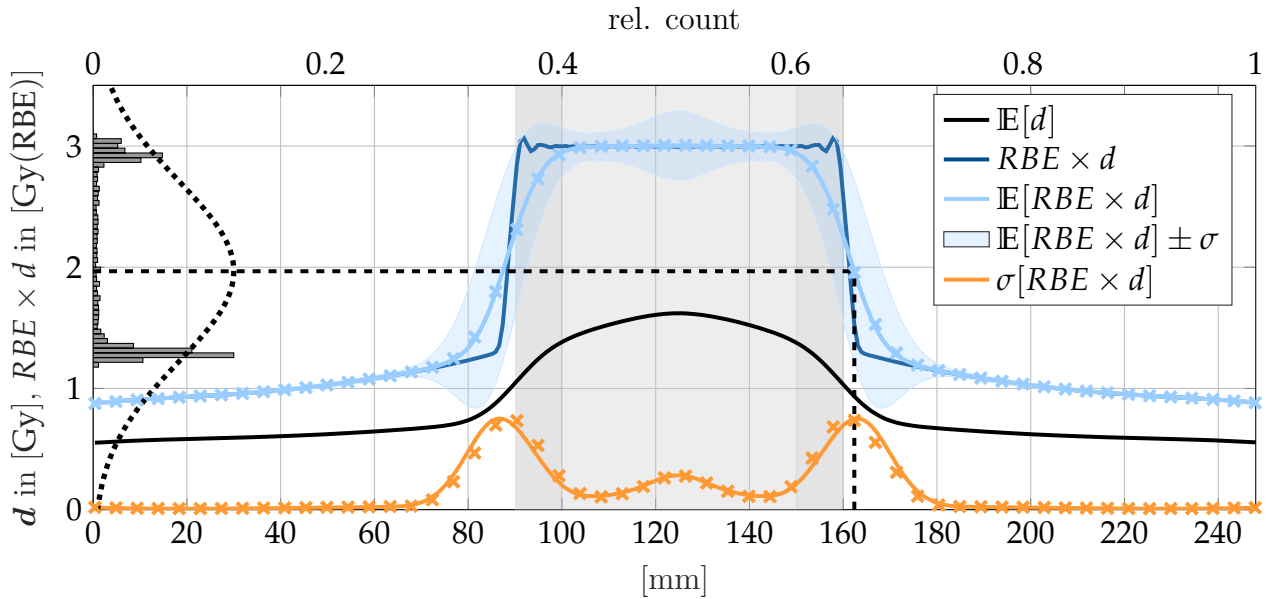


Figure IV.11: One-dimensional SOBP of two opposing carbon ion beams modelling a range uncertainty of 3.5%. The profiles are based on Figure IV.9 and present the results after propagating the statistical moments to the RBE weighted dose domain. (—) denotes the expected physical dose, (—) the nominal RBE weighted dose, (—), the expected RBE weighted dose, (—) the standard deviation of the RBE weighted dose and (—) highlights the 68% confidence limit. Crosses (\times, \times) denote sampling results.

The maximum relative difference for $\mathbb{E}[RBE \times d]$ (—) amounts to 0.96 % and a γ -analysis with (DTA=1 mm, $\Delta d = 1\%$) consequently yielded a pass rate of 100 %. In contrast, the maximum relative difference for $\sigma[RBE \times d]$ equals 13.7 % and the γ -analysis with (DTA=3 mm, $\Delta d = 3\%$) resulted in a pass rate of 99.6 %. The discrepancies for the standard deviation can also be observed in Figure IV.11 when visually comparing (—) to (✖). In particular, differences arise at locations where the standard deviation rises relative to the expectation value yielding in the error-propagation with the fourth order Taylor expansion to a decreased approximation quality of $\sigma[RBE \times d]$. As already pointed out for the standard deviation of the biological effect $\sigma[\varepsilon]$ the accuracy of $\sigma[RBE \times d]$ could in principle be increased by replacing the approximations with the full analytical expressions.

Considering the artificial and homogeneous one-dimensional phantom represents a rather extreme example with high-dose gradients, the differences in $\sigma[RBE \times d]$ (—) compared to sampled references (✖) are willingly accepted in order to keep the computational complexity low. Although opposing beam directions are considered to be a first measure to create robust treatment plans alongside simple margin extensions from the CTV to the PTV, there is still a non-negligible uncertainty present throughout the whole CTV structure (see (✖) in Figure IV.11). Thus these two approaches might not reduce dose uncertainties within the CTV sufficiently and directly motivate the application of robust/probabilistic optimization.

Biological Uncertainties So far 3.5 % range uncertainties were considered for uncertainty quantification in the previous section. In contrast, this section considers now 25 % biological uncertainty. As described in Section III.3.3 biological uncertainties were only modeled within the APM formalism in the linear $\alpha_c d$ component and are as a first approximation neglected in the quadratic component of the biological effect. Notably, random sampling accounted for a 25 % biological uncertainty in ω^α as well as independently in ω^β whereas the latter exhibited a minor to negligible impact on the resulting uncertainty in $RBE \times d$.

Moment calculations based on APM presented in Section III.3 are shown in Figure IV.12 and were compared to estimated moments grounded on 5000 random samples. Focusing on the expectation value of the RBE weighted dose $\mathbb{E}[RBE \times d]$ then it can be observed the expectation value (—) is slightly underestimated compared to the nominal $RBE \times d$ (—) due to non-linearities as pointed out in Section III.3.4. Nevertheless, sampling (•) revealed a maximum relative difference of 0.45 % and a global γ -pass rate of 100 % using (DTA=1 mm, $\Delta d = 1\%$).

Analyzing the standard deviation of the RBE weighted dose $\sigma[RBE \times d]$ resulted in a maximum relative difference of 3.9 %. Further, a γ -analysis with relaxed criteria of (DTA=3 mm, $\Delta d = 3\%$) yielded a reduced pass rate of 84.4 %, which can also be observed by visually comparing (—) and (•). The discrepancy originated from the non-linearities from Section III.3.4 and the fact that random sampling also accounted for a 25 % biological uncertainty in the quadratic component ($\sqrt{\beta_c} d$) of the biological effect which is not modeled in this first approximation of APM. Nevertheless, it can be seen that the general shape and mag-

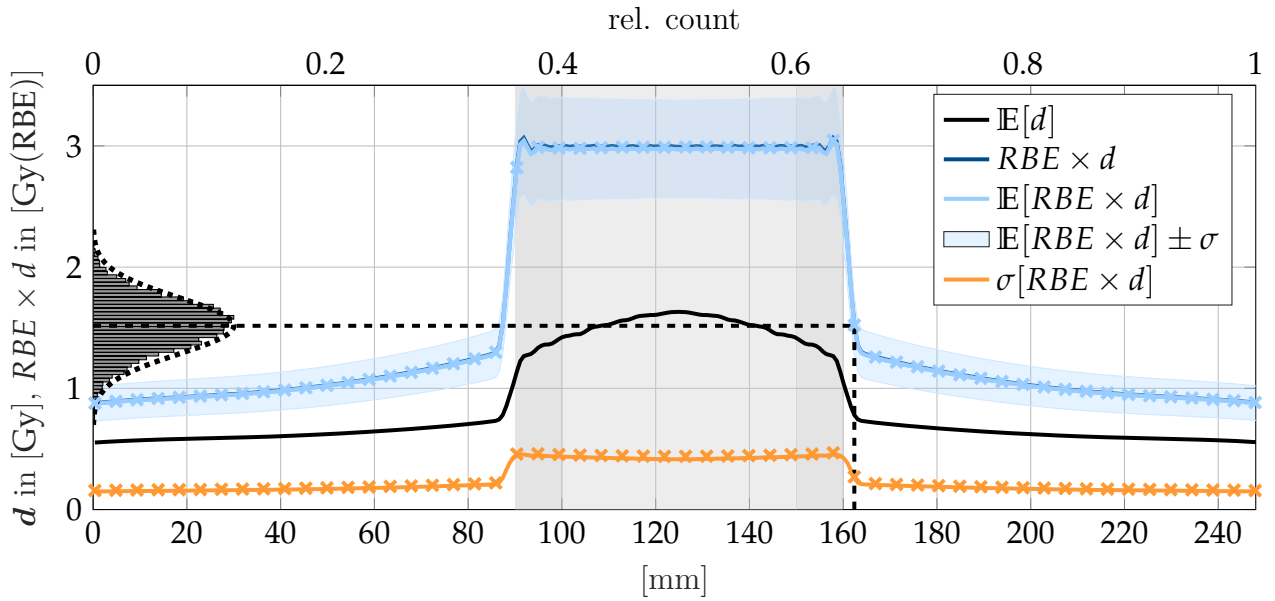


Figure IV.12: One-dimensional SOBP of two opposing carbon ion beams modeling a biological uncertainty of 25%. The profiles are based on Figure IV.9 and present the results after propagating the statistical moments to the RBE weighted dose domain. (—) denotes the expected physical dose, (—) the nominal RBE weighted dose which is in this case overlaid by the expected RBE weighted dose (—). (—) shows the standard deviation of the RBE weighted dose and (—) highlights the 68% confidence limit. Crosses (×, ×) represent sampling results.

nitude of the standard deviation of the RBE weighted dose $\sigma[RBE \times d]$ is still captured by the linear component. Performing random sampling only for the linear component of the biological effect yields a γ -pass rate of 100% using (DTA=1 mm, $\Delta d = 1\%$) proving a correct implementation.

A relative biological uncertainty assumption of 25% yields an uncertainty level of ~ 0.45 Gy(RBE) inside the PTV which equals an uncertainty of $\sim 15\%$. Similar to (Böhlen et al., 2012; Friedrich et al., 2013a), the resulting uncertainty level in a mixed-radiation field is generally lower than the initial uncertainty assumptions of the individual parameter. Further, modeling biological uncertainties via a Gaussian process in individual pencil beams induces a probability distribution over ε which is in turn of Gaussian shape due to its closure under linear combinations. This behavior is indicated by the histogram on the vertical axis which represents the sampling result of the $RBE \times d$ at voxel $x = 162$ mm.

Biological and Physical Uncertainties This section now combines the consideration of 3.5% range uncertainties together with 25% biological uncertainties. The uncertainty quantification result of the one-dimensional SOBP is presented in Figure IV.13 and indicates good agreement between the analytical expectation value $E[RBE \times d]$ (—) and sampled references (×). The maximum relative discrepancy amounts to 0.71% and a global γ -analysis with (DTA=1 mm, $\Delta d = 1\%$) yields a pass rate of 100%. However, discrepancies increase compared to sampled references (×) for the standard deviation $\sigma[RBE \times d]$ (—) indicated by a maximum relative difference of 11.5%. Furthermore, the γ -analysis reveals a pass rate of 98.89% considering the following relaxed criteria (DTA=3 mm, $\Delta d = 3\%$). The decreased

global γ -pass rate can be explained by three superimposed approximation effects. First, physical range uncertainties are only modeled in the linear component of the biological effect. Second, biological uncertainties are in turn only considered in the linear and not in the quadratic component of the biological effect. Third, the errors introduced by the error propagation using Gaussian approximations, which decreases in quality for increasing standard deviation relative to the mean.

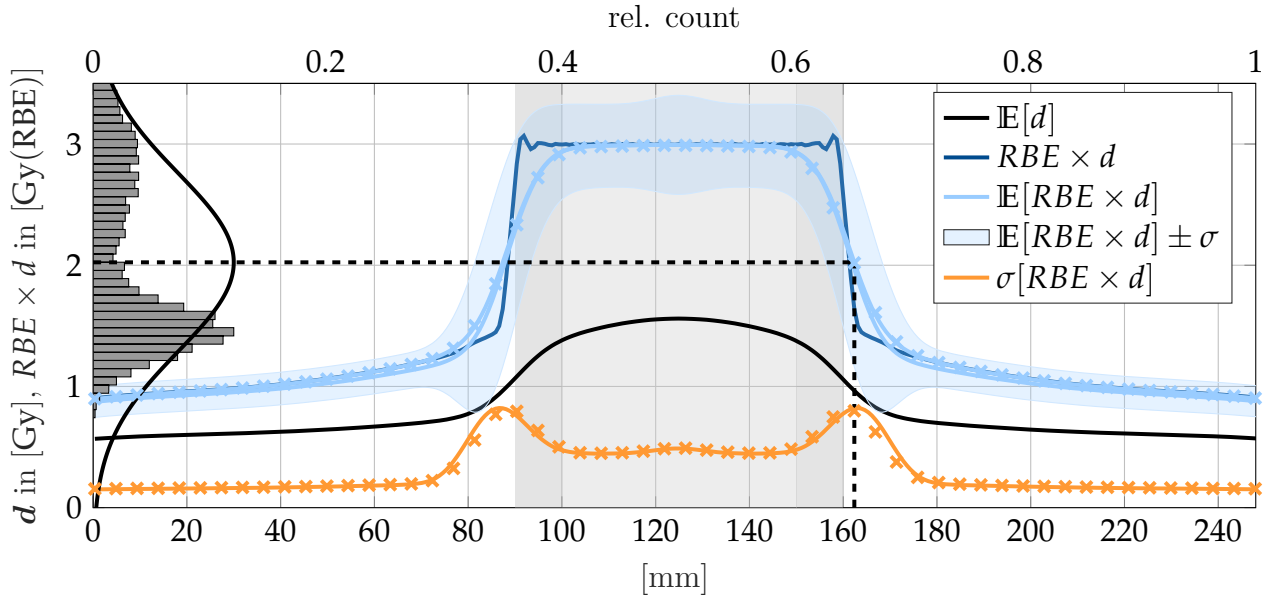


Figure IV.13: One-dimensional SOBP of two opposing carbon ion beams modelling a 3.5% range uncertainty and a biological uncertainty of 25%. The profiles are based on Figure IV.9 and present the results after propagating the statistical moments to the RBE weighted dose domain. (—) denotes the expected physical dose, (—) the nominal RBE weighted dose and (—) the expected RBE weighted dose. (—) presents the standard deviation of the RBE weighted dose and (□) highlights the 68% confidence limit. Crosses (×, ×) depict sampling results.

The discrepancies in the standard deviation of the RBE weighted dose $\sigma[RBE \times d]$ were at this point knowingly accepted in exchange for the significantly reduced computational complexity. If a higher accuracy for the uncertainty quantification is required, approximations can be replaced by full analytical calculations.

IV.2.1.2 Conventional vs. Probabilistic Optimization

By means of APM, physical and biological uncertainties can be quantified in closed-form and an integral variance influence matrix (Ω) can be calculated as laid out in Section III.4 in Equation III.47. In a further step, probabilistic optimization of the squared deviation objective can be carried out for the biological effect. In contrast to conventional optimization which uses the PTV (□) as target structure, probabilistic optimization considers throughout this work the CTV (□) as target structure if physical uncertainties are modeled. In the following, three different uncertainty assumptions were considered for probabilistic optimization to analyze their impact separately. First (i) only physical uncertainties are used for probabilistic optimization. In the second case (ii) only biological uncertainties and in the last case (iii) both physical and biological uncertainties were considered during probabilistic optimization.

Physical Uncertainties Figure IV.14(a) presents the optimization result of a conventional optimization assuming physical treatment plan uncertainties. The nominal RBE weighted dose is given in (—) and covers the PTV (□) with 3 Gy(RBE). Further, (—) denotes the physical dose, (—) the RBE, (—) individual pencil beam doses and lastly (---) presents the relative dose-averaged linear energy transfer LET. Considering now 3.5 % range uncertainty for uncertainty quantification yielded a standard deviation shown in (—). Performing a subsequent probabilistic optimization on the CTV (□) accounting for 3.5 % range uncertainties resulted in the treatment plan shown in Figure IV.14(b).

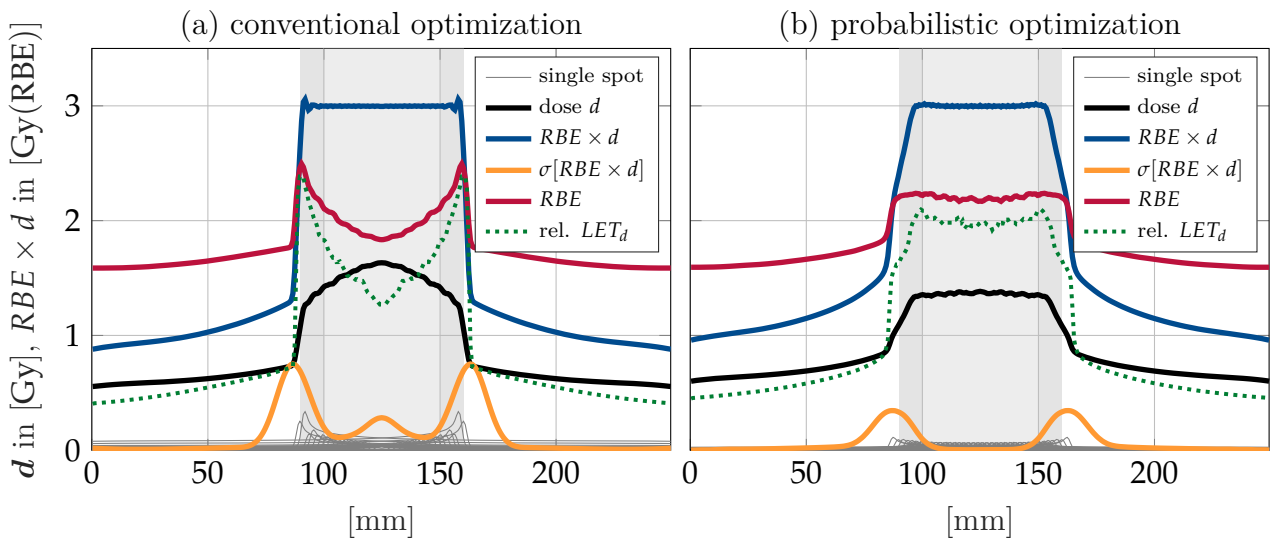


Figure IV.14: Comparison of conventional optimization shown in Figure (a) and probabilistic optimization presented in Figure (b). (—) denotes the nominal RBE weighted dose ($RBE \times d$), (—) the RBE, (—) the physical dose and (---) the relative dose-averaged LET. Moreover, (—) depicts the physical dose of individual pencil beams. Figure (a) presents in (—) the standard deviation considering 3.5 % range uncertainties from a conventional optimization. This information is then used for probabilistic optimization and Figure (b) highlights the corresponding standard deviation (—) again considering 3.5 % range uncertainties.

Several things can be observed in this Figure. First, the nominal RBE weighted dose (—) of the robust plan sufficiently covers the CTV (□) and the $RBE \times d$ -gradient of the probabilistic plan is reduced in the fall of region thereby increasing dose to the normal tissue which can be seen in the dose-level of the beam entrance. This can be understood as the price to achieve robustness. Lastly, and most interestingly the physical dose (—), the RBE (—) as well as the dose-averaged LET (---) are homogenized inside the CTV (□) during probabilistic optimization. Thus not only physical but also biological related quantities are homogenized in this beam setup indicating physical range uncertainties make the treatment plan also biologically more robust when using opposing beams.

The lines (—) in Figure IV.14 denote individual pencil beam doses and are in Figure IV.14(b) modulated to a lesser extent because of probabilistic optimization. The corresponding standard deviation of the RBE weighted dose is given by (—) in Figure IV.14(b) and shows not only reduced standard deviation bumps at the edges of the PTV but also a reduced standard deviation inside the CTV.

To better understand the impact of probabilistic optimization Figure IV.15 presents the biological effect of each beam direction from of conventional and probabilistic optimization.

The first beam enters from the left whereas the second beam impinges from the right. In conventional optimization for intensity-modulated particle therapy, it can be the case that a single beam mainly covers specific target regions. This phenomenon can be seen in Figure IV.15 in (—, —), where the distal regions of the PTV are for the most part covered by a single beam from the other side.

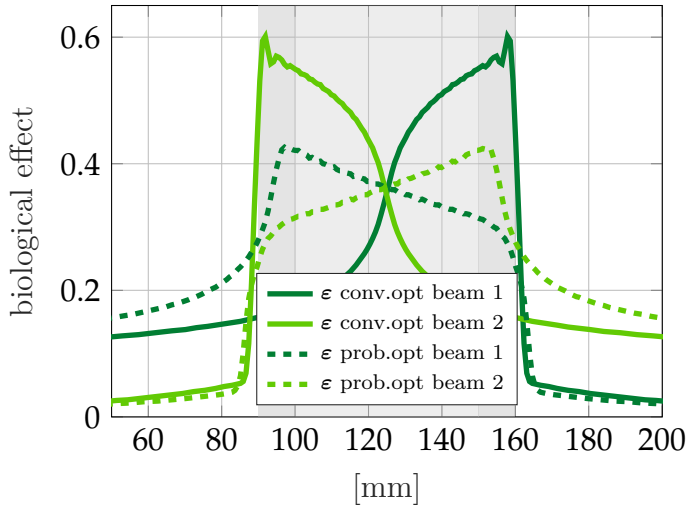


Figure IV.15: Biological effect beam contributions of conventional (—, —) and probabilistic (---, ---) optimization.

Furthermore, each beam direction covers respectively not the proximal but the distal part of the target structure. Thus, the highest RBE and LET occur in the distal region of the PTV as confirmed by Figure IV.14(a). This poses a risk for the adjacent healthy tissue when range uncertainties are present. In contrast, probabilistic optimization inverts the biological effect profiles (---, ---) and creates falling wedges with reduced steepness towards the distal edges of the target structure thereby avoiding RBE and

LET peaks in distal regions. As a result, the target structure is more evenly covered by both beams which makes the treatment plan less sensitive to range uncertainties.

Biological Uncertainties Figure IV.16 presents the impact of only considering biological uncertainties for uncertainty quantification and probabilistic optimization. Specifically, Figure IV.16(a) presents in (—) the standard deviation of the RBE weighted dose considering 25 % biological uncertainties. Incorporating this information into probabilistic optimization yields IV.16(b). It can be observed that biological uncertainties have in this opposing beam setup only a negligible impact on probabilistic optimization as indicated by almost identical dose profiles in Figure IV.16(a) and (b). This is caused by the standard deviation profile of Figure IV.16(a) which is almost constant relative to the $RBE \times d$ (—) trend inside the PTV. Hence the optimizer has no margin/leeway to reduce the standard deviation. Different to physical uncertainties this *in-silico* experiment considers the PTV as target structure for probabilistic optimization.

One additional aspect needed to be considered for probabilistic optimization including biological uncertainties which holds also for the upcoming experiments considering physical and biological uncertainties. The optimizer aims to first establish a constant biological effect of 0.75 ($=3 \text{ Gy(RBE)}$) of the expected biological effect inside the PTV and second to reduce the level of uncertainty by lowering the integral variance. Once the optimizer found pencil beam weights that sufficiently cover the target, the contribution to the objective function value becomes low, whereas the contribution from the integral variance $\mathbf{w}^T \Omega \mathbf{w}$ stays more or less

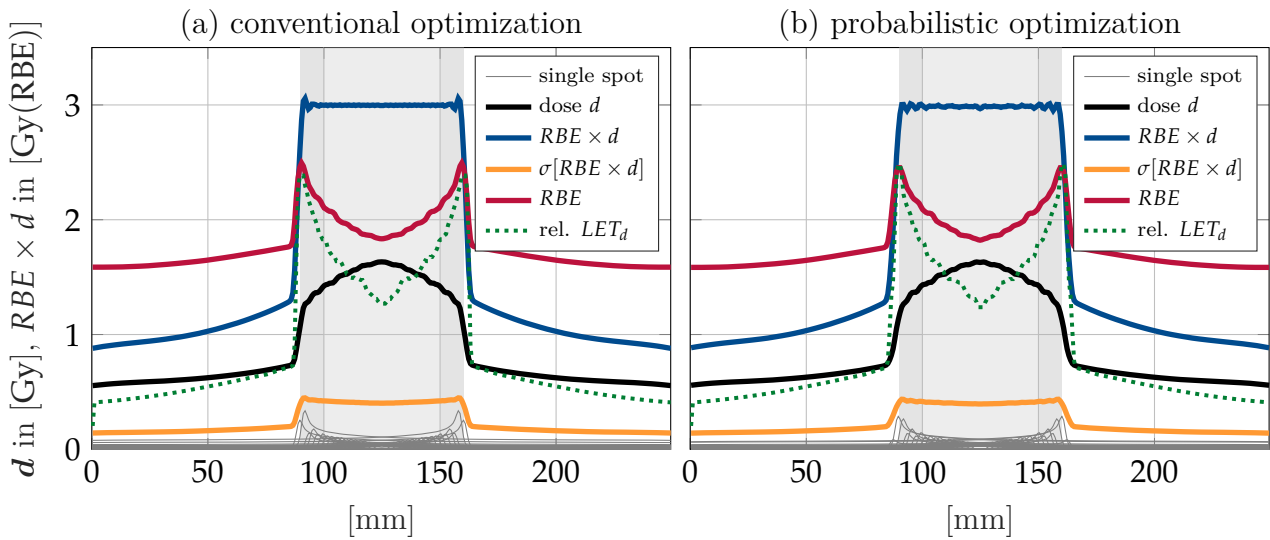


Figure IV.16: Comparison of conventional optimization shown in Figure (a) and probabilistic optimization presented in Figure (b). (—) denotes the nominal RBE weighted dose ($RBE \times d$), (—) the RBE, (—) the physical dose and (---) the relative dose-averaged LET. Furthermore, (—) depicts the physical dose of individual pencil beams. Probabilistic optimization considers in this case only 25% biological uncertainties. The corresponding standard deviation based on the conventional optimization is shown in Figure (a) by (—). Figure (b) highlights the standard deviation (—) considering 25% biological uncertainties based on probabilistic optimization.

identical. Logically the contribution from the integral variance to the total objective function value becomes relatively more important. Therefore, the optimizer aims to minimize in further iterations the integral variance which is simply achieved by lowering the dose level in the PTV. As a result, the squared deviation contribution becomes again more important until convergence is reached. In other words when the squared deviation and the integral variance generate the minimum objective function value which is for 25% biological uncertainties the case when the PTV is slightly underdosed of about 5%. To counteract against this phenomenon, a minimum mean constraint was applied on the expected biological effect for the PTV to avoid this under dose effect during probabilistic optimization. Another observation made here, is that if the penalty of the overdose objective for the normal tissue is too low and pencil beams are also defined outside of the target, the optimizer will "turn" them on to cover the tumor with the respective entrance channel of each pencil beam. Particularly, in the example of Figure IV.16 this would mean that pencil beams entering from the left would not stop around ~ 150 mm but instead around ~ 180 mm to reduce biological uncertainties in the target. This is because uncertainties are most prominent at the peak of each respective pencil beam. This topic will be further discussed at the end of this manuscript in Section V.5.

Physical and Biological Uncertainties In the last scenario, both physical and biological uncertainties are considered. The corresponding standard deviation of the RBE weighted dose (—) of a conventional optimization on the PTV is shown in Figure IV.17(a). Using the statistical moments accounting for biological and physical uncertainties for probabilistic optimization on the CTV yields Figure IV.17(b). The resulting dose profiles are similar to the ones shown in Figure IV.14(b) which only accounts for physical uncertainties for

probabilistic optimization indicating the additional consideration of biological uncertainties for probabilistic optimization has only a minor impact.

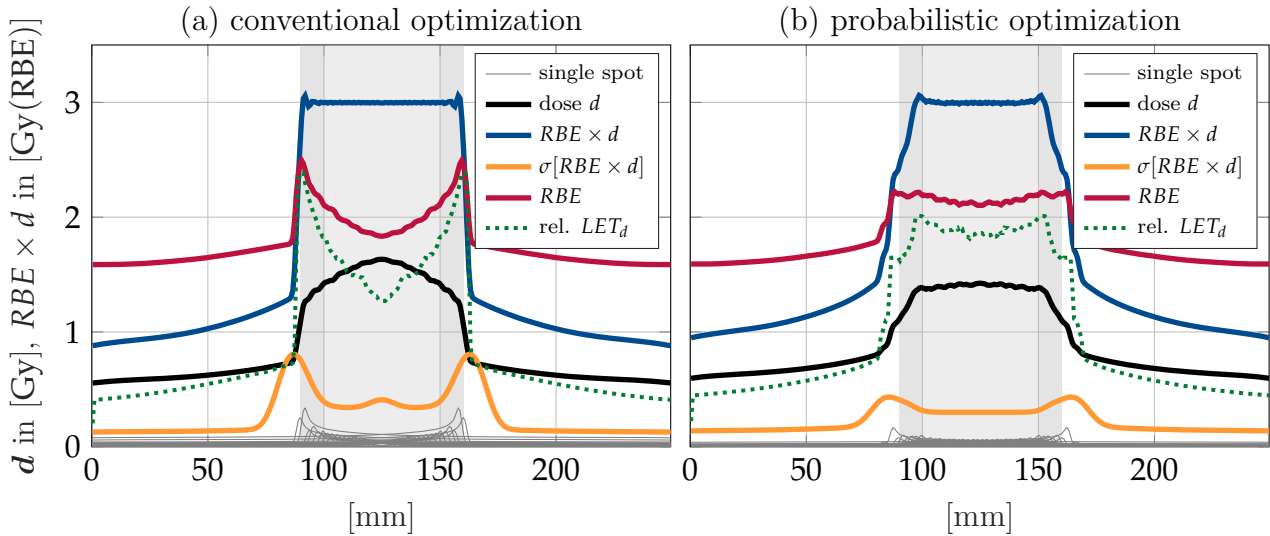


Figure IV.17: Comparison of conventional optimization shown in Figure (a) and probabilistic optimization presented in Figure (b). (—) denotes the nominal RBE weighted dose ($RBE \times d$), (—) the RBE, (—) the physical dose and (—) the relative dose-averaged LET. Furthermore, (—) depicts the physical dose of individual pencil beams. Probabilistic optimization considers in this case both, range and biological uncertainties. The corresponding standard deviation based on the conventional optimization is shown in Figure (a) by (—). Figure (b) highlights the standard deviation (—) also considering 3.5% range and 25% biological uncertainties.

Nevertheless, it can be seen in Figure IV.17 the consideration of physical and biological uncertainties also yielded a homogenization of the physical dose (—), the LET (—) and consequently the RBE (—) as it was the case for only accounting for physical uncertainties.

The last Figure IV.18 highlights a direct comparison of the impact of different sources of uncertainties on probabilistic optimization. First, (—) in Figure IV.18 denotes $\sigma[RBE \times d]$ of a conventional optimization as a reference and is identical to (—) from Figure IV.17(a). For the remaining lines in Figure IV.18 the pencil beams are probabilistically optimized considering first only biological, then only physical and lastly both uncertainties for probabilistic optimization. The robust pencil beam weights are then used to quantify treatment plan uncertainties accounting for both biological and physical uncertainties and the resulting $\sigma[RBE \times d]$ are shown in (—, —, —).

Considering biological uncertainties from Figure IV.16(a) for probabilistic optimization and then physical and biological uncertainties for uncertainty quantification yields (—). It can be seen that for the one-dimensional phantom, biological uncertainties have only a minor to negligible impact on the re-modulation of pencil beam weights as $\sigma[RBE \times d]_{bio}$ is similar to (—) from conventional optimization.

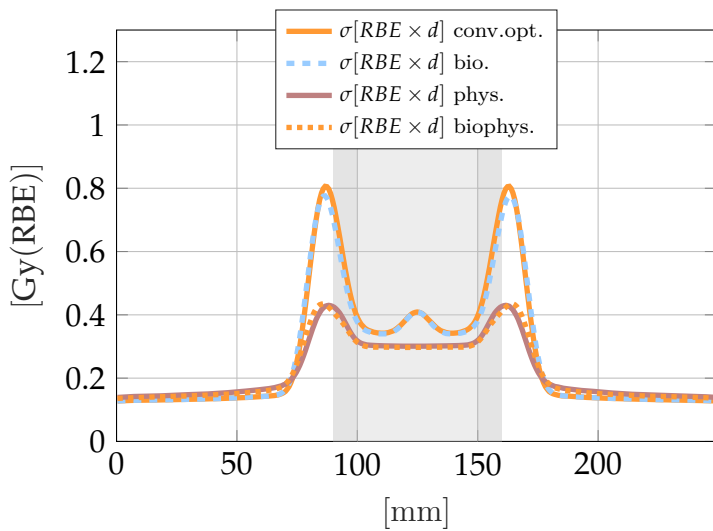


Figure IV.18: All $\sigma[RBE \times d]$ lines account for physical and biological errors for quantification. (—) shows $\sigma[RBE \times d]$ of a conventional optimization as a reference. (---) accounts only for biological uncertainties for probabilistic optimization, whereas (—) only considers physical uncertainties. Lastly (.....) uses both uncertainty sources for probabilistic optimization.

Further, (----) indicates that accounting for biological uncertainties during probabilistic optimization does not make the plan robust at all as suggested by the bumps in the PTV margin. The remaining two lines (—) and (.....) correspond to considering only physical and both physical and biological uncertainties for probabilistic optimization, respectively. The line (.....) is identical to (—) in Figure IV.17. Analyzing (—) and (.....) indicates only minor differences in the additional consideration of biological uncertainties for probabilistic optimization. Calculating the γ -index as a measure of

similarity between the standard deviation (—) and (.....) in Figure IV.18 allows quantifying the impact of additionally accounting for biological uncertainties for probabilistic optimization for this two opposing beam setup. Using the following criteria (DTA=2mm, $\Delta d = 2\%$) resulted in a global γ pass rate of 95.2% indicating good agreement between the two probabilistic optimizations. Consequently, considering additionally biological uncertainties for probabilistic optimization played in this one-dimensional example a negligible role.

IV.2.1.3 Robustness Analysis for different Probability Density Functions

As described in Chapter III.2.1 this thesis consistently works with Gaussian uncertainties, i.e., it is assumed that all unknown parameters follow a multidimensional Normal distribution. This allows then to calculate statistical moments of treatment plan quality indicators such as the biological effect in closed-form.

Figure IV.19 presents a histogram of the Gaussian range error assumption of an individual pencil beam considering $\sigma = \pm 3.5\%$ of the original pencil beam range. This section presents a comparison of uncertainty quantifications assuming each time a different PDF for random sampling. Here only physical range uncertainties are considered and the ray-wise correlation model is assumed which means for the one-dimensional phantom, range errors are

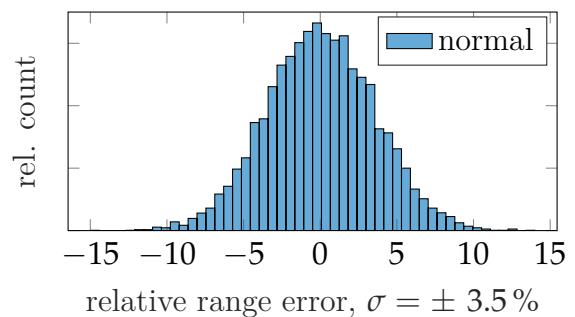


Figure IV.19: Histogram of 5000 random samples taken from a Normal distribution with $\sigma = \pm 3.5\%$

correlated within the beam but uncorrelated to the other beam direction. In particular, it is investigated if the current Gaussian range error assumption stands against other PDFs. Hence this section presents the dosimetric consequences if the current Gaussian uncertainty model is inaccurate and consequently deviates from the actual 'unknown' error distribution. Further, the comparison is performed for both conventional and a probabilistic optimization for which a normally distributed range error with $\sigma = \pm 3.5\%$ is considered for optimization.

Figure IV.20 presents different probability distributions that were tested against the Gaussian uncertainty model. To cover different types of PDFs a bitriangular (blue), a skewed (grey), a uniform (red) and a triangular (green) distribution were considered. Lastly also a Normal distribution with $\sigma = \pm 5.25\%$ was evaluated to mimic an underestimated range error during optimization.

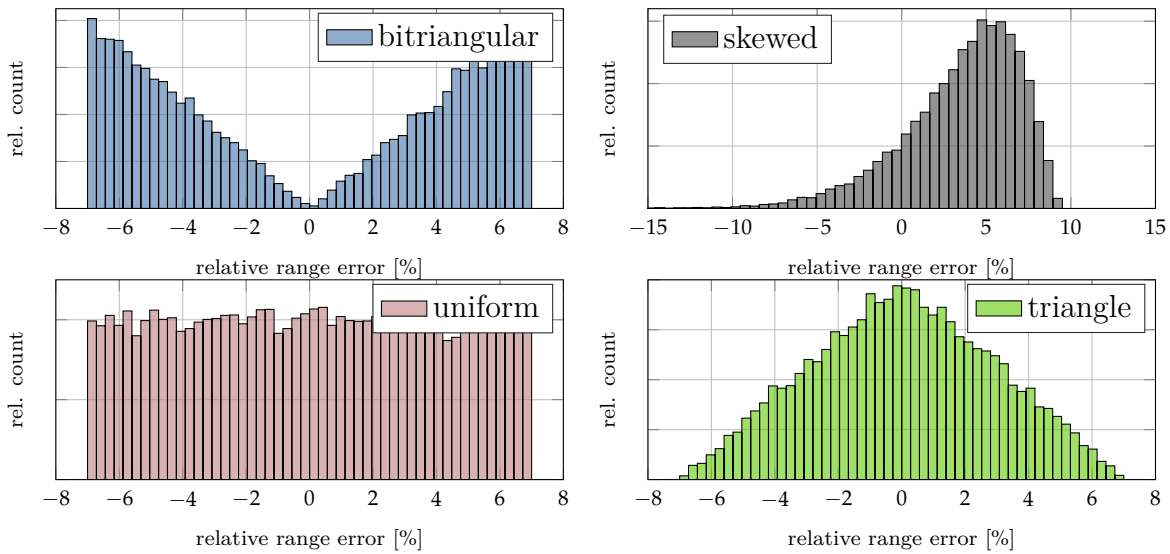


Figure IV.20: Different probability density functions used for random sampling to estimate the expectation value and standard deviation of the RBE weighted dose.

For each probability density function shown in Figure IV.20, random sampling (N=5000) was performed to estimate the corresponding expectation value and standard deviation. Afterward, the estimated moments are compared to reference moments calculated by APM assuming 3.5% normally distributed range errors.

Table IV.2: Global γ -pass rates for the expectation value (column 2 and 6) and standard deviation (column 4 and 8) of the RBE-weighted dose on basis of 5000 random samples using each time a different probability distributions. The results are compared to quantities obtained via APM using Gaussian error assumptions. A distance to agreement of 3 mm and a dose difference criteria of 3% was used for the γ -analysis. Further, the maximum relative difference (ΔE , $\Delta\sigma$) is shown to highlight the maximum discrepancy. The last row depicts results for a normal distribution with $\sigma = \pm 5.25\%$.

| PDF | conv.opt. | | | | prob.opt. | | | |
|--------------|----------------------------|------------|------------------------|----------------|----------------------------|------------|------------------------|----------------|
| | $\mathbb{E}[RBE \times d]$ | ΔE | $\sigma[RBE \times d]$ | $\Delta\sigma$ | $\mathbb{E}[RBE \times d]$ | ΔE | $\sigma[RBE \times d]$ | $\Delta\sigma$ |
| triangular | 100.00 % | 2.00 % | 72.07 % | 34.13 % | 100.00 % | 1.24 % | 88.28 % | 21.06 % |
| uniform | 100.00 % | 5.98 % | 79.27 % | 26.17 % | 100.00 % | 2.03 % | 85.58 % | 30.78 % |
| bitriangular | 89.78 % | 12.46 % | 66.96 % | 39.40 % | 100 % | 5.36 % | 56.45 % | 49.23 % |
| skewed | 67.86 % | 24.07 % | 86.48 % | 34.60 % | 92.19 % | 9.75 % | 80.18 % | 52.04 % |
| normal | 91.29 % | 7.89 % | 66.36 % | 29.74 % | 100.00 % | 3.37 % | 20.72 % | 47.22 % |

Table IV.2 summarizes results of the γ -analysis using (DTA=3 mm, $\Delta d = 3\%$) and the

maximum relative deviation (ΔE , $\Delta \sigma$). It can be seen from Table IV.2 the agreement of quantified moments is apart from the skewed distribution reasonably good.

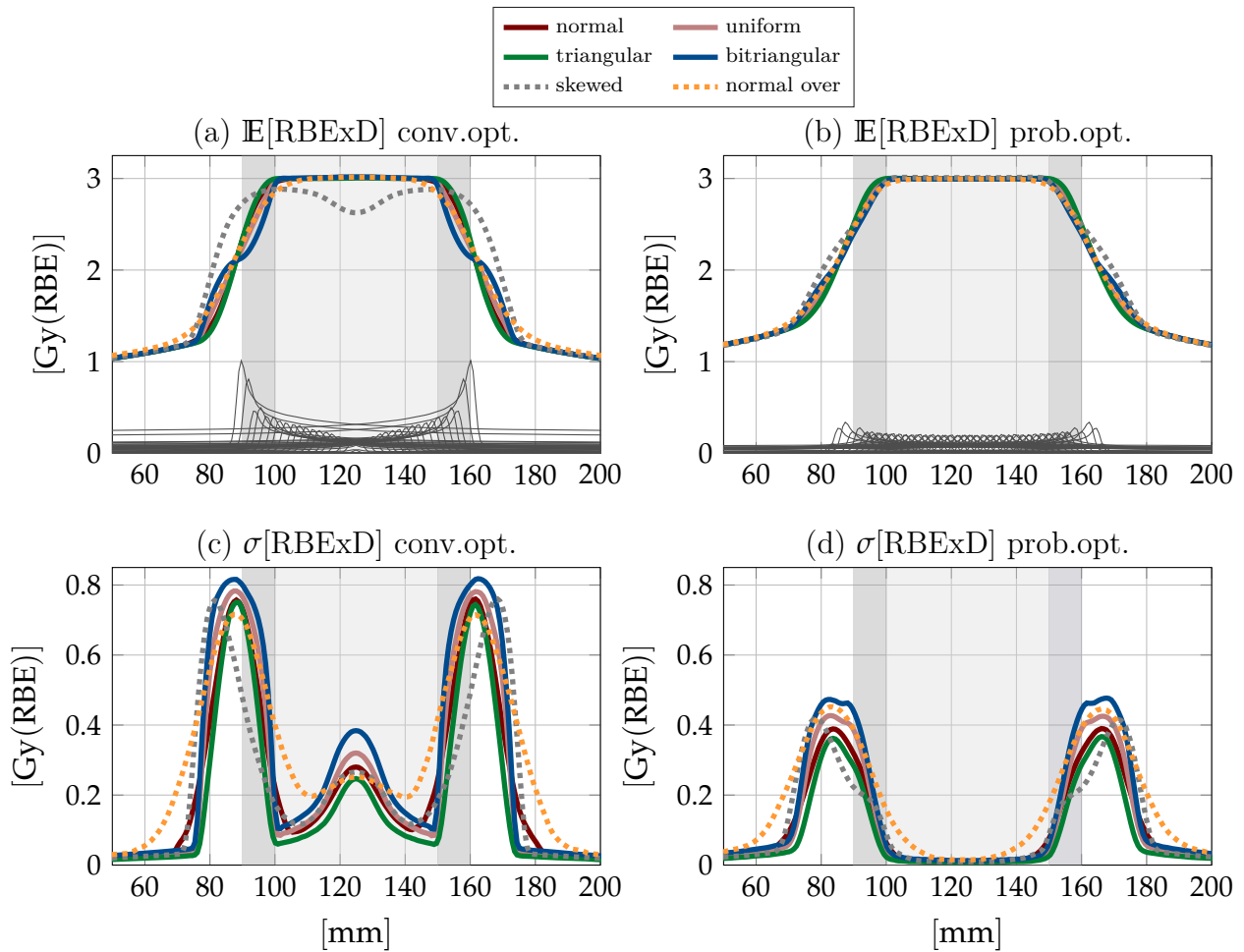


Figure IV.21: Comparison of the expectation value in (a) and (b) and standard deviation in (c) and (d) utilizing different PDFs for random sampling. Thin gray lines depict the dose of individual pencil beams. The left column shows the result of conventional optimization and the right column presents the results based on probabilistic optimization considering normally distributed range errors of 3.5%.

Additionally, Figure IV.21 provides a visual impression of the estimated expectation values and standard deviations. The reference expectation value obtained via APM is shown in the upper row by (—) and the standard deviation of the RBE weighted dose is presented in the lower row by (—). Analyzing the estimated moments (—) of the triangular distribution, it can be seen that both the expectation value and the standard deviation of conventional and probabilistic optimization are in good agreement (see also Table IV.2) to moments calculated with APM. This is because the triangular distribution possesses a similar shape to the Normal distribution. Highest probability at the center and symmetrically decreasing probability away from the center.

A similar result can be obtained for the uniform distribution, however, focusing on the bitriangular distribution the disagreement increases. The bitriangular distribution is symmetric and shows an increasing probability with greater distance to the mean. Hence, in this case, the chance is highest to either have a $\pm 7\%$ range over/undershoot. Considering the fact that the bitriangular distribution differs substantially from the Normal distribution, the discrep-

ancies of the resulting expectation value and standard deviation are moderate. Interestingly, albeit optimizing for normally distributed range errors, the resulting probabilistic treatment plan is still robust against other probability distributions as shown in the lower right plot of Figure IV.21. It can be seen, that for every PDF the standard deviation is substantially lower compared to the conventional treatment plan even if the Gaussian error assumption used for optimization is wrong.

Focusing on the only asymmetric distribution, a skewed Normal distribution where a positive range error is far more likely, the resulting expectation value of the RBE weighted dose deviates significantly for the conventional treatment plan proven by a γ -pass rate of 67.86 % and a visual comparison of (.....) in the upper left plot of Figure IV.21(a). The deviation can be explained by the asymmetric distribution as range errors are not compensated by the opposing beam. But again, performing probabilistic optimization based on normally distributed range errors, also creates a reasonable robust treatment plan for range errors obeying a skewed probability distribution. Here the corresponding γ -pass rate of the expectation value yields 92.19 %.

Looking at the estimated moments assuming a Normal distribution (.....) with $\sigma = \pm 5.25\%$ during random sampling, it can be seen that the result is logically a more washed out version of the expectation value and a higher standard deviation. This holds for conventional as well as for probabilistic optimization. Despite underestimating the range error of 1.75 % probabilistic optimization still outputs a robust treatment plan.

IV.2.1.4 Probabilistic Optimization of different LEM Versions

In this section, the clinical impact of probabilistic optimization for carbon ions using different LEM versions is demonstrated. In this *in-silico* experiment the LEM I, which is currently used clinically, is compared to recalculations using the latest successor LEM IV. First, conventional optimization without considering physical and biological uncertainties is performed to optimize a homogenous dose of 3 Gy(RBE) in the PTV from 80 mm to 170 mm. Furthermore, a tissue characterized by an $\frac{\alpha_x}{\beta_x}$ of 2 Gy with $\alpha_x = 0.1 \text{ Gy}^{-1}$ and $\beta_x = 0.05 \text{ Gy}^{-2}$ is used for the LEM I. This setup is referred to as AB2 I and was originally established for the first clinical trials at GSI[†]. AB2 I indicates a tissue characterized by $\frac{\alpha_x}{\beta_x} = 2 \text{ Gy}$ used in combination with the first version of the LEM to predict the response of charged particles. Initially, these parameters denote late toxicity in the central nervous system (Karger et al., 2006) as the endpoint, however, due to the lack of reference data at that time these parameters were and are still used for chordoma tissue. The underlying assumption is a similar biological response (Grün et al., 2012). The two different tissues used in this section are highlighted in Table IV.3. The result of the optimization is shown in Figure IV.22 by (—). The corresponding standard deviation assuming 3.5 % range and 25 % biological uncertainty is presented by (—).

[†]Helmholtz Center for Heavy Ion Research

Table IV.3: LEM parameter for two different configurations labelled as AB2 I (—) and AB2 IV (·-·-·) similar to (Grün et al., 2012).

| label | LEM version | α_x [Gy^{-1}] | β_x [Gy^{-2}] | $\frac{\alpha_x}{\beta_x}$ [Gy] | D_t [Gy] |
|----------------|-------------|---------------------------------|--------------------------------|---------------------------------|------------|
| AB2 I (—) | I | 0.1 | 0.05 | 2 | 30 |
| AB2 IV (·-·-·) | IV | 0.003 | 0.0015 | 2 | 22 |

Using the conventionally optimized pencil beam weights and considering AB2 IV as tissue for forward dose calculation results in (·-·-·). Note that AB2 IV represents the updated LEM parameter for the same endpoint. From Figure IV.22(a) it can be seen, that LEM I currently predicts a lower RBE at high LET regions, which were in this case occurring at the PTV margin. Further, higher gradients in (·-·-·) also result in a higher standard deviation (·-·-·), specifically in the distal fall-off regions.

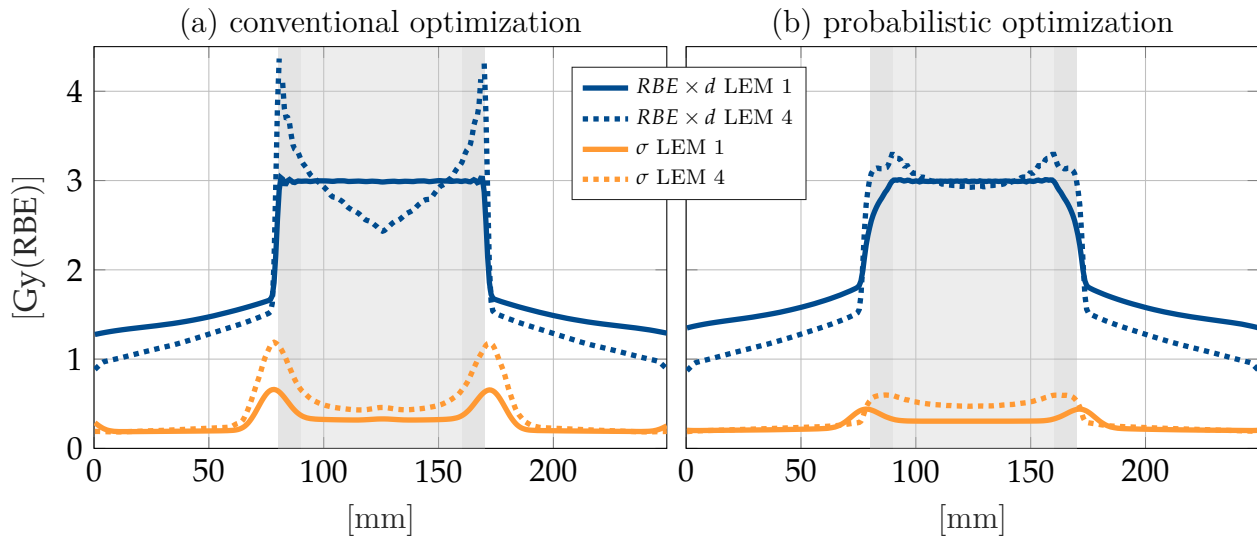


Figure IV.22: Comparison of conventional optimization shown in Figure (a) and probabilistic optimization presented in Figure (b). (—) denotes the optimized RBE weighted dose ($RBE \times d$) based on AB2 I, whereas (·-·-·) presents a forward dose calculation using instead of AB2 I, AB2 IV. Furthermore, (—) and (·-·-·) highlight the corresponding standard deviation considering 3.5% range and 25% biological uncertainties.

Performing again probabilistic optimization on the CTV considering AB2 I results in a RBE weighted dose as highlighted by (—) in Figure IV.22(b). The dose gradients in the fall-off regions are reduced and create a treatment plan with lower standard deviation. As already shown in previous Figures IV.14 and IV.17, the consideration of range uncertainties yielded a homogenization of the LET and consequently also a homogenization of the RBE when performing probabilistic optimization. This can be observed in Figure IV.22(b) for the forward dose calculation on the basis of the AB 2 IV (LEM IV) shown in (·-·-·). Due to the homogenized RBE, the RBE weighted dose (·-·-·) exhibited in the right plot only a maximum dose of 3.3 Gy(RBE) and a minimum dose inside the CTV of 2.93 Gy(RBE). In contrast, conventional optimization outputs a maximum dose of 4.3 Gy(RBE) and a minimum dose of 2.43 Gy(RBE) inside the CTV.

If we believe in the successor LEM IV, then probabilistic/robust optimization might reduce the standard deviation for LEM IV because of a more homogenous radiation quality and

consequently minimizes the discrepancy between the two model versions. Ultimately, robust/probabilistic optimization might provide a lower variability in patient outcome due to an indirect homogenization of the radiation quality.

IV.2.1.5 Fractionation

This subsection investigates the aspect of fractionation on the one-dimensional carbon ion treatment plan. In this *in-silico* experiment a systematic relative range error of $\Delta_z^{sys} = 3.5\%$, a random absolute range error of $\Delta_z^{abs} = 4$ mm and a systematic relative biological error of $\Delta_\omega^{sys} = 25\%$ were assumed. To facilitate a comparison to sampled references, a low number of fractions $F = 3$ was selected in addition to a relatively large absolute random range error of $\Delta_z^{abs} = 4$ mm to emphasis the impact of random errors on a low number of $F = 3$ fractions. Each fraction f was repeatedly sampled 250 times each time with a different random error and then summed up. In total, 100 courses of radiation treatments were sampled to capture systematic errors and to assess subsequently the expectation value and standard deviation of the total treatment. Hence, the overall number of individual samples was 75000. The treatment plan was optimized for a total dose of 9 Gy(RBE) delivered in $F = 3$ fractions. The results of APM moment calculations and estimated moments from random sampling are presented in Figure IV.23.

Similar to before, the left Figure IV.23(a) highlights the outcome of conventional optimization on the PTV and Figure IV.23(b) shows the results obtained from probabilistic optimization using the CTV as the target structure.

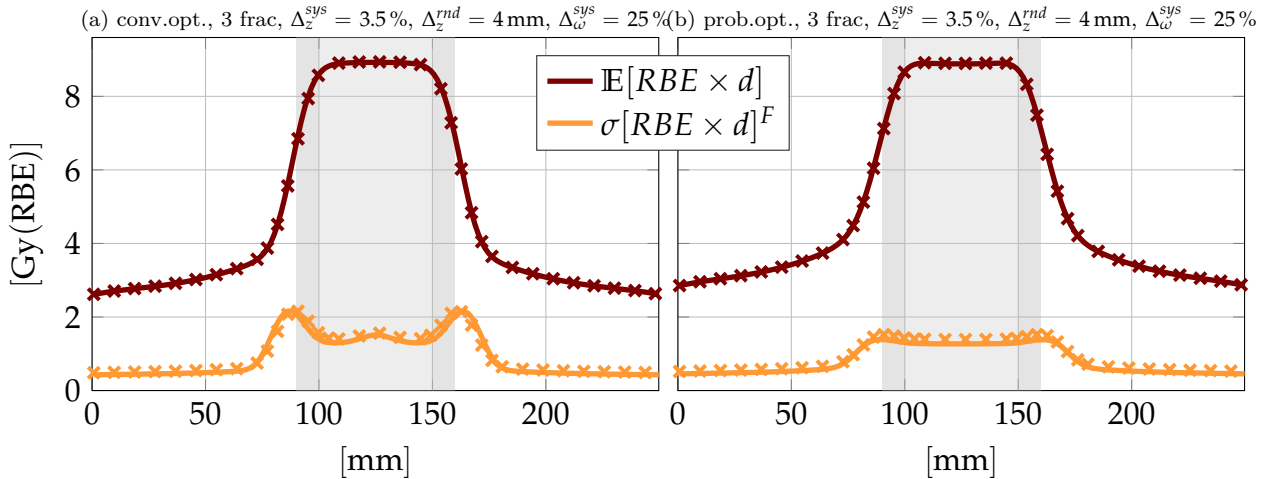


Figure IV.23: Comparison of a fractionated carbon ion treatment $F = 3$ for conventional optimization shown in Figure (a) and probabilistic optimization presented in Figure (b). (—) denotes the optimized expected RBE weighted dose ($\mathbb{E}[RBE \times d]$) divided by factor three. The line (—) indicates the standard deviation of RBE weighted dose ($\sigma[RBE \times d]^F$). Crosses highlight estimated moments based on references. This scenario models a systematic relative range uncertainty of $\Delta_z^{sys} = 3.5\%$, a random absolute range uncertainty of $\Delta_z^{abs} = 4$ mm and systematic relative biological uncertainty of $\Delta_\omega^{sys} = 25\%$. Crosses (×, ×) indicate an excerpt from the reference result obtained from sampling.

It can be seen from Figure IV.23 for both conventional and probabilistic optimization that the expectation value (—) is visually in good agreement to sampled references (×). This

is confirmed by a maximum relative difference of 1.03 % and 0.22 % as well as by global γ -pass rates of 100 % in both cases using (DTA=1 mm, $\Delta d = 1$ %). In Figure IV.23 denotes (—) the analytical and (✖) the sampled standard deviation assuming $F = 3$ fractions. The analytical $\sigma[RBE \times d]^F$ was calculated on the basis of Equations III.31 and III.32 in the method Section III.2.4. Very similar to previous *in-silico* experiments, the agreement to sampled references decreases for the standard deviation where the maximum relative difference amounts to 12.3 % for conventional optimization and to 6.5 % for probabilistic optimization. Consequently the γ -pass rate with relaxed criteria of (DTA=3 mm, $\Delta d = 3$ %) yields to 94.0 % and to 97.6 %.

The discrepancy in the analytically calculated standard deviation of the RBE weighted dose (—) to the estimated standard deviation (✖) from sampling can be explained by the approximations made in the quadratic term of the biological effect in the respective calculation to account for physical and biological uncertainties. In addition, errors introduced by the moment propagation to the RBE weighted dose domain and the sampling error itself superimpose errors introduced by the approximations. Despite differences between (—) and (✖) in Figure IV.23 the primary trend and characteristic of the uncertainty in the total RBE weighted dose can still be captured via APM.

IV.2.2 Implementation of APM in a validated Treatment Planning System

In the previous section, different aspects of APM were investigated on a one-dimensional treatment plan. Building on this, the implementation and functionality of the APM formalism in the three-dimensional TPS matRad is presented here. First, Subsection IV.2.2.1 presents the uncertainty quantification in form of statistical moments of the RBE weighted dose of three carbon ion therapy treatment cases considering physical uncertainties. Further, APM based moment calculations were compared to estimated moments obtained from sampling using the γ -analysis. Lastly, the impact of probabilistic optimization is analyzed.

Subsection IV.2.2.2 presents a comprehensive analysis of various carbon ion treatment planning scenarios, however, this time considering biological and physical treatment planning uncertainties simultaneously.

IV.2.2.1 Proof of concept - physical uncertainties

This section presents the expectation value (= first raw moment) and the standard deviation (= second central moment) of the RBE weighted dose calculated by the APM formalism presented in Chapter III of three carbon ion treatment plans based on conventional optimization (conv.opt.). The three patient cases were introduced along with plan parameters in Table III.2. The physical range uncertainty was modelled via $\sigma_z^{sys} = 3.5$ %, $\sigma_z^{rnd} = 1$ mm and the physical lateral positioning uncertainty was defined to be $\sigma_{lat}^{sys} = 1$ mm, $\sigma_{lat}^{rnd} = 2$ mm. In this

first evaluation, which was initially published in (Wieser et al., 2017b) biological uncertainties were not considered.

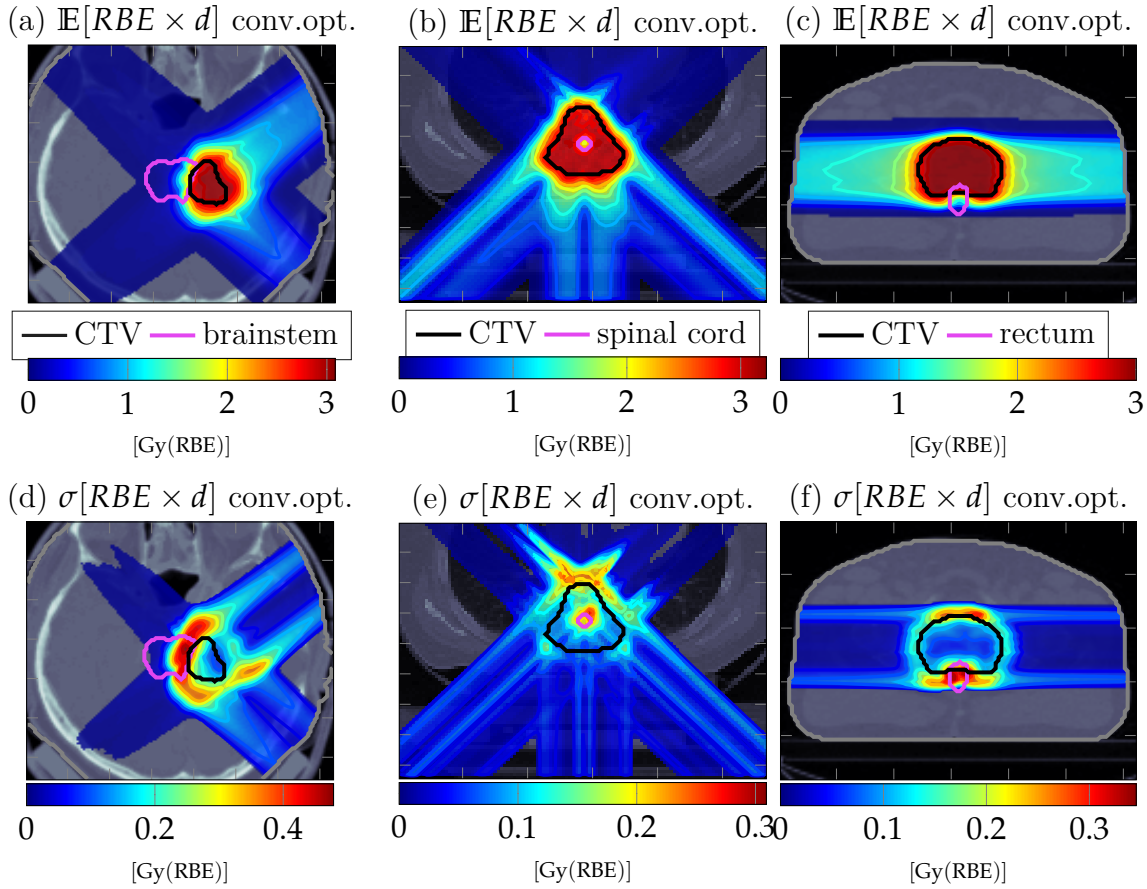


Figure IV.24: Transversal slices at iso-center of three scanned carbon ion therapy treatment plans as defined in Table III.2. For the standard deviation calculation a different number of fraction were assumed each time ($f=1,5$ and 20). The CT image is overlaid with transparent dose colorwash, solid isodose lines and contours. Plots in the upper row (a), (b) and (c) represent the expected RBE weighted dose ($\mathbb{E}[RBE \times d]$) assuming physical range and physical lateral errors. The corresponding standard deviation ($\sigma[RBE \times d]$) of these conventionally optimized treatment plans are shown in the lower row in (d), (e) and (f). (Wieser et al., 2017b)

The expected dose for the intra-cranial, para-spinal and prostate case are shown in the upper row in Figure IV.24(a), (b) and (c). The black contour (—) indicates the CTV in each scenario while the pink contour (—) denotes the organ at risk - brainstem, spinal cord, and rectum, respectively. It can be seen from Figure IV.24 that because of physical uncertainties the expectation value of the RBE weighted dose ($\mathbb{E}[RBE \times d]$) may locally drop in the CTV below the prescribed dose of 3 Gy(RBE) , especially in distal regions.

The lower row (d), (e) and (f) of Figure IV.24 presents the corresponding standard deviation of the RBE weighted dose ($\sigma[RBE \times d]$). To reduce the computation time, $\sigma[RBE \times d]$ is only calculated for voxels possessing an expectation value $\mathbb{E}[RBE \times d]$ greater than 1% of the global maximum dose. By this means $\sigma[RBE \times d]$ was not calculated in low dose regions.

Focusing on the intra-cranial case in Figure IV.24(a) and (d), which is comprised of two beam directions, one can observe the $\sigma[RBE \times d]$ becomes highest in the brainstem located at the distal edge of the CTV. For the spinal case irradiated with three beams, peaks in $\sigma[RBE \times d]$ can not only be seen in distal regions but also inside the CTV around the spinal

cord. As carbon ion pencil beams stop directly before the spinal cord, they cause an increased standard deviation at this location. For the prostate case with the two opposing beams setup, $\sigma[RBE \times d]$ becomes highest in the lateral dose fall-off regions resulting in a peaked standard deviation of 0.35 Gy(RBE) in the rectum.

As shown by Figure IV.24 carbon ion treatment plan uncertainties can be quantified using APM formalism assuming various fractionation schemes. The next section investigates the accuracy of the quantified moments.

Validation via random sampling This section compares analytical moment calculations of the RBE weighted dose of the three patient cases, shown in the previous Section IV.2.2.1, against estimated moments from 5000 random samples. The similarity between analytical and estimated moments was quantified using the global γ -analysis with the following criteria: (DTA=2 mm, $\Delta d = 2\%$). The comparison was based on a single fractionated treatment and assumes physical setup and physical range uncertainties and does not account for biological uncertainties. Further, the comparison was carried out for moments based on two sets of pencil beam weights translating to two different fluences. The first set stemmed from conventional and the second one originated from probabilistic optimization. The results are presented in Table IV.4 and provide analysis not only for the RBE weighted dose but also for the biological effect. This allows establishing the impact of the approximations due to the error propagation from moments of the biological effect to moments of the RBE weighted dose presented in Chapter III.5.

Table IV.4: Global γ -pass rates for the expectation value and standard deviation of the biological effect (ε) and RBE-weighted dose ($RBE \times d$) obtained from APM and estimations based on random sampling (5000 samples). Three patient cases (intra-cranial, para-spinal, prostate) are under investigation assuming a single fraction. The abbreviation conv.opt indicates conventional optimization whereas prob.opt. denotes probabilistic optimization. A distance to agreement of 2 mm and a dose difference criteria of 2% was used for the γ -analysis. (Wieser et al., 2017b)

| case | resolution [mm] | conv.opt. | | prob.opt. | |
|---------------|---------------------------|----------------------------|------------------------|----------------------------|------------------------|
| | | $\mathbb{E}[\varepsilon]$ | $\sigma[\varepsilon]$ | $\mathbb{E}[\varepsilon]$ | $\sigma[\varepsilon]$ |
| intra-cranial | $1.1 \times 1.1 \times 3$ | 100 % | 99.88 % | 100 % | 99.82 % |
| paraspinal | $3 \times 3 \times 3$ | 99.71 % | 97.56 % | 99.98 % | 98.30 % |
| prostate | $3 \times 3 \times 3$ | 100 % | 99.41 % | 99.49 % | 98.70 % |
| | | $\mathbb{E}[RBE \times d]$ | $\sigma[RBE \times d]$ | $\mathbb{E}[RBE \times d]$ | $\sigma[RBE \times d]$ |
| intra-cranial | $1.1 \times 1.1 \times 3$ | 100 % | 98.82 % | 100 % | 99.44 % |
| paraspinal | $3 \times 3 \times 3$ | 99.99 % | 94.95 % | 99.15 % | 96.28 % |
| prostate | $3 \times 3 \times 3$ | 100 % | 98.76 % | 97.63 % | 97.56 % |

Table IV.4 indicates generally good agreement between APM results and sampled references which is justified by global γ -pass rates of $\geq 94.95\%$. Similar to the one-dimensional phantom previously investigated, pass rates are consistently higher for the expectation value $\mathbb{E}[\cdot]$ than for the corresponding standard deviation $\sigma[\cdot]$. In addition, Table IV.4 indicates that due to the moment propagation to the RBE weighted dose domain, the agreement of the standard deviation of the RBE weighted dose $\sigma[RBE \times d]$ is mainly lower compared to the standard

deviation of the biological effect $\sigma[\varepsilon]$. Nevertheless, the accuracy of moments in the RBE weighted dose domain $\sigma[RBE \times d]$ is still reasonably accurate compared to moments based on a relatively large number of 5000 random samples.

Probabilistic optimization The ultimate goal of probabilistic optimization is to create a treatment plan that is less sensitive to treatment planning uncertainties. To demonstrate this for the three carbon ion therapy treatment plans shown previously in Figure IV.24, Figure IV.25 presents the corresponding SDDVH based on conventional biological effect based optimization without considering uncertainties by solid lines. In contrast, probabilistic optimization of the expected squared difference of the biological effect considering uncertainties is given by dotted lines. Here, only physical uncertainties are considered for uncertainty quantification and probabilistic optimization.

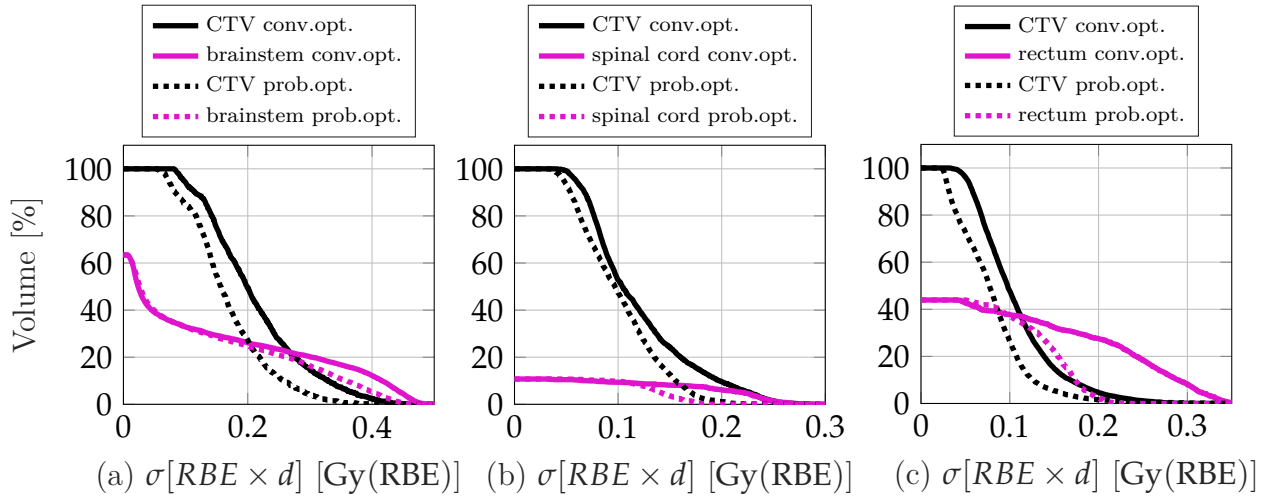


Figure IV.25: Standard deviation RBE weighted dose volume histograms (SDDVH) for the intra-cranial case assuming 1 fraction, the para-spinal case assuming 5 fraction, and the prostate case assuming 30 fractions. Solid lines (—, —) represent the results obtained from conventional optimization (conv.opt.) and dashed lines are based on probabilistic optimization (prob.opt.). Solid lines corresponding the standard deviations shown in Figures IV.24(d)-(f)

From Figure IV.24 it can be seen for all three patient cases that probabilistic optimization reduces not only the standard deviation inside the CTV (· · · ·) compared to conventional optimization (—) but also for the organ at risk as indicated by (· · · ·). The dose uncertainty for specific VOIs in Figure IV.25 provides comprehensive information on the treatment plan robustness. Ultimately the treatment planner can create patient- and uncertainty-specific robust carbon ion therapy treatment plans that are less sensitive to physical uncertainties.

IV.2.2.2 Proof of concept - biological and physical uncertainties

This section presents carbon ion therapy treatment plans modeling uncertainties with $\sigma_z^{sys} = 3.5\%$, $\sigma_z^{rnd} = 1$ mm, lateral positioning uncertainties via $\sigma_{lat}^{sys} = 1$ mm, $\sigma_{lat}^{rnd} = 2$ mm and biological uncertainties by $\sigma[\omega_\alpha^{sys}] = 25\%$ for different beam configurations under fractionation ($F = 20$) if not explicitly stated otherwise. Each case is analyzed individually hereafter for conventional and probabilistic optimization on the basis of the expected objective func-

tion value of the squared deviation between the target effect and the prescribed effect as introduced in Section III.4.

Single beam setup - liver For the single beam configuration, a liver patient case is presented. The carbon ion liver treatment plan is comprised of a single beam impinging from a gantry angle of 300° . The corresponding couch angle is 0° . The treatment plan was conventionally optimized on the PTV using a squared deviation objective. Figure IV.26(a) presents the expected RBE weighted dose ($\mathbb{E}[RBE \times d]$) considering the aforementioned physical and biological uncertainties. Next, Figure IV.26(b) presents the standard deviation of the RBE weighted dose ($\sigma[RBE \times d]$) of only considering physical uncertainties (physUCT) applied in 20 fractions. Complementary presents IV.26(c) the $\sigma[RBE \times d]$ of exclusively accounting for biological uncertainties (bioUCT) which introduce a significant level of uncertainty in the carbon ion treatment plan. Identical to the one-dimensional treatment plan and findings reported in (Böhlen et al., 2012; Friedrich et al., 2013a), the biological uncertainty level is generally damped in a mixed-radiation field compared to the initial uncertainty assumptions of 25%. Lastly, Figure IV.26(d) highlights $\sigma[RBE \times d]$ considering both physical and biological uncertainties (biophysUCT) simultaneously.

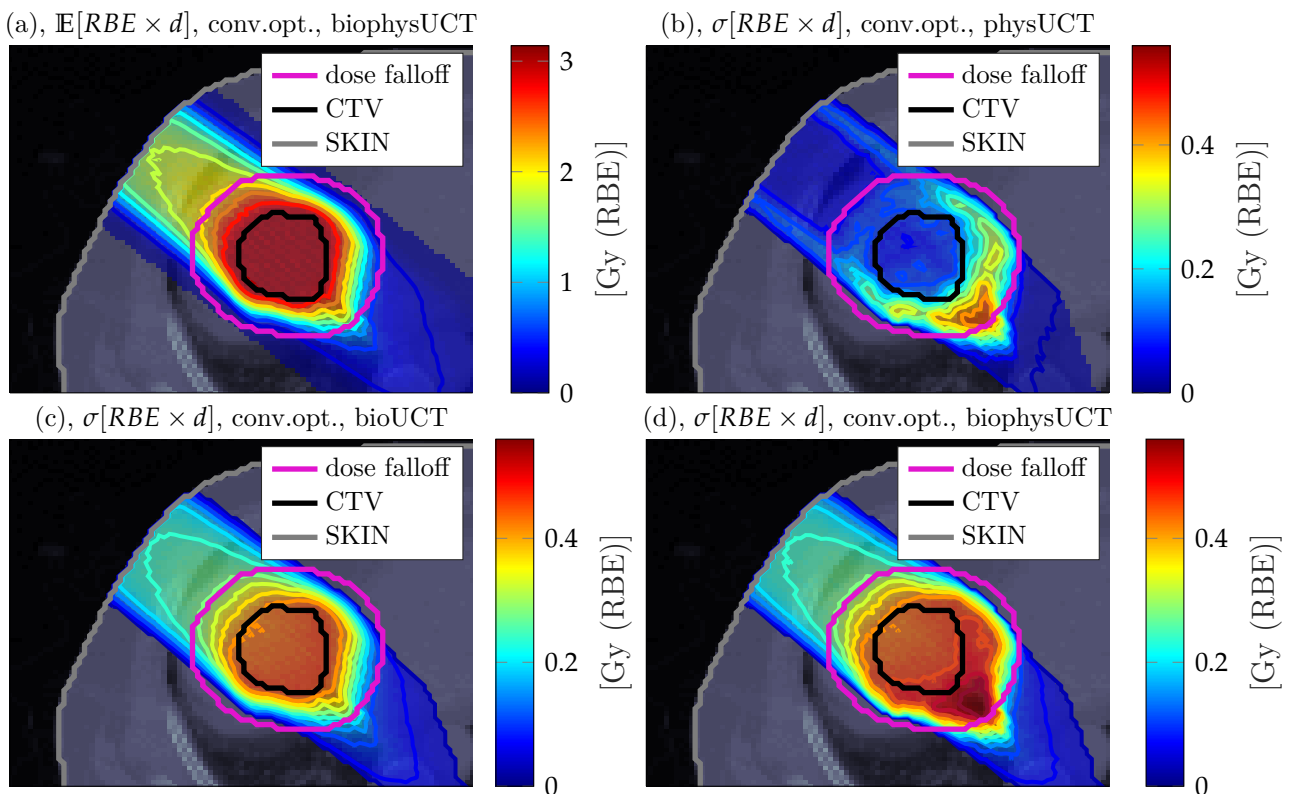


Figure IV.26: Uncertainty quantification of a liver treatment plan on the basis of conventional optimization. The transversal CT image is superimposed by transparent dose colorwash, solid iso-dose lines and solid contours. Figure (a) shows the expected RBE weighted dose ($\mathbb{E}[RBE \times d]$) assuming biological and physical uncertainties (biophysUCT). Figure (b) shows the uncertainty in the RBE weighted dose originating from physical uncertainties (physUCT) whereas Figure(c) highlights the uncertainty in dose stemming from biological uncertainties (bioUCT). Figure (d) shows the uncertainty ($\sigma[RBE \times d]$) of the combined consideration of physical and biological uncertainties (biophysUCT).

Figure IV.26(b) reveals $\sigma[RBE \times d]$ increases towards the distal edge of the dose falloff

structure (—) and reaches a maximum value of 0.44 Gy(RBE) on this slice. The mean $\sigma[RBE \times d]$ value inside the CTV (—) is notably low with a value of 0.08 Gy(RBE). Biological uncertainties shown in Figure IV.26(c) induced uncertainty in the RBE weighted dose that is marginally increasing towards the distal edge of the CTV (—) thereby revealing a similar trend as the RBE or the LET distribution which is not shown here. A maximum value of 0.44 Gy(RBE) is reached for $\sigma[RBE \times d]$, whereas the mean uncertainty in dose is raised to 0.43 Gy(RBE). Despite assuming a relative biological uncertainty of 25 %, the resulting uncertainty level only amounts to 16 %. The combined consideration of physical and biological uncertainties further elevates $\sigma[RBE \times d]$ and causes biological uncertainties from Figure IV.26(b) to also spread longitudinally in the depth due to range uncertainties. The maximum value of $\sigma[RBE \times d]$ in IV.26(d) is 0.55 Gy(RBE) and the mean $\sigma[RBE \times d]$ equals 0.46 Gy(RBE).

Comparing $\mathbb{E}[RBE \times d]$ from Figure IV.26(a) and $\sigma[RBE \times d]$ from Figure IV.26(d) to sampled references results in global γ -pass rates of 99.98 % and 98.78 %.

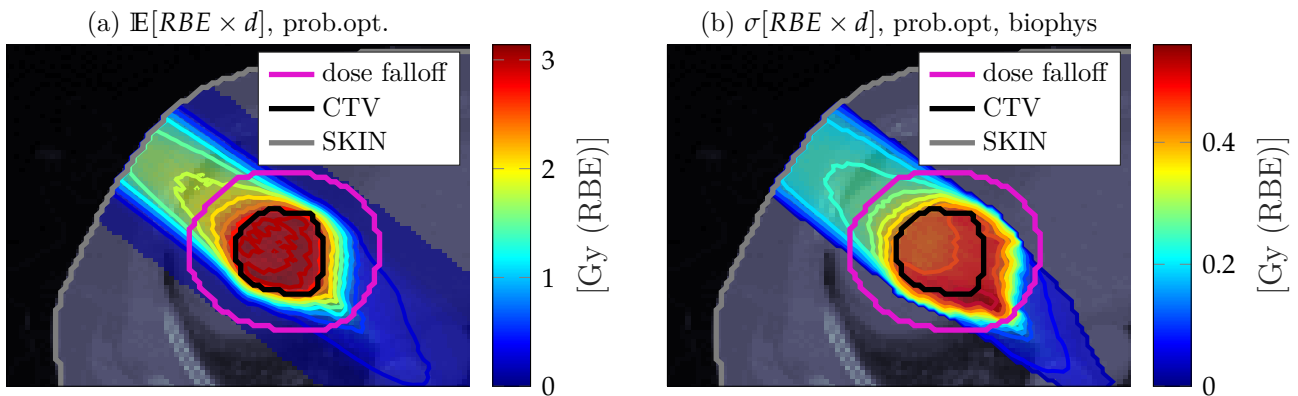


Figure IV.27: Transversal CT image with transparent dose colorwash, solid contours and solid isodose lines represent the expected RBE weighted dose after probabilistic optimization in Figure (a) and the corresponding standard deviation in Figure (b). The probabilistic optimization is done on the CTV and not on the PTV accounting for biological and physical uncertainties (biophysUCT).

Performing a probabilistic biological effect based optimization accounting for physical uncertainties on the CTV using the expected squared deviation objective according to Section III.4 yields Figure IV.27. In detail, Figure IV.27(a) presents the $\mathbb{E}[RBE \times d]$ and IV.27(b) highlights the corresponding uncertainty in dose by means of $\sigma[RBE \times d]$. Focusing on Figure IV.27(a) then it can be seen, that parts of the CTV receive a higher $\mathbb{E}[RBE \times d]$ than 3 Gy(RBE) which is confirmed by the Expected RBE weighted Dose Volume Histogram (EDVH) presented in Figure IV.28(a). Here $\mathbb{E}[RBE \times d]$ and $\sigma[RBE \times d]$ from a conventional optimization (—, —) are compared to probabilistic optimization (- - - -, - - - -). Further, through probabilistic optimization the mean of the expected RBE inside the CTV was increased from 2.17 to 2.33.

Focusing on Figure IV.26(d) and Figure IV.27(b) then it can be seen that probabilistic optimization on the CTV reduces the integral dose and the uncertainty in dose significantly in the dose fall-off structure compared to conventional optimization on the PTV. In particular, the mean uncertainty in the dose fall-off structure is reduced from 0.30 Gy(RBE) to 0.20 Gy(RBE).

This phenomenon is confirmed by the corresponding SDDVH presented in IV.28(b).

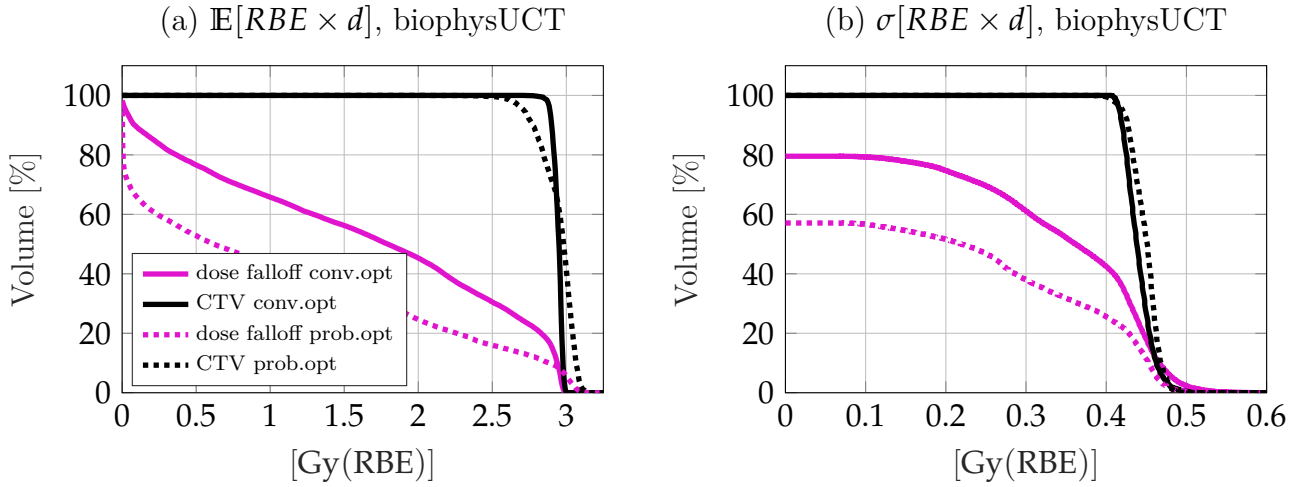


Figure IV.28: (a) Expected RBE weighted dose volume histogram (EDVH) of conventional optimization (solid lines) and probabilistic optimization (dashed lines). (b) Standard deviation RBE weighted dose volume histogram (SDDVH) of conventional optimization (solid lines) and probabilistic optimization (dashed lines)

Moreover, Figure IV.28(b) indicates the uncertainty in the CTV cannot be minimized by probabilistic optimization (---), it even slightly increases. This can be attributed firstly to the higher dose that is applied to the CTV as indicated by (---) in Figure IV.28(a) and secondly to the usage of a single beam, which limits the optimizer's freedom to create robustness. Nevertheless, $\sigma[RBE \times d]$ is reduced significantly in the dose falloff structure as indicated by (---) in Figure IV.28(b) suggesting probabilistic optimization might also be a valuable tool for single beam configurations.

The last Figure IV.29 presents the standard deviation of the RBE weighted dose ($\sigma[RBE \times d]$) from conventional optimization considering physical and biological uncertainties for two different fractionation assumptions. First Figure IV.29(a) shows $\sigma[RBE \times d]$ assuming in the calculation of the standard deviation in Equation III.31 a single fraction and Figure IV.29(b) denotes $\sigma[RBE \times d]$ modeling $F = 20$. Figure IV.29(a) has to be interpreted with caution as it represents $\sigma[RBE \times d]$ of applying 3 Gy(RBE) once and does not allow due to the fractionation effect to derive $\sigma[RBE \times d]$ for e.g. 60 Gy(RBE) delivered in a single fraction (see also Equation III.21).

It can be seen from Figure IV.29(a) that the uncertainty level for $F = 1$ is higher than in Figure IV.29(b) assuming $F = 20$. This can be explained by random uncertainties which are most influential for $F = 1$ as there is no compensation of random errors in upcoming fractions. Thus random uncertainties are responsible for the increased uncertainty in dose at the distal edge of the CTV for $F = 1$ (see Figure IV.29(a)). It can also be seen how the influence of random uncertainties compensate over the course of treatment when comparing Figure IV.29(a) to Figure IV.29(b). Further Figure IV.29 proves that neglecting fractionation effects considerably overestimates the uncertainty in dose which was also observed by (Bangert et al., 2013; Lowe et al., 2016; Sakama et al., 2016)

Objectives and optimization parameters remained unchanged for conventional and probabilistic optimization. The only difference was to use the CTV as target structure instead of

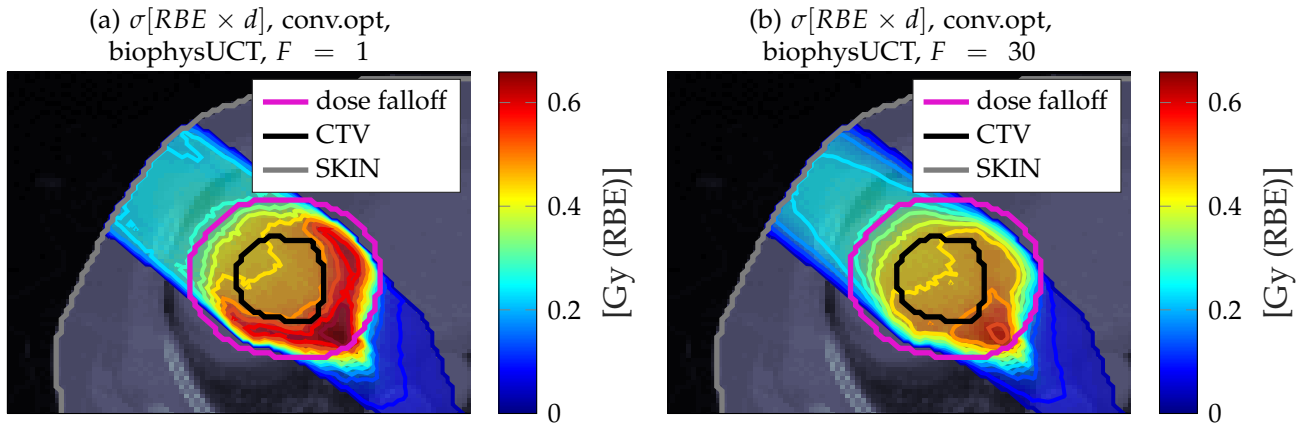


Figure IV.29: Transversal CT image of the liver case overlaid with transparent dose colorwash, solid contours and solid iso-dose lines to visualize the standard deviation of RBE weighted dose $\sigma[RBE \times d]$ after conventional optimization. Figure (a) assumes a single fraction in the calculation of $\sigma[RBE \times d]$ whereas Figure (b) presents the $\sigma[RBE \times d]$ assuming $F = 20$.

the PTV for probabilistic optimization. The background here is probabilistic optimization should find a patient- and uncertainty-specific high dose margin autonomously to deliver sufficient dose to the CTV.

Two beam setup - intra-cranial This section presents again the intra-cranial case previously introduced only for physical uncertainties in the proof of concept Section IV.2.2.1 but this time also with the consideration of biological uncertainties.

Figure IV.30(a) shows the expected RBE weighted dose ($\mathbb{E}[RBE \times d]$) considering physical and biological uncertainties (biophysUCT) from a PTV based conventional optimization. Different from the previous evaluation from Section IV.2.2.1 here the number of fractions is set to $F = 20$ and the pencil beam placement is slightly adapted. These two reasons explain why the standard deviation in RBE weighted dose ($\sigma[RBE \times d]$) accounting for physical uncertainties in Figure IV.30(b) is slightly different to Figure IV.24(d).

The mean value of $\sigma[RBE \times d]$ in the CTV in Figure IV.30(b) resulted in 0.14 Gy(RBE) and the maximum $\sigma[RBE \times d]$ value on this slice was 0.43 Gy(RBE). Additionally, Figure IV.30(c) shows the uncertainty in dose of exclusively considering biological uncertainties which introduced again a significant level of uncertainty in dose characterized by a mean value of $\sigma[RBE \times d]$ in the CTV (—) of 0.45 Gy(RBE). Complementary, Figure IV.30(d) highlights $\sigma[RBE \times d]$ for the combined consideration of physical and biological uncertainties and further elevates the uncertainty level to a mean value of $\sigma[RBE \times d]$ in CTV to 0.49 Gy(RBE). It can be seen from Figure IV.30 that APM allows quantifying the impact of individual sources of uncertainty under fractionation on the resulting carbon ion therapy treatment plan by calculating the expectation value and standard deviation in closed-form. Compared to sampled references the global γ -index for $\mathbb{E}[RBE \times d]$ (in Figure IV.30(a)) and $\sigma[RBE \times d]$ (in Figure IV.30(d)) yielded a pass rate of 100% and 99.23%.

Using the information shown in Figure IV.30(a) and (d) for probabilistic biological effect based optimization on the CTV results in Figure IV.31. Similar to the liver case, $\mathbb{E}[RBE \times d]$

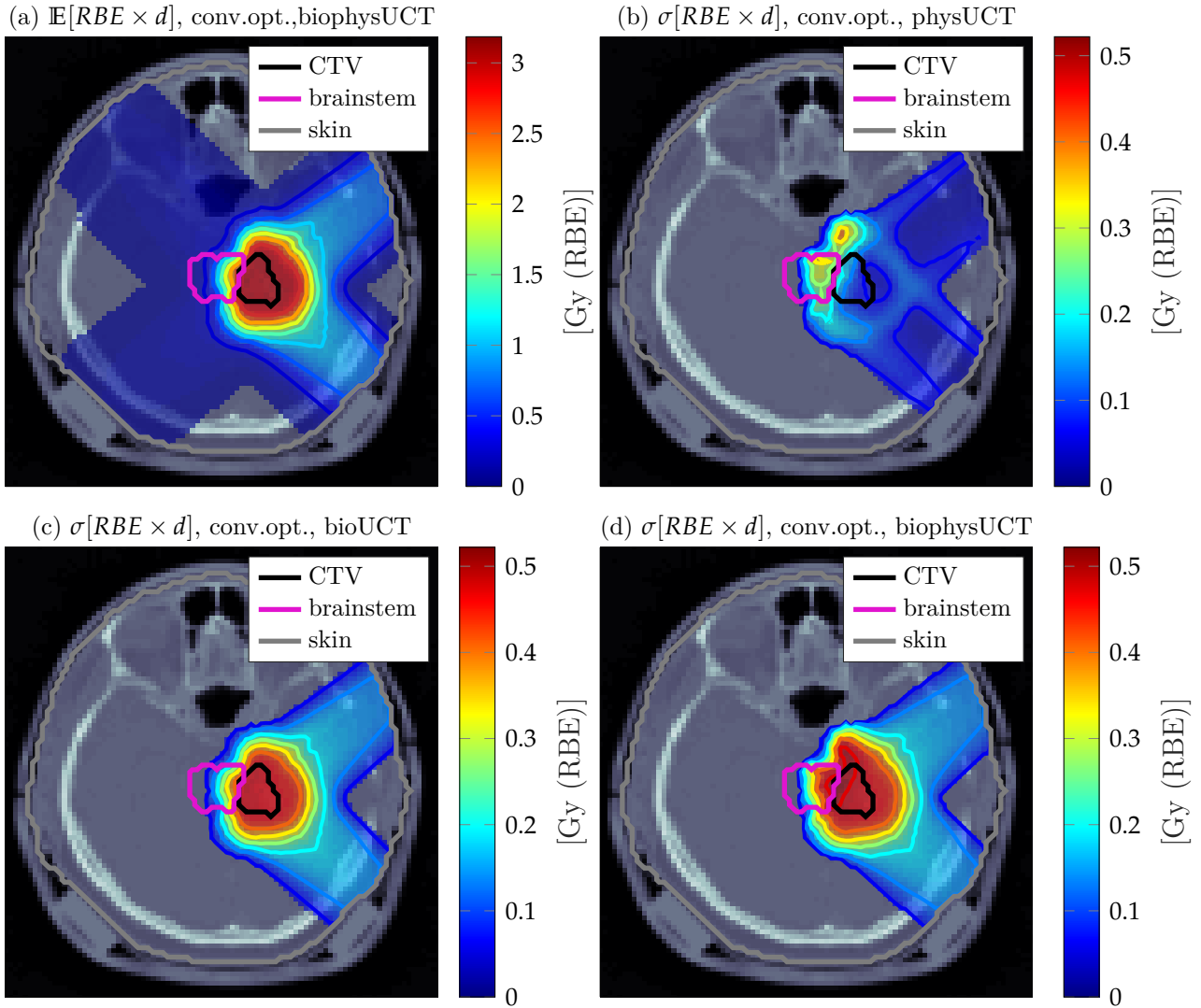


Figure IV.30: Uncertainty quantification of an intra-cranial carbon ion treatment plan on the basis of conventional optimization. The transversal CT image is superimposed by transparent dose colorwash, solid isodose lines and solid contours. Figure (a) shows $\mathbb{E}[RBE \times d]$ assuming physical and biological uncertainties (biophysUCT). Figure (b) shows $\sigma[RBE \times d]$ modelling physical uncertainties (physUCT) whereas Figure(c) highlights $\sigma[RBE \times d]$ stemming from biological uncertainties. Lastly, Figure (d) shows $\sigma[RBE \times d]$ of the combined consideration of physical and biological uncertainties. All uncertainty quantifications consider 20 fractions.

level is increased in the CTV quantified by a mean $\mathbb{E}[RBE \times d]$ increase from 2.93 Gy(RBE) to 2.98 Gy(RBE) to avoid under-dosage due to wash-out effects induced by physical uncertainties. This characteristic is reflected in the corresponding EDVH by comparing (—) to (----) in Figure IV.32(a).

Comparing IV.30(a) and IV.31(a) reveals that the high dose margin of $\mathbb{E}[RBE \times d]$ is after probabilistic optimization tighter. Focusing on $\sigma[RBE \times d]$ in Figure IV.30(d) and on Figure IV.31(b) allows for a fair comparison of the impact of probabilistic optimization on treatment plan uncertainties for an identical uncertainty quantification considering biological and physical uncertainties (biophysUCT). Although the uncertainty level could only be reduced marginally in the CTV, it was minimized in the brainstem and in the skin structure. The former is also confirmed by the corresponding SDDVH in Figure IV.32(b).

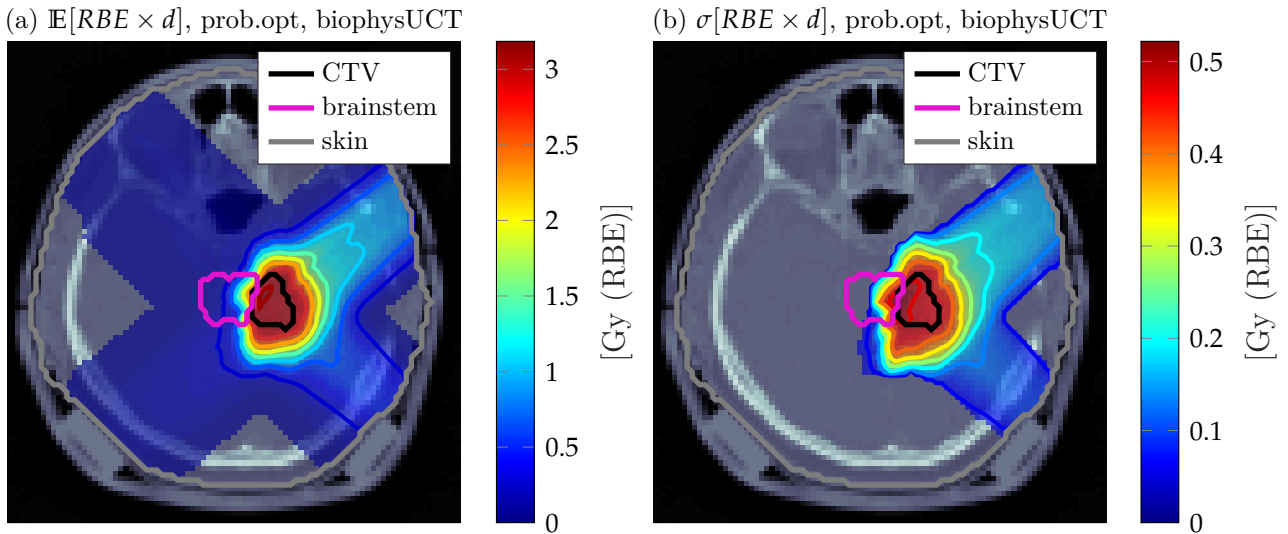


Figure IV.31: Transversal CT image with transparent dose colorwash, solid contours and solid isodose lines represent the expected RBE weighted dose after probabilistic optimization in Figure (a) and the corresponding standard deviation in Figure (b). The probabilistic optimization is done on the CTV and not on the PTV and accounts for biological and physical uncertainties (biophysUCT).

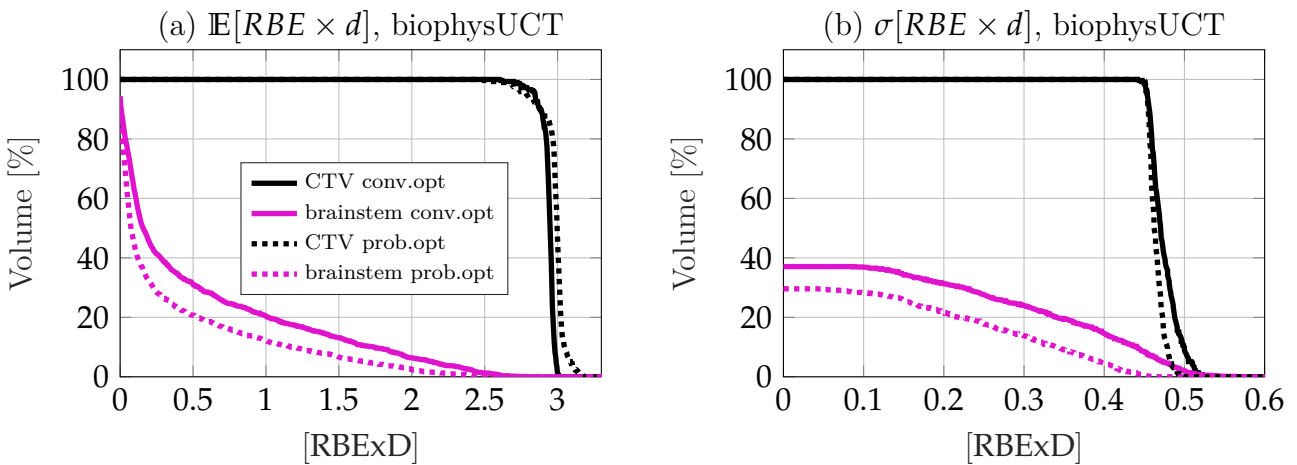


Figure IV.32: (a) Expected RBE weighted dose volume histogram (EDVH) of conventional optimization (solid lines) and probabilistic optimization (dashed lines). (b) Standard deviation RBE weighted dose volume histogram (SDDVH) of conventional optimization (solid lines) and probabilistic optimization (dashed lines)

Lastly, Figure IV.33 presents transversal CT images overlaid by $\sigma[RBE \times d]$ accounting for biological and physical uncertainties (biophysUCT) originating from conventional (IV.33(a)) and probabilistic optimization (IV.33(b)) both modeling a single fractionated treatment. It can be seen that the standard deviation hot-spots in IV.33(a) were reduced in IV.33(b) resulting in a minimized uncertainty in the brainstem (---). Complementary, Figure IV.33(c) and Figure IV.33(d) shows the mitigation of physical uncertainties after probabilistic optimization for a single fraction. A lower standard deviation level throughout the CTV can be observed after probabilistic optimization.

Although uncertainties in dose could be mitigated through probabilistic optimization, the RBE distribution itself changed only marginally manifested by a slight increase of the mean expected RBE in the CTV from 2.86 to 2.95.

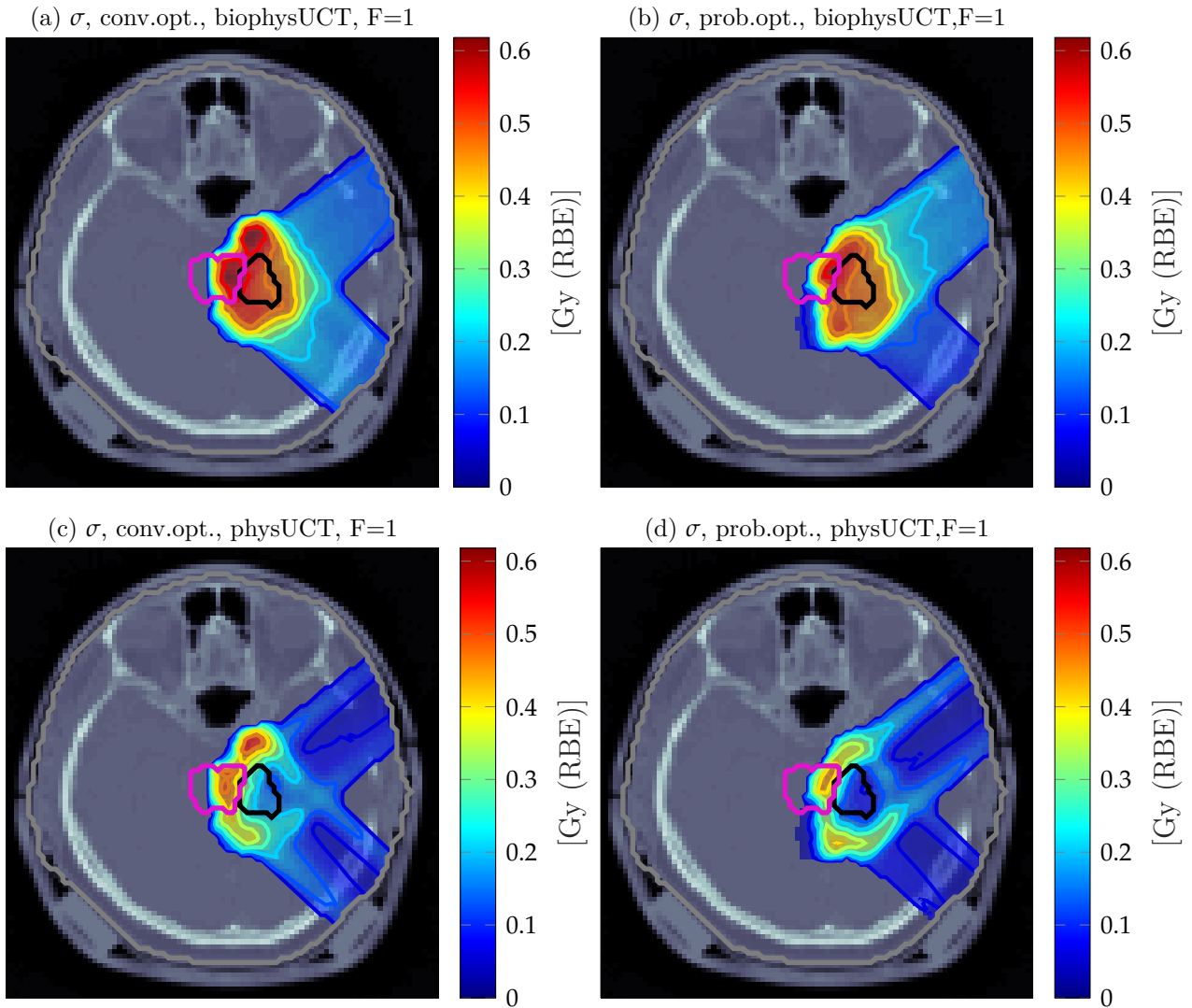


Figure IV.33: Transversal CT image with transparent dose colorwash, solid contours and solid isodose lines showing $\sigma[RBE \times d]$ based on conventional optimization and a single fraction in (a). Complementary highlights (b) $\sigma[RBE \times d]$ based on probabilistic optimization for 20 fractions but for uncertainty quantification also a single fraction is considered.

Two beam setup - lung This section presents the evaluation of a lung case assuming increased physical uncertainties of $\sigma_z^{sys} = 4\%$, $\sigma_z^{rnd} = 2\text{ mm}$ and $\sigma_{lat}^{sys} = 3\text{ mm}$, $\sigma_{lat}^{rnd} = 3\text{ mm}$. Biological uncertainties were kept constant at $\sigma[\omega_\alpha^{sys}] = 25\%$. The results of conventional optimization on the PTV are shown in Figures IV.34(a) and (c). In contrast, Figures IV.34(b) and (d) show the results of probabilistic optimization.

In this evaluation, the $\sigma[RBE \times d]$ was only calculated for voxels if the corresponding $\mathbb{E}[RBE \times d]$ exceeded 5% of the maximal dose. The analysis by means of EDVH is shown in Figure IV.35 and revealed a decrease of the mean dose in the Internal Target Volume (ITV) to 2.73 Gy(RBE). Performing probabilistic optimization elevated the mean dose back to 2.97 Gy(RBE). Concerning uncertainties in dose, they could slightly be reduced for the ITV as well as for the surrounding organs at risk. In addition probabilistic optimization yielded to an increase in the mean of the expected RBE in the ITV from 2.52 to 2.58.

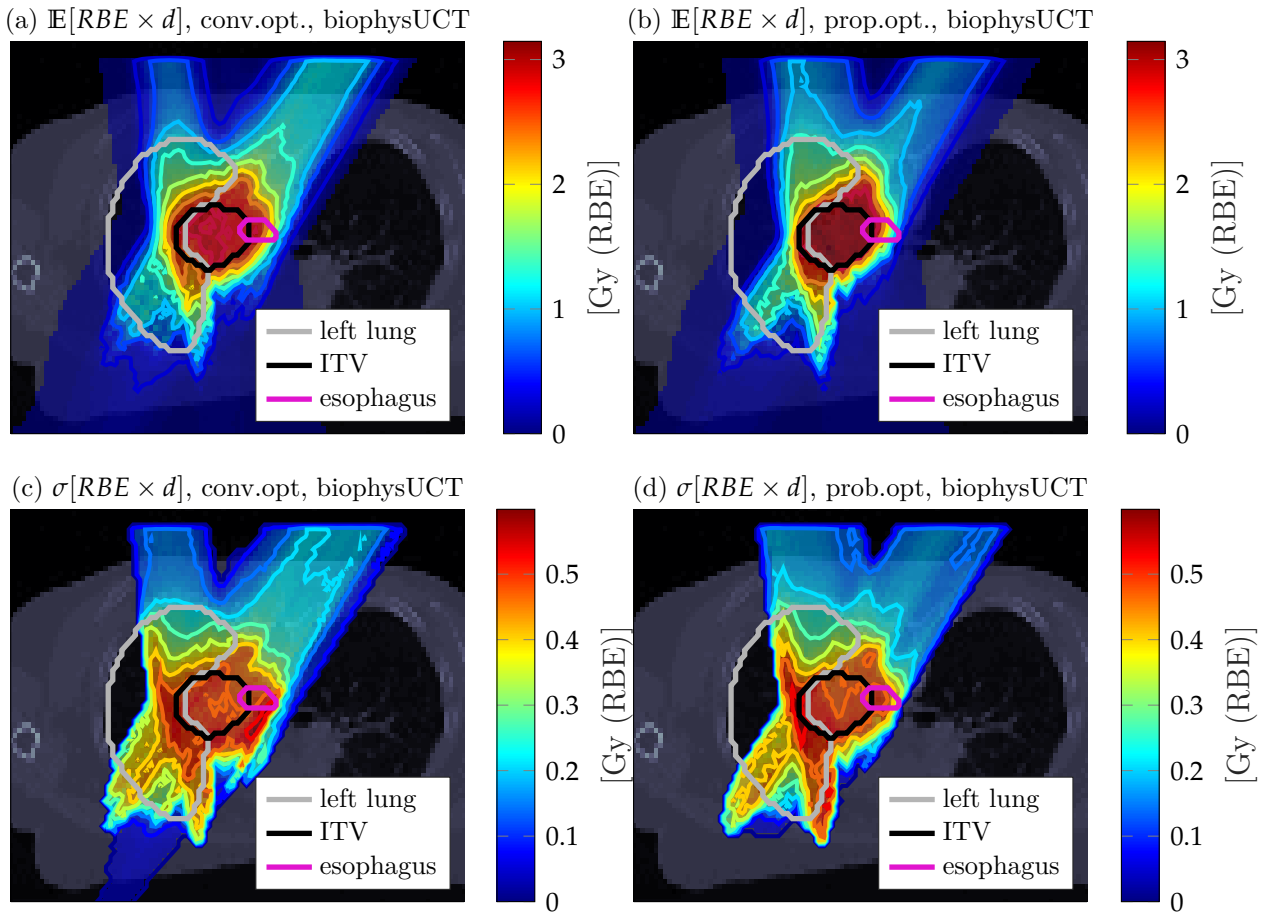


Figure IV.34: Transversal CT image with transparent dose colorwash, solid contours and solid isodose lines representing quantified treatment plan uncertainties on the basis of conventional optimization in (a) and (c) as well as of probabilistic optimization in (b) and (d).

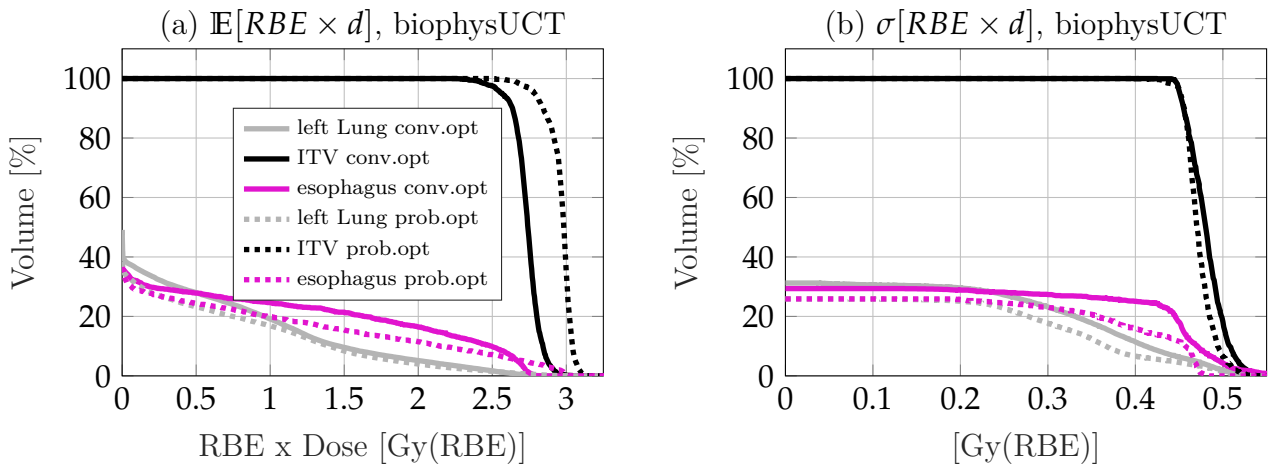


Figure IV.35: (a) Expected RBE weighted dose volume histogram (EDVH) of conventional optimization (solid lines) and probabilistic optimization (dashed lines). (b) Standard deviation RBE weighted dose volume histogram (SDDVH) of conventional optimization (solid lines) and probabilistic optimization (dashed lines)

Two opposing beams setup - cranial This section presents a carbon ion treatment plan for a cranial patient with an opposing beams configuration for uncertainties assumptions described in Section IV.2.2.2. Figure IV.36(a) presents the $\mathbb{E}[RBE \times d]$ from a conventional optimization and IV.36(b) $\mathbb{E}[RBE \times d]$ from a probabilistic optimization. Figure IV.36(c) and

(d) depict the corresponding $\sigma[RBE \times d]$ of exclusively assuming physical uncertainties for 20 fractions.

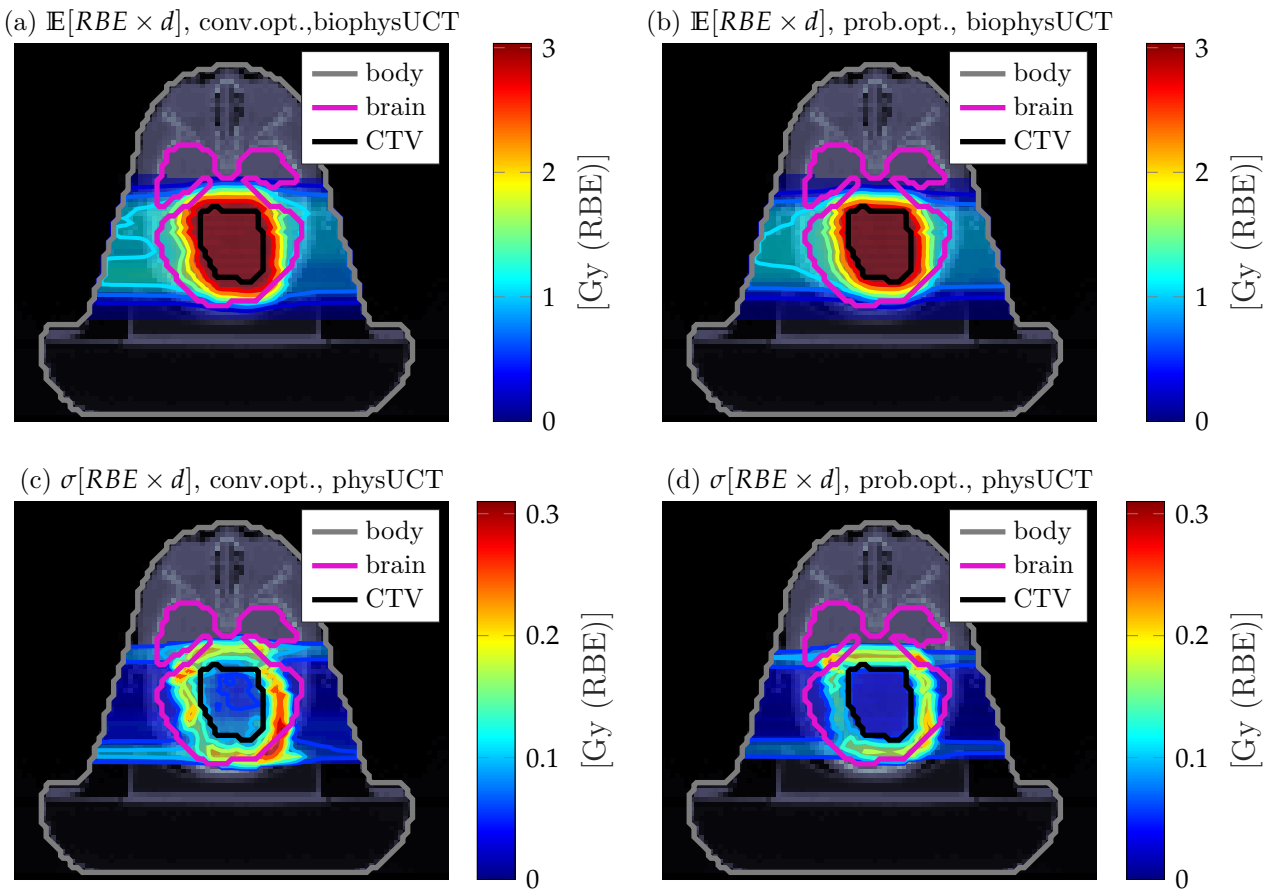


Figure IV.36: Transversal CT image of a cranial patient with transparent dose colorwash, solid contours and solid isodose lines representing quantified treatment plan uncertainties on the basis of conventional optimization in (a) and (c) as well as of probabilistic optimization in (b) and (d).

Figure IV.36 shows the $\sigma[RBE \times d]$ is reduced in the CTV through probabilistic optimization characterized by a drop in mean $\sigma[RBE \times d]$ from 0.06 Gy(RBE) to 0.03 Gy(RBE). The corresponding evaluation of the EDVH and SDDVH are presented in Figure IV.37 and show especially a decrease of integral dose to the ring structure, a uniform extension of the CTV by 10 mm which was used for optimization to create a high dose gradient. Further, the uncertainty peaks around the CTV in Figure IV.36(b) are reduced through probabilistic optimization which can be observed by comparing (—) to (----) in Figure IV.37(b).

Figure IV.38 depicts $\mathbb{E}[RBE \times d]$ of the left (270°) carbon ion beam of conventional optimization in Figure IV.38(a) and probabilistic optimization in Figure IV.38(b). It can be seen that probabilistic optimization reduced the modulation of individual beam doses and minimized as a consequence the in-field dose gradient to obtain a more homogenous beam dose distribution. Identical observations were made for the first beam but are not explicitly shown.

Exemplarily shows Figure IV.39 the expected relative biological effectiveness $\mathbb{E}[RBE]$ in the CTV for conventional optimization in Figure IV.39(a) and probabilistic optimization in IV.39(b). Identical to the previous patient cases the mean $\mathbb{E}[RBE]$ increased from 2.38 to 2.48 in the CTV which can also be visually observed in Figure IV.39. Further, $\mathbb{E}[RBE]$ IV.39(b)

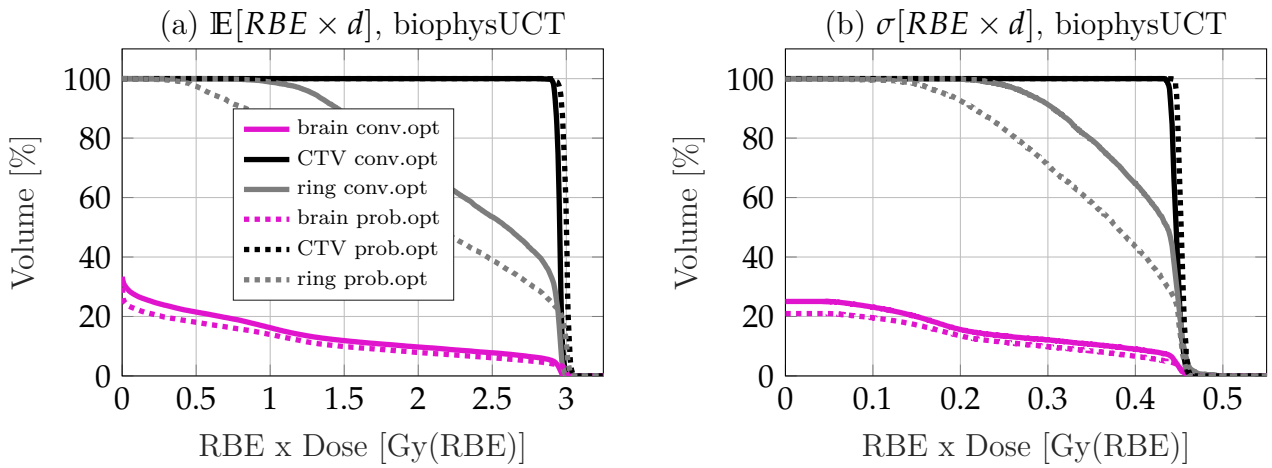


Figure IV.37: (a) Expected RBE weighted dose volume histogram (EDVH) of conventional optimization (solid lines) and probabilistic optimization (dashed lines). (b) Standard deviation RBE weighted dose volume histogram (SDDVH) of conventional optimization (solid lines) and probabilistic optimization (dashed lines)

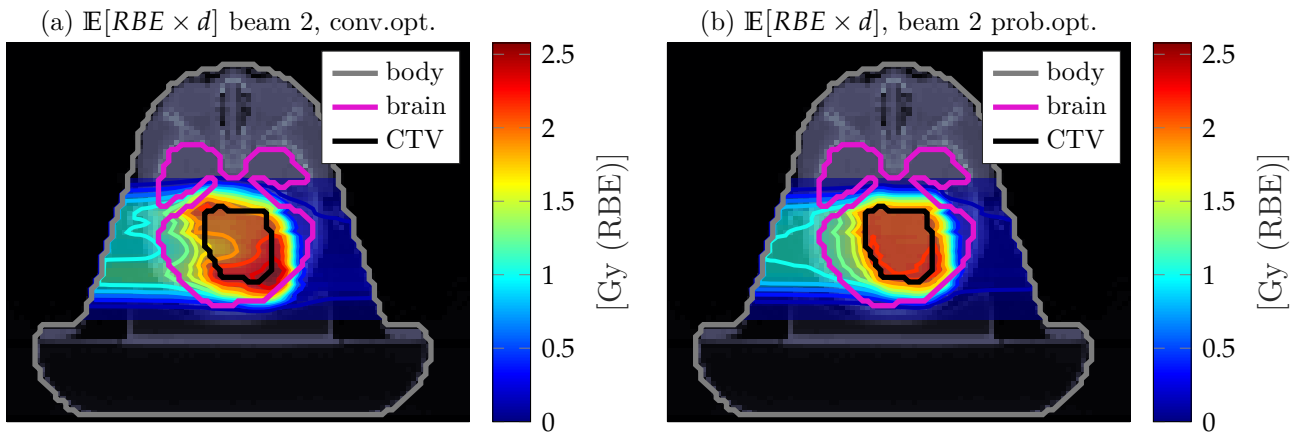


Figure IV.38: Transversal CT image with transparent dose colorwash, solid contours and solid isodose lines representing $\mathbb{E}[RBE \times d]$ of the second beam direction on the basis of conventional optimization in (a) and probabilistic optimization in (b).

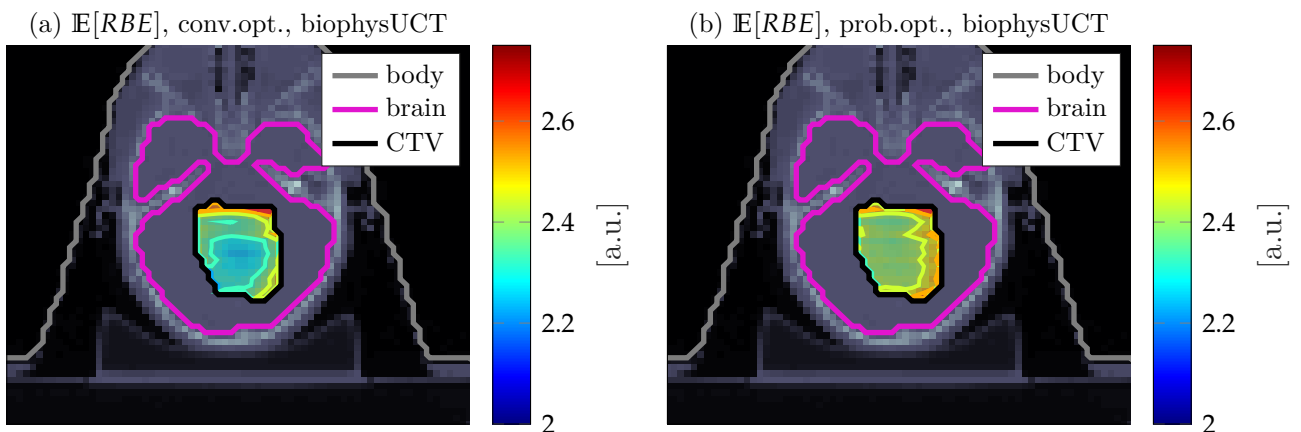


Figure IV.39: Transversal CT image with transparent dose colorwash, solid contours and solid isodose lines characterizing the expected RBE in the CTV structure on the basis of conventional optimization in (a) and probabilistic optimization in (b).

shows a more homogenous $\mathbb{E}[RBE]$ than in Figure IV.39(a).

IV.2.2.3 Comparison of robust optimization techniques

This section presents for the intra-cranial case a comparison between scenario based robust optimization and probabilistic optimization on the expectation value of the squared deviation objective. For robust optimization, the scenario based min max (composite worst case) optimization, as proposed by (Fredriksson et al., 2011) and described in Section II.5.3.2, was implemented in the validated treatment planning system matRad. In total, 9 scenarios were considered comprised of the nominal scenario, and eight worst case scenarios modeled via individual ± 3 mm single iso-center shifts in x,y,z and two fully correlated over and undershoot scenarios of $4\% \pm 2$ mm. The resulting optimized pencil beam intensities were then used as input for uncertainty quantification via APM.

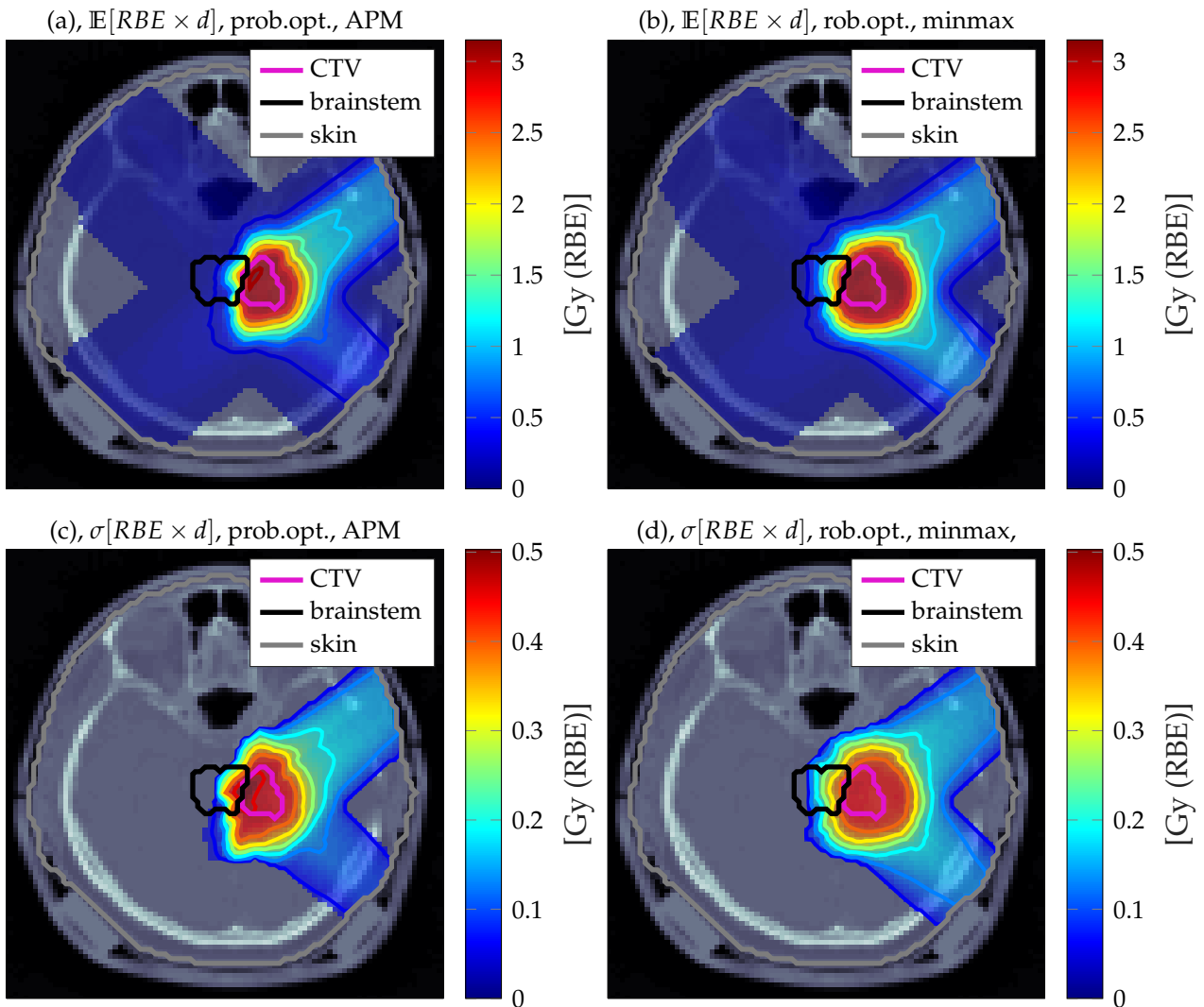


Figure IV.40: Uncertainty quantification of an intra-cranial carbon ion treatment plan using probabilistic optimization in Figures (a) and (c) and scenario based robust optimization in Figures (b) and (d). The transversal CT image is superimposed by transparent dose colorwash, solid isodose lines and solid contours. All uncertainty quantifications consider 20 fractions.

In contrast, probabilistic optimization models the standard deviation of input uncertainties by a range error of $\sigma_z^{sys} = 3.5\%$, $\sigma_z^{rnd} = 1$ mm, and the lateral positioning error via $\sigma_{lat}^{sys} = 1$ mm, $\sigma_{lat}^{rnd} = 2$ mm. Admittedly, the quantified input uncertainties in σ units for probabilistic

optimization cannot be directly related to the maximum shifts and range errors defined in the composite worst case optimization. For uncertainty quantification an additional biological uncertainty of $\sigma[\omega_{\alpha}^{sys}] = 25\%$ and 20 fractions were assumed. Further, both optimization techniques considered the CTV as target structure and neglected the PTV.

On the one hand, Figure IV.40(a) shows the expectation value $\mathbb{E}[RBE \times d]$ and Figure IV.40(c) the corresponding standard deviation $\sigma[RBE \times d]$ on the basis of probabilistic optimization (prob.opt). Please note that these results are identical to Figure IV.31.

On the other hand, present Figure IV.40(b) and (d) the $\mathbb{E}[RBE \times d]$ and the $\sigma[RBE \times d]$ of the robustly optimized (rob.opt) treatment plan. The treatment planning uncertainties were quantified via APM assuming the same uncertainty assumptions. Thus identical physical and biological uncertainties were used for quantification in Figure IV.40(a,c) and (b,d). The only difference is the optimization technique to obtain pencil beam intensities.

Firstly, both optimization techniques created a high dose margin around the CTV to create robustness. Herewith, the size of the high dose margin strongly depends on the quantified input uncertainties used for the respective optimization technique. Focusing on Figure IV.40(a) and (b) allows to make the following observation. The optimization of the expectation value of the squared deviation objectives in Figure IV.40(a) created a much tighter high dose margin around the CTV and might as a consequence not be robust against actual worst cases. Vice versa might the integral dose of the composite worst optimization in Figure IV.40(b) be unnecessarily high as the optimizer has no incentive to optimize more probable scenarios (Unkelbach and Paganetti, 2018). Analyzing the uncertainty in dose in Figure IV.40(c) and (d) resulted in a mean $\sigma[RBE \times d]$ in the PTV (not shown) of 0.42 Gy(RBE) and 0.46 Gy(RBE) and is consequently lower for probabilistic optimization.

IV.2.2.4 Smooth Animations

The new sampling strategy explained in Section III.6.4 was applied to the three-dimensional intra-cranial carbon ion treatment plan to produce smooth animations of the RBE weighted dose assuming physical setup and range uncertainties. Biological uncertainties were not modeled as they do due to their perfect Gaussian correlation assumption not have any impact on the covariance structure of dose. By means of APM, uncertainties of $RBE \times d$ were quantified (mean and covariance) for conventional and probabilistic optimization and were subsequently used to create smooth animations. Figure IV.41(a) shows animated samples on the basis of conventional optimization and in (b) identical samples from the exact same circle path around the hypersphere, but considered pencil beam weights from probabilistic optimization.

It can be seen from Figure IV.41(b) that physical uncertainties affect the resulting probabilistic optimized treatment to a lesser extent compared to Figure IV.41(a) as cold and hot spots in dose occur firstly more often and secondly to a more significant extent.

The animations provide an intuitive way for the treatment planner to quickly assess the impact of the uncertainty structure on the resulting dose distribution.

Figure IV.41: Smooth animations of discrete samples for the intra-cranial carbon ion treatment plan on the basis of conventional optimization and considering physical uncertainties is shown in plot (a). The transversal CT image is superimposed by transparent dose colorwash, solid isodose lines and solid contours. On the contrary, Figure (b) shows smooth animations of identical samples, however, pencil beam weights originate from a probabilistic optimization. In the digital version of the PDF, continuous samples are drawn for animation to express the covariance in dose. Animations are based on (Hennig, 2013).



Discussion

Particle therapy is prone to uncertainties. This manuscript addresses this issue and provides analytical expressions for the expectation value and standard deviation of the biological effect and the RBE weighted dose for three-dimensional intensity modulated carbon ion treatment plans on the basis of the analytical pencil beam algorithm. The proposed pipeline considers a variable RBE and models range-, setup- and biological-uncertainties alongside fractionation effects. All analytical formulations found in this work are compatible with the core advantages of APM initially published for protons and photons (Bangert et al., 2013). In particular, the developed analytical pipeline (i) enables the consideration of multi-dimensional linearly correlated random input variables, (ii) the modeling of arbitrary correlation structures to best reflect real-world conditions and (iii) generalizes to probabilistic optimization.

To perform treatment planning, basic carbon ion dose calculation- and optimization- functionalities were implemented in the open-source treatment planning toolkit matRad. After validating the functionality of each module, the APM formalism was implemented on top in a prototype. The adapted dose calculation engine outputs in addition to the conventional dose influence matrix the probabilistic counterparts characterized by expected influence matrices and variance influence tensor. For a given set of pencil beam weights \mathbf{w} , the analytically quantified uncertainties in dose were characterized by the mean (first raw moment) and the standard deviation (second central moment) and were in a subsequent step compared to estimated moments based on random sampling showing a reasonably good agreement. A subsequent probabilistic optimization avoided under-dosage of the CTV, less integral dose and yielded to a mitigation of uncertainties in the RBE weighted dose of carbon ion treatment plans.

A large number of studies is available on the proton side (Perkó et al., 2016; Unkelbach et al., 2018) but investigations on the application of uncertainty quantification (Kamp et al., 2015; Sakama et al., 2016) and robust/probabilistic optimization techniques (Steitz et al., 2016) to carbon ion treatment planning are limited. The two central differences to existing approaches

are that first APM does not rely on the computation of discrete error scenarios to quantify uncertainties and second, APM allows computing expected influence matrices and variance influence tensors that can directly be used for uncertainty quantification and probabilistic optimization. The remainder of this chapter further addresses specific methodological choices that were made for this thesis, provides additional interpretation of the established results, and discusses potential extensions of this work.

V.1 Numerical Approximations

Switching to a parameterized representation of tabulated carbon ion base data together with Gaussian error assumptions, modeled in the pencil beam space, enabled a straightforward execution of the *method of moments* to obtain raw and central moments of the biological effect ε in closed-form. In the proposed analytical pipeline the biological effect becomes a function of uncertain input parameters such as the setup and range error. The integration over the Gaussian error assumptions allows to derive raw moments. It was explicitly decided to build the analytical pipeline upon the biological effect ε to avoid integrating over the square root dependence of the RBE weighted dose from Equation II.23. The derived full analytical moment calculations of the biological effect ε cannot be directly applied to clinical treatment planning scenarios because of its computational complexity. For that reason an approximated solution is proposed reducing the number of operations for the expected biological effect $\mathbb{E}[\varepsilon]$ from $\mathcal{O}(I \times J^2)$ to $\mathcal{O}(I \times J)$ and for the standard deviation of the biological effect $\sigma[\varepsilon]$ from $\mathcal{O}(I \times J^4)$ to $\mathcal{O}(I \times J^2)$ at reasonable loss in accuracy. In detail, the approximations neglect correlation in terms containing the squared βd component of the biological effect ε . Compared to sampled references this approximation resulted in excellent results for the expectation value of the biological effect in the one-dimensional as well as in three-dimensional patient cases manifested by γ -pass rates of 100 %. The situation for the standard deviation of the biological effect is different as it is afflicted to a greater extent by the approximations leading to γ -pass rates of >94 %. It is important to add, that discrepancies between APM and random sampling can only partly be attributed to the approximations in the analytical calculation as there is also a residual statistical sampling uncertainty in the estimated moments from random sampling.

In this work, the approximations provide a significant increase in speed in exchange of accuracy. Nevertheless, if more accurate results are required third and fourth order influence tensors presented in the result section IV.2.1.1, can be added step by step to increase the accuracy of the uncertainty estimate. Vice versa if calculation speed is to be increased for the price of accuracy then influence tensors of second, third and fourth central moments can be represented by the outer product of lower order moments as it is already done for the proposed approximations. Assuming the presented uncertainty estimate should be improved for a potential clinical application in the future, the best trade-off to increase the accuracy of the standard deviation of the biological effect is to fully calculate the sub tensor $\Xi_{ijm}^{\alpha\beta}$ of the

original expression $\Xi_{ijmo}^{\alpha 2\beta}$ from Equation III.16 to cover the interdependence of the linear and quadratic term of the biological effect.

The approximations and results presented in this manuscript are mainly based on LEM IV predictions modeling a generic tissue characterized with $\alpha_x = 0.1$ [Gy^{-1}] and $\beta_x = 0.05$ [Gy^{-2}]. In addition, the approximations were also checked and hold true for radio-sensitive tissues characterized by $\alpha_x = 0.5$ [Gy^{-1}] and $\beta_x = 0.05$ [Gy^{-2}] but explicit results are not presented here. Moreover, switching the biophysical model version from LEM IV to the first model version I will probably lower the quality of the proposed approximations and consequently minimize the accuracy of the uncertainty estimate in dose. That is because the squared component of the biological effect, for which approximations were mainly introduced in the moment calculation, possesses for LEM I a slightly increased contribution to the total biological effect than in the fourth model version. This topic will be discussed later in Subsection V.8 with respect to proton therapy.

The analytical biological effect calculation fully relied laterally and in depth upon Gaussian components which allowed to model setup and range uncertainties in the respective mean position of the Gaussian component. Complementary, biological uncertainties introduce a new complexity and were modeled via an uncertainty in the weight of each Gaussian component thereby expressing uncertainty in magnitude/effectiveness of each pencil beam. By this means physical and biological uncertainties can be considered together without increasing the computational complexity. This is a key feature of APM because different to scenario-based approaches the computational complexity stays constant.

Covariances matrices, presented in Sections III.2 and III.3.3, need to be defined by the treatment planer and allow to model the level and structure of uncertainty, i.e., the correlation of individual pencil beams for each uncertainty source. In detail, four different covariance structures were used throughout this work. First, setup uncertainties are correlated within a beam direction, second range uncertainties are only correlated if the respective pencil beams are located on the same ray position as they penetrate the same tissue (Bangert et al., 2013) and thirdly biological uncertainties are assumed to be fully correlated. The usage of an additional correlation model enables the consideration of fractionation effects, which effectively doubles the number of computations for any arbitrary number of fractions. Further, APM permits to break down the level of uncertainty into the related physical and biological sources considering fractionation which is not possible in sampling approaches relying on discrete scenarios. Thus, the impact of physical- and biological uncertainties can either be assessed individually or can be calculated for a combined consideration accounting for fractionation effects at almost constant runtime.

Another approximation is made for the unknown distribution of ε . Although the first raw and second central moment of ε are correctly calculated from a mathematical point of view, having only these two parameter limits the representation of more complex bimodal distributions. Therefore it is assumed in a first approximation the biological effect ε obeys a Normal distribution. It was demonstrated for the one-dimensional phantom this assumption

becomes increasingly inaccurate in high dose gradient regions. In contrast, the distribution of the biological effect agrees better with a Normal distribution the lower the dose gradient becomes. To more accurately estimate the unknown non-Gaussian distribution of the biological effect ε higher order moments need to be calculated that allow the representation of skewed or bimodal distributions. The assumption of a normally distributed biological effect is used not only for probabilistic effect based optimization employing the expected objective function value but also for the moment/error propagation to convert moments of the biological effect to moments of the clinically relevant RBE weighted dose domain.

The error propagation from the biological effect to RBE weighted dose introduces an additional layer of uncertainty. Although linear transformations of Normal distributions can be calculated analytically, the non-linear transformations from the square root dependence of the RBE weighted dose does not possess an exact solution. To approximate the square root, we perform a Taylor expansion around the mean of the biological effect and evaluate partial derivatives. Despite using a fourth order Taylor expansion, this method gets increasingly inaccurate when the standard deviation of the biological effect becomes large relative to the corresponding mean value because the probability mass on the negative orthant \mathbb{R}_- increases and the discrepancy to the actual unknown probability distribution become larger as a negative biological effect does not exist. The moment propagation can be improved in the future, by either calculating higher order moments or by using of a different PDF (beta distribution) for the distribution of biological effect $p(\varepsilon)$ that does not allow negative values.

V.2 Accuracy of Pencil Beam Algorithm

The closed-form moment calculations on the basis of APM are exact, given a correct modelling of input uncertainties and assuming the analytical pencil beam algorithm used for dose calculation is accurate. The uncertainty assumptions are discussed later in Section V.6 and the dose calculation accuracy is addressed next.

A limitation of the presented APM formalism is that it only works in conjunction with the analytical pencil beam dose calculation algorithm and does not easily generalize to other dose calculation algorithms. It is commonly known (Taylor et al., 2017) that the pencil beam dose calculation shows limited accuracy when high tissue heterogeneities and low to high-density interfaces are present in the beam path which was already addressed in detail in Section II.5.1. These inaccuracies can be revealed by a Monte Carlo forward dose calculation given optimized pencil beam weights, which is actually the most prominent use case for Monte Carlo simulations in particle therapy. Although this work facilitates an improved version of the pencil beam algorithm which takes the actual radiological depth of voxel i into account and not its projection onto the pencil beam central axis, the dose distribution might still be inaccurate for certain tumor sites (e.g. lung).

An approach called pencil beam fine sampling (Soukup et al., 2005) which also generalizes to APM could further improve the accuracy of the current pencil beam algorithm. Here the

primary fluence is decomposed into several sub-pencil beams of Gaussian shape located on pre-defined sub-rays and their superposition results again in the primary fluence. This is methodically identical to APM where a superposition of Gaussian components represents depth related pencil beam components. It was shown by (Soukup et al., 2005) that this adaption of a 'finer' pencil beam algorithm improves the dosimetric accuracy with reference to Monte Carlo simulations.

Although Monte Carlo dose calculation is assumed to be the gold standard for accurate dose calculation (Battistoni et al., 2016), also the accuracy of this approach is compromised, analog to the pencil beam algorithm, by the imperfect knowledge of the patient's tissue densities. The value of having an accurate dose calculation algorithm that assumes perfect conditions (neglecting the impact of uncertainties) is to be questioned. The latter statement directly motivates the use of robust or probabilistic optimization. However, it is computationally demanding to create a Monte Carlo based dose influence matrix with sufficient statistics. This becomes even more problematic for robust optimization where E error scenarios require E Monte Carlo based dose influence matrices (Unkelbach et al., 2018). For such computationally demanding treatment planning cases (robust/probabilistic or 4D) the analytical pencil beam algorithm is still valuable.

Monte Carlo simulations compensate dosimetric uncertainties introduced by the pencil beam algorithm but not uncertainties originating from changes in the patient geometry (Paganetti, 2012). Thus, Monte Carlo simulations produce an accurate dose prediction, however, only for the best case scenario (=nominal scenario). In contrast, APM generates a less accurate dose prediction but provides, in addition, a full probabilistic description of the treatment plan (Bangert et al., 2013; Wahl et al., 2017; Wieser et al., 2017b). To fully understand the probabilistic consequences of using the analytical pencil beam algorithm within the APM framework, Monte Carlo random sampling with high statistics needs to be carried out in the future to estimate the expectation value and standard deviation based on accurate dosimetric samples. This would permit to relate moments calculated via APM to moments estimated from Monte Carlo random sampling and might reveal potential differences.

Throughout this work APM related calculations are based on the single Gaussian lateral pencil beam model whereas the validation of the implemented TPS is done for the double Gaussian lateral beam model (Parodi et al., 2013). The reason for using the single Gaussian beam model for APM is the unsuitable radial symmetric parametrization of the double Gaussian beam model.

In detail, the double Gaussian beam model is comprised of a weight w , σ_{narr} denoting the narrow Gaussian component and σ_{broad} depicting the broad Gaussian component that models the low dose halo. These parameters do not allow to decompose the lateral dose L_{tot} into $L_{tot}^x L_{tot}^y$ to model setup errors individually in the spatial x and y dimensions. Let L_{narr} be the radial dose of the narrow Gaussian component and analog let L_{broad} be the radial dose of the broad Gaussian component. Then the total lateral dose L_{tot} is defined in the double Gaussian beam model to be $L_{tot} = (1 - w)L_{narr}^x L_{narr}^y + wL_{broad}^x L_{broad}^y$. In contrast, APM

currently assumes L_{tot} to factor into $L_{tot}^x L_{tot}^y$ and would require the following parametrization $L_{tot} = (1 - w)L_{narr}^x L_{bro}^x + wL_{narr}^y L_{braod}^y$.

Another solution to this is to either directly obtain moments of the two-dimensional distribution $L_{tot}(x, y)$ or to approximate the uncertainty quantification by only considering the narrow Gaussian component. Since the broader Gaussian component is at least 4 times the value of σ_{narr} , setup errors will have a minor impact on the broad Gaussian component.

The last paragraph discusses beneficial mathematical aspects of the Gaussian parametrization over tabulated base data used for the analytical pencil beam algorithm (Bangert et al., 2013; Wieser et al., 2017b). Beyond the possibility to perform uncertainty quantification on the basis of APM, the Gaussian parametrization permits, for instance, to efficiently model range straggling in lung tissue in closed-form. The parametrization not only reduces the number of parameters, it mathematically opens the door to use features of the well studied Gaussian bell curve. In the future, also other quantities as the LET might be parameterized with a superposition of Gaussian components. The linear dependency of the dose averaged LET on the fluence would allow to directly derive the expected LET and the standard deviation of LET within APM. In combination with future probabilistic constraints, discussed in the next section, the dose-averaged LET might be controlled during optimization in a probabilistic manner.

V.3 Probabilistic Optimization

Throughout this work, uncertainties were quantified with APM and subsequently used for optimizing the penalized expected squared deviation objective of the biological effect $\mathbb{E}[f_{sq dev}(\varepsilon)]$ of carbon ion treatment plans. In line with other publication based on protons (Unkelbach et al., 2018, 2007; Unkelbach and Paganetti, 2018) probabilistically optimized treatment plans were for every patient more robust against uncertainties than the conventionally optimized treatment plan on the PTV. However, the possibility to only probabilistically optimize the squared deviation objective represent a limitation. State of the art treatment planning systems facilitate in addition to the squared deviation objective more advanced objective functions and constraints as illustrated in Table II.1 in Section II.4.4.2. The problem from optimizing $\mathbb{E}[f_{sq dev}]$ is on the one hand that the resulting pencil beam intensities might be too less conservative and consequently not be robust enough against actual worst cases (see comparison of results IV.2.2.3). On the other hand, worst case optimization might be too conservative by applying to much dose in the high dose margin around the CTV as their no incentive during optimization to improve plan quality for more probable scenarios (Unkelbach and Paganetti, 2018).

An intermediate solution is given by a distributionally robust approach that allows to scale between worst case approaches and stochastic programming (Unkelbach et al., 2018). (Fredriksson, 2012) proposed another intermediate solution called conditional value at risk optimization which is a generalization of worst case and expectation value optimization

and enables to optimize the average objective function value of the worst $X\%$ of error scenarios. However, both approaches would require an analytical probabilistic representation of objectives to be used in combination with APM.

For that reason (Wahl, 2018) investigated the moment calculation of other treatment plan metrics and could derive exact and approximated expressions for the expectation value and standard deviation of the mean dose, DVH points and the Equivalent Uniform Dose (EUD). In further consequence Wahl established analytical expressions for novel probabilistic objectives and constraints for the physical dose. Among other, analytical probabilistic expressions were found for the expected piecewise squared deviation function that allowed the use of expected squared over- and under-dose objectives for optimization.

But still the underlying problem of probabilistic and robust optimization is the treatment planner can only indirectly steer the robustness of the resulting treatment plan by manipulating input uncertainties without directly knowing how robust the resulting plan is going to be. Objectives including probabilistic objectives are considered as *cost functions* that are minimized during optimization. This means objectives are traded against each other to obtain a minimal objective function value because no boundary condition (constraint) is defined. Thus it is desirable in current clinical practice to be able to quantify and control the acceptable level of robustness for robust/probabilistic optimization by using probabilistic constraints.

Because of the limitation mentioned above other treatment plan quality indicators such as probabilistic min/max-dose, -EUD, -DVH constraints were developed by (Wahl, 2018) and their applicability was tested for protons on a simplified one-dimensional prototype. However, such advanced constraints, for instance, the α -DVH which represent the DVH for a certain confidence level α require covariance information from the co-variance influence tensor \mathfrak{C}_{ijlm} in $\in \mathbb{R}^{I \times J \times I \times J}$ which cannot be stored for three-dimensional patient cases on disk. Therefore efficient and accurate tensor approximation (tensor decomposition) might be of interest in the future.

V.4 Sampling

The quantified uncertainties were compared to estimated moments based on random sampling. Using 5000 samples ensured reliable reference estimates as the relative accuracy drops below the 1% level (Wahl, 2018; Wahl et al., 2017). Run-times for random sampling were between 1-2 days* per patient case motivating the use of APM as it provides a better trade off between speed and accuracy. The γ -pass rates were all above 94% using (DTA=2mm, $\Delta d = 2\%$) thereby indicating good agreement between moments calculated via APM and estimated moments. The approximations introduced in the analytical computations, the moment propagation to the RBE weighted dose domain and the sampling statistics explain the discrepancies.

*on a CPU based implementation in matRad using a computer with i7 processor and 32 GB of RAM

Random sampling considers the effect of range errors induced by lateral shift but performing random sampling in clinical practice to quantify uncertainties in dose is currently not feasible. Although the effect of range errors caused by lateral shift could be modeled in APM via a higher dimensional correlation model it results in prohibitive computational effort. At the moment, the effect of range errors caused by lateral shifts are currently not modeled in APM. But since the γ -pass rates were high, it is believed that it may not have a major impact, at least for the patient cases considered. Further, the study of (Wahl et al., 2017) demonstrated for protons that APM provides consistently more accurate uncertainty estimates of dose than grid or importance sampling strategies although the effect of range errors caused by lateral shifts is not modeled in APM.

V.5 Impact of Biological Uncertainties

While physical uncertainties, i.e., range and setup errors, can be modeled with an uncertainty about the location of the dose (i.e. geometrical shifts of the dose), biological uncertainties have to be modeled as an uncertainty about the absolute magnitude of the effect within the patient. Consequently, biological uncertainties were modeled throughout this manuscript with a Gaussian uncertainty in the weight of each Gaussian component constituting the depth-dependent $\alpha_c d$ component of the biological effect. This represents a methodical extension of the existing APM approach applied to protons (Bangert et al., 2013; Wahl et al., 2017, 2018a). Here, a relative uncertainty in α_c of 25 % directly translated to a relative uncertainty in the respective weight ω^α of the $\alpha_c d$ profile. The corresponding covariance matrix allowed to model the uncertainty structure of biological uncertainties. As thirteen Gaussian components were used to represent depth-dependent $\alpha_c d$ profiles, the freedom to design an uncertainty band for the respective profile is limited because of the number and the position of the Gaussian components. For instance the carbon ion dose tail is mostly represented by a single broad Gaussian component which constraints the flexibility in this region. Whereas 25 equally spaced (with respect to the mean) Gaussian components would permit to model more complex uncertainty bands with abrupt changes of uncertainty at specific locations. Further, the uncertainty band could even act as a surrogate for the LET but biological uncertainties would not be represented anymore.

The covariance matrix modeling biological uncertainties assumes a perfect correlation between all Gaussian components of pencil beam j to all Gaussian components of pencil beam m . Hence biological uncertainties are independent of the irradiation geometry and represent herewith a systematic non-patient-specific uncertainty source. As biological uncertainties are modeled identical to physical uncertainties in the pencil beam space and not the voxel domain, this approach only allows modeling systematic biological uncertainties stemming from the tissue response to ion radiation. The current implementation principally also permits modelling random biological uncertainties which would express differently in each fraction, but still in the pencil beam space. That means no voxel-specific information can be included.

Instead, it is desirable to model random biological uncertainties in the voxel domain. Future advanced functional imaging techniques could maybe highlight radio-resistance or radio-sensitive regions along with an uncertainty estimate about the effectiveness in the tumor upfront to the treatment. This would then trigger a potential adaption of the LQM parameter α_c and β_c and the corresponding probability distributions $p(\alpha_c)$ and $p(\alpha_b)$ in these voxels.

The parametric representation of the base data via Gaussians allowed deriving closed-form expressions for the first raw and second central moments of the RBE weighted dose considering physical and biological uncertainties. The additional consideration of biological uncertainties was associated with negligible overhead in computational complexity. Different to other robust optimization techniques that rely on discrete error scenarios, every additional source of uncertainty drastically increases the number of combinations (the curse of dimensionality) that need to be covered for an accurate uncertainty estimate. In contrast, the computational complexity within APM stayed constant for the additional consideration of biological uncertainties.

Also, other correlation assumption like the beam wise correlation utilized for setup uncertainties can easily be used for biological uncertainties, however, there is no argument supporting this aspect from theoretical considerations.

In this manuscript, biological uncertainties are only modeled in the linear component of the biological effect but can in principle also be considered in the quadratic component. It would even be possible to model correlation or anti-correlation between α_c and β_c as described in Section III.3.3. Further, it is at the moment not possible to directly model differences between in-vivo and in-vitro data since one specific set of photon reference parameter α_x and β_x characterizes a certain endpoint for specific conditions. In the current implementation a change of α_x and β_x , triggers new LEM IV predictions, which is decoupled from the treatment planning and requires subsequently to fit new Gaussian components.

Throughout this work, biological uncertainties are modeled in the tissue response to ion radiation originating from the LQM reference parameter α_x and β_x of photons. To complete the picture, it is necessary to also assume coherently uncertainty in these parameters for the back transformation of the biological effect to the RBE weighted dose domain after optimization. Ideally, the transformation into the RBE weighted dose domain in Equation II.23 needs to be solved in a probabilistic manner by assuming probability distributions in the involved parameters: $\alpha_x \sim \mathcal{N}(\alpha_x, \mu^\alpha, \sigma^\alpha)$ and $\beta_x \sim \mathcal{N}(\beta_x, \mu^\beta, \sigma^\beta)$. Therefore, it is important in the future to report such values with the corresponding PDF to increase the informative value. The back transformation for probabilistic quantities itself is not trivial since the division of Normal distributions with different means and variances is not straightforward. This issue has not yet been solved for which reason this study is only capable of modeling uncertainties in the tissue response of ion radiation.

Biological uncertainties exclusively influence the standard deviation and not the expectation value as the expectation value equals the nominal biological effect if biological uncertainties are modeled via a Normal distribution. Nevertheless, this will change when biological

uncertainties are modeled with a different PDF (e.g., a skewed Normal distribution). The uncertainty quantification in dose introduced by systematic biological uncertainties through standard deviation was demonstrated. Due to the averaging effects of a mixed radiation field the uncertainty in dose becomes smaller than the initial assumption of 25 %. This result is in line with findings made in (Böhlen et al., 2012; Friedrich et al., 2013a).

The uncertainty in dose can be used for probabilistic optimization to minimize the expected objective function value. As mentioned already for the one dimensional phantom case in Section IV.2.1.2 the sole consideration of biological uncertainties leads for probabilistic optimization of the biological effect to an under-dosage of the target structure and ultimately to inferior dose distributions. To address this problem a minimum mean dose constraint was used for the target structure. With this setup, probabilistic optimization accounting for physical or biological and physical uncertainties resulted in very similar (almost identical) results. Thus, the additional consideration of normally distributed biological uncertainties to physical uncertainties did not yield improved treatment plans. Accounting for biological uncertainties during probabilistic optimization it became even harder to steer the optimization by adapting the penalties of objectives to obtain a reasonable good treatment plan. This was the case because the integral variance term strongly out-weights the contribution of the squared deviation objective on the expected biological effect.

To demonstrate the impact of only considering biological uncertainties for probabilistic optimization Figure V.1 is presented. This treatment plan presents an artificial box phantom filled with water and irradiated with two carbon ion beam directions with gantry angle of 0° and 90° . The corresponding couch angles were 0° . For this example, neither a minimum mean dose constraint for the PTV nor a squared deviation objective were defined for the body structure (—). Figure V.1(a) presents the expectation value of the RBE weighted dose $\mathbb{E}[RBE \times d]$ based on conventional optimization (conv.opt) considering biological uncertainties (bioUCT). Note that as explained previously for normally distributed biological uncertainties $\mathbb{E}[RBE \times d] \approx RBE \times d$. Figure V.1(b) presents $\mathbb{E}[RBE \times d]$ from a probabilistic optimization considering biological uncertainties.

From Figure V.1 it can be seen that after probabilistic optimization each beam significantly overshoots the target to create robustness for biological uncertainties. The optimizer favors this solution as the entrance channel of each pencil beam entails a lower biological uncertainty compared to the peak position. Although this plan might be biologically robust, it is not clinically favorable because of hot spots outside the target volume and on top the plan is not robust against physical uncertainties. The second important observation made here, which was also shown in the results (see IV.2.1.2), the mean dose inside the PTV dropped down from 2.988 Gy(RBE) to 2.89 Gy(RBE) since no minimum mean dose constraint was used.

To create biological robustness (Böhlen et al., 2012; Friedrich et al., 2013a) suggested to aim for a more homogenous radiation quality, e.g. LET, throughout the target volume. It was observed in this manuscript that probabilistic optimization yielded treatment plans with damped RBE peaks and consequently to a more homogenous LET. This phenomenon was

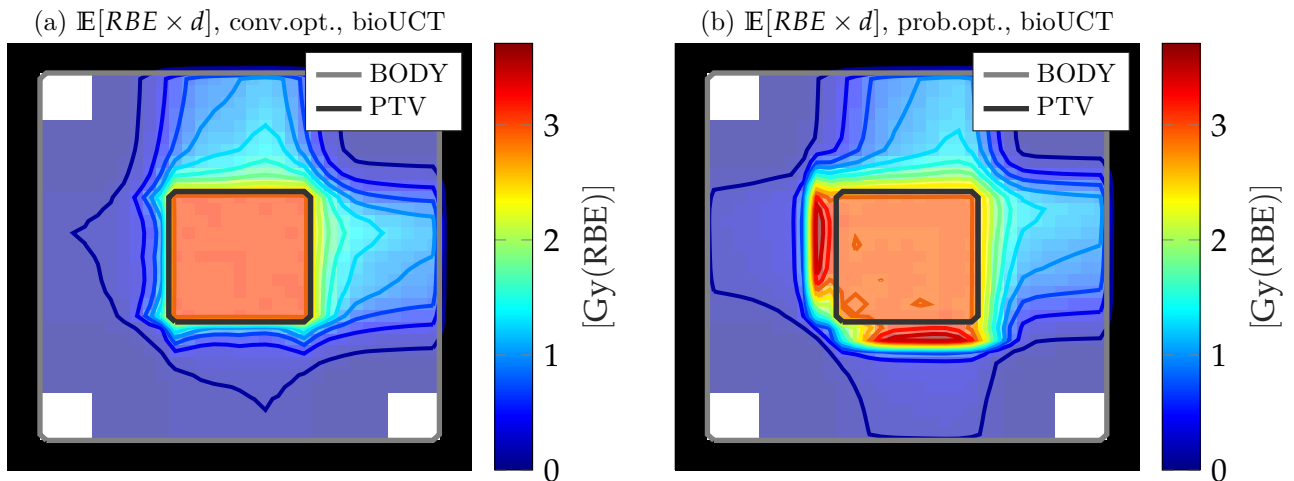


Figure V.1: Transversal CT image of an artificial box phantom with transparent dose colorwash, solid contours and solid isodose lines represent the expected RBE weighted dose ($\mathbb{E}[RBE \times d]$) after conventional optimization in Figure (a). Figure (b) presents $\mathbb{E}[RBE \times d]$ from a probabilistic optimization accounting for biological uncertainties (bioUCT).

indirectly the result of considering physical uncertainties, however, a direct probabilistic optimization on the LET or $LET \times d$ might result in a more homogenous LET. The future challenge is to create treatment plans that are on the one hand robust against physical and biological uncertainties and on the other hand homogenize and increase the LET in the target volume as much as possible by still satisfying given toxicity constraints.

V.6 Gaussian Error Assumption

Through this manuscript, all sources of uncertainties are assumed to obey a Normal distribution. While this is a common standard in radiotherapy, more studies similar to (Holloway et al., 2017) are needed, presenting a method to obtain site-specific probability distributions, in this case for range uncertainties. It is important to mention the APM formalism is not limited to only consider Normal distributions. Other probability distributions can be used too as long as the integral from the method of moments in Equation III.1 can be solved in closed-form. If a proper analytical description of the probability distribution to be modeled does not exist, then it can also be represented with a superposition of Gaussian components. Approximating a non-integrable function by a superposition of Gaussians is one of the core methodical steps of APM. Not only depth-dependent profiles and the lateral pencil beam profile but also the probability distribution of input uncertainties itself can be represented by a superposition of Gaussian components. Therefore the APM formalism is considered flexible in that regard. Following that thought raises the question about the impact of using different PDF in the error assumption which is discussed next.

According to Kamp et al. the shape of the probability distribution modeling the input uncertainties considered for uncertainty analysis for an artificial carbon ion treatment plan was of lower importance. A change from Gaussian distributions to uniformly distributed

random input errors did not have a substantial effect on the sensitivity values and the trends observed in the sensitivity analysis presented by (Kamp et al., 2014). This finding is also confirmed in this manuscript in Section IV.2.1.3 which compared moments from different error assumptions. In particular, other probability distributions were benchmarked against the Gaussian error assumption. The bottom line of the analysis from Section IV.2.1.3 is that the shape of the probability distribution plays an inferior role and that Gaussian error assumptions produce treatment plans that are also robust against other non-Gaussian probability distributions.

According to (Bangert et al., 2013) the uncertainty structure (co-variance) of input uncertainties determines the shape and magnitude of the resulting standard deviation in dose. Further studies are required to best reflect real world conditions with respective co-variance matrices. For instance, instead of the ray-wise correlation assumption for range uncertainties where all pencil beams on the same ray are perfectly correlated and completely uncorrelated otherwise, a smooth transition might be more realistic. Meaning that pencil beams from neighboring rays, e.g. within 2 sigma of the lateral dose, could be modeled as partly correlated.

A Gaussian error assumption for biological uncertainties, where the nominal weights ω^α of individual Gaussian components directly represent the mean value, did not result in improved treatment plans after probabilistic optimization. This might be different when other more complex PDFs are assumed. In particular, the study of (Friedrich et al., 2010) suggests that the α_c parameter might follow a skewed Normal distribution, which causes the expectation value to be different and would as a consequence produce a different probabilistic treatment plan.

As of now, it is possible to model range-, setup- and biological uncertainties within APM, however, geometrical uncertainties induced from motion cannot be modeled (Knopf et al., 2013; Lomax, 2008c)

V.7 Performance

Treatment planning for carbon ions as it is implemented in this work requires to store two influence matrices representing the linear and quadratic component of the biological effect. Therefore treatment planning for carbon ions needs approximately twice the number of numerical computation compared to protons. It was shown in Sections III.2.1 and III.2.2 that the computational complexity of the expected biological effect via APM could be reduced from $\mathcal{O}(I \times J^2)$ to $\mathcal{O}(I \times J)$ through approximations with negligible loss in accuracy. Thus the calculation of the expectation value of the RBE weighted dose is ultimately as expensive as calculating its nominal value. An even bigger reduction in computation complexity could be achieved with the approximations for the standard deviation of the biological effect by reducing the complexity from $\mathcal{O}(I \times J^4)$ to $\mathcal{O}(I \times J^2)$. Considering the twice as many numerical operations for carbon ion treatment planning compared to protons, the complexity class of the standard deviation is identical.

As indicated by the complexity specification \mathcal{O} , the main determining factors for the computation time are the number of voxels I paired with the number of pencil beams J . Although carbon ions entail a reduced lateral scattering of factor ~ 3 compared to protons, the number of dose deposition points in a discretized geometry is usually higher because of the fragmentation tail. Consequently, APM computations for carbon ions are generally longer than for protons. In addition, the correlation model also influences the computation time for the standard deviation significantly. It can be expected that individual voxels of a carbon ion treatment plan possess a higher number of pencil beam contributions compared to protons which lengthens the evaluation of pencil beam combinations jm for certain correlation assumptions. For perfect correlation, as it is the case for biological uncertainties, a quadratic form needs to be fully computed to evaluate all pencil beam combinations. Whereas the ray-wise correlation model used for range uncertainties only requires to evaluate pencil beam combination that are on the same ray.

According to Wahl et al. an approximated standard deviation can be derived by sampling a subset of pencil beam combinations (Wahl et al., 2017). Specifically, the diagonal of pencil beam combinations jj plus sampled off-diagonal combinations were considered. Using sample sizes of 50%, practically halves the computation time and yielded γ -pass rates of $\sim 95\%$ compared to exact reference results depicting three patient cases. This approach offers another way to trade accuracy for performance within the APM formalism.

During the course of this work, it was further investigated to find analytical approximations for the standard deviation to reduce the computational complexity from $\mathcal{O}(I \times J^2)$ to $\mathcal{O}(I \times J)$ to avoid the evaluation of pencil beam combinations for each voxel. The aim was to linearize the second raw moment calculation by using the outer product of the first raw moment plus a correction term accounting for all off-diagonal information. This investigation did not yield meaningful results and was stopped in further consequence, as the uncertainty structure, stored in off-diagonal elements in the covariance matrix is a key factor for calculating the standard deviation.

Once the expectation value and the integral variance influence matrix Ω are available, probabilistic optimization entails a negligible overhead in computation complexity compared to conventional optimization because the Ω matrix is only in $\in \mathbb{R}^{J \times J}$ whereas the expectation value itself is in $\in \mathbb{R}^{I \times J}$. Compared to scenario based robust optimization, which requires the evaluation of individual dose influence error scenario in each step during the optimization, probabilistic optimization based on the probabilistic quantities $\mathbb{E}[\varepsilon]$ and Ω is per definition faster.

The APM prototype was implemented upon a validated treatment planning system in the interpreted numerical programming language Matlab. The computation time for three-dimensional patient cases with a coarse voxel resolution varied from 4 to 8 hours depending on the treatment plan complexity. The given computation time included a conventional optimization, uncertainty quantification, probabilistic optimization and followed again by an uncertainty quantification. The parallel computing toolbox of Matlab using eight parallel

threads along with MEX files evaluating covariance tensor elements was used to speed up the computation time. The run-times are still rather slow compared to a prototype implementation in our C++ based in-house treatment planning system based on the MITK[†] framework (Wolf et al., 2005). It was shown by (Wahl et al., 2017) for protons assuming a constant RBE that APM computations only requires several minutes on a regular desktop machine. A similar runtime can be expected for carbon ion treatment planning accounting for twice the number of numerical operations.

In general, APM provides a better accuracy-performance trade-off, meaning that for the same level of accuracy APM is faster than scenario based sampling (Wahl et al., 2017). The same holds for carbon ions as APM calculation for the patient cases were roughly by factor 4 faster than random sampling, especially for the consideration of fractionation effect.

V.8 Applicability to other Ion Types

This manuscript presents the impact of physical and biological uncertainties on the RBE weighted dose considering a dependence of the RBE on the particle spectra, tissue type and dose level for carbon ion therapy. These aspects are not considered in the work of (Bangert et al., 2013; Wahl et al., 2017, 2018a) who model the impact of physical uncertainties on the physical dose for protons considering a constant RBE of 1.1, which prohibits their application to heavier charged particles showing a stronger RBE dependence. In contrast, the methodology presented here is in general applicable to any other ion type (protons or helium ions) that is based on biological effect based treatment planning. Notwithstanding special care must be taken when the proposed approximations for carbon ions are used for other ion types as they might not be valid per se and yield inaccurate uncertainty estimates.

In recent years, the topic of using a variable RBE model also for protons has been receiving increased attention (Giovannini et al., 2016; McNamara et al., 2015; Wedenberg et al., 2013). There are arguments at the moment on both sides for whether using a constant or variable RBE ranging from the lack of clinical evidence for switching to a different RBE model to a free of doubt correlation between LET and RBE. A potential application of the developed analytical pipeline to protons using a variable RBE is discussed in the following paragraph.

Through LEM IV or other phenomenological RBE models established from in-vitro and partly from in-vivo data, the tissue response to ion radiation can be predicted. Further, they can be processed to obtained dose-averaged radio sensitivity parameter within the LQM for each tissue type and for each initial beam energy. Analog to the work presented here, Gaussian components can be fitted to these profiles and enable a subsequent application of APM. However, the approximations in the analytical moment computation for carbon ions cannot be transferred directly to protons as the squared component of the biological effect exhibits a far bigger contribution to the biological effect than for carbon ions. This

[†]<http://mitk.org> [accessed October 2018]

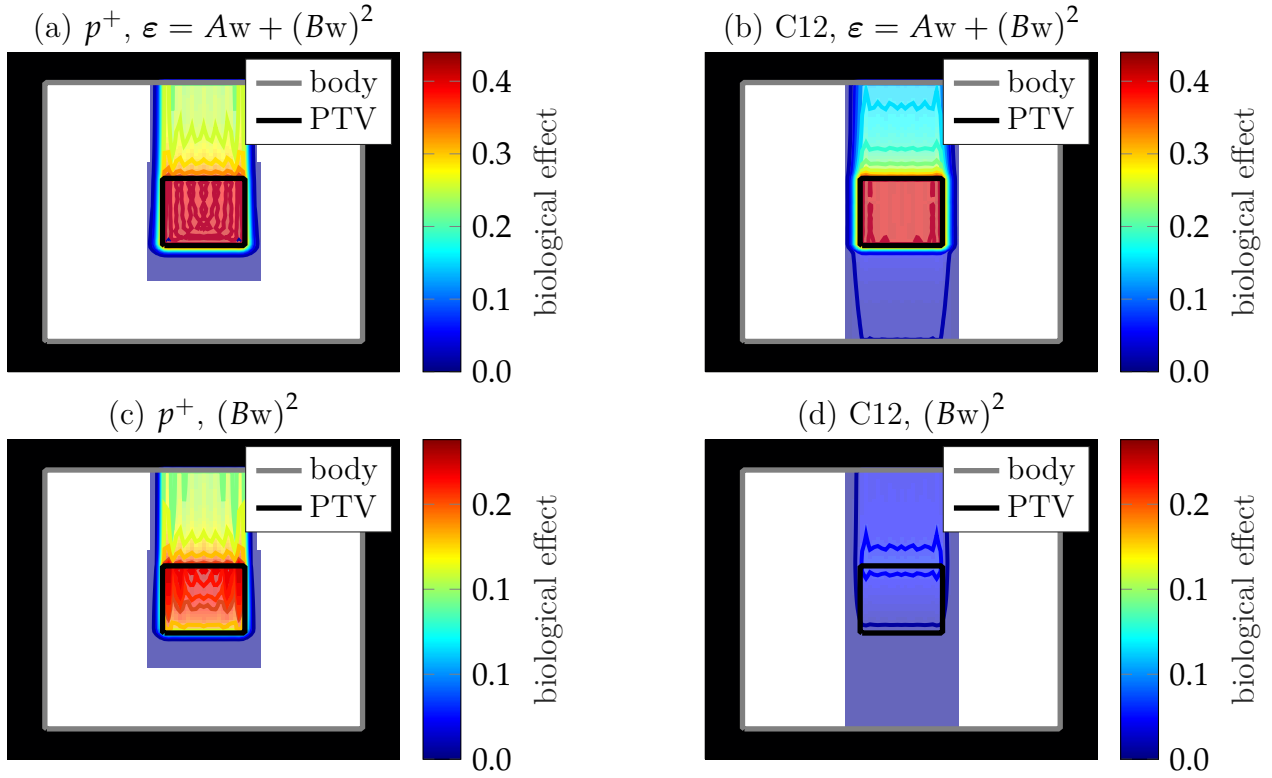


Figure V.2: The biological effect ε of an optimized treatment plan for 2Gy(RBE) for protons in Figure (a) and carbon ions in Figure (b). A tissue characterized with LQM parameter $\alpha_x = 0.1$ [Gy^{-1}] and $\beta_x = 0.05$ [Gy^{-2}] is considered. For protons a variable RBE was used for dose calculation. The quadratic component $(Bw)^2$ of the optimized biological effect is shown for protons in Figure (c) and for carbon ions in Figure (d).

phenomenon is illustrated in Figure V.2 which shows an artificial box phantom irradiated with a single proton beam and a single carbon ion beam. The plan was optimized for 2Gy(RBE) in the PTV which equals for $\alpha_x = 0.1$ [Gy^{-1}] and $\beta_x = 0.05$ [Gy^{-2}] to a prescribed biological effect of 0.4. Figure V.2(a) shows the biological effect ε of protons using the variable RBE model presented in (McNamara et al., 2015). The corresponding quadratic term $(Bw)^2$ of the biological effect is shown in Figure V.2(c). In contrast, Figure V.2(b) denotes ε from an identical treatment plan, however, irradiated with carbon ions using LEM IV. Figure V.2(d) shows the quadratic term $(Bw)^2$ of the biological effect which is in contrast to protons much smaller. Hence the approximations for carbon ions are probably not valid for protons. One theoretical solution to this problem is to perform the full analytical calculation of the standard deviation which is practically infeasible. Thus another approach might be finding new approximations that allow obtaining reasonably accurate results. Concretely, in addition to the second raw moment influence tensor Ξ_{ijm}^α of the αd profile, which needs to be fully calculated for carbon ions, the second raw moment influence tensor for Ξ_{ijm}^β of the βd profile and the second raw moment influence tensor of their combination (mixed components) $\Xi_{ijm}^{\alpha\beta}$ probably need to be computed to include the most important information to calculate an accurate uncertainty estimate.

VI

Conclusion

The two main objectives of this manuscript were to quantify and to mitigate carbon ion treatment plan uncertainties considering physical and biological errors alongside fractionation effects. To address the research questions arising in this context, the thesis facilitated Analytical Probabilistic Modeling (APM), a novel approach for uncertainty management in radiation therapy planning that does not rely on scenario sampling but instead uses closed-form expressions to directly compute and control probabilistic descriptors of radiation therapy treatment plans.

Previously, APM has only been applied for range and setup uncertainties influencing physical dose in photon and proton treatments. In Chapter III it was shown that it is possible to also accommodate the non-linearities emerging from the computation of the relative biological effectiveness of carbon ions within APM for range and setup uncertainties. Specifically, it was demonstrated that it is possible to derive closed-form expressions of the expected biological effect and its covariance. Hereby, the input error space was propagated through the particle dose calculation engine to obtain uncertainties of the biological effect. Representing depth-dependent base data used for analytical carbon ion dose calculation by a superposition of thirteen Gaussian components resulted in a maximum deviation of 0.25 %. This Gaussian parametrization of the dose calculation engine together with Gaussian error assumptions allowed to directly exercise the *method of moments*. Further, APM allowed defining arbitrary linear correlation models to represent setup and range uncertainties. Not only exact analytical expressions were derived in Chapter III but also fast low-rank tensor approximations to calculate the expectation value and standard deviation with minimal loss of accuracy at identical computational complexity to the physical dose. It was shown for the one-dimensional carbon ion SOBP that the biological effect can exactly be calculated, however, the exact computations $\mathcal{O}(I \times J^4)$ are associated with a prohibitive computational effort to be applied for clinical cases. For that reason approximations $\mathcal{O}(I \times J^2)$ were utilized throughout this manuscript. Statistical moments of the biological effect were then in a final

step propagated to moments of the RBE weighted dose using a fourth-order Taylor expansion.

For uncertainties within the biological model that is used to compute RBE weighted dose, a novel uncertainty structure was invented at the end of Chapter III to represent uncertainties in the tissue response from carbon ion irradiation. A key feature of the analytical formulation is that the additional consideration of biological uncertainties did not increase the computational complexity.

Chapter IV.2 demonstrated first for the one-dimensional carbon ion SOBP uncertainty quantification results for the individual and combined consideration of range and biological uncertainties on the RBE weighted dose. The global γ -pass rate yielded for the combined consideration a value of 98.89 % considering (DTA=3 mm, $\Delta d = 3\%$). Modeling the fully-fledged interplay between systematic and random uncertainties on three fractions resulted in an agreement of 94.0 % to sampled references. The imperfect agreement between moments obtained from APM and random sampling can be explained by (i) the approximations made for physical uncertainties, (ii) employed approximations for biological uncertainties, (iii) moment propagation errors from the Taylor expansion and (iv) sampling uncertainties itself. The lower accuracy from the approximations was willingly accepted in exchange for the significantly improved performance.

Section IV.2.1.3 revealed that the Gaussian range error assumptions in combination with probabilistic optimization produce robust treatment plans that are also reasonably robust against other PDFs. Herewith, it is demonstrated that the choice of PDF describing input uncertainties only played an inferior role in probabilistic optimization. For instance, also the assumption of uniformly distributed range errors would be a legitimate choice.

In addition, current clinical practice was mimicked in Section IV.2.1.4 by using LEM I for conventional and probabilistic optimization. A forward dose calculation employing LEM IV revealed, compared to the reference plan, a more homogenous dose for the probabilistically optimized plan. This showed that probabilistic optimization considering range uncertainties reduces discrepancies between different LEM versions due to a homogenization of the LET.

Accordingly, a general observation made for probabilistic optimization considering range uncertainties was an indirect homogenization of the LET and RBE. Thus, a probabilistic optimization accounting for range uncertainties caused a smoothing of LET and RBE peaks. Further, it was shown that the consideration of normally distributed biological uncertainties for probabilistic optimization did not yield improved treatment plans. Consequently, biological uncertainties did not play a decisive role for optimization.

In order to investigate the uncertainty quantification and minimization with APM for realistic treatment scenarios, the open-source treatment planning toolkit matRad was developed in the context of this thesis. Its dose calculation and optimization functionality was successfully validated against the clinically used treatment planning system SyngoRT planning at the Heidelberg Ion-Beam Therapy Center showing beautiful agreement quantified by global γ -pass rates $\geq 99.67\%$ for elementary pencil beams as well as complex patient cases (compare Chapter IV.1). matRad is completely implemented in the interpreted programming language

Matlab, yet still enabled treatment planning for clinically realistic use cases within a couple of minutes. Due to its flexibility and efficiency, matRad also became interesting for colleagues in the field; meanwhile it is used by more than 25 international research groups*.

In a further step, the carbon ion APM algorithm was implemented on top of matRad. The proposed approximations were analyzed in detail in Chapter IV.2 on three-dimensional patient cases revealing good agreement to sampled references as indicated by a minimum global γ -pass rate of 94.95%. Observations made for the one-dimensional SOBP were here confirmed for the three-dimensional patient cases. Regarding computational performance, APM offered a better trade-off between speed and accuracy compared to random sampling.

A subsequent probabilistic optimization, presented in Chapter IV.2 (i) avoided underdosage of the CTV because of wash-out effects, (ii) resulted in a reduced integral dose and (iii) minimized uncertainty in dose for all patient cases. Robustness was created by reducing the in-field dose gradient of each carbon ion beam. Another observation made here was a slight increase of the mean RBE inside the target volume after probabilistic optimization.

A central aspect of the proposed analytical pipeline is that it is not required to calculate individual error scenarios as APM outputs expected- and covariance-influence matrices/tensors which can directly be used for uncertainty quantification and probabilistic optimization.

In conclusion, this manuscript presents first a flexible and accurate analytical method that allows to quantify the uncertainty in dose of carbon ion treatment plans. In a second step, it was demonstrated that the analytical model could be used in probabilistic optimization to minimize uncertainties in dose by remodulating pencil beam intensities in a robust manner. The latter yielded treatment plans that were more robust against involved uncertainties as demonstrated for a number of different clinical scenarios. Along these lines of research, this thesis provides a general characterization of the role of biological models within robust treatment plan optimization.

Future robust treatment planning for carbon ions should first focus on physical uncertainties and LET rather than on biological uncertainties as the inclusion of range uncertainties yields biologically more robust plans. The consideration of normally distributed biological uncertainties does not result in improved treatment plans. Further, it is worth investigating the extension of APM to handle motion uncertainties which is at the moment not possible. This would require to model uncertainties not in the pencil-beam space but instead in the voxel-domain.

It would be interesting to derive new tensor approximations for the standard deviation of the RBE weighted dose assuming a variable RBE for protons. Although the exact analytical expressions, given in this manuscript, are generally valid, it is interesting in this regard which correlation terms need to be considered to obtain a reasonably accurate uncertainty estimate for protons. Another appealing idea is to represent the LET as a superposition of Gaussian

*www.tinyurl.com/matradmap [accessed May, 2019]

to derive by means of APM the complete probabilistic information of the LET. Last but not least, to make full use of the probabilistic information, probabilistic constraints need to be developed for the biological effect to be able to control treatment plan uncertainties.

VII

Summary

Probabilistic Treatment Planning for Carbon Ion Therapy

Intensity-modulated scanned particle therapy in combination with the characteristic depth dose deposition of carbon ions entail a higher sensitivity to physical changes of the patient geometry as compared to photons. As a result, carbon ions may stop at different spatial locations than predicted during treatment planning. But also the patient's response to radiation is uncertain thereby further compromising the quality of the radiation treatment plan. The unknown level of uncertainty in the carbon ion dose requires a patient specific uncertainty analysis and uncertainty mitigation. For this reason the thesis at hand presents a novel method to assess and quantify carbon ion treatment plan uncertainties considering physical uncertainties, biological uncertainties as well as fractionation effects. Second, the manuscript demonstrated how uncertainties were in a subsequent probabilistic optimization mitigated. The proposed methodology was applied to multiple clinical scenarios and its advantageous impact on the carbon ion treatment plan robustness was demonstrated.

On the basis of a concept called Analytical Probabilistic Model (APM) that was used to quantify uncertainties of the proton dose deposition modeling setup and range errors alongside fractionation effects in closed-form, this manuscript presents the extension of APM to carbon ion treatment planning.

Unlike protons, carbon ion treatment planning needs to account for the increased non-linear cell killing of carbon ions in a mixed radiation field which increases the treatment planning complexity. With respect to uncertainties, not only the location of dose deposition is uncertain for carbon ions but also their effectiveness which consequently introduces biological uncertainties to treatment planning.

Different to scenario based approaches, this work presents exact and approximated non-linear closed-form calculations of the expectation value and covariance of the RBE weighted

dose accounting for setup-, range- and biological-uncertainties in fractionated carbon ion therapy. The developed analytical pipeline allows propagating linearly correlated Gaussian input uncertainties through the carbon ion pencil beam dose calculation algorithm to obtain uncertainties in dose.

With I and J being the number of voxels and pencil beams, respectively, low-rank tensor approximations were derived for the expectation value and standard deviation reducing the computational complexity from $\mathcal{O}(I \times J^2)$ to $\mathcal{O}(I \times J)$ and from $\mathcal{O}(I \times J^4)$ to $\mathcal{O}(I \times J^2)$ with minimal loss in accuracy. The consideration of biological errors introduces a new uncertainty structure in the analytical pipeline without increasing the computational complexity. The calculation of expected dose and variance influence information via APM allows performing a subsequent probabilistic optimization.

A proof of concept and several aspects such as accuracy, fractionation and the impact of different probability densities to model input uncertainties were studied in detail on a one-dimensional phantom case. Further, basic three-dimensional dose calculation and optimization functionalities were implemented in the open-source treatment planning system matRad. A subsequent validation against a clinical reference system revealed excellent agreement for elementary pencil beams and patient cases as indicated by γ -pass rates above 99.67%. Theoretical APM derivations were implemented on top and were then applied to clinical carbon ion patient cases. The expectation value and standard deviation of the RBE weighted dose were compared to estimated analogs stemming from 5000 random samples. The γ -pass rate exceeded 94.95% in all patient cases thereby proving the validity of the proposed analytical pipeline. A subsequent probabilistic optimization avoided underdosage of the target volume, reduced the integral dose and resulted in carbon ion treatment plans with a minimized standard deviation of RBE weighted dose. Thus the developed Analytical Probabilistic Model facilitates a flexible, effective and accurate probabilistic description of the radiation treatment plan and generalizes to probabilistic optimization.

In conclusion, the manuscript presents an analytical method to quantify and minimize the uncertainty in the delivery of carbon ion treatment plans. As a result, treatment plans became more robust against the involved uncertainties as demonstrated for a number of clinical scenarios.

VIII

Zusammenfassung

Probabilistische Bestrahlungsplanung für die Kohlenstofftherapie

Die intensitätsmodulierte Partikeltherapie mit beschleunigten Kohlenstoffionen ist aufgrund ihrer charakteristischen Dosisdeposition, im Vergleich zur Photonentherapie, anfälliger gegenüber geometrischen Veränderungen im Patienten. Aus diesem Grund können Kohlenstoffionen an einem anderen Ort im Patienten stoppen als in der Bestrahlungsplanung vorhergesagt. Jedoch wird die Strahlentherapie sowohl durch physikalische Unsicherheiten als auch durch biologische Reaktionen des Patientengewebes beeinflusst, was zu weiteren Unsicherheiten in der vorhergesagten Dosis führt. Die Dosis-Unsicherheiten verlangen eine patientenspezifische Unsicherheitsanalyse sowie eine anschließende Minimierung. Aus diesem Grund beschäftigt sich die vorliegende Arbeit, mit der zentralen Frage wie Unsicherheiten in der Dosis unter der Berücksichtigung von physikalischen und biologischen Variabilitäten sowie Fraktionierungseffekte quantifiziert werden können. Darüber hinaus zeigt diese Arbeit wie die gewonnenen Informationen in einer probabilistischen Optimierung verwendet werden können, um robuste Bestrahlungspläne für Kohlenstoffionen zu erhalten. Die vorgestellte Methode wurde an mehreren klinischen Patientenfällen evaluiert und der vorteilhafte Einfluss der entwickelten Methode wurde an robusten Bestrahlungsplänen dargelegt.

Basierend auf den Ergebnissen zur Analytisch Probabilistischen Modellierung (APM) von Dosisunsicherheiten in der Protonentherapie unter der Berücksichtigung von Positionierungsfehlern, Tiefenunsicherheiten und Fraktionierungseffekte, beschreibt diese Arbeit die konzeptionelle Erweiterung zur Anwendung in der Kohlenstofftherapie. Im Gegensatz zur Photon- und Protontherapie muss jedoch bei der Bestrahlungsplanung mit Kohlenstoffionen die erhöhte nicht-lineare biologische Wirksamkeit in einem gemischten Strahlenfeld berücksichtigt werden. Angesichts dieser Unsicherheiten ist nicht nur der exakte Ort der Energiedeposition unklar sondern auch die biologische Wirksamkeit wodurch nun auch biologische

Unsicherheiten in der Bestrahlungsplanung miteinzubeziehen sind.

Im Unterschied zu szenarienbasierten Ansätzen zeigt diese Arbeit exakte und angenäherte nicht-lineare Berechnungen in geschlossener Form, um den Erwartungswert und die Kovarianz der biologisch wirksamen Dosis für Positionierungsfehler, Tiefen- und Biologischenunsicherheiten in der fraktionierten Kohlenstofftherapie zu berechnen. Der entwickelte analytische Algorithmus ermöglicht es, linear korrelierte Eingangsunsicherheiten in Form von Normalverteilungen durch den Nadelstrahldosisalgorithmus zu propagieren um auf Unsicherheiten in der Dosis zu schließen.

Angenommen I und J repräsentieren die Anzahl der Voxel, sowie die Anzahl der Nadelstrahlen, dann wurden Annäherungen gefunden, welche die Rechenkomplexität bei minimalem Verlust an Genauigkeit für den Erwartungswert von $\mathcal{O}(I \times J^2)$ auf $\mathcal{O}(I \times J)$ und für Standardabweichungen von $\mathcal{O}(I \times J^4)$ auf $\mathcal{O}(I \times J^2)$ reduzieren. Die zusätzliche Betrachtung von biologischen Unsicherheiten erhöht dabei jedoch nicht die ursprüngliche Rechenkomplexität. Die Berechnung von probabilistischen Größen der Dosis ermöglichte in weiterer Folge die Anwendung einer probabilistischen Dosisoptimierung.

Anhand eines eindimensionalen Softwareprototypen wurden die analytisch berechneten probabilistischen Größen auf unterschiedliche Aspekte, wie Genauigkeit, Fraktionierung Validität der Gaußschen Unsicherheitsannahmen analysiert. Anschließend wurden essentielle Dosisberechnungs- und Optimierungsmodule in einem dreidimensionalen Bestrahlungsplanungssystem implementiert und gegen ein klinisches Referenzsystem validiert. Eine γ -Analyse zeigte eine globale Passrate von $\geq 99.67\%$ und bestätigt somit eine fast perfekte Übereinstimmung zu der klinischen Referenzplattform. Darauf basierend wurde APM implementiert und an klinischen Patientenfällen getestet. Die quantifizierten Unsicherheiten in der biologisch effektiven Dosis wurden gegen Schätzungen aus 5000 zufälligen Stichproben verglichen und lieferten in der γ -Analyse eine Übereinstimmung von $\geq 94.95\%$. Dieser Wert lässt auf eine ordnungsgemäße Implementierung und Funktionalität von APM schließen. Eine probabilistische Optimierung verhinderte eine potentielle Unterdosierung des Zielvolumens und resultierte in Bestrahlungsplänen mit reduzierter Unsicherheit in der biologisch effektiven Dosis, wodurch diese als robuster zu betrachten sind. Somit ermöglicht die Analytisch Probabilistischen Modellierung eine flexible, effektive und genaue Unsicherheitsabschätzung der biologisch effektiven Dosis in der Kohlenstofftherapie und erlaubt eine probabilistische Optimierung.

Zusammengefasst stellt die vorliegende Arbeit eine neue analytische Methode zur Quantifizierung und Minimierung von Bestrahlungsplanungsunsicherheiten in der Strahlentherapie mit Kohlenstoff Ionen vor. Die berechneten Bestrahlungspläne für klinische Szenarien wurden durch die vorgestellte Methode robuster gegenüber den involvierten Unsicherheiten.

A

Appendix A

I.1 Properties of Multivariate Normal distributions:

Let $\mathbf{x}, \boldsymbol{\mu}$ be in \mathbb{R}^D and $\Sigma \in \mathbb{R}^{D \times D}$, then a D -dimensional Normal distribution is given by:

$$\mathcal{N}(\mathbf{x}, \boldsymbol{\mu}, \Sigma) = \frac{1}{(2\pi)^{D/2} |\Sigma|^{\frac{1}{2}}} e^{\left[-\frac{1}{2} (\mathbf{x} - \boldsymbol{\mu})^T \Sigma^{-1} (\mathbf{x} - \boldsymbol{\mu}) \right]} \quad (\text{A.1})$$

The integration of a multivariate Normal distribution yields one.

$$\int \mathcal{N}(\mathbf{x} | \boldsymbol{\mu}, \Sigma) d\mathbf{x} = 1 \quad (\text{A.2})$$

Let \mathbf{x} be $[x_1, x_2, \dots, x_r, x_{r+1}, \dots, x_R] \sim \mathcal{N}(\mathbf{x} | \boldsymbol{\mu}, \Sigma)$, then the marginal distribution of a multivariate Normal distribution results again in a multivariate Normal distribution.

$$\begin{aligned} \int \mathcal{N}(\mathbf{x} | \boldsymbol{\mu}, \Sigma) d\mathbf{x} &= \int dx_1 dx_2 \dots, dx_r dx_{r+1} \dots dx_R \mathcal{N}(\mathbf{x} | \boldsymbol{\mu}, \Sigma) = 1 \\ &= \int dx_1 dx_2 \dots, dx_r \mathcal{N}_{1:r}(\mathbf{x}_{1:r} | \boldsymbol{\mu}_{1:r}, \Sigma_{1:r}) \end{aligned} \quad (\text{A.3})$$

The product of two D -dimensional Normal distributions results in turn in a Normal distribution:

$$\mathcal{N}(\mathbf{x} | \boldsymbol{\mu}_1, \Sigma_1) \mathcal{N}(\mathbf{x} | \boldsymbol{\mu}_2, \Sigma_2) = \kappa \mathcal{N}(\mathbf{x} | \boldsymbol{\mu}_3, \Sigma_3) \quad (\text{A.4})$$

$$\text{with: } \kappa = \frac{1}{(2\pi)^{D/2} |\Sigma_1 + \Sigma_2|^{\frac{1}{2}}} e^{\left[-\frac{1}{2} (\boldsymbol{\mu}_1 - \boldsymbol{\mu}_2)^T (\Sigma_1 + \Sigma_2)^{-1} (\boldsymbol{\mu}_1 - \boldsymbol{\mu}_2) \right]}$$

$$\text{with: } \Sigma_3 = (\Sigma_1^{-1} + \Sigma_2^{-1})^{-1} \quad \text{and} \quad \boldsymbol{\mu}_3 = (\Sigma_1^{-1} \boldsymbol{\mu}_1 + \Sigma_2^{-1} \boldsymbol{\mu}_2) \Sigma_3$$

Looking at the moments of a multivariate Normal distribution then the first and second raw moments of \mathbf{x} are given by:

$$\mathbb{E}[\mathbf{x}] = \int \mathcal{N}(\mathbf{x}|\boldsymbol{\mu}, \Sigma) \mathbf{x} d\mathbf{x} = \boldsymbol{\mu} \quad (\text{A.5})$$

$$\mathbb{E}[\mathbf{x}\mathbf{x}^T] = \int \mathcal{N}(\mathbf{x}|\boldsymbol{\mu}, \Sigma) \mathbf{x}\mathbf{x}^T d\mathbf{x} = \boldsymbol{\mu}\boldsymbol{\mu}^T + \Sigma \quad (\text{A.6})$$

I.2 Recurring Symbols and Notation:

Table A.1: Notation and symbols used to describe analytical probabilistic modeling for biological treatment planning

| Notation | Meaning | Description | Complexity |
|----------------------------------|---|--|-------------------------------|
| L | L | lateral dose in x, y | $\mathcal{O}(I \times J)$ |
| \mathcal{L} | $\mathbb{E}[L]$ | 1 st raw moment of lateral dose | $\mathcal{O}(I \times J)$ |
| Y | $\mathbb{E}[L^2]$ | 2 nd raw moment of lateral dose | $\mathcal{O}(I^2 \times J^2)$ |
| Z | Z | depth dose in z | $\mathcal{O}(I \times J)$ |
| \mathcal{Z} | $\mathbb{E}[Z]$ | 1 st raw moment of depth dose | $\mathcal{O}(I \times J)$ |
| Ξ | $\mathbb{E}[Z^2]$ | 2 nd raw moment of depth dose | $\mathcal{O}(I^2 \times J^2)$ |
| D | $L^x L^y Z$ | dose influence matrix | $\mathcal{O}(I \times J)$ |
| \mathcal{D} | $\mathbb{E}[D] = \mathcal{L}^x \mathcal{L}^y \mathcal{Z}$ | expected dose influence matrix | $\mathcal{O}(I \times J)$ |
| \mathfrak{D} | $\mathbb{E}[D^2] = Y^x Y^y \Xi$ | 2 nd raw moment of dose influence matrix | $\mathcal{O}(I^2 \times J^2)$ |
| \mathfrak{V} | $Y^x Y^y \Xi - \mathcal{D}^2 (i = l)$ | variance influence tensor | $\mathcal{O}(I \times J^2)$ |
| \mathfrak{C} | $Y^x Y^y \Xi - \mathcal{D}^2 (i \neq l)$ | covariance influence tensor | $\mathcal{O}(I^2 \times J^2)$ |
| Z^α | Z^α | depth component αd in z | $\mathcal{O}(I \times J)$ |
| \mathcal{Z}^α | $\mathbb{E}[Z^\alpha]$ | 1 st raw moment of depth αd | $\mathcal{O}(I \times J)$ |
| Ξ^α | $\mathbb{E}[Z^{\alpha 2}]$ | 2 nd raw moment of depth αd | $\mathcal{O}(I^2 \times J^2)$ |
| Z^β | Z^β | depth component $\sqrt{\beta} d$ | $\mathcal{O}(I \times J)$ |
| \mathcal{Z}^β | $\mathbb{E}[Z^\beta]$ | 1 st raw moment of depth $\sqrt{\beta} d$ | $\mathcal{O}(I \times J)$ |
| Ξ^β | $\mathbb{E}[Z^{\beta 2}]$ | 2 nd raw moment of depth $\sqrt{\beta} d$ | $\mathcal{O}(I^2 \times J^2)$ |
| A | $L^x L^y Z^\alpha$ | influence matrix of the linear term | $\mathcal{O}(I \times J)$ |
| \mathcal{A} | $\mathbb{E}[A] = \mathcal{L}^x \mathcal{L}^y \mathcal{Z}^\alpha$ | expected linear term of bio. effect | $\mathcal{O}(I \times J)$ |
| Ψ | $\mathbb{E}[A^2] = Y^x Y^y \Xi^\alpha$ | 2nd central moment of linear term of bio. effect | $\mathcal{O}(I^2 \times J^2)$ |
| B | $L^x L^y Z^\beta$ | influence matrix of the squared term | $\mathcal{O}(I \times J)$ |
| \mathcal{B} | $\mathbb{E}[B] = \mathcal{L}^x \mathcal{L}^y \mathcal{Z}^\beta$ | expected squared term of bio. effect | $\mathcal{O}(I \times J)$ |
| Φ | $\mathbb{E}[B^2] = Y^x Y^y \Xi^\beta$ | 2nd central moment of squared term of bio. effect | $\mathcal{O}(I^2 \times J^2)$ |
| ε | $\mathcal{A}\mathbf{w} + (\mathcal{B}\mathbf{w})^2$ | biological effect | $\mathcal{O}(I \times J)$ |
| $\mathbb{E}[\varepsilon]$ | $\mathcal{A}\mathbf{w} + \mathbf{w}^T \Phi \mathbf{w}$ | expected bio. effect | $\mathcal{O}(I \times J^2)$ |
| $\hat{\mathbb{E}}[\varepsilon]$ | $\mathcal{A}\mathbf{w} + (\mathcal{B}\mathbf{w})^2$ | approx. expected bio. effect | $\mathcal{O}(I \times J)$ |
| \mathfrak{D}^ε | - | 2 nd raw moment of bio. effect | $\mathcal{O}(I^2 \times J^4)$ |
| $\hat{\mathfrak{D}}^\varepsilon$ | - | approx. 2 nd raw moment of bio. effect | $\mathcal{O}(I^2 \times J^2)$ |
| $\hat{\mathfrak{C}}^\varepsilon$ | $\hat{\mathfrak{D}}^\varepsilon - \hat{\mathbb{E}}[\varepsilon]^2 (i \neq l)$ | approx. covariance influence tensor of bio. effect | $\mathcal{O}(I^2 \times J^2)$ |

B

Appendix B

II.1 Analytical Moment Calculations

The following sections contain detailed analytical derivations to calculate statistical moments of the lateral dose and the depth dose components as part of the analytical pencil beam dose calculation of charged particles.

II.1.1 First raw moment of the biological effect considering setup and range uncertainties

Let i be the voxel index $\{i \in \mathbb{N} | 1 \leq i \leq I\}$, j, m be pencil beam indices $\{j \in \mathbb{N} | 1 \leq j \leq J\}$ and $\{m \in \mathbb{N} | 1 \leq m \leq M\}$ with J, M defining the total number of pencil beams. Then the expectation value $\mathbb{E}[\cdot]$ of the biological effect ε_i can be derived via:

$$\begin{aligned}
 \mathbb{E}[\varepsilon_i] &= \int d\Delta^x d\Delta^y d\Delta^z p(\Delta^x) p(\Delta^y) p(\Delta^z) \varepsilon_i(\Delta^x, \Delta^y, \Delta^z) \\
 &= \int d\Delta^x d\Delta^y d\Delta^z p(\Delta^x) p(\Delta^y) p(\Delta^z) \left[\sum_{j=1}^J w_j L_{ij}^x L_{ij}^y Z_{ij}^\alpha + \left(\sum_{j=1}^J w_j L_{ij}^x L_{ij}^y Z_{ij}^\beta \right)^2 \right] \\
 &= \sum_j w_j \left\{ \int_{-\infty}^{\infty} d\Delta^x p(\Delta^x) L_{ij}^x \right\} \left\{ \int_{-\infty}^{\infty} d\Delta^y p(\Delta^y) L_{ij}^y \right\} \left\{ \int_{-\infty}^{\infty} d\Delta^z p(\Delta^z) Z_{ij}^\alpha \right\} + \\
 &\quad \sum_{jm} w_j w_m \left\{ \int_{\mathbb{R}^2} d\Delta^x p(\Delta^x) L_{ij}^x L_{im}^x \right\} \left\{ \int_{\mathbb{R}^2} d\Delta^y p(\Delta^y) L_{ij}^y L_{im}^y \right\} \left\{ \int_{\mathbb{R}^2} d\Delta^z p(\Delta^z) Z_{ij}^\beta Z_{im}^\beta \right\} \\
 &= \sum_j w_j \mathcal{L}_{ij}^x \mathcal{L}_{ij}^y Z_{ij}^\alpha + \sum_{jm} w_j w_m Y_{ijim}^x Y_{ijim}^y \Xi_{ijim}^{\sqrt{\beta}} \tag{B.1}
 \end{aligned}$$

where $L_{ij}^{x/y}$ denotes the lateral dose component and $Z_{ij}^{\alpha/\beta}$ the depth dose components of the biological effect. As independent error sources in x, y, z are assumed the integration can be carried out for each component separately. [Link back to main text III.8](#)

II.1.2 Second raw moment of the biological effect considering setup and range uncertainties

Let i, l be the voxel indices in $\{i \in \mathbb{N} | 1 \leq i \leq I\}$ and $\{l \in \mathbb{N} | 1 \leq l \leq L\}$. Further, let j, m, o, q be pencil beam indices and J, M, O, Q be the total number of pencil beams. Then the second raw moment of the biological effect $\mathbb{E}[\varepsilon_i \varepsilon_l]$ can be derived via:

$$\begin{aligned}
 \mathbb{E}[\varepsilon_i \varepsilon_l] &= \int d\Delta^x d\Delta^y d\Delta^z p(\Delta^x) p(\Delta^y) p(\Delta^z) \varepsilon_i(\Delta^x, \Delta^y, \Delta^z) \varepsilon_l(\Delta^x, \Delta^y, \Delta^z) \\
 &= \int d\Delta^x d\Delta^y d\Delta^z p(\Delta^x) p(\Delta^y) p(\Delta^z) \left\{ \sum_j^J w_j L_{ij}^x L_{ij}^y Z_{ij}^\alpha + \left(\sum_j^J w_j L_{ij}^x L_{ij}^y Z_{ij}^\beta \right)^2 \right\} \\
 &\quad \left\{ \sum_m^M w_m L_{lm}^x L_{lm}^y Z_{lm}^\alpha + \left(\sum_m^M w_m L_{lm}^x L_{lm}^y Z_{lm}^\beta \right)^2 \right\}
 \end{aligned} \tag{B.2}$$

Multiplying the curly bracket out and grouping spatial (x, y, z) components together yields:

$$\begin{aligned}
 &= \sum_{jm}^J w_j w_m \left\{ \int d\Delta^x p(\Delta^x) L_{ij}^x L_{lm}^x \right\} \left\{ \int d\Delta^y p(\Delta^y) L_{ij}^y L_{lm}^y \right\} \left\{ \int d\Delta^z p(\Delta^z) Z_{ij}^\alpha Z_{lm}^\alpha \right\} \\
 &+ \sum_{jmq}^J w_j w_m w_q \left\{ \int d\Delta^x p(\Delta^x) L_{ij}^x L_{lm}^x L_{lq}^x \right\} \left\{ \int d\Delta^y p(\Delta^y) L_{ij}^y L_{lm}^y L_{lq}^y \right\} \left\{ \int d\Delta^z p(\Delta^z) Z_{ij}^\alpha Z_{lm}^\beta Z_{lq}^\beta \right\} \\
 &+ \sum_{jmo}^J w_j w_m w_o \left\{ \int d\Delta^x p(\Delta^x) L_{ij}^x L_{lm}^x L_{io}^x \right\} \left\{ \int d\Delta^y p(\Delta^y) L_{ij}^y L_{lm}^y L_{io}^y \right\} \left\{ \int d\Delta^z p(\Delta^z) Z_{ij}^\alpha Z_{lm}^\beta Z_{io}^\beta \right\} \\
 &+ \sum_{jmoq}^J w_j w_m w_o w_q \left\{ \int d\Delta^x p(\Delta^x) L_{ij}^x L_{io}^x L_{lm}^x L_{lq}^x \right\} \left\{ \int d\Delta^y p(\Delta^y) L_{ij}^y L_{io}^y L_{lm}^y L_{lq}^y \right\} \\
 &\quad \left\{ \int d\Delta^z p(\Delta^z) Z_{ij}^{\alpha\beta} Z_{io}^\beta Z_{lm}^\beta Z_{lq}^\beta \right\}
 \end{aligned} \tag{B.3}$$

where for example $\int d\Delta^x p(\Delta^x) L_{ij}^x L_{lm}^x$ represent elements of the second central moment influence tensor of the lateral dose in x dimension. Analog denotes $\int d\Delta^x p(\Delta^x) L_{ij}^x L_{io}^x L_{lm}^x L_{lq}^x$ elements of the fourth central moment influence tensor of the lateral dose. Accordingly can the remaining terms in Equation B.3 be interpreted. Solving the central moment calculations results in:

$$\begin{aligned}
 \mathbb{E}[\varepsilon_i \varepsilon_l] &= \sum_{jm}^J w_j w_m Y_{ijlm}^x Y_{ijlm}^y \Xi_{ijlm}^\alpha + 2 \sum_{jmo}^J w_j w_m w_o Y_{ijlmo}^x Y_{ijlmo}^y \Xi_{ijlmo}^{\alpha 2\beta} + \\
 &\quad \sum_{jmoq}^J w_j w_m w_o w_q Y_{ijlmiolq}^x Y_{ijlmiolq}^y \Xi_{ijlmiolq}^\beta
 \end{aligned} \tag{B.4}$$

As the variance of each voxel i is stored along the diagonal of the covariance matrix $i = l$, we can drop the voxel index l to obtain:

$$\begin{aligned}
 \mathbb{E}[\varepsilon_i \varepsilon_i] &= \sum_{jm}^J w_j w_m Y_{ijm}^x Y_{ijm}^y \Xi_{ijm}^\alpha + 2 \sum_{jmo}^J w_j w_m w_o Y_{ijmo}^x Y_{ijmo}^y \Xi_{ijmo}^{\alpha 2\beta} + \\
 &\quad \sum_{jmoq}^J w_j w_m w_o w_q Y_{ijmoq}^x Y_{ijmoq}^y \Xi_{ijmoq}^\beta
 \end{aligned} \tag{B.5}$$

Equation B.5 was used throughout this thesis to compute the variance of the biological effect. Link back to text III.15

II.1.3 First raw moment of lateral dose component considering setup uncertainties

Assuming $p(\cdot)$ denotes a multivariate Gaussian distribution depicting the setup error in x with mean zero and covariance Σ^x allows deriving the expectation value of the lateral dose \mathcal{L}_{ij}^x via:

$$\begin{aligned}
\mathcal{L}_{ij}^x &= \mathbb{E}[L_{ij}^x(\Delta^x)] = \int_{-\infty}^{\infty} d\Delta^x p(\Delta^x) L_{ij}^x(\Delta^x) \\
&= \int_{-\infty}^{\infty} d\Delta^x \mathcal{N}(\Delta^x|0, \Sigma^x) L_{ij}^x(\Delta^x) = \int_{-\infty}^{\infty} d\Delta_j^x \mathcal{N}(\Delta_j^x|0, \Sigma_{jj}^x) L_{ij}^x(\Delta_j^x) \quad (\text{B.6}) \\
&= \int_{-\infty}^{\infty} d\Delta_j^x \frac{1}{\sqrt{2\pi\Sigma_{jj}^x}} e^{-\frac{(\Delta_j^x)^2}{2\Sigma_{jj}^x}} \frac{1}{\sqrt{2\pi\lambda_{ij}^2}} e^{-\frac{(x_{ij}-\mu_j^x+\Delta_j^x)^2}{2\lambda_{ij}^2}} \\
&= \frac{1}{\sqrt{2\pi(\Sigma_{jj}^x + \lambda_{ij}^2)}} e^{-\frac{(x_{ij}-\mu_j^x)^2}{2(\Sigma_{jj}^x + \lambda_{ij}^2)}} \underbrace{\int d\Delta_j^x \frac{1}{\sqrt{2\pi\tilde{\sigma}^2}} e^{-\frac{(\tilde{\mu}-\Delta_j^x)^2}{2\tilde{\sigma}^2}}}_{=1} \quad (\text{B.7})
\end{aligned}$$

where i indicates the linear voxel index and j the linear pencil beam index. The marginalization property of multivariate Normal distributions introduced in A.3 is used in line B.6. Further, $\tilde{\mu}$ and $\tilde{\sigma}$ represent the parameters of a new Normal distribution (see Equation A.4) whose integration equals 1. Link back to text III.11

II.1.4 Second raw moment of lateral dose component considering setup uncertainties

Let $\mathcal{N}(\Delta_{jm}^x | \mu_{jm}^x, \Lambda_{ijlm})$ denote a bivariate Gaussian distribution with:

$$\text{with: } \mathbf{x}_{ijlm} = \begin{pmatrix} x_{ij} \\ x_{lm} \end{pmatrix}, \boldsymbol{\mu}_{jm}^x = \begin{pmatrix} \mu_j^x \\ \mu_m^x \end{pmatrix}, \boldsymbol{\Delta}_{jm}^x = \begin{pmatrix} \Delta_j^x \\ \Delta_m^x \end{pmatrix}, \Lambda_{ijlm} = \begin{pmatrix} \lambda_{ij}^2 & 0 \\ 0 & \lambda_{lm}^2 \end{pmatrix}, \Sigma_{jm}^x = \begin{pmatrix} \Sigma_{jj}^x & \Sigma_{jm}^x \\ \Sigma_{mj}^x & \Sigma_{mm}^x \end{pmatrix}$$

Then elements of the second raw moment influence tensor of the lateral dose Y_{ijlm}^x can be computed via:

$$\begin{aligned}
Y_{ijlm}^x &= \mathbb{E}[L_{ij}^x L_{lm}^x] = \int d\Delta^x p(\Delta^x) L_{ij}^x L_{lm}^x = \int_{-\infty}^{\infty} d\Delta^x \mathcal{N}(\Delta^x|0, \Sigma^x) L_{ij}^x(\Delta^x) L_{lm}^x(\Delta^x) = \\
&= \int_{-\infty}^{\infty} d\Delta^x \frac{1}{2\pi\sqrt{|\Sigma^x|}} e^{-\frac{1}{2}\Delta^{xT}(\Sigma^x)^{-1}\Delta^x} \frac{1}{\sqrt{2\pi\lambda_{ij}^2}} e^{-\frac{(x_{ij}-\mu_j^x+\Delta_j^x)^2}{2\lambda_{ij}^2}} \frac{1}{\sqrt{2\pi\lambda_{lm}^2}} e^{-\frac{(x_{lm}-\mu_m^x+\Delta_m^x)^2}{2\lambda_{lm}^2}}
\end{aligned}$$

$$\begin{aligned}
 &= \int_{-\infty}^{\infty} d\Delta^x \frac{1}{2\pi\sqrt{|\Sigma^x|}} e^{-\frac{1}{2}\Delta^x T (\Sigma^x)^{-1} \Delta^x} \frac{1}{2\pi\sqrt{|\Lambda_{ijlm}|}} e^{-\frac{1}{2}(\mathbf{x}_{ijlm} - \boldsymbol{\mu}_{jm}^x + \Delta_{jm}^x)^T (\Lambda_{ijlm})^{-1} (\mathbf{x}_{ijlm} - \boldsymbol{\mu}_{jm}^x + \Delta_{jm}^x)} \\
 &= \int_{-\infty}^{\infty} d\Delta^x \frac{1}{2\pi\sqrt{|\Sigma^{jm}|}} e^{-\frac{1}{2}\Delta_{jm}^x T (\Sigma^{jm})^{-1} \Delta_{jm}^x} \frac{1}{2\pi\sqrt{|\Lambda_{ijlm}|}} e^{-\frac{1}{2}(\mathbf{x}_{ijlm} - \boldsymbol{\mu}_{jm}^x + \Delta_{jm}^x)^T (\Lambda_{ijlm})^{-1} (\mathbf{x}_{ijlm} - \boldsymbol{\mu}_{jm}^x + \Delta_{jm}^x)} \\
 &= \frac{1}{2\pi\sqrt{|\Lambda_{ijlm} + \Sigma^{jm}|}} e^{-\frac{1}{2}(\mathbf{x}_{ijlm} - \boldsymbol{\mu}_{jm}^x)^T (\Lambda_{ijlm} + \Sigma^{jm})^{-1} (\mathbf{x}_{ijlm} - \boldsymbol{\mu}_{jm}^x)} \tag{B.8}
 \end{aligned}$$

For a specific voxel combination il , the integration over bivariate Gaussian distributions results in turn in bivariate Gaussian distribution with an adapted width. Link back to text III.18.

II.1.5 Third raw moment of lateral dose component considering setup uncertainties

Let i, l, n be linear voxel indices and j, m, o be linear pencil beam indices. Further, let $\mathcal{N}(\mathbf{x}_{ijlmno} | \boldsymbol{\mu}_{jmo}^x, \Lambda_{ijlmno})$ be a trivariate Gaussian distribution with the following parameter:

$$\mathbf{x}_{ijlmno} = \begin{pmatrix} x_{ij} \\ x_{lm} \\ x_{no} \end{pmatrix}, \boldsymbol{\mu}_{jmo}^x = \begin{pmatrix} \mu_j^x \\ \mu_m^x \\ \mu_o^x \end{pmatrix}, \Lambda_{ijlmno} = \begin{pmatrix} \lambda_{ij}^2 & 0 & 0 \\ 0 & \lambda_{lm}^2 & 0 \\ 0 & 0 & \lambda_{no}^2 \end{pmatrix} \tag{B.9}$$

$$\Delta_{jmo}^x = \begin{pmatrix} \Delta_j^x \\ \Delta_m^x \\ \Delta_o^x \end{pmatrix}, \Sigma^{jmo} = \begin{pmatrix} \Sigma_{jj}^x & \Sigma_{jm}^x & \Sigma_{jo}^x \\ \Sigma_{mj}^x & \Sigma_{mm}^x & \Sigma_{mo}^x \\ \Sigma_{oj}^x & \Sigma_{om}^x & \Sigma_{oo}^x \end{pmatrix} \tag{B.10}$$

Elements of the third central moment influence tensor of the lateral dose component Y_{ijlmno}^x can be derived as follows:

$$\begin{aligned}
 Y_{ijlmno}^x &= \int d\Delta^x p(\Delta^x) L_{ij}^x L_{lm}^x L_{no}^x \\
 &= \int d\Delta^x p(\Delta^x) \frac{1}{\sqrt{2\pi\lambda_{ij}^2}} e^{-\frac{(x_{ij} - \mu_j^x + \Delta_j^x)^2}{2\lambda_{ij}^2}} \frac{1}{\sqrt{2\pi\lambda_{lm}^2}} e^{-\frac{(x_{lm} - \mu_m^x + \Delta_m^x)^2}{2\lambda_{lm}^2}} \frac{1}{\sqrt{2\pi\lambda_{no}^2}} e^{-\frac{(x_{no} - \mu_o^x + \Delta_o^x)^2}{2\lambda_{no}^2}} \\
 &= \int d\Delta^x \frac{1}{(2\pi)^{\frac{3}{2}} \sqrt{|\Sigma^x|}} e^{-\frac{1}{2}\Delta^x T (\Sigma^x)^{-1} \Delta^x} \\
 &\quad \frac{1}{(2\pi)^{\frac{3}{2}} \sqrt{|\Lambda_{ijlmno}|}} e^{-\frac{1}{2}(\mathbf{x}_{ijlmno} - \boldsymbol{\mu}_{jmo}^x + \Delta_{jmo}^x)^T (\Lambda_{ijlmno})^{-1} (\mathbf{x}_{ijlmno} - \boldsymbol{\mu}_{jmo}^x + \Delta_{jmo}^x)}
 \end{aligned}$$

$$\begin{aligned}
 &= \int d\Delta_{jmo}^x \frac{1}{(2\pi)^{\frac{3}{2}} \sqrt{|\Sigma_{jmo}^x|}} e^{-\frac{1}{2} \Delta_{jmo}^{xT} (\Sigma_{jmo}^x)^{-1} \Delta_{jmo}^x} \\
 &\quad \frac{1}{(2\pi)^{\frac{3}{2}} \sqrt{|\Lambda_{ijlmno}|}} e^{-\frac{1}{2} (\mathbf{x}_{ijlmno} - \boldsymbol{\mu}_{jmo}^x + \Delta_{jmo}^x)^T (\Lambda_{ijlmno})^{-1} (\mathbf{x}_{ijlmno} - \boldsymbol{\mu}_{jmo}^x + \Delta_{jmo}^x)} \\
 &= \int d\Delta_{jmo}^x \mathcal{N}(\Delta_{jmo}^x, \mathbf{0}, \Sigma^{jmo}) \mathcal{N}(\mathbf{x}_{ijmo} + \Delta_{jmo}^x, \boldsymbol{\mu}_{jmo}^x, \Lambda_{ijlmno}) \\
 &= \underbrace{\zeta \int d\Delta_{jmo}^x \mathcal{N}(\Delta_{jmo}^x, \boldsymbol{\mu}_{New}^x, \Sigma_{New}^x)}_{=1} \\
 &= \underbrace{\frac{1}{(2\pi)^{\frac{3}{2}} \sqrt{|\Lambda_{ijlmno} + \Sigma^{jmo}|}} e^{-\frac{1}{2} (\mathbf{x}_{ijlmno} - \boldsymbol{\mu}_{jmo}^x)^T (\Lambda_{ijlmno} + \Sigma^{jmo})^{-1} (\mathbf{x}_{ijlmno} - \boldsymbol{\mu}_{jmo}^x)}}_{=\zeta} = 1 \quad (\text{B.11})
 \end{aligned}$$

Link back to text III.18.

II.1.6 First raw moment of depth component considering range uncertainties

Let i be the voxel index $\{i \in \mathbb{N} | 1 \leq i \leq I\}$, j be the pencil beam index with $\{j \in \mathbb{N} | 1 \leq j \leq J\}$, k be the index for the k -th Gaussian component $\{k \in \mathbb{N} | 1 \leq k \leq K\}$, μ_{jk}^z , δ_{jk} , ω_{jk} be the fitted parameter of the k -th Gaussian component of pencil beam j . Then the expectation value $\mathbb{E}[Z_{ij}]$ of depth dependent components Z_{ij} can be derived via:

$$\begin{aligned}
 \mathcal{Z}_{ij} &= \mathbb{E}[Z_{ij}(\Delta^z)] = \int_{-\infty}^{\infty} d\Delta^z p(\Delta^z) Z_{ij}(\Delta^z) \\
 &= \int_{-\infty}^{\infty} d\Delta^z \mathcal{N}(\Delta^z | 0, \Sigma^z) Z_{ij}(\Delta^z) = \int_{-\infty}^{\infty} d\Delta_j^z \mathcal{N}(\Delta_j^z | 0, \Sigma_{jj}^z) Z_{ij}(\Delta_j^z) \\
 &= \int_{-\infty}^{\infty} d\Delta_j^z \frac{1}{\sqrt{2\pi \Sigma_{jj}^z}} e^{-\frac{(\Delta_j^z)^2}{2\Sigma_{jj}^z}} \sum_{k=1}^K \frac{\omega_{jk}}{\sqrt{2\pi \delta_{jk}^2}} e^{-\frac{(z_{ij} - \mu_{jk}^z + \Delta_j^z)^2}{2\delta_{jk}^2}} \\
 &= \sum_{k=1}^K \frac{\omega_{jk}}{\sqrt{2\pi(\delta_{jk}^2 + \Sigma_{jj}^z)}} e^{-\frac{(z_{ij} - \mu_{jk}^z)^2}{2(\delta_{jk}^2 + \Sigma_{jj}^z)}} \quad (\text{B.12})
 \end{aligned}$$

The equation is valid for any depth dose profile (physical dose-, αd - and βd -profile) represented by a superposition of Gaussian components. Link back to text III.12

II.1.7 Second raw moment of depth component considering range uncertainties

For the following considerations the subscript α/β is dropped to provide a generic formulation because the fitted Gaussian parameter could in principle represent any arbitrary profile. Let i, l be voxel indices, j, m be pencil beam indices, k, p be individual Gaussian components

and let $\mathcal{N}(z_{ijlm} | \boldsymbol{\mu}_{jkmp}, \theta_{jkmp})$ denote a bivariate Gaussian distribution, then the second raw moment of the depth dose component Ξ_{ijlm} can be obtained:

$$\text{with: } z_{ijlm} = \begin{pmatrix} z_{ij} \\ z_{lm} \end{pmatrix}, \boldsymbol{\mu}_{jkmp} = \begin{pmatrix} \mu_{jk} \\ \mu_{mp} \end{pmatrix}, \boldsymbol{\Delta}_{jm}^z = \begin{pmatrix} \Delta_j^z \\ \Delta_m^z \end{pmatrix}, \theta_{jkmp} = \begin{pmatrix} \delta_{jk}^2 & 0 \\ 0 & \delta_{mp}^2 \end{pmatrix}, \boldsymbol{\Sigma}^{jm} = \begin{pmatrix} \Sigma_{jj}^z & \Sigma_{jm}^z \\ \Sigma_{mj}^z & \Sigma_{mm}^z \end{pmatrix}$$

$$\begin{aligned} \Xi_{ijlm} &= \mathbb{E}[Z_{ij}Z_{lm}] = \int d\boldsymbol{\Delta}^z Z_{ij}Z_{lm} \int_{-\infty}^{\infty} d\boldsymbol{\Delta}^z \mathcal{N}(\boldsymbol{\Delta}^z | 0, \boldsymbol{\Sigma}^z) Z_{ij}(\boldsymbol{\Delta}^z) Z_{lm}(\boldsymbol{\Delta}^z) = \\ &= \int_{-\infty}^{\infty} d\boldsymbol{\Delta}^z \frac{1}{2\pi\sqrt{|\boldsymbol{\Sigma}^z|}} e^{-\frac{1}{2}\boldsymbol{\Delta}^{zT}(\boldsymbol{\Sigma}^z)^{-1}\boldsymbol{\Delta}^z} \sum_{k=1}^K \frac{\omega_{jk}}{\sqrt{2\pi\delta_{jk}^2}} e^{-\frac{(z_{ij}-\mu_{jk}+\Delta_j^z)^2}{2\delta_{jk}^2}} \sum_{p=1}^{PQ} \frac{\omega_{mp}}{\sqrt{2\pi\delta_{mp}^2}} e^{-\frac{(z_{lm}-\mu_{mp}+\Delta_m^z)^2}{2\delta_{mp}^2}} \end{aligned} \quad (\text{B.13})$$

$$\begin{aligned} &= \int_{-\infty}^{\infty} d\boldsymbol{\Delta}^z \frac{1}{2\pi\sqrt{|\boldsymbol{\Sigma}^z|}} e^{-\frac{1}{2}\boldsymbol{\Delta}^{zT}(\boldsymbol{\Sigma}^z)^{-1}\boldsymbol{\Delta}^z} \\ &\quad \sum_{kp} \frac{\omega_{jk}\omega_{mp}}{2\pi\sqrt{|\theta_{jkmp}|}} e^{-\frac{1}{2}(z_{ijlm}-\boldsymbol{\mu}_{jkmp}+\boldsymbol{\Delta}_{jm}^z)^T(\theta_{jkmp})^{-1}(z_{ijlm}-\boldsymbol{\mu}_{jkmp}+\boldsymbol{\Delta}_{jm}^z)} \\ &= \int_{-\infty}^{\infty} d\boldsymbol{\Delta}_{jm}^z \frac{1}{2\pi\sqrt{|\boldsymbol{\Sigma}^{jm}|}} e^{-\frac{1}{2}\boldsymbol{\Delta}_{jm}^{zT}(\boldsymbol{\Sigma}^{jm})^{-1}\boldsymbol{\Delta}_{jm}^z} \\ &\quad \sum_{kp} \frac{\omega_{jk}\omega_{mp}}{2\pi\sqrt{|\theta_{jkmp}|}} e^{-\frac{1}{2}(z_{ijlm}-\boldsymbol{\mu}_{jkmp}^z+\boldsymbol{\Delta}_{jm}^z)^T(\theta_{jkmp})^{-1}(z_{ijlm}-\boldsymbol{\mu}_{jkmp}^z+\boldsymbol{\Delta}_{jm}^z)} \\ &= \sum_{kp} \frac{\omega_{jk}\omega_{mp}}{2\pi\sqrt{|\theta_{jkmp} + \boldsymbol{\Sigma}^{jm}|}} e^{-\frac{1}{2}(z_{ijlm}-\boldsymbol{\mu}_{jkmp})^T(\theta_{jkmp} + \boldsymbol{\Sigma}^{jm})^{-1}(z_{ijlm}-\boldsymbol{\mu}_{jkmp})} \end{aligned} \quad (\text{B.14})$$

Link back to text III.19.

II.1.8 Third raw moment of depth component considering range uncertainties

As an example, the deviation for $\Xi_{ijlmno}^{\alpha 2\beta}$ is presented below. Given i, l, n denote voxel indices, j, m, o pencil beam indices and k, p, r individual Gaussian components, we can define

$$\begin{aligned} \mathbf{z}_{ijlmno} &= \begin{pmatrix} z_{ij} \\ z_{lm} \\ z_{no} \end{pmatrix}, \quad \boldsymbol{\mu}_{jkmpor}^z = \begin{pmatrix} \mu_{jk}^\alpha \\ \mu_{mp}^\beta \\ \mu_{or}^\beta \end{pmatrix}, \quad \Delta_{jmo}^z = \begin{pmatrix} \Delta_j^z \\ \Delta_m^z \\ \Delta_o^z \end{pmatrix} \\ \Theta_{jkmpor} &= \begin{pmatrix} \delta_{jk}^{\alpha 2} & 0 & 0 \\ 0 & \delta_{mp}^{\beta 2} & 0 \\ 0 & 0 & \delta_{or}^{\beta 2} \end{pmatrix}, \quad \Sigma^{jmo} = \begin{pmatrix} \Sigma_{jj}^z & \Sigma_{mj}^z & \Sigma_{oj}^z \\ \Sigma_{jm}^z & \Sigma_{mm}^z & \Sigma_{om}^z \\ \Sigma_{jo}^z & \Sigma_{mo}^z & \Sigma_{oo}^z \end{pmatrix} \end{aligned} \quad (\text{B.15})$$

to solve:

$$\begin{aligned} \Xi_{ijlmno}^{\alpha 2\beta} &= \int d\Delta^z p(\Delta^z) Z_{ij}^\alpha Z_{lm}^\beta Z_{no}^\beta \\ &= \int d\Delta^z p(\Delta^z) \sum_{kpr=1}^{13} \frac{\omega_{jk}^\alpha}{\sqrt{2\pi\delta_{jk}^{\alpha 2}}} e^{\frac{(z_{ij}-\mu_{jk}^\alpha)^2}{2\delta_{jk}^{\alpha 2}}} \frac{\omega_{mp}^\beta}{\sqrt{2\pi\delta_{mp}^{\beta 2}}} e^{\frac{(z_{lm}-\mu_{mp}^\beta)^2}{2\delta_{mp}^{\beta 2}}} \frac{\omega_{or}^\beta}{\sqrt{2\pi\delta_{or}^{\beta 2}}} e^{\frac{(z_{no}-\mu_{or}^\beta)^2}{2\delta_{or}^{\beta 2}}} \\ &= \int d\Delta^z p(\Delta^z) \sum_{kpr=1}^{13} \frac{\omega_{jk}^\alpha \omega_{mp}^\beta \omega_{or}^\beta}{(2\pi)^{\frac{3}{2}} \sqrt{|\Theta_{jkmpor}|}} e^{-\frac{1}{2}(\mathbf{z}_{ijlmno} - \boldsymbol{\mu}_{jkmpor}^z)^T (\Theta_{jkmpor})^{-1} (\mathbf{z}_{ijlmno} - \boldsymbol{\mu}_{jkmpor}^z)} \\ &= \sum_{kpr=1}^{13} \omega_{jk}^\alpha \omega_{mp}^\beta \omega_{or}^\beta \int d\Delta_{jmo}^z \frac{1}{(2\pi)^{\frac{3}{2}} \sqrt{|\Sigma^{jmo}|}} \\ &\quad \frac{1}{(2\pi)^{\frac{3}{2}} \sqrt{|\Theta_{jkmpor}|}} e^{-\frac{1}{2}(\mathbf{z}_{ijlmno} - \boldsymbol{\mu}_{jkmpor}^z)^T (\Theta_{jkmpor})^{-1} (\mathbf{z}_{ijlmno} - \boldsymbol{\mu}_{jkmpor}^z)} \\ &= \sum_{kpr=1}^{13} \frac{\omega_{jk}^\alpha \omega_{mp}^\beta \omega_{or}^\beta}{(2\pi)^{\frac{3}{2}} \sqrt{|\Theta_{jkmpor} + \Sigma^{jmo}|}} e^{-\frac{1}{2}(\mathbf{z}_{ijlmno} - \boldsymbol{\mu}_{jkmpor}^z)^T (\Theta_{jkmpor} + \Sigma^{jmo})^{-1} (\mathbf{z}_{ijlmno} - \boldsymbol{\mu}_{jkmpor}^z)} \end{aligned} \quad (\text{B.16})$$

II.1.9 Second central moment considering fractionation

The second central moment of the biological effect $\mathbb{E}[\varepsilon_i^F \varepsilon_l^F]$ in a fractionated carbon ion treatment can be derived by:

$$\begin{aligned}
 \mathbb{E}[\varepsilon_i^F \varepsilon_l^F] &= \int_{-\infty}^{\infty} d\Delta^{sys} \mathcal{N}(\Delta^{sys}|0, \Sigma^{sys}) d\Delta_f^{rnd} \mathcal{N}(\Delta_f^{rnd}|0, \Sigma^{rnd}) \\
 &\quad \left\{ \sum_{f=1}^F \left[\sum_{j=1}^J w_j A_{ij}^f(\Delta^{sys}, \Delta_f^{rnd}) + \left(\sum_{j=1}^J w_j B_{ij}^f(\Delta^{sys}, \Delta_f^{rnd}) \right)^2 \right] \right\}^2 \\
 &= \int_{-\infty}^{\infty} d\Delta^{sys} \mathcal{N}(\Delta^{sys}|0, \Sigma^{sys}) d\Delta_f^{rnd} \mathcal{N}(\Delta_f^{rnd}|0, \Sigma^{rnd}) \\
 &\quad \sum_{f=1}^F \sum_{g=1}^F \left\{ \left[\sum_{j=1}^J w_j A_{ij}^f(\Delta^{sys}, \Delta_f^{rnd}) + \left(\sum_{j=1}^J w_j B_{ij}^f(\Delta^{sys}, \Delta_f^{rnd}) \right)^2 \right] \right. \\
 &\quad \left. \left[\sum_{m=1}^M w_m A_{lm}^g(\Delta^{sys}, \Delta_g^{rnd}) + \left(\sum_{m=1}^M w_m B_{lm}^g(\Delta^{sys}, \Delta_g^{rnd}) \right)^2 \right] \right\}
 \end{aligned} \tag{B.17}$$

(B.18)

In Equation B.17, terms are multiplied out and the sum over f and g is applied to each resulting term to derive:

$$\begin{aligned}
 \mathbb{E}[\varepsilon_i^F \varepsilon_l^F] &= \int_{-\infty}^{\infty} d\Delta^{sys} \mathcal{N}(\Delta^{sys}|0, \Sigma^{sys}) d\Delta_f^{rnd} \mathcal{N}(\Delta_f^{rnd}|0, \Sigma^{rnd}) \\
 &\quad \left\{ \underbrace{\sum_{fg=1}^F \left[\left(\sum_j^B w_j A_{ij}^f \right) \left(\sum_m^M w_m A_{lm}^g \right) \right]}_{\sum_{jm}^J Y_{ijlm}^x Y_{ijlm}^y \Xi_{ijlm}^\alpha} + \underbrace{\sum_{fg=1}^F \left[\left(\sum_j^B w_j A_{ij}^f \right) \left(\sum_m^M w_m B_{lm}^g \right)^2 \right]}_{\sum_{jmo}^J Y_{ijlmo}^x Y_{ijlmo}^y \Xi_{ijlmo}^{\alpha 2\beta}} + \right. \\
 &\quad \left. \underbrace{\sum_{fg=1}^F \left[\left(\sum_m^M w_m A_{lm}^g \right) \left(\sum_j^B w_j B_{ij}^f \right)^2 \right]}_{\sum_{jmo}^J Y_{ijlmo}^x Y_{ijlmo}^y \Xi_{ijlmo}^{\alpha 2\beta}} + \underbrace{\sum_{fg=1}^F \left[\left(\sum_j^B w_j B_{ij}^f \right)^2 \left(\sum_m^M w_m B_{lm}^g \right)^2 \right]}_{\text{see Equation III.15}} \right\}
 \end{aligned} \tag{B.19}$$

Link back to text III.27.

II.1.10 First raw moment of depth components considering biological and range uncertainties

Exemplary, the computation of the expectation value of the Z^α depth component is shown. Let $p(\omega^\alpha)$ obey a Normal distribution with $\mathcal{N}(\omega^\alpha | \mu^{\omega^\alpha}, \Sigma^{\omega^\alpha})$ with $\mu^{\omega^\alpha} = \omega^\alpha$.

$$\begin{aligned}
Z_{ij}^\alpha &= \mathbb{E}[Z_{ij}^\alpha(\Delta^z, \omega^\alpha)] = \int_{-\infty}^{\infty} \int_{-\infty}^{\infty} d\Delta^z d\omega^\alpha p(\Delta^z) p(\omega^\alpha) Z_{ij}^\alpha(\Delta^z, \omega^\alpha) \\
&= \int_{-\infty}^{\infty} d\omega^\alpha p(\omega^\alpha) \sum_{k=1}^K \frac{\omega_{jk}^\alpha}{\sqrt{2\pi(\delta_{jk}^{\alpha 2} + \Sigma_{jj}^z)}} e^{-\frac{(z_{ij} - \mu_{jk}^\alpha)^2}{2(\delta_{jk}^{\alpha 2} + \Sigma_{jj}^z)}} \\
&= \int_{-\infty}^{\infty} d\omega^\alpha \mathcal{N}(\omega^\alpha | \mu^{\omega^\alpha}, \Sigma^{\omega^\alpha}) \sum_{k=1}^K \frac{\omega_{jk}^\alpha}{\sqrt{2\pi(\delta_{jk}^{\alpha 2} + \Sigma_{jj}^z)}} e^{-\frac{(z_{ij} - \mu_{jk}^\alpha)^2}{2(\delta_{jk}^{\alpha 2} + \Sigma_{jj}^z)}} \\
&= \sum_{k=1}^K \underbrace{\int_{-\infty}^{\infty} d\omega_{jk}^\alpha \frac{1}{\sqrt{2\pi\Sigma_{jkk}^{\omega^\alpha}}} e^{-\frac{(\omega_{jk}^\alpha - \mu_{jk}^{\omega^\alpha})^2}{2\Sigma_{jkk}^{\omega^\alpha}}}}_{=1} \frac{\omega_{jk}^\alpha}{\sqrt{2\pi(\delta_{jk}^{\alpha 2} + \Sigma_{jj}^z)}} e^{-\frac{(z_{ij} - \mu_{jk}^\alpha)^2}{2(\delta_{jk}^{\alpha 2} + \Sigma_{jj}^z)}} \\
&= \sum_{k=1}^K \frac{\omega_{jk}^\alpha}{\sqrt{2\pi(\delta_{jk}^{\alpha 2} + \Sigma_{jj}^z)}} e^{-\frac{(z_{ij} - \mu_{jk}^\alpha)^2}{2(\delta_{jk}^{\alpha 2} + \Sigma_{jj}^z)}} \tag{B.20}
\end{aligned}$$

Link back to text III.40.

II.1.11 Second raw moment of depth components considering biological and range uncertainties

Exemplary, the computation of the second raw moment the Z^α depth component is shown below. Again it is assumed $p(\omega^\alpha)$ obeys a Normal distribution $\mathcal{N}(\omega^\alpha | \boldsymbol{\mu}^{\omega^\alpha}, \boldsymbol{\Sigma}^{\omega^\alpha})$ with $\boldsymbol{\mu}^{\omega^\alpha} = \boldsymbol{\omega}^\alpha$.

$$\begin{aligned}
\Xi_{ijlm}^\alpha &= \mathbb{E}[Z_{ij}^\alpha(\Delta^z, \boldsymbol{\omega}^\alpha), Z_{lm}^\alpha(\Delta^z, \boldsymbol{\omega}^\alpha)] \\
&= \int_{-\infty}^{\infty} \int_{-\infty}^{\infty} d\Delta^z d\boldsymbol{\omega}^\alpha p(\Delta^z) p(\boldsymbol{\omega}^\alpha) Z_{ij}^\alpha(\Delta^z, \boldsymbol{\omega}^\alpha) Z_{lm}^\alpha(\Delta^z, \boldsymbol{\omega}^\alpha) \\
&= \int_{-\infty}^{\infty} d\boldsymbol{\omega}^\alpha \mathcal{N}(\boldsymbol{\omega}^\alpha | \boldsymbol{\mu}^{\omega^\alpha}, \boldsymbol{\Sigma}^{\omega^\alpha}) \\
&\quad \sum_{kp} \frac{\omega_{jk}^\alpha \omega_{mp}^\alpha}{2\pi \sqrt{|\theta_{jkmp}^\alpha + \boldsymbol{\Sigma}^{jm}|}} e^{-\frac{1}{2}(\mathbf{z}_{ijlm} - \boldsymbol{\mu}_{jkmp}^\alpha)^T (\boldsymbol{\theta}_{jkmp}^\alpha + \boldsymbol{\Sigma}^{jm})^{-1} (\mathbf{z}_{ijlm} - \boldsymbol{\mu}_{jkmp}^\alpha)} \\
&= \underbrace{\int_{-\infty}^{\infty} d\boldsymbol{\omega}^\alpha \mathcal{N}(\boldsymbol{\omega} | \boldsymbol{\mu}^{\omega^\alpha}, \boldsymbol{\Sigma}^{\omega^\alpha}) \omega_j^\alpha \omega_m^{\alpha T}}_{\mathbb{E}[\omega_j^\alpha \omega_m^{\alpha T}] = \boldsymbol{\mu}^{\omega^\alpha} \boldsymbol{\mu}^{\omega^\alpha T} + \boldsymbol{\Sigma}^{\omega^\alpha} = \boldsymbol{\omega}_j^\alpha \boldsymbol{\omega}_m^{\alpha T} + \boldsymbol{\Sigma}^{\omega^\alpha}} \\
&\quad \sum_{kp} \frac{1}{2\pi \sqrt{|\theta_{jkmp}^\alpha + \boldsymbol{\Sigma}^{jm}|}} e^{-\frac{1}{2}(\mathbf{z}_{ijlm} - \boldsymbol{\mu}_{jkmp}^\alpha)^T (\boldsymbol{\theta}_{jkmp}^\alpha + \boldsymbol{\Sigma}^{jm})^{-1} (\mathbf{z}_{ijlm} - \boldsymbol{\mu}_{jkmp}^\alpha)} \\
&= \sum_{kp} \frac{\omega_{jk}^\alpha \omega_{mp}^\alpha + \boldsymbol{\Sigma}_{kp}^{\omega_{jm}}}{2\pi \sqrt{|\theta_{jkmp}^\alpha + \boldsymbol{\Sigma}^{jm}|}} e^{-\frac{1}{2}(\mathbf{z}_{ijlm} - \boldsymbol{\mu}_{jkmp}^\alpha)^T (\boldsymbol{\theta}_{jkmp}^\alpha + \boldsymbol{\Sigma}^{jm})^{-1} (\mathbf{z}_{ijlm} - \boldsymbol{\mu}_{jkmp}^\alpha)} \tag{B.21}
\end{aligned}$$

Link back to Equation III.44.

Bibliography

- Ahn, S. and Fessler, J. A. (2003). Standard Errors of Mean, Variance, and Standard Deviation Estimators. 77
- Albertini, F., Hug, E. B., and Lomax, A. J. (2011). Is it necessary to plan with safety margins for actively scanned proton therapy? *Physics in Medicine and Biology*, 56(14):4399–4413. 35, 37
- Anderson, T. V. and Mattson, C. A. (2012). Propagating Skewness and Kurtosis Through Engineering Models for Low-Cost, Meaningful, Nondeterministic Design. *Journal of Mechanical Design*, 134(10):100911. 72
- Atun, R., Jaffray, D. A., Barton, M. B., Bray, F., Baumann, M., Vikram, B., Hanna, T. P., Knaul, F. M., Lievens, Y., Lui, T. Y., Milosevic, M., O’Sullivan, B., Rodin, D. L., Rosenblatt, E., Van Dyk, J., Yap, M. L., Zubizarreta, E., and Gospodarowicz, M. (2015). Expanding global access to radiotherapy. *The Lancet Oncology*, 16(10):1153–1186. 1
- Bai, X., Lim, G., Wieser, H.-P., Bangert, M., Grosshans, D., Mohan, R., and Cao, W. (2019). Robust optimization to reduce the impact of biological effect variation from physical uncertainties in intensity-modulated proton therapy. *Physics in Medicine & Biology*, 64(2):025004. 164
- Bangert, M., Hennig, P., and Oelfke, U. (2013). Analytical probabilistic modeling for radiation therapy treatment planning. *Physics in medicine and biology*, 58:5401–19. ii, 39, 40, 42, 43, 47, 56, 59, 70, 111, 122, 124, 126, 127, 129, 133, 135
- Battistoni, G., Bauer, J., Boehlen, T. T., Cerutti, F., Chin, M. P. W., Dos Santos Augusto, R., Ferrari, A., Ortega, P. G., Kozłowska, W., Magro, G., Mairani, A., Parodi, K., Sala, P. R., Schoofs, P., Tessonier, T., and Vlachoudis, V. (2016). The FLUKA Code: An Accurate Simulation Tool for Particle Therapy. *Frontiers in Oncology*. 126
- Baum, C., Alber, M., Birkner, M., and Nüsslin, F. (2004). Treatment simulation approaches for the estimation of the distributions of treatment quality parameters generated by geometrical uncertainties. *Physics in medicine and biology*, 49(24):5475–5488. 35
- Baum, C., Alber, M., Birkner, M., and Nüsslin, F. (2006). Robust treatment planning for intensity modulated radiotherapy of prostate cancer based on coverage probabilities. *Radiotherapy and oncology : journal of the European Society for Therapeutic Radiology and Oncology*, 78(1):27–35. 39
- Bellinzona, V., Ciocca, M., Embriaco, a., Fontana, a., Mairani, a., Mori, M., and Parodi, K. (2015). On the parametrization of lateral dose profiles in proton radiation therapy. *Physica Medica*, 31(5):1–9. 22
- Bethe, H. (1930). Zur Theorie des Durchgangs schneller Korpuskularstrahlen durch Materie. *Annalen der Physik*, 397(3):325–400. 7
- Bichsel, H. (2013). *Stochastics of Energy Loss and Biological Effects of Heavy Ions in Radiation Therapy*, volume 65. Elsevier Inc. 6
- Bishop, C. M. (2006). *Pattern Recognition and Machine Learning*. Springer Verlag. 67
- Bloch, F. (1933). Zur Bremsung rasch bewegter Teilchen beim Durchgang durch Materie. *Annalen der Physik*, 408(3):285–320. 7
- Böhlen, T. T., Brons, S., Dosanjh, M., Ferrari, A., Fossati, P., Haberer, T., Patera, V., and Mairani, A. (2012). Investigating the robustness of ion beam therapy treatment plans to uncertainties in biological treatment parameters. *Physics in Medicine and Biology*, 57(23):7983–8004. 33, 34, 93, 109, 131
- Bortfeld, T. (1997). An analytical approximation of the Bragg curve for therapeutic proton beams. *Medical Physics*, 24(12):2024. 7, 42
- Bortfeld, T. (2006). IMRT: a review and preview. *Physics in medicine and biology*, 51(13):R363–R379. 3
- Bortfeld, T., Jiang, S. B., and Rietzel, E. (2004). Effects of motion on the total dose distribution. *Seminars in radiation oncology*, 14(1):41–51. 36
- Brüningk, S. C., Kamp, F., and Wilkens, J. J. (2015). EUD-based biological optimization for carbon ion therapy. *Medical Physics*, 42(11):6248–6257. 28
- Casiraghi, M., Albertini, F., and Lomax, a. J. (2013). Advantages and limitations of the ‘worst case scenario’ approach in IMPT treatment planning. *Physics in medicine and biology*, 58(5):1323–39. 35, 36
- Charlie Ma, C.-M. and Lomax, T., editors (2012). *Proton and Carbon Ion Therapy*. CRC Press. 2
- Chen, W., Unkelbach, J., Trofimov, A., Madden, T., Kooy, H., Bortfeld, T., and Craft, D. (2012). Including robustness in multi-criteria optimization for intensity-modulated proton therapy. *Physics in Medicine and Biology*, 57:591–608. 37, 38
- Cisternas, E., Mairani, A., Ziegenhein, P., Jaekel, O., and Bangert, M. (2015). matRad - a multi-modality open source 3D treatment planning toolkit. *IFMBE Proceedings*, 51:1608–1611. 21, 80
- Civinini, C., Bonanno, D., Brianzi, M., Carpinelli, M., Cirrone, G., Cuttone, G., Presti, D. L., Maccioni, G., Pallotta, S., Randazzo, N., Scaringella, M., Romano, F., Sipala, V., Talamonti, C., Vanzi, E., and Bruzzi, M. (2017). Proton Computed Tomography: iterative image reconstruction and dose evaluation. *Journal of Instrumentation*, 12(01):C01034–C01034. 34
- Combs, S. E. and Debus, J. (2013). Treatment with heavy charged particles: Systematic review of clinical data and current clinical (comparative) trials. *Acta Oncologica*, 52(7):1272–1286. 2
- Craft, D., Bangert, M., Long, T., Papp, D., and Unkelbach, J. (2014). Shared data for intensity modulated radiation therapy (IMRT) optimization research: the CORT dataset. *GigaScience*, 3(1):37. 74

- Durante, M. and Paganetti, H. (2016). Nuclear physics in particle therapy: a review. *Reports on Progress in Physics*, 79(9):096702. 6
- Elsässer, T., Cunrath, R., Krämer, M., and Scholz, M. (2008). Impact of track structure calculations on biological treatment planning in ion radiotherapy. *New Journal of Physics*, 10. 17, 33
- Elsässer, T. and Scholz, M. (2007). Cluster Effects within the Local Effect Model. *Radiation Research*, 167(3):319–329. 17
- Elsässer, T., Weyrather, W. K., Friedrich, T., Durante, M., Iancu, G., Krämer, M., Kragl, G., Brons, S., Winter, M., Weber, K. J., and Scholz, M. (2010). Quantification of the relative biological effectiveness for ion beam radiotherapy: Direct experimental comparison of proton and carbon ion beams and a novel approach for treatment planning. *International Journal of Radiation Oncology Biology Physics*, 78:1177–1183. 17
- Fano, U. (1963). Penetration of Protons, Alpha Particles, and Mesons. *Annual Review of Nuclear Science*, 13(1):1–66. 7
- Fredriksson, A. (2012). A characterization of robust radiation therapy treatment planning methods—from expected value to worst case optimization. *Medical Physics*, 39(8):5169–5181. 127
- Fredriksson, A. and Bokrantz, R. (2014). A critical evaluation of worst case optimization methods for robust intensity-modulated proton therapy planning. *Medical Physics*, 41(8):081701. 38
- Fredriksson, A. and Bokrantz, R. (2016). The scenario-based generalization of radiation therapy margins. *Physics in medicine and biology*, 61(5):2067–82. 37
- Fredriksson, A., Forsgren, A., and Hardemark, B. (2011). Minimax optimization for handling range and setup uncertainties in proton therapy. *Medical physics*, 38(3):1672–84. 29, 37, 38, 119
- Friedrich, T., Grün, R., Scholz, U., Elsässer, T., Durante, M., and Scholz, M. (2013a). Sensitivity analysis of the relative biological effectiveness predicted by the local effect model. *Physics in medicine and biology*, 58:6827–49. 4, 33, 65, 93, 109, 131
- Friedrich, T., Scholz, U., Elsässer, T., Durante, M., and Scholz, M. (2013b). Systematic analysis of RBE and related quantities using a database of cell survival experiments with ion beam irradiation. *Journal of Radiation Research*, 54(3):494–514. 4, 33
- Friedrich, T., Weyrather, W., Elsässer, T., Durante, M., and Scholz, M. (2010). Accuracy of RBE: experimental and theoretical considerations. *Radiation and Environmental Biophysics*, 49(3):345–349. 33, 133
- Giovannini, G., Böhlen, T., Cabal, G., Bauer, J., Tessonier, T., Frey, K., Debus, J., Mairani, A., and Parodi, K. (2016). Variable RBE in proton therapy: comparison of different model predictions and their influence on clinical-like scenarios. *Radiation Oncology*, 11(1):68. 135
- Gordon, J. J., Sayah, N., Weiss, E., and Siebers, J. V. (2010). Coverage optimized planning: probabilistic treatment planning based on dose coverage histogram criteria. *Medical physics*, 37(2):550–563. 39
- Graeff, C. (2014). Motion mitigation in scanned ion beam therapy through 4D-optimization. *Physica Medica*, 30(5):570–577. 37
- Grün, R., Friedrich, T., Elsässer, T., Krämer, M., Zink, K., Karger, C. P., Durante, M., Engenhart-Cabillic, R., and Scholz, M. (2012). Impact of enhancements in the local effect model (LEM) on the predicted RBE-weighted target dose distribution in carbon ion therapy. *Physics in Medicine and Biology*, 57(22):7261–7274. 102, 103
- Haberer, T., Becher, W., Schardt, D., and Kraft, G. (1993). Magnetic scanning system for heavy ion therapy. *Nuclear Inst. and Methods in Physics Research, A*, 330(1-2):296–305. 20
- Hennig, P. (2013). Animating samples from gaussian distributions. (8):1–6. 68, 69, 79, 121
- Holloway, S. M., Holloway, M. D., and Thomas, S. J. (2017). A method for acquiring random range uncertainty probability distributions in proton therapy. *Physics in Medicine & Biology*. 132
- Hong, L., Goitein, M., Bucciolini, M., Comiskey, R., Gottschalk, B., Rosenthal, S., Serago, C., and Urie, M. (1996). A pencil beam algorithm for proton dose calculations. *Physics in Medicine and Biology*, 41(8):1305–1330. 21
- Hueso-González, F., Rabe, M., Ruggieri, T. A., Bortfeld, T., and Verburg, J. M. (2018). A full-scale clinical prototype for proton range verification using prompt gamma-ray spectroscopy. *Physics in Medicine & Biology*, 63(18):185019. 34
- Hysing, L. B., Söhn, M., Muren, L. P., and Alber, M. (2011). A coverage probability based method to estimate patient-specific small bowel planning volumes for use in radiotherapy. *Radiotherapy and Oncology*, 100(3):407–411. 39
- ICRU (2008). *Relative Biological Effectiveness in Ion Beam Therapy*. Number 46. 11
- Imhof, J. P. (1961). Computing the Distribution of Quadratic Forms in Normal Variables. *Biometrika*, 48(3/4):419. 39, 70
- Inaniwa, T., Kanematsu, N., Matsufuji, N., Kanai, T., Shirai, T., Noda, K., Tsuji, H., Kamada, T., and Tsujii, H. (2015). Reformulation of a clinical-dose system for carbon-ion radiotherapy treatment planning at the National Institute of Radiological Sciences, Japan. *Physics in Medicine and Biology*, 60(8):3271–3286. 4
- Jensen, A. D., Nikoghosyan, A. V., Lossner, K., Herfarth, K. K., Debus, J., and Mütner, M. W. (2012). IMRT and carbon ion boost for malignant salivary gland tumors: Interim analysis of the COSMIC trial. *BMC Cancer*, 12. 31
- Kamada, T., Tsujii, H., Blakely, E. A., Debus, J., De Neve, W., Durante, M., Jäkel, O., Mayer, R., Orecchia, R., Pötter, R., Vatnitsky, S., and Chu, W. T. (2015). Carbon ion radiotherapy in Japan: An assessment of 20 years of clinical experience. *The Lancet Oncology*, 16(2):e93–e100. 2

- Kamp, F., Brüningk, S., Cabal, G., Mairani, A., Parodi, K., and Wilkens, J. (2014). Variance-based sensitivity analysis of biological uncertainties in carbon ion therapy. *Physica Medica*, 30(5):583–587. 33, 34, 48, 132, 133
- Kamp, F., Cabal, G., Mairani, a., Parodi, K., Wilkens, J., and Carlson, D. (2015). Fast Biological Modeling for Voxel-based Heavy Ion Therapy Treatment Planning using the Mechanistic Repair-Misrepair-Fixation (RMF) Model and Nuclear Fragment Spectra. *International Journal of Radiation Oncology*Biophysics*Physics*. 122
- Kanai, T., Furusawa, Y., Fukutsu, K., Itsukaichi, H., Eguchi-Kasai, K., and Ohara, H. (1997). Irradiation of mixed beam and design of spread-out Bragg peak for heavy-ion radiotherapy. *Radiation research*, 147(1):78–85. 4
- Karger, C. P. and Peschke, P. (2017). RBE and related modeling in carbon-ion therapy. *Physics in Medicine & Biology*, 63(1):01TR02. 4, 32
- Karger, C. P., Peschke, P., Sanchez-Brandelik, R., Scholz, M., and Debus, J. (2006). Radiation tolerance of the rat spinal cord after 6 and 18 fractions of photons and carbon ions: Experimental results and clinical implications. *International Journal of Radiation Oncology Biology Physics*, 66(5):1488–1497. 33, 102
- Kellerer, A. M. and Rossi, H. H. (1978). A Generalized Formulation of Dual Radiation Action. *Radiation Research*, 75(3):471. 12
- Kellnberger, S., Assmann, W., Lehrack, S., Reinhardt, S., Thirolf, P., Queirós, D., Sergiadis, G., Dollinger, G., Parodi, K., and Ntziachristos, V. (2016). Ionoacoustic tomography of the proton Bragg peak in combination with ultrasound and optoacoustic imaging. *Scientific Reports*, 6(1):29305. 34
- Knopf, A. C., Boye, D., Lomax, A., and Mori, S. (2013). Adequate margin definition for scanned particle therapy in the incidence of intrafractional motion. *Physics in Medicine and Biology*. 133
- Kraft, G. (2000). Tumor therapy with heavy charged particles. *Progress in Particle and Nuclear Physics*, 45(Supplement 2):473–544. 12
- Kraft, G. and Krämer, M. (1993). Linear energy transfer and track structure. *Advances in Radiation Biology*, 17:1–507. 14
- Krämer, M., Jäkel, O., Haberer, T., Kraft, G., Scharadt, D., and Weber, U. (2000). Treatment planning for heavy-ion radiotherapy: physical beam model and dose optimization. *Physics in medicine and biology*, 45(11):3299–317. 20
- Krämer, M. and Scholz, M. (2000). Treatment planning for heavy-ion radiotherapy: calculation and optimization of biologically effective dose. *Physics in medicine and biology*, 45:3319–3330. 11, 22, 23, 83
- Krämer, M. and Scholz, M. (2006). Rapid calculation of biological effects in ion radiotherapy. *Physics in Medicine and Biology*, 51(8):1959–1970. 23, 83
- Lehrack, S., Assmann, W., Bertrand, D., Henrotin, S., Herault, J., Heymans, V., Stappen, F. V., Thirolf, P. G., Vidal, M., Van de Walle, J., and Parodi, K. (2017). Submillimeter ionoacoustic range determination for protons in water at a clinical synchrocyclotron. *Physics in Medicine & Biology*, 62(17):L20–L30. 34
- Liebl, J., Paganetti, H., Zhu, M., and Winey, B. A. (2014). The influence of patient positioning uncertainties in proton radiotherapy on proton range and dose distributions. *Medical Physics*, 41(9):091711. 31
- Liu, H., Tang, Y., and Zhang, H. H. (2009). A new chi-square approximation to the distribution of non-negative definite quadratic forms in non-central normal variables. *Computational Statistics & Data Analysis*, 53(4):853–856. 39, 70
- Liu, W., Frank, S. J., Li, X., Li, Y., Park, P. C., Dong, L., Ronald Zhu, X., and Mohan, R. (2013). Effectiveness of robust optimization in intensity-modulated proton therapy planning for head and neck cancers. *Medical physics*, 40(5):051711. 37
- Lomax, A. (1999). Intensity modulation methods for proton radiotherapy. *Physics in Medicine and Biology*, 44(1):185–205. 29
- Lomax, A. J. (2008a). Intensity Modulated Proton Therapy. In DeLaney, T. and Kooy, H., editors, *Proton and Charged Particle Radiotherapy*. Boston: Lippincott Williams & Wilkins. 29
- Lomax, A. J. (2008b). Intensity modulated proton therapy and its sensitivity to treatment uncertainties 1: the potential effects of calculational uncertainties. *Physics in Medicine and Biology*, 53(4):1027–1042. 30, 31, 32, 37
- Lomax, A. J. (2008c). Intensity modulated proton therapy and its sensitivity to treatment uncertainties 2: the potential effects of inter-fraction and inter-field motions. *Physics in Medicine and Biology*, 53(4):1043–1056. 133
- Lomax, A. J. (2009). Charged particle therapy: The physics of interaction. *Cancer Journal*, 15(4):285–291. 6
- Lomax, A. J., Bortfeld, T., Goitein, G., Debus, J., Dykstra, C., Tercier, P. A., Coucke, P. A., and Mirimanoff, R. O. (1999). A treatment planning inter-comparison of proton and intensity modulated photon radiotherapy. *Radiotherapy and Oncology*, 51(3):257–271. 3
- Low, D. A., Harms, W. B., Mutic, S., and Purdy, J. A. (1998). A technique for the quantitative evaluation of dose distributions. *Medical Physics*, 25(5):656. 77, 78
- Lowe, M., Albertini, F., Aitkenhead, A., Lomax, A. J., and MacKay, R. I. (2016). Incorporating the effect of fractionation in the evaluation of proton plan robustness to setup errors. *Physics in Medicine and Biology*, 61(1):413–429. 35, 37, 111
- Maleike, D., Unkelbach, J., and Oelfke, U. (2006). Simulation and visualization of dose uncertainties due to interfractional organ motion. *Physics in Medicine and Biology*, 51(9):2237–2252. 35
- McNamara, A. L., Schuemann, J., and Paganetti, H. (2015). A phenomenological relative biological effectiveness (RBE) model for proton therapy based on all published in vitro cell survival data. *Physics in Medicine and Biology*, 60(21):8399–8416. 135, 136

Bibliography

- Mescher, H., Ulrich, S., and Bangert, M. (2017). Coverage-based constraints for IMRT optimization. *Physics in Medicine & Biology*, 62(18):N460–N473. 39
- Newhauser, W. D. and Zhang, R. (2015). The physics of proton therapy. *Physics in Medicine & Biology*, 60(8):R155. 6, 8, 18
- Nocedal, J., Wächter, A., and Waltz, R. A. (2009). Adaptive Barrier Update Strategies for Nonlinear Interior Methods. *SIAM Journal on Optimization*, 19(4):1674–1693. 27
- O. Jäkel, M. Krämer, C. P. Karger, J. D. (2001). Treatment planning for heavy ion radiotherapy : clinical implementation and application. *Physics in Medicine & Biology*, 46(4):1101–1116. 4
- Oelfke, U. and Bortfeld, T. (2001). Inverse planning for photon and proton beams. *Medical dosimetry : official journal of the American Association of Medical Dosimetrists*, 26(2):113–24. 28
- Paganetti, H. (2012). Range uncertainties in proton therapy and the role of Monte Carlo simulations. *Physics in Medicine and Biology*, 57:R99–R117. 30, 31, 36, 126
- Park, P. C., Cheung, J., Zhu, X. R., Sahoo, N., Court, L., and Dong, L. (2012). Fast range-corrected proton dose approximation method using prior dose distribution. *Physics in Medicine and Biology*, 57(11):3555–3569. 36
- Parodi, K., Mairani, A., Brons, S., Hasch, B. G., Sommerer, F., Naumann, J., Jäkel, O., Haberer, T., and Debus, J. (2012). Monte Carlo simulations to support start-up and treatment planning of scanned proton and carbon ion therapy at a synchrotron-based facility. *Physics in Medicine and Biology*, 57(12):3759–3784. 22
- Parodi, K., Mairani, A., and Sommerer, F. (2013). Monte Carlo-based parametrization of the lateral dose spread for clinical treatment planning of scanned proton and carbon ion beams. *Journal of Radiation Research*, 54(SUPPL.1):91–96. 22, 126
- Perkó, Z., van der Voort, S. R., van de Water, S., Hartman, C. M. H., Hoogeman, M., and Lathouwers, D. (2016). Fast and accurate sensitivity analysis of IMPT treatment plans using Polynomial Chaos Expansion. *Physics in medicine and biology*, 61(12):4646–64. 36, 122
- Pflugfelder, D., Wilkens, J. J., and Oelfke, U. (2008). Worst case optimization: a method to account for uncertainties in the optimization of intensity modulated proton therapy. *Phys. Med. Biol. Phys. Med. Biol.*, 53(53):1689–1700. 37
- PTCOG (2018). Particle Therapy Co-Operative Group. 2
- Puck, T. T. and Marcus, P. I. (1956). Action of x-rays on mammalian cells. *The Journal of experimental medicine*, 103(5):653–66. 12
- Saager, M., Glowa, C., Peschke, P., Brons, S., Grün, R., Scholz, M., Huber, P. E., Debus, J., and Karger, C. P. (2015). Split dose carbon ion irradiation of the rat spinal cord: Dependence of the relative biological effectiveness on dose and linear energy transfer. *Radiotherapy and Oncology*, 117(2):358–363. 15, 33
- Saager, M., Glowa, C., Peschke, P., Brons, S., Grün, R., Scholz, M., Huber, P. E., Debus, J., and Karger, C. P. (2016). The relative biological effectiveness of carbon ion irradiations of the rat spinal cord increases linearly with LET up to 99 keV/μm. *Acta Oncologica*, 55(12):1512–1515. 15, 33
- Saager, M., Glowa, C., Peschke, P., Brons, S., Scholz, M., Huber, P. E., Debus, J., and Karger, C. P. (2014). Carbon ion irradiation of the rat spinal cord: Dependence of the relative biological effectiveness on linear energy transfer. *International Journal of Radiation Oncology Biology Physics*, 90(1):63–70. 15, 33
- Sakama, M., Kanematsu, N., and Inaniwa, T. (2016). A robustness analysis method with fast estimation of dose uncertainty distributions for carbon-ion therapy treatment planning. *Physics in Medicine and Biology*, 61(15):5818–5836. 36, 39, 40, 111, 122
- Sanchez-Parcerisa, D. (2009). Experimental and computational investigations on the water-to-air stopping power ratio for ion chamber dosimetry in carbon ion radiotherapy. *PhD Thesis*, (November). 7
- Schaffner, B. and Pedroni, E. (1998). The precision of proton range calculations in proton radiotherapy treatment planning: experimental verification of the relation between CT-HU and proton stopping power. *Physics in Medicine and Biology*, 43(6):1579–1592. 30
- Schaffner, B., Pedroni, E., and Lomax, A. (1999). Dose calculation models for proton treatment planning using a dynamic beam delivery system: an attempt to include density heterogeneity effects in the analytical dose calculation. *Physics in medicine and biology*, 44(1):27–41. 21
- Schardt, D., Elsässer, T., and Schulz-Ertner, D. (2010). Heavy-ion tumor therapy: Physical and radiobiological benefits. *Reviews of Modern Physics*, 82(1):383–425. 6, 12
- Schölkopf, B. (2002). Learning with kernels. *Journal of the Electrochemical Society*, 129(November):2865. 43
- Scholz, M., Kellerer, a. M., Kraft-Weyrather, W., and Kraft, G. (1997). Computation of cell survival in heavy ion beams for therapy. *Radiation and Environmental Biophysics*, 36(1):59–66. 4, 14, 17, 22
- Scholz, M. and Kraft, G. (1996). Track structure and the calculation of biological effects of heavy charged particles. *Advances in Space Research*, 18(1-2):5–14. 14, 16, 17
- Schwaab, J., Brons, S., Fieres, J., and Parodi, K. (2011). Experimental characterization of lateral profiles of scanned proton and carbon ion pencil beams for improved beam models in ion therapy treatment planning. *Physics in Medicine and Biology*, 56(24):7813–7827. 22
- Seco, J., Robertson, D., Trofimov, A., and Paganetti, H. (2009). Breathing interplay effects during proton beam scanning: simulation and statistical analysis. *Physics in Medicine and Biology*, 54(14):N283–N294. 31
- Seltzer, S. M., Bartlett, D. T., Burns, D. T., Dietze, G., Menzel, H.-G., Paretzke, H. G., Wambersie, A., and Tada, J. (2011). Fundamental Quantities And Units For Ionizing Radiation (Revised) ICRU-report No 85. *Journal of the ICRU*, 11(1):1–35. 6, 10

- Serber, R. (1947). Nuclear Reactions at High Energies. *Physical Review*, 72(11):1114–1115. 9
- Siddon, R. L. (1985). Fast calculation of the exact radiological path for a three-dimensional CT array. *Medical Physics*, 12(2):252–255. 18
- Siggel, M., Ziegenhein, P., Nill, S., and Oelfke, U. (2012). Boosting runtime-performance of photon pencil beam algorithms for radiotherapy treatment planning. *Physica Medica*, 28(4):273–280. 87
- Sigmund, P., Bimbot, R., Geissel, H., Paul, H., Schinner, A., Wambersie, A., DeLuca, P. M., and Seltzer, S. M. (2005). Stopping of ions heavier than helium. *Journal of the International Commission on Radiation Units and Measurements*, 5(1):0–0. 7
- Sinclair, W. (1966). The shape of radiation survival curves of mammalian cells cultured in vitro. 12
- Sobotta, B., Söhn, M., and Alber, M. (2010). Robust optimization based upon statistical theory. *Medical Physics*, 37(8):4019–4028. 39
- Sobotta, B., Söhn, M., and Alber, M. (2012). Accelerated evaluation of the robustness of treatment plans against geometric uncertainties by Gaussian processes. *Physics in Medicine and Biology*, 57(23):8023–8039. 35, 36
- Soukup, M., Fippel, M., and Alber, M. (2005). A pencil beam algorithm for intensity modulated proton therapy derived from Monte Carlo simulations. *Physics in medicine and biology*, 50(21):5089–5104. 125, 126
- Steitz, J., Naumann, P., Ulrich, S., Haefner, M. F., Sterzing, F., Oelfke, U., and Bangert, M. (2016). Worst case optimization for interfractional motion mitigation in carbon ion therapy of pancreatic cancer. *Radiation Oncology*, 11(1):134. 40, 122
- Stewart, B. W. and Wild, C. P. (2014). World Cancer Report 2014 [Online]. *World Health Organization*. 1
- Suit, H., DeLaney, T., Goldberg, S., Paganetti, H., Clasié, B., Gerweck, L., Niemierko, A., Hall, E., Flanz, J., Hallman, J., and Trofimov, A. (2010). Proton vs carbon ion beams in the definitive radiation treatment of cancer patients. *Radiotherapy and Oncology*, 95(February 2009):3–22. 4, 29
- Taylor, P. A., Kry, S. F., and Followill, D. S. (2017). Pencil Beam Algorithms Are Unsuitable for Proton Dose Calculations in Lung. *International Journal of Radiation Oncology Biology Physics*, 99(3):750–756. 31, 125
- Tommasino, F. and Durante, M. (2015). Proton radiobiology. *Cancers*, 7(1):353–381. 13
- Ulrich, S., Wieser, H.-P., Cao, W., Mohan, R., and Bangert, M. (2017). Impact of respiratory motion on variable relative biological effectiveness in 4D-dose distributions of proton therapy. *Acta Oncologica*, 56(11):1420–1427. 165
- Unkelbach, J. (2006). Inclusion of organ motion in IMRT optimization using probabilistic treatment planning. page 124. 39
- Unkelbach, J., Alber, M., Bangert, M., Bokrantz, R., Chan, T. C. Y., Deasy, J. O., Fredriksson, A., Gorissen, B. L., Herk, M. V., Liu, W., Mahmoudzadeh, H., Nohadani, O., Siebers, J. V., Witte, M., and Xu, H. (2018). Robust radiotherapy planning. 37, 39, 122, 126, 127
- Unkelbach, J., Bortfeld, T., Martin, B. C., and Soukup, M. (2009). Reducing the sensitivity of IMPT treatment plans to setup errors and range uncertainties via probabilistic treatment planning. *Medical physics*, 36(1):149–163. 39, 47, 71
- Unkelbach, J., Chan, T. C. Y., and Bortfeld, T. (2007). Accounting for range uncertainties in the optimization of intensity modulated proton therapy. *Physics in Medicine and Biology*, 52(10):2755–2773. 39, 127
- Unkelbach, J. and Paganetti, H. (2018). Robust Proton Treatment Planning: Physical and Biological Optimization. *Seminars in Radiation Oncology*, 28(2):88–96. 37, 120, 127
- Van Herk, M. (2004). Errors and Margins in Radiotherapy. *Seminars in Radiation Oncology*, 14(1):52–64. 36
- van Herk, M., Remeijer, P., and Lebesque, J. V. (2002). Inclusion of geometric uncertainties in treatment plan evaluation. *International journal of radiation oncology, biology, physics*, 52(5):1407–22. 35
- Veiga, C., Janssens, G., Teng, C.-L., Baudier, T., Hotoiu, L., McClelland, J. R., Royle, G., Lin, L., Yin, L., Metz, J., Solberg, T. D., Tochner, Z., Simone, C. B., McDonough, J., and Kevin Teo, B.-K. (2016). First Clinical Investigation of Cone Beam Computed Tomography and Deformable Registration for Adaptive Proton Therapy for Lung Cancer. *International Journal of Radiation Oncology Biology Physics*, 95(1):549–559. 34
- Wächter, A. and Biegler, L. T. (2006). *On the Implementation of a Primal-Dual Interior Point Filter Line Search Algorithm for Large-Scale Nonlinear Programming*, volume 106. 27
- Wahl, N. (2018). *Analytical models for probabilistic inverse treatment planning in intensity-modulated proton therapy*. PhD thesis, University of Heidelberg. 71, 128
- Wahl, N., Hennig, P., Wieser, H. P., and Bangert, M. (2017). Efficiency of analytical and sampling-based uncertainty propagation in intensity-modulated proton therapy. *Physics in medicine and biology*, 62(14):5790–5807. ii, 35, 36, 40, 43, 71, 75, 77, 126, 128, 129, 134, 135, 165
- Wahl, N., Hennig, P., Wieser, H.-P., and Bangert, M. (2018a). Analytical incorporation of fractionation effects in probabilistic treatment planning for intensity-modulated proton therapy. *Medical Physics*, 45:1317–1328. ii, 40, 43, 129, 135, 164
- Wahl, N., Hennig, P., Wieser, H.-P., and Bangert, M. (2018b). Analytical probabilistic models for dose quality metrics and optimization objectives. In *ESTRO 37 Abstract Book*. Elsevier. 166
- Wahl, N., Hennig, P., Wieser, H.-P., and Bangert, M. (2018c). Smooth animations of the probabilistic analog to worst-case dose distributions. In *ESTRO 37 Abstract Book*. 166
- Wahl, N., Wieser, H.-P., and Bangert, M. (2016). Analytical Probabilistic Modeling for Proton and Carbon Ion Radiotherapy. In *Novel Techniques in Ion Beam Radiotherapy*. 166
- Wedenberg, M., Lind, B. K., and Hårdemark, B. (2013). A model for the relative biological effectiveness of

- protons: the tissue specific parameter α/β of photons is a predictor for the sensitivity to LET changes. *Acta oncologica (Stockholm, Sweden)*, 52(3):580–8. 135
- WHO (2018). World Health Organisation. 1
- Wieser, H.-P. (2018a). matRad - Ein open-source Planungssystem für strahlentherapeutische Krebsbehandlung. In *Matlab EXPO Munich*. 165
- Wieser, H.-P. (2018b). matRad as a collaboration tool in radiation oncology. In *matRad Workshop in Santiago de Chile*. 165
- Wieser, H.-P., Cisternas, E., Wahl, N., Ulrich, S., Stadler, A., Mescher, H., Müller, L.-R., Klinge, T., Gabrys, H., Burigo, L., Mairani, A., Ecker, S., Ackermann, B., Ellerbrock, M., Parodi, K., Jäkel, O., and Bangert, M. (2017a). Development of the open-source dose calculation and optimization toolkit matRad. *Medical Physics*, 44(6):2556–2568. ii, 21, 22, 28, 74, 80, 86
- Wieser, H.-P., Hennig, P., Wahl, N., and Bangert, M. (2017b). Analytical probabilistic modeling of RBE-weighted dose for ion therapy. *Physics in Medicine and Biology*, 62:8959–8982. ii, 35, 88, 90, 106, 107, 126, 127
- Wieser, H.-P., Hennig, P., Wahl, N., and Bangert, M. (2017c). Analytical probabilistic modelling of RBE-weighted dose for ion therapy. In *1st ESTRO Physics Workshop, Session: LET, RBE and the handling of their consequences in treatment planning*. 165
- Wieser, H.-P., Mairani, A., Ackermann, B., Tessonier, T., Ciocca, M., Parodi, K., Jäkel, O., and Bangert, M. (2016a). Validation of a proton dose calculation engine for the open-source treatment planning software matRad. In *PTCOG Prague - Poster*. 166
- Wieser, H.-P., Mairani, A., Ciocca, M., Jäkel, O., and Bangert, M. (2015). matRad - Open Source Toolkit für biologische Bestrahlungsplanung mit Kohlenstoff Ionen. In *DGMP Tagung Marburg*. 165
- Wieser, H.-P., Wahl, N., Hennig, P., and Bangert, M. (2016b). Analytical probabilistic modeling of range and setup uncertainties in carbon ion therapy planning. In *18th ICCR Conference*. 165
- Wieser, H.-P., Wahl, N., Hubert, G., Müller, L.-R., Pezzano, G., Winter, J., Ulrich, S., Burigo, L., Jäkel, O., and Bangert, M. (2018). matRad - An open-source treatment planning toolkit for educational purposes. *Medical Physics International Journal*, 6(1). ii, 22
- Wilkins, J. J. and Oelfke, U. (2006). Fast multifield optimization of the biological effect in ion therapy. *Physics in medicine and biology*, 51:3127–3140. 25, 29, 70, 75
- Wilson, R. R. (1946). Radiological Use of Fast Protons. *Radiology*, 47(5):487–491. 2
- Wohlfahrt, P., Möhler, C., Richter, C., and Greilich, S. (2018). Evaluation of Stopping-Power Prediction by Dual- and Single-Energy Computed Tomography in an Anthropomorphic Ground-Truth Phantom. *International Journal of Radiation Oncology Biology Physics*, 100(1). 34
- Wolf, I., Vetter, M., Wegner, I., Böttger, T., Nolden, M., Schöbinger, M., Hastenteufel, M., Kunert, T., and Meinzer, H. P. (2005). The medical imaging interaction toolkit. *Medical Image Analysis*. 135
- Wu, Q. and Mohan, R. (2000). Algorithms and functionality of an intensity modulated radiotherapy optimization system. *Medical Physics*, 27(4):701–711. 28
- Xie, Y., Bentefour, E. H., Janssens, G., Smeets, J., Vander Stappen, F., Hotoiu, L., Yin, L., Dolney, D., Avery, S., O’Grady, F., Prieels, D., McDonough, J., Solberg, T. D., Lustig, R. A., Lin, A., and Teo, B.-K. K. (2017). Prompt Gamma Imaging for InäVivo Range Verification of Pencil Beam Scanning Proton Therapy. *International journal of radiation oncology, biology, physics*, 99(1):210–218. 34
- Yang, M., Zhu, X. R., Park, P. C., Titt, U., Mohan, R., Virshup, G., Clayton, J. E., and Dong, L. (2012). Comprehensive analysis of proton range uncertainties related to patient stopping-power-ratio estimation using the stoichiometric calibration. *Physics in Medicine and Biology*, 57(13):4095–4115. 30
- Zaider, M. and Rossi, H. H. (1980). The Synergistic Effects of Different Radiations. *Source: Radiation Research*, 83(3):732–739. 24, 25

Disclosure

This work was funded by the German Research Foundation Grant No. BA 2279/3-1. Patient data originated from open-source data with one exception. One patient case referred to as *cranial* was provided by the MD Anderson Cancer Center, Houston. The proposed methodology for carbon ions presented in Chapter III was entirely developed by myself. Result generation and data evaluation for the validation of the open-source treatment planning system matRad (Chapter IV.1) and for the developed methodology (Chapter IV.2) were fully carried out on my own. In particular, the latter represents the central result of this dissertation.

Parts of the results presented in this thesis were published in advance in peer reviewed journals:

Publication 1: Wieser, H.-P., Cisternas, E., Wahl, N., Ulrich, S., Stadler, A., Mescher, H., Müller, L.-R., Klinge, T., Gabrys, H., Burigo, L., Mairani, A., Ecker, S., Ackermann, B., Ellerbrock, M., Parodi, K., Jäkel, O., and Bangert, M. Development of the open-source dose calculation and optimization toolkit matRad. *Medical Physics*, 44(6):25562568

Publication 1 presents a comprehensive report on the development of the open-source treatment planning toolkit matRad, which was validated against results from the clinical treatment planning system used at the Heidelberg Ion Therapy center. Multiple people contributed to this paper either through direct code commits, generation of reference results or provided base data to analytically model the interaction of charged particles with matter. Dr. Bangert M. and I were the main developers of matRad at that time, whereas I solely developed the carbon ion related functionalities. The core result of Publication 1 is given by the validation, which was carried out by me. In detail, the own contribution consisted of developing the matRad code base for carbon ions, generating results based on matRad also for all other radiation modalities, data evaluation and writing the manuscript. The background to this paper is presented in Chapter II.4.1 to II.4.3 and corresponding results are shown in Chapter IV.1. Publication 1 builds the foundation of the results presented in Chapter IV.2.

Publication 2: Wieser, H.-P., Hennig, P., Wahl, N., and Bangert, M. Analytical probabilistic modeling of RBE-weighted dose for ion therapy. *Physics in Medicine and Biology*, 62(23):8959-8982

Publication 2 presents a new methodology to perform uncertainty quantification and prob-

abilistic treatment plan optimization for carbon ion therapy considering setup and range uncertainties. The proposed theoretical methodology is presented in Chapter III.2 and was developed by me. In a further step, I implemented the new methodology into the treatment planning system matRad. Results were generated, evaluated and described in the manuscript by myself. Results of Publication 2 are presented in Chapter IV.1.

Publication 3: Wieser, H.-P., Wahl, N., Hubert, G., Müller, L.-R., Pezzano, G., Winter, J., Ulrich, S., Burigo, L., Jäkel, O., and Bangert, M. matRad - An open-source treatment planning toolkit for educational purposes. *Medical Physics International Journal*, Vol. 6(1)

Publication 3 represents a joint publication. Due to the worldwide growing interest in our open-source treatment planning system matRad, we published a comprehensive description of matRad functionalities with an emphasis on educational purposes. Each of the co-authors contributed either via direct code commits or wrote a specific method section in the manuscript. My own contribution consisted of creating the results and writing the introduction, one method section, results, discussion and the conclusion. The technical descriptions of Publication 3 are not included in this dissertation, but provide valuable information on the software tool developed in this dissertation. This is especially important for the scientific community using the developed open source platform for instance to reproduce results.

Besides the three lead author papers above I contributed to the following publications which are not part of this manuscript but partly related to this topic:

Publication 4: Bai, X., Lim G., Wieser H. P., Bangert M., Grosshans D., Mohan r., Cao W. (2019). Robust optimization to reduce the impact of biological effect variation from physical uncertainties in intensity-modulated proton therapy. *Physics in Medicine & Biology* 62(2), (Bai et al., 2019)

I contributed to the Material and Methods section by providing the underlying data for the analysis (dose- and LET influence matrices).

Publication 5: Wahl, N., Hennig, P., Wieser, H.-P., and Bangert, M. (2018a). Analytical incorporation of fractionation effects in probabilistic treatment planning for intensity-modulated proton therapy. *Medical Physics* 45(4):1317-1328, (Wahl et al., 2018a)

I contributed to the C++ based software implementations of the proposed methodology and was involved in discussing the methodology and the results. Results are not part of this dissertation.

Publication 6: Wahl, N., Hennig, P., Wieser, H. P., and Bangert, M. (2017). Efficiency of analytical and sampling-based uncertainty propagation in intensity-modulated proton

therapy. *Physics in medicine and biology*, 62(14):57905807, (Wahl et al., 2017)

I contributed to the C++ based software implementations of the proposed methodology and was involved in discussing the methodology and the results. Results are not part of this dissertation.

Publication 7: Ulrich, S., Wieser, H.-P., Cao, W., Mohan, R., and Bangert, M. (2017). Impact of respiratory motion on variable relative biological effectiveness in 4D-dose distributions of proton therapy. *Acta Oncologica*, 56(11):14201427, (Ulrich et al., 2017)

I implemented variable relative biological effectiveness related functionalities in matRad whereas 4D functionalities were implemented by Ulrich S. and Bangert M.. In addition, I wrote the introduction, half of the method section and created figures for the publication. Results are not part of this dissertation.

The following list contains my scientific contributions grouped together in workshop talks, conference talks and posters from 2015 to 2018:

Wieser, H.-P. and Bangert, M. matRad as a collaboration tool in radiation oncology, workshop talk, related to matRad and thesis, Santiago de Chile, 2018, (Wieser, 2018b)

Wieser, H.-P., Hennig, P., Wahl N. and Bangert, M. Analytical probabilistic modelling of RBE-weighted dose for carbon ion therapy, workshop talk, related to thesis finding, ESTRO, Glasgow, 2017, (Wieser et al., 2017c)

Wieser, H.-P. and Bangert, M. Ein open-source Planungssystem für strahlentherapeutische Krebsbehandlung, conference talk, related to thesis, Matlab EXPO, Munich, 2018, (Wieser, 2018a)

Wieser, H.-P., Hennig, P. and Bangert, M. Simultaneous consideration of biological and physical uncertainties in robust ion therapy planning, conference talk, related to thesis findings, ESTRO 37, Barcelona, 2018 (Wieser, 2018a)

Wieser, H.-P., Hennig, P., Wahl N. and Bangert, M. Analytical probabilistic modeling of range and setup uncertainties in carbon ion therapy planning, conference talk, thesis findings, ICCR 18, London, 2016, (Wieser et al., 2016b)

Wieser, H.-P. and Bangert, M. matRad - Open Source Toolkit für biologische Bestrahlungsplanung mit Kohlenstoff Ionen, conference talk, thesis findings, DGMP 46, Marburg, 2015, (Wieser et al., 2015)

Wahl N., Wieser, H.-P., Hennig, P. and Bangert, M. Analytical probabilistic models for dose

quality metrics and optimization objectives, conference poster, related to thesis, ESTRO 37, Barcelona, 2018, (Wahl et al., 2018b)

Wahl N., Wieser, H.-P., Hennig, P. and Bangert, M. Smooth animations of the probabilistic analog to worst-case dose distributions, conference poster, related to thesis, ESTRO 37, Barcelona, 2018, (Wahl et al., 2018c)

Wahl N., Wieser, H.-P., Hennig, P. and Bangert, M. Analytical Probabilistic Modeling for Proton and Carbon Ion Radiotherapy, conference poster, thesis findings, Novel Techniques in Ion Beam Radiotherapy Heidelberg, 2016, (Wahl et al., 2016)

Wieser, H.-P. and Bangert, M. et.al. Validation of a proton dose calculation engine for the open-source treatment planning software matRad, conference poster, thesis findings, PTCOG 55, Prague, 2016, (Wieser et al., 2016a)

Curriculum Vitae

- today scientific staff member, **Ludwig-Maximilians University**
FEB. 2019 *Munich, Germany* - Chair of Experimental Physics and Medical Physics
focus on ionoacoustic <https://www.med.physik.uni-muenchen.de>
- AUG. 2018 PhD student, **German Cancer Research Center**
FEB. 2015 *Heidelberg, Germany* - Radiotherapy Optimization,
emphasis on probabilistic optimization <https://www.dkfz.de/radopt>
- MAY 2017 Internship, **Max Planck Institute for Intelligent Systems**
AUG. 2017 *Tübingen, Germany* - Probabilistic Numerics Group,
developing closed-form uncertainty propagation algorithms for radiotherapy
- FEB. 2017 Internship, **University of Texas MD Anderson Cancer Center**
APR. 2017 *Houston, USA* - research intern in the radiotherapy department,
purpose: robust treatment planning for protons
- MAY 2016 Internship, **Max Planck Institute for Intelligent Systems**
AUG. 2016 *Tübingen, Germany* - Probabilistic Numerics Group,
developing closed-form uncertainty propagation algorithms for radiotherapy
- NOV. 2013 Master of Science (Dipl.-Ing.), **Carinthia University of Applied Sciences**
SEPT. 2011 *Klagenfurt, Austria* - Health Care Information Technology
emphasis on medical devices and medical image processing
- AUG. 2013 Intern at **University of Texas MD Anderson Cancer Center**
FEB. 2013 *Houston, USA* - research intern in the diagnostic radiology department
purpose: automated prostate zone segmentation
- JULY 2011 Bachelor of Science, **Carinthia University of Applied Sciences**
SEPT. 2008 *Klagenfurt, Austria* - Medical Information Technology
emphasis on medical image processing, mathematics and electrical engineering
- JUNE 2008 University-Entrance Diploma, **HTL**
SEPT. 2003 *Salzburg, Austria* - Secondary School for Electrical Engineering
focus on power engineering and industrial electronics

Acknowledgments

First, I would like to express my gratitude and thank my supervisor Dr. Mark Bangert for providing the opportunity to work on this exciting subject. I have always been enjoying working with him and his group Radiotherapy Optimization for the past 3.5 years. In particular, I appreciate his professionalism, openness and friendly personality which is one of the main reasons for the pleasant atmosphere in his group and explains why time has flown by so fast. The weekly discussions and feedback either in person or via video conferences pushed and supported me in pursuing my doctoral degree. Further, I am thankful that there was, besides the main project work, always enough room to develop my own ideas.

Second, I would like to thank my doctoral father Prof. Dr. Christian Karger for providing important clinical feedback and experience throughout my PhD. Also Dr. Dr. Amir Abdollahi and Prof. Dr. Jan Wilkens should definitely be mentioned for being my thesis advisors and for their constructive input and support during several thesis advisory committee meetings. I also thank Dr. Philipp Hennig for his excellent guidance and helpfulness during the algorithm development during my two stays at the Max Planck Institute for Intelligent Systems in Tübingen. In addition, I am thankful to Prof. Dr. Radhe Mohan, Dr. Uwe Titt and Dr. Wenhua Cao for hosting me three months at the MD Anderson Cancer Center in Houston.

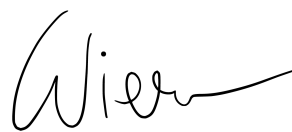
I am grateful to all colleagues of the medical physics department in radiation oncology who made my stay at the German Cancer Research Center in Heidelberg a very enjoyable period of my life, both at work and at various social events. In particular, I would like to thank my buddies Niklas Wahl, Hubert Gabrys, Henning Mescher and Amit Ben Antony Bennan for their exceptional helpfulness and their valuable support in countless situations. I will definitely miss Heidelberg and our various team sport activities we had together, although swimming in the Neckar was not one of my best experiences. Let's go "BEAM ON !!!" Also a big shout out and thanks to the growing matRad community across the globe and the increasing interest in this open source project. In that regard, I would like to thank Mark Bangert and Eduardo Cisternas who initially started establishing matRad. This allowed me to build upon their work and experiences quickly.

I would also like to thank my mother and father as well as my parents in law Magdalena and Miguel for supporting me throughout the past years. Last but not least my gratitude goes to my wife, the most important person in my life. Madeleine, I'm deeply thankful for consistently supporting me, for your endurance and for the sacrifices you have made to help me to get to this point. Without such supportive family and friends this wouldn't have been possible. Thank you.

Eidesstattliche Versicherung

1. Bei der eingereichten Dissertation zu dem Thema
Probabilistic Treatment Planning for Carbon Ion Therapy
handelt es sich um meine eigenständig erbrachte Leistung.
2. Ich habe nur die angegebenen Quellen und Hilfsmittel benutzt und mich keiner unzulässigen Hilfe Dritter bedient. Insbesondere habe ich wörtlich oder sinngemäß aus anderen Werken übernommene Inhalte als solche kenntlich gemacht.
3. Die Arbeit oder Teile davon habe ich bislang nicht an einer Hochschule des In- oder Auslands als Bestandteil einer Prüfungs- oder Qualifikationsleistung vorgelegt.
4. Die Richtigkeit der vorstehenden Erklärungen bestätige ich.
5. Die Bedeutung der eidesstattlichen Versicherung und die strafrechtlichen Folgen einer unrichtigen oder unvollständigen eidesstattlichen Versicherung sind mir bekannt. Ich versichere an Eides statt, dass ich nach bestem Wissen die reine Wahrheit erkläre und nichts verschwiegen habe.

Munich, May 2, 2019

A handwritten signature in black ink, appearing to read 'Wieder', written over a horizontal line.

Ort, Datum

Unterschrift